ASME
SETTING THE STANDARD

Transactions of the ASME, Journal of Heat Transfer (ISSN 0022-1481) is published monthly by The American Society of Mechanical Engineers, Three Park Avenue, New York, NY 10016. Periodicals postage paid at New York, NY and additional mailing offices. POSTMASTER: Send address changes to Transactions of the ASME, Journal of Heat Transfer, c/o THE AMERICAN SOCIETY OF MECHANICAL ENGINEERS, 22 Law Drive, Box 2300, Fairfield, NJ 07007-2300. **CHANGES OF ADDRESS** must be received at Society headquarters seven weeks before they are to be effective. Please send old label and new address. **STATEMENT from By-Laws.** The Society shall not be responsible for statements or opinions advanced in papers or ... printed in its publications (B7.1, Para. 3).

Journal of Heat Transfer

Published Monthly by ASME

VOLUME 128 • NUMBER 6 • JUNE 2006

RESEARCH PAPERS

TECHNICAL BRIEFS

(**Contents continued on inside back cover**)

This journal is printed on acid-free paper, which exceeds the ANSI Z39.48-1992 specification for permanence of paper and library materials. ♾™
♻ 85% recycled content, including 10% post-consumer fibers.

Journal of Heat Transfer **Volume 128, Number 6** **JUNE 2006**

The ASME Journal of Heat Transfer is abstracted and indexed in the following:

Applied Science and Technology Index, Chemical Abstracts, Chemical Engineering and Biotechnology Abstracts (Electronic equivalent of Process and Chemical Engineering), Civil Engineering Abstracts, Compendex (The electronic equivalent of Engineering Index), Corrosion Abstracts, Current Contents, E & P Health, Safety, and Environment, Ei EncompassLit, Engineered Materials Abstracts, Engineering Index, Enviroline (The electronic equivalent of Environment Abstracts), Environment Abstracts, Environmental Engineering Abstracts, Environmental Science and Pollution Management, Fluidex, Fuel and Energy Abstracts, Index to Scientific Reviews, INSPEC, International Building Services Abstracts, Mechanical & Transportation Engineering Abstracts, Mechanical Engineering Abstracts, METADEX (The electronic equivalent of Metals Abstracts and Alloys Index), Petroleum Abstracts, Process and Chemical Engineering, Referativnyi Zhurnal, Science Citation Index, SciSearch (The electronic equivalent of Science Citation Index), Theoretical Chemical Engineering

Simulation of Film Cooling Enhancement With Mist Injection

Xianchang Li
e-mail: xli8@uno.edu

Ting Wang

Energy Conversion & Conservation Center,
University of New Orleans,
2000 Lakeshore Dr.,
New Orleans, LA 70148-2220

Cooling of gas turbine hot-section components, such as combustor liners, combustor transition pieces, and turbine vanes (nozzles) and blades (buckets), is a critical task for improving the life and reliability of them. Conventional cooling techniques using air-film cooling, impingement jet cooling, and turbulators have significantly contributed to cooling enhancements in the past. However, the increased net benefits that can be continuously harnessed by using these conventional cooling techniques seem to be incremental and are about to approach their limit. Therefore, new cooling techniques are essential for surpassing these current limits. This paper investigates the potential of film-cooling enhancement by injecting mist into the coolant. The computational results show that a small amount of injection (2% of the coolant flow rate) can enhance the adiabatic cooling effectiveness about 30–50%. The cooling enhancement takes place more strongly in the downstream region, where the single-phase film cooling becomes less powerful. Three different holes are used in this study including a two-dimensional (2D) slot, a round hole, and a fan-shaped diffusion hole. A comprehensive study is performed on the effect of flue gas temperature, blowing angle, blowing ratio, mist injection rate, and droplet size on the cooling effectiveness with 2D cases. Analysis on droplet history (trajectory and size) is undertaken to interpret the mechanism of droplet dynamics. [DOI: 10.1115/1.2171695]

Keywords: film cooling, turbine-blade cooling, mist cooling

Introduction

Cooling of gas turbine hot-section components, such as combustor liners, combustor transition pieces, turbine vanes (nozzles) and blades (buckets), has always been a critical task for improving the life and reliability of hot-section components. Air-film cooling has widely been used and intensively studied as an effective scheme for more than half a century [1,2]. To improve the performance of air-film cooling, many studies have been conducted by examining the effect of flow and geometric parameters, including injection angles, injection hole configuration, density ratio, and blowing ratio. For example, Jia et al. [3] investigated a slot jet film cooling by using numerical simulations coupled with LDV experiments. Different jet angles from 15 deg to 60 deg with jet-blowing ratios ranging from 2 to 9 were studied. Their results showed a recirculation bubble downstream of the jet vanishes when the angle is 30 deg or less. They also found the blowing ratio has a large effect on the size of recirculation and, consequently, on film cooling. Kwak and Han [4] measured heat transfer coefficients and film-cooling effectiveness on a gas turbine blade tip. Their results showed as the blowing ratio increased, the heat transfer coefficient decreased while film effectiveness increased. Heat transfer coefficient and film effectiveness were found to increase with increasing tip gap clearance. Wang et al. [5] conducted an experimental study focusing on the flow mixing behavior inside the slots. Various parameters, including orientation angle, inclination angle, slot width, effect of primary flow, and slot depth, were systematically examined. The optimum slot depth was found to range from 2 to 2.8 times the jet diameter. The compound angle configuration (60 deg jet orientation and 30 deg slot inclination angles) was discovered to be the best choice.

Among the typical holes are simple-angle holes with lateral or forward diffusion and compound-angle holes with forward diffusion. The performance of film cooling with different holes varies by 30–50% subject to geometric and flow conditions. Bell et al. [6] studied film cooling from shaped holes and measured the local and spatially averaged adiabatic film-cooling effectiveness. They found laterally diffused, compound-angle holes and forward-diffused, compound-angle holes produce higher effectiveness magnitudes over much wider ranges of blowing ratio and momentum flux ratio compared to the other three simple-angle configurations tested. All the three simple-angle hole geometries (cylindrical round, simple-angle holes; laterally diffused, simple-angle holes; and forward-diffused, simple-angle holes) show larger increases of spanwise-averaged adiabatic effectiveness as the density ratio increases from 0.9 to 1.4. Brittingham and Leylek [7] performed numerical simulation on film cooling with compound-angle-shaped holes and concluded that superposition of individual effects for compound-angle cylindrical holes and streamwise-shaped holes do not necessarily apply to compound-angle-shaped holes. The compound-angle-shaped holes can be designed to minimize uncooled hot region between adjacent holes and, thus, somewhat mimic slot-jet performance. From many of the previous studies, the optimal blowing ratio is discovered ranging from 0.5 to 1.0. The 35 deg injection angle and the shaped holes are found to be the most effective.

As next-generation turbines will be required to burn alternate fuels with high hydrogen (H_2) and carbon monoxide (CO) content from coal-derived syngas, cooling gas turbines becomes more difficult and more important. The high contents of H_2 and CO will increase flame temperatures and flame speeds from those of natural-gas combustion. Although conventional cooling techniques using air-film cooling, impingement-jet cooling, and turbulators have significantly contributed to cooling enhancements in the past, the increased net benefits, which can be continuously harnessed by using these conventional cooling techniques, seem to be incremental and are about to approach their limit. Therefore, new cooling techniques are essential. This paper investigates the potential of film-cooling enhancement by injecting mist into the coolant. Film cooling with mist injection can improve single-phase air-film cooling due to the following mechanisms: (a) the latent heat of evaporation serves as a heat sink to absorb large amounts of heat; (b) direct contact of liquid droplets with the cooling wall can significantly increase heat transfer from wall; (c) steam and water have higher specific heats (c_p) than air. In a

Contributed by the Heat Transfer Division of ASME for publication in the JOURNAL OF HEAT TRANSFER. Manuscript received April 5, 2005; final manuscript received December 9, 2005. Review conducted by Phillip M. Ligrani.

single-phase air cooling, film cooling becomes less and less effective as it moves into the downstream region. By taking advantage of the residence time needed to evaporate tiny water droplets, mist can also be strategically used to blanket weakened air cooling in the downstream region. Significant enhancement of film cooling can reduce the cooling air and, thus, lower the pressure drop along the cooling channel.

Mist has been used to enhance heat transfer in gas turbine systems in many different ways. A well-known application is gas turbine inlet air fog cooling [8], in which the droplets evaporate to lower the air inlet temperature until the relative humidity reaches 100%. In addition, fog overspray is used in industry to provide cooling in the compressor. Petr [9] shows the results of thermodynamic analysis of the gas turbine cycle with wet compression based on detailed simulation of a two-phase compression process. In 1998, Nirmalan et al. [10] applied a water-air mixture as the impingement coolant to cool gas turbine vanes. They used an airfoil containing a standard impingement tube that distributes the water-air mixture over the inner surface of the airfoil. The water flash vaporizes off the airfoil inner wall, and very high cooling rates were achieved. To explore an innovative approach to cool future high-temperature gas turbines, Guo et al. [11] studied the mist/steam cooling in a heated straight tube by injecting 7 μm (average diameter) of water droplets into the steam flow. The highest local heat transfer enhancement of 200% was achieved with 1–5% (weight) mist, and the average enhancement was 100%. Guo et al. [12] also conducted a mist/steam cooling study in a 180 deg tube bend. The overall cooling enhancement ranged from 40% to 300% with the maximum local cooling enhancement being over 800%, which occurred at about 45 deg downstream of the inlet of the test section. Li et al. [13] reported results of mist/steam cooling with a slot jet on a heated flat surface. Their results showed a 200% cooling enhancement near the stagnation point by adding 1.5% mist (in mass) to the steam flow. The mist enhancement declined to near zero by five slot widths downstream. Li et al. [14] also investigated a mist/steam slot jet impinging on a concave surface. Enhancements of 30–200% were achieved within a five-slot distance by adding 0.5% (weight) mist.

Injecting water mist into film-cooling flow has not been favored by gas turbine manufacturers because of concerns on potential erosion and corrosion problems on turbine airfoils. However, the current concern, from the point of practical applications, should not hinder the exploration of new ideas that may provide an attractive reward. The objective of this study is to initiate a preliminary investigation on whether there is potential merit in injecting mist into film-cooling flow. A numerical simulation is performed in this paper. Three different holes are used in this study, including a 2D slot, a round hole, and a diffusion hole. The computational results show that a small amount of injection (2% of the coolant flow rate) can significantly increase the cooling effectiveness up to 50%. A comprehensive investigation is also given to the effect of mainstream temperature, blowing angle, blowing ratio, mist injection rate, and droplet size on the cooling effectiveness. The adiabatic film-cooling effectiveness is compared for different cases.

Numerical Model

To study the mist effect on air-film cooling, a 2D slot is first used in this study. As shown in Fig. 1, the slot width (b) is 4 mm. The computational domain has a length of 80b and a height of 20b. The slot jet is set to 20b from the entrance of mainstream. The injection angle is 35 deg, which is considered as the optimal value [6,7]. A smaller angle (30 deg) is also examined. The vertical height of the jet hole is 1.74b, which gives an actual jet hole length of 3.04b. Note that the length of jet holes as well as the settling chamber before the jet holes can affect the numerical results of film cooling. Since this study focuses on the mist effect, the upstream condition of coolant in the chamber is not included in this paper, but in another paper [19]. Two three-dimensional (3D) holes are adopted to investigate the effect of mist transport

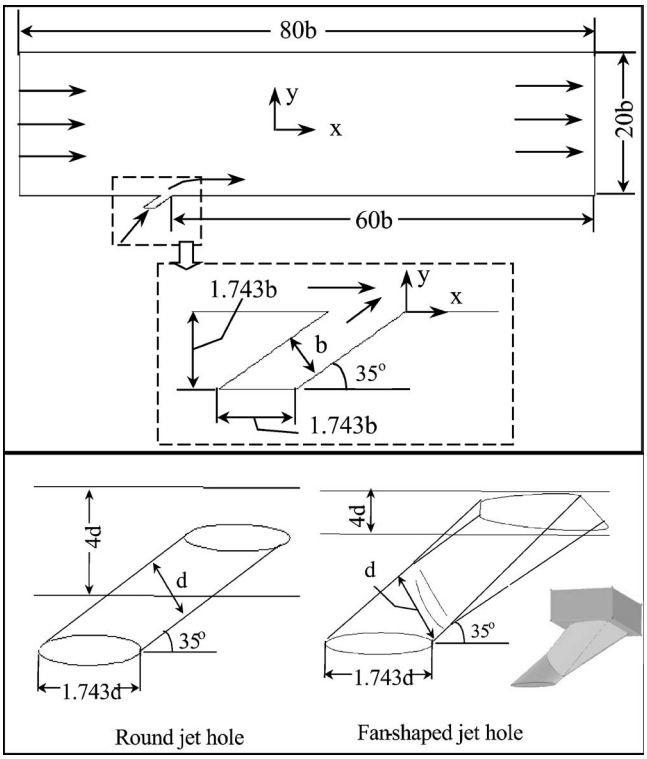

Fig. 1 Computational domain and film hole configurations

encountering the 3D effect: One is a round hole with a simple blowing angle of 35 deg, and the other is a fan-shaped hole with the same blowing angle. Both holes have a diameter (d) of 8 mm, and the lateral diffusion angle of the fan-shaped hole is 28 deg. Other different diffusion angles, for example, in [15], are not investigated in this study. The length and width of the 3D domain are kept the same as the slot hole case, and the domain has a depth of 4d, as shown in Fig. 1(b).

The commercial software package FLUENT (version 6.1.22), from Fluent, Inc., is used in this study. The simulation uses the segregated solver, which employs an implicit pressure-correction scheme [16]. The SIMPLE algorithm is used to couple the pressure and velocity. A second-order upwind scheme is used for spatial discretization of the convective terms and species. The Lagrangian trajectory calculations were employed to model the dispersed phase of droplets, including coupling with the continuous phase. The impact of the droplets on the continuous phase is considered as source terms to the governing equations. After obtaining an approximate flow field of the continuous phase (airflow in this study), FLUENT traces the droplet trajectories and computes heat and mass transfer between the droplets and the airflow.

Continuous Phase (Air/Steam)

Governing Equations. The standard 2D/3D, time-averaged, steady-state Navier-Stokes equations as well as equations for mass, energy, and species transport are solved. The governing equations for conservation of mass, momentum, and energy can be given as

$$\frac{\partial}{\partial x_i}(\rho u_i) = S_m \tag{1}$$

$$\frac{\partial}{\partial x_i}(\rho u_i u_j) = \rho \vec{g}_j - \frac{\partial P}{\partial x_j} + \frac{\partial \tau_{ij}}{\partial x_i} + F_j \tag{2}$$

$$\frac{\partial}{\partial x_i}(\rho c_p u_i T) = \frac{\partial}{\partial x_i}\left(\lambda_{\text{eff}}\frac{\partial T}{\partial x_i}\right) + \mu\Phi + S_h \tag{3}$$

where the source terms (S_m, F_j, and S_h) are used to include the contributions from the dispersed phase. τ_{ij} is the symmetric stress tensor, which can be expressed as

$$\tau_{ij} = \mu\left(\frac{\partial u_j}{\partial x_i} + \frac{\partial u_i}{\partial x_j} - \frac{2}{3}\delta_{ij}\frac{\partial u_k}{\partial x_k}\right) \tag{4}$$

$\mu\Phi$ is the heat of dissipation and λ_{eff} is the effective heat conductivity. When turbulence effect is considered, both τ_{ij} and λ_{eff} need to be modeled.

Since evaporation of droplets releases water vapor into the main airflow, species transport needs to be considered. There are three species considered, water vapor (H_2O), oxygen (O_2), and nitrogen (N_2). Dry airflow is simulated as 23% O_2 and 77% N_2 by mass. The equation for species transport is

$$\frac{\partial}{\partial x_i}(\rho u_i C_j) = \frac{\partial}{\partial x_i}\left(\rho D_{\text{eff},j}\frac{\partial C_j}{\partial x_i}\right) + S_j \tag{5}$$

where C_j is the mass fraction of one of the species (j) in the mixture, and S_j is the source term for this species. $D_{\text{eff},j}$ is the effective diffusion coefficient considering the turbulence effect.

Turbulence Model. The main flow in this study has a velocity of 10 m/s, which gives a passage Reynolds number of 30,000, based on air flow at 400 K with a length scale of 20*b* or 0.08 m. Therefore, the turbulence model must be considered. The interaction between the injected flow and the approaching flow could be anisotropic and nonequilibrium with multiscaled integral and dissipation length scales. Since the focus of this paper is not searching for a better turbulence model to account for the anisotropic turbulence structure, the effect of turbulence models on the computational results are not investigated in this paper, but in another paper by Li and Wang [19]. Comparing the current study to the existing literature shows the standard k-ε with enhanced wall treatment is one of the robust turbulence models for film-cooling flow; thus, the standard k-ε model is used in this study. The equations for the turbulent kinetic energy (k) and its dissipation rate (ε) are

$$\frac{\partial}{\partial x_i}(\rho u_i k) = \frac{\partial}{\partial x_i}\left[\left(\mu + \frac{\mu_t}{\sigma_k}\right)\frac{\partial k}{\partial x_i}\right] + G_k - \rho\varepsilon \tag{6}$$

$$\frac{\partial}{\partial x_i}(\rho u_i \varepsilon) = \frac{\partial}{\partial x_i}\left[\left(\mu + \frac{\mu_t}{\sigma_\varepsilon}\right)\frac{\partial \varepsilon}{\partial x_i}\right] + C_{1\varepsilon}G_k\frac{\varepsilon}{k} - C_{2\varepsilon}\rho\frac{\varepsilon^2}{k} \tag{7}$$

The term G_k is the generation of turbulence kinetic energy due to the mean velocity gradients. The turbulent viscosity μ_t is calculated from

$$\mu_t = \rho C_\mu \frac{k^2}{\varepsilon} \tag{8}$$

and the effective heat conductivity (λ_{eff}) and the effective diffusion coefficient are calculated by the following two equations, respectively,

$$\lambda_{\text{eff}} = \lambda + \frac{c_p\mu_t}{\text{Pr}_t} \tag{9}$$

$$D_{\text{eff}} = D + \mu_t/\text{Sc}_t \tag{10}$$

The constants $C_{1\varepsilon}$, $C_{2\varepsilon}$, C_μ, σ_k, and σ_ε used are: $C_{1\varepsilon}=1.44$, $C_{2\varepsilon}=1.92$, $C_\mu=0.09$, $\sigma_k=1.0$, $\sigma_\varepsilon=1.3$ [17]. The turbulence Prandtl number Pr_t is set to 0.85, and the turbulence Schmidt number Sc_t is set to 0.7. The equations may include more other source terms, for example, turbulence kinetic energy due to buoyancy and the contribution of fluctuating dilatation in compressible turbulence.

In the enhanced wall treatment, the standard two-layer model is combined with wall functions. To apply the two-layer approach, the computational domain is separated into a viscosity-affected region and a fully turbulent region by defining a turbulent Reynolds number Re_y, which is based on the distance from the wall,

$$\text{Re}_y = \frac{yk^{1/2}}{\nu} \tag{11}$$

where k is the turbulence kinetic energy and y is the distance from the wall. The flow is assumed in the fully turbulent region if $\text{Re}_y > 200$, and the k-ε model is used. Otherwise, the flow is in the viscosity-affected region, and the one-equation model of Wolfstein [18] is used. The turbulent viscosities calculated from the two regions are blended with a blending function (θ) to make the transition smooth.

$$\mu_{t,\text{enhanced}} = \theta\mu_t + (1-\theta)\mu_{t,l} \tag{12}$$

where μ_t is the viscosity from the k-ε model of high Reynolds number, and $\mu_{t,l}$ is the viscosity from the near-wall one-equation model. The blending function is defined so that it is 0 at the wall and 1 in the fully turbulent region. The wall functions are also enhanced by blending linear (laminar) and logarithmic (turbulent) laws of the wall to make the applicability throughout the entire near-wall region.

Boundary Conditions. The main flow is assumed to be dry air (zero humidity), and the jet flow is saturated air (100% relative humidity). Uniform velocity and temperature are assigned to the domain inlet and jet-hole inlet. The mainstream velocity is 10 m/s, and its temperature is 400 K. The jet velocity is also 10 m/s, and the temperature is 300 K. Note that these parameters are referenced in many previous studies of air-film cooling (for example, [6]), although they are not corresponding to the real conditions in gas turbine applications. Although the current paper serves as conceptual study on film cooling with mist injection, further research is to be performed with more realistic parameters for gas turbine application. To compare the results of this study to other published work, these values used by the previously published work are adopted in this study. Other values of the flow temperature and jet velocity are also assigned to study the effect of mist under different blowing and temperature ratios. The inlet conditions of the turbulence are 1 m^2/s^2 for the turbulence kinetic energy and 1 m^2/s^3 for the dissipation rate, which is equivalent to a turbulent intensity of 8.7%. The flow exit (outlet) of main computational domain is assumed to have a constant pressure. The backflow (reverse flow), if any, is set to 400 K. A more detailed study on various models and boundary conditions has been conducted by the authors in [19], whereas this paper focuses on modeling water-droplet evaporation dynamics and examining the potential mist-cooling enhancement.

All the walls in the computational domain are adiabatic and have a nonslip boundary condition. Zero velocity and temperature gradients are assigned to the side boundaries of the 3D computational domain (i.e., symmetric boundary condition).

Discrete Phase (Water Droplets)

Droplet Flow and Heat Transfer. Basically, the droplets in the airflow can encounter inertia and hydrodynamic drags. Because of the forces experienced by a droplet in a flow field, the droplet can be either accelerated or decelerated. The velocity change can be formulated by

$$m_p\frac{d\mathbf{v}_p}{dt} = F_d + F_g + F_o \tag{13}$$

where F_d is the drag of the fluid on the droplet and F_g is the gravity. F_o represents the other forces, and $\mathbf{v_p}$ is the droplet velocity (vector). The forces represented by F_o typically include the "virtual mass" force, thermophoretic force, Brownian force, Saffman's lift force, etc.

Theoretically, evaporation occurs at two stages: (i) When tem-

perature is higher than the saturation temperature (based on local water vapor concentration), water evaporates and the evaporation is controlled by the water vapor partial pressure until 100% relative humidity is achieved; and (ii) When the boiling temperature (determined by the air-water mixture pressure) is reached, water continues to evaporate. After the droplet is evaporated due to either high-temperature or low-moisture partial pressure, the vapor diffuses into the main flow and is transported away. The rate of vaporization is governed by the concentration difference between the surface and the airstream, and the corresponding mass change rate of the droplet can be given by

$$\frac{dm_p}{dt} = \pi d^2 k_c (C_s - C_\infty) \tag{14}$$

where k_c is the mass transfer coefficient and C_s is the concentration of the vapor at the droplet surface, which is evaluated by assuming that the flow over the surface is saturated. C_∞ is the vapor concentration of the bulk flow, obtained by solving the transport equations. The values of k_c can be calculated from empirical correlations by [20,21]

$$\mathrm{Sh}_d = \frac{k_c d}{D} = 2.0 + 0.6\mathrm{Re}_d^{0.5}\mathrm{Sc}^{0.33} \tag{15}$$

where Sh is the Sherwood number, Sc is the Schmidt number (defined as ν/D), and D is the diffusion coefficient of vapor in the bulk flow.

When the droplet temperature reaches the boiling point, the following equation can be used to evaluate its evaporation rate [22]:

$$\frac{dm_p}{dt} = \pi d^2 \left(\frac{\lambda}{d}\right)(2.0 + 0.46\mathrm{Re}_d^{0.5})\frac{1}{c_p}\ln\left(1 + \frac{c_p(T_\infty - T)}{h_{fg}}\right) \tag{16}$$

where λ is the heat conductivity of the gas/air and h_{fg} is the droplet latent heat. c_p is the specific heat of the bulk flow.

The droplet temperature can also be changed due to heat transfer between droplets and the continuous phase. Without considering radiation heat transfer, the droplet's sensible heat change depends on the convective heat transfer and latent heat h_{fg}, as shown in the following:

$$m_p c_p \frac{dT}{dt} = \pi d^2 h(T_\infty - T) + \frac{dm_p}{dt} h_{fg} \tag{17}$$

where the convective heat transfer coefficient (h) can be obtained with an empirical correlation similar to Eq. (15) [20,21]

$$\mathrm{Nu}_d = \frac{hd}{\lambda} = 2.0 + 0.6\mathrm{Re}_d^{0.5}\mathrm{Pr}^{0.33} \tag{18}$$

where Nu is the Nusselt number and Pr is the Prandtl number.

In mist film cooling, the temperature of main flow will be above the water boiling temperature. Note the characteristic velocity in Re_d is the relative velocity between the droplet and airflow, which is usually small for droplets in micrometers. Therefore, Re_d is also very small. In addition, the term $c_p(T_\infty - T)/h_{fg}$ in Eq. (16) can be much smaller than 1 (0.04 in this study). By ignoring the term with Re and using $\ln(1+\delta)=\delta$, the approximate droplet evaporation time can be obtained as

$$t = \frac{h_{fg}\rho d^2}{2\lambda(T_\infty - T)} \tag{19}$$

It can be seen that the evaporation time is proportional to the square of diameter. Assuming $d=10$ μm and $T_\infty - T = 100$ K, the evaporation time will be 0.038 s. If the average velocity of droplets is 6 m/s, the distance to evaporate the droplets is 0.23 m. Considering the length of 0.24 m downstream of the slot in this study, this means theoretically most of the droplets less than 10 μm are expected to evaporate inside the computational domain; whereas, the droplets larger than 10 μm or at a higher speed will not evaporate within the computational domain. Lower temperature difference will lengthen the evaporation, but the neglected term means an even shorter time in reality.

Stochastic Particle Tracking. The effects of turbulence on the dispersion of droplets/particles is considered by using stochastic tracking. Basically, the droplet trajectories are calculated by using the instantaneous flow velocity ($\bar{u}+u'$) rather than the average velocity ($\bar{u}$). The velocity fluctuations are then given as

$$u' = \varsigma(\overline{u'^2})^{0.5} = \varsigma\left(\frac{2k}{3}\right)^{0.5} \tag{20}$$

where ς is a normally distributed random number. This velocity will apply during the characteristic lifetime of the eddy t_e, a time scale defined by either of the following equations:

$$t_e = \frac{0.3k}{\varepsilon} \tag{21}$$

$$t_e = -0.15\frac{k}{\varepsilon}\log(r) \tag{22}$$

where r is a uniform distributed random number ranging from 0 to 1. In case the droplet slip velocity is so large that the time for the droplet to cross the eddy is shorter than the time defined above, the droplet eddy crossing time will be used, which is defined as

$$t_{\mathrm{cross}} = -t_p \ln\left[1 - \frac{L_e}{t_p|u - u_p|}\right] \tag{23}$$

where t_p is the particle relaxation time with $t_p = \rho_p d_p^2/(18\rho_g \nu_g)$, L_e is the eddy length scale, and $|u-u_p|$ is the magnitude of the relative velocity. After this time period, the instantaneous velocity will be updated with a new ς value until a full trajectory is obtained. The random effect of the turbulence on the droplets can be reasonably predicted only if a sufficient number of trajectories are calculated. In this study, the trajectory number is chosen to be 25 and several test runs indicated that increasing this number does not make the result much different.

Mist Injection and Droplet Sizes. For the 2D slot case, the mist is injected at 25 locations uniformly distributed in the jet inlet. For 3D holes, the injection is also uniform in the surface perpendicular to the hole centerline. The total number of injections is 904 for the round hole and 941 for the fan-shaped hole. The injection flow rate varies from 1% to 5% of the coolant air in mass. For example, considering the 2D slot case with a depth of 1 m, the droplets flow rate will be 3.5×10^{-4} to 1.75×10^{-3} kg/s. The injection rate at each location is 1.4×10^{-5} kg/s for 2% injection. It is known that the droplet size can strongly affect the evaporation of the mist in the main airflow. Uniform droplets with different sizes (5, 10, 20, and 50 μm) are used in this study to examine the effect on film cooling performance. Nonuniform droplets in a real application are assumed to perform as a combination of droplet with different uniform sizes. This assumption is based on the results found in [23], which showed that the effect of nonuniform particle size is bounded by the uniform droplet sizes between larger and smaller droplets. The boundary condition of droplets at all the walls is assigned as "reflect," which means the droplets are elastically rebound off once reaching the wall. At the outlet, the droplets just simply flee/escape from the computational domain. A more complex model will be developed in the future to determine if the droplets breakup, rebound, or are trapped by the wall when they hit it.

Meshes and Convergence

Grid Independence Study. Structured but nonuniform grids are used for the 2D slot case in this study. The grids near the jet wall and the bottom wall of the main domain are denser than the other area. For the 3D cases, unstructured grids are applied to the jet

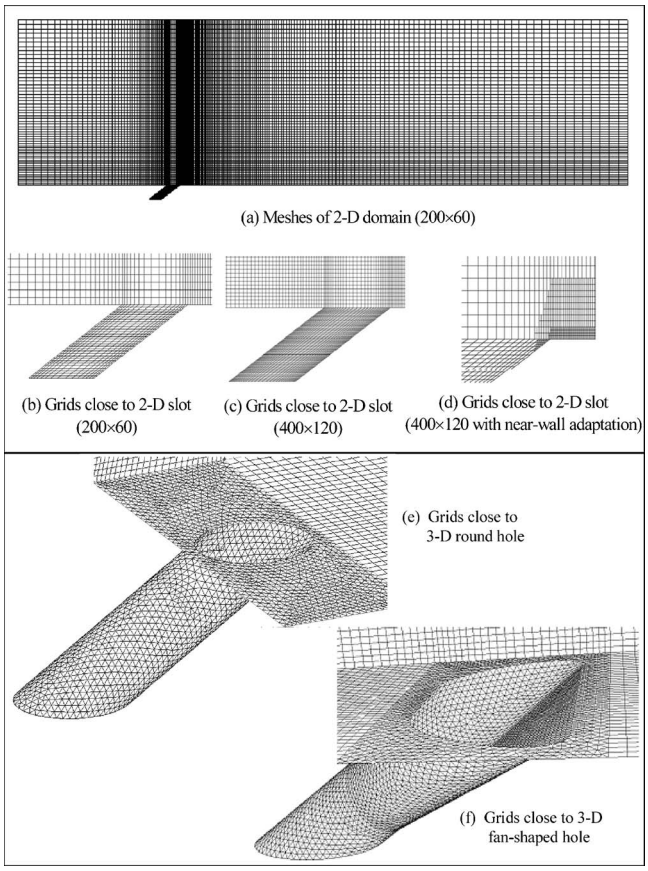

Fig. 2 Meshes

holes and a small volume in the main domain close to the jet outlet. Structured grids are used for the rest of domain. Figure 2 shows the grids of the 2D case and representative planes for 3D cases. The basic mesh system used in this study has 200 grids in the longitudinal (streamwise) direction and 60 grids in both the transverse y and spanwise z directions. There are 360,000 cells for the round-hole case and 386,000 cells for the fan-shaped hole case.

Different meshes have been tested for grid dependence study. For example, the average cooling effectiveness (defined later) changes only 0.8% when the density of the basic 2D mesh of 200×60 is doubled to 400×120. Grid adaptation is then applied to the near-wall region as shown in Fig. 2(d). Figure 3 shows the results of temperature and velocity profiles for the 2D slot jet using different meshes. It can be seen that the difference due to the number of grids is not discernable. The results using the mesh with adaptation overlap with the others, so that they are not shown in Fig. 3 to keep the figure clear. A detailed study of wall grid effect on film-cooling effectiveness calculation in [19] showed that the result is not sensitive to the $y+$ ranging from 1 to 5. Therefore, no finer grids are attempted.

Convergence. Converged results can be reached after iteration proceeds alternatively between the continuous and discrete phases. Ten iterations in the continuous phase are conducted between two iterations in the discrete phase. A typical converged result renders mass residual of 10^{-3}, energy residual of 10^{-6}, and momentum and turbulence kinetic energy residuals of 10^{-4}. These residuals are the summation of the imbalance for each cell, scaled by a representative of the flow rate. Typically, 1000–2000 iterations are needed to obtain a converged result, which takes about 1–2 hr for a 2D case and 10–20 hr for a 3D case on a PC with Pentium 4 processor of 2.4 GHz.

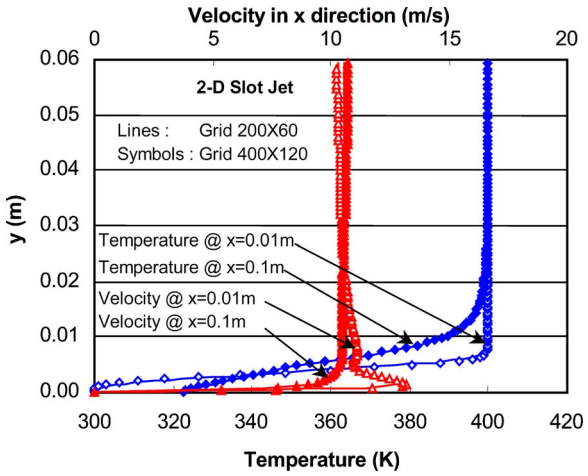

Fig. 3 Grid independence study (slot jet)

Results and Discussion

As a reference case, the overall temperature distribution of film cooling with the 2D slot is shown in Fig. 4, in which Fig. 4(a) is the case without mist and Fig. 4(b) is the case with 2% mist injection using 10 μm droplets. The temperatures of jet and main flow are 300 K and 400 K, respectively. The blowing ratio, defined as $M=(\rho u)_c/(\rho u)_g$, is 1.3 in this case, while the ratio of velocity is 1. Here the subscript c represents the coolant or jet flow, and the subscript g represents the main gas flow. The overall temperature distribution with mist is not much different from that of a typical air-film cooling. The cold jet sticks to the cooling surface but gradually becomes hot and diffuses into the mainstream by shear layer mixing. It seems that the 2% mist injection has little effect on the overall temperature profile in the main flow. However, a detailed study can find that the temperature very close to the cooling surface decreases due to mist injection as shown in Fig. 5. The adiabatic wall temperature decreases about 9 K downstream of the jet at $x=25b$. Note that the origin of the x coordinate is set at the downstream end of the jet holes for both 2D and 3D cases. At the beginning of film cooling, the evaporation of droplets is negligible because of the low flow temperature.

The adiabatic cooling effectiveness η is used to examine the performance of mist film cooling. The definition of η is

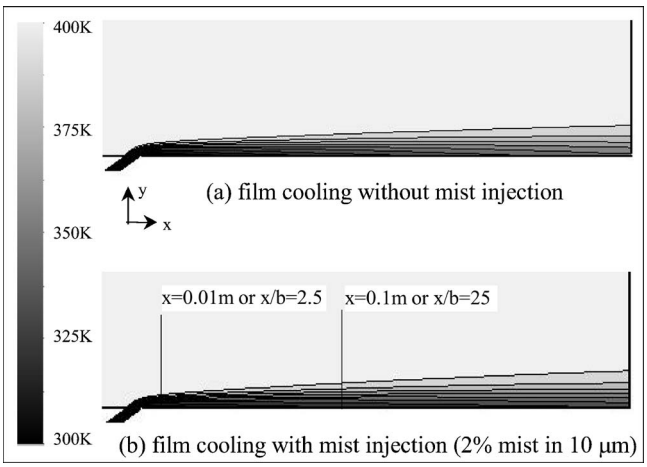

Fig. 4 Temperature distribution of air-film cooling with and without mist injection (slot jet)

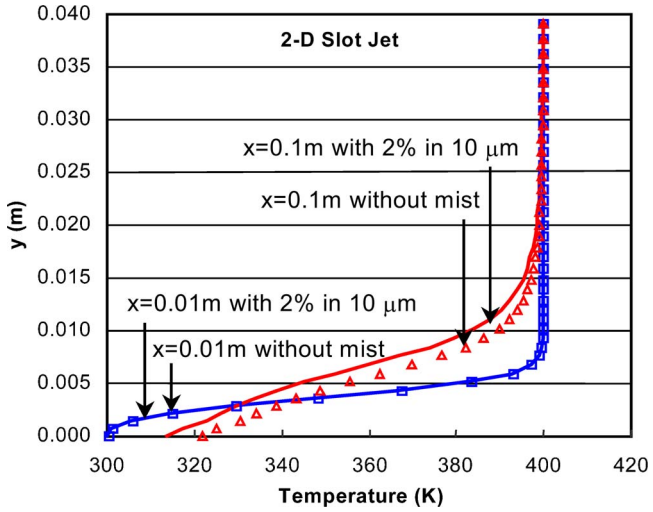

Fig. 5 Effect of 2% mist injection on temperature distribution at different locations (slot jet)

$$\eta = \frac{(T_g - T_{aw})}{(T_g - T_c)} \tag{24}$$

where T_g is the mainstream hot-gas temperature, T_c is the temperature of the coolant (jet), and T_{aw} is the adiabatic wall temperature. η is between zero (no cooling) and 1 (the wall temperature is the same as the coolant temperature). Figure 6 shows the effectiveness along the cooling surface. Note that $2b$ is used to scale the distance downstream because it is the hydraulic diameter of a slot. It can be seen that film cooling is significantly enhanced by mist injection, especially in the downstream region, where the evaporation of droplets becomes stronger because of the higher flow temperature. Because of continuous mixing between coolant and the main flow, the cooling inevitably becomes less effective downstream, and it has been a serious challenge to enhance cooling downstream of $x/2b=15$. The injection of water droplets works very well to meet this challenge. Also shown in Fig. 6 is the ratio of the film-cooling effectiveness with and without mist (η_{mist}/η_0). The mist-cooling enhancement can be defined as ($\eta_{mist}/\eta_0 - 1$). It can be seen that the maximum enhancement can reach 38% further downstream ($x/2b=30$) with an average cooling enhancement of 14.5%. The enhancement mechanism of mist

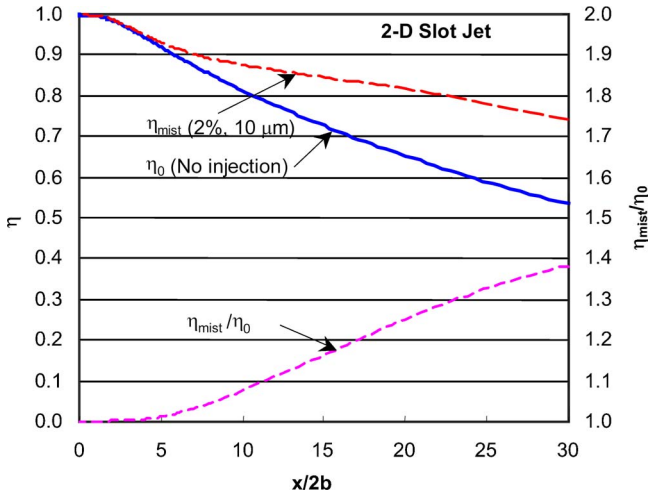

Fig. 6 Adiabatic film-cooling effectiveness and mist enhancement (2D slot)

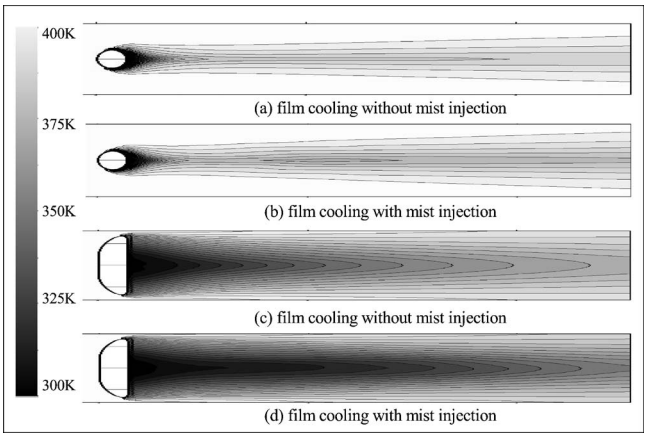

Fig. 7 Wall temperature distributions of air-film cooling on the cooling surface for both round and fan-shaped holes

cooling is discussed in the Introduction. Actually, the most important feature of mist cooling is its "distributed-cooling" characteristics. Each droplet acts as a cooling sink, and it flies a distance before it completely vaporizes. The reduced temperature near the surface because of droplet evaporation plays more of a major role in protecting the surface from the hot gas than the reduced bulk temperature. The droplet evaporation will reduce the coolant density and result in a reduced jet velocity, which may help improve cooling coverage in the near-hole region.

Mist Film Cooling With 3D Injection Holes. Although a slot hole is ideal to study fundamental characteristics of film cooling, 3D holes are more practical due to mechanical structural and manufacturing considerations. A simple-angle round hole and a fan-shaped hole are studied. Figure 7 shows the results of temperature distributions on the cooling surface for both the round and fan-shaped holes. The mist injection is 2% of the mass of jet airflow. Both holes have the same inlet velocity and, thus, the same flow rate. It can be seen that the mist lowers the surface temperature in both cases. The fan-shaped hole produces a lower temperature than the round hole. More discussions will be given later.

The adiabatic cooling effectiveness is given in Figs. 8 and 9 to examine the mist film-cooling performance. For the round hole, the cooling effectiveness along the centerline drops sharply at the beginning within a $4d$ distance, and the effect of mist is small. Starting at about $4d$ downstream, the mist shows its strong con-

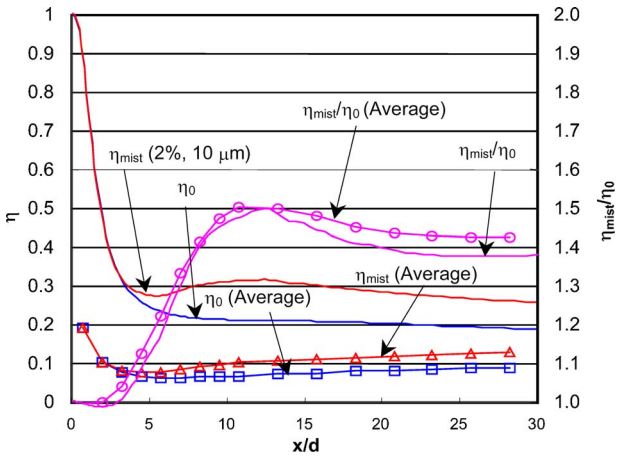

Fig. 8 Centerline and spanwise average adiabatic cooling effectiveness and mist-cooling enhancement (roundhole)

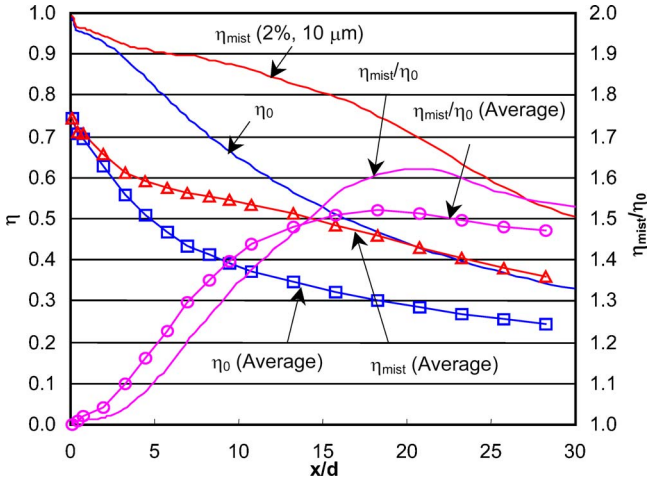

Fig. 9 Centerline and spanwise average adiabatic cooling effectiveness and mist-cooling enhancement (fan-shaped hole)

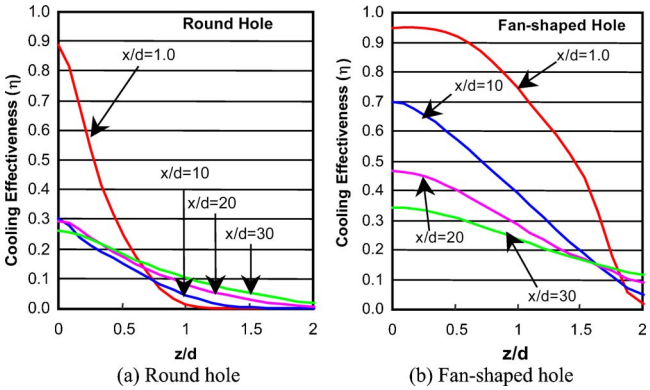

Fig. 11 Spanwise distributions of cooling effectiveness for round and fan-shaped holes (film cooling without mist)

tribution. The same trend can be seen for the cooling effectiveness averaged along the spanwise direction (z) except the averaged effectiveness has a minimum around $x/d=5$. The cooling enhancement of 2% mist is about 43% downstream ($x/d=30$) with a maximum of 50% near $x/d=12$. The effectiveness of the round hole is low when it is compared to the fan-shaped hole; therefore, its enhancement is essential. Figure 9 shows the performance of film cooling with the fan-shaped hole. Compared to the round hole, the fan-shaped hole produces higher cooling effectiveness along the centerline and on spanwise average. The mist-cooling enhancement is about the same as the round-hole case: 47% downstream ($x/d=30$) with a maximum of 52%. However, the maximum enhancement moves to about $x/d=18$.

The different behaviors between the round hole and fan-shaped hole can be further analyzed with Figs. 10 and 11. Figure 10 shows the flow field and temperature distribution on a cross section in the x direction. It can be seen that the center of coolant jet from the round hole is detached away from the cooling surface, and the secondary flow of the round-hole case is strong and entrains surrounding hot gas to the surface. These features reduce the blanket effect of the cooling layer. On the other hand, the fan-shaped hole can keep the jet center close to the surface, and the secondary flow is weak. It is expected that the evaporation of mist be strongly affected by the jet flow itself. The flow structure determines the cooling effectiveness along the z direction. As shown in Fig. 11, the round hole gives a narrower spanwise film-cooling coverage than the fan-shaped hole.

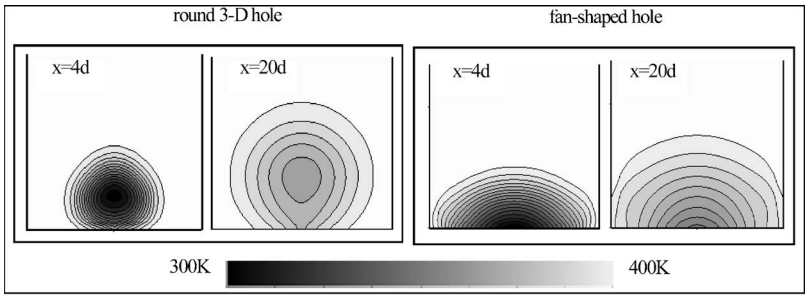

(a) Temperature distribution

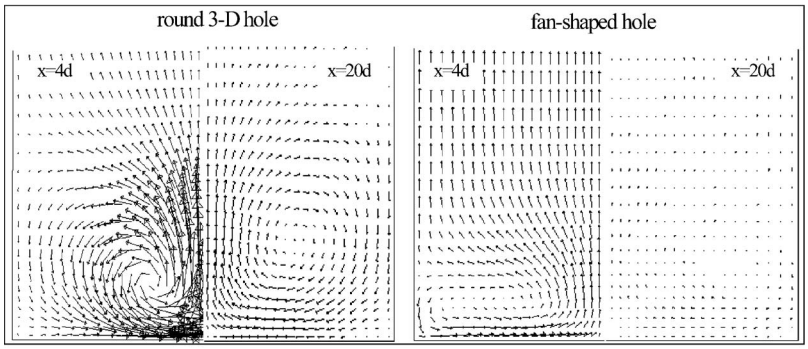

(b) Velocity vector

Fig. 10 Cross-sectional temperature distributions and velocity fields in the streamwise direction (film cooling without mist)

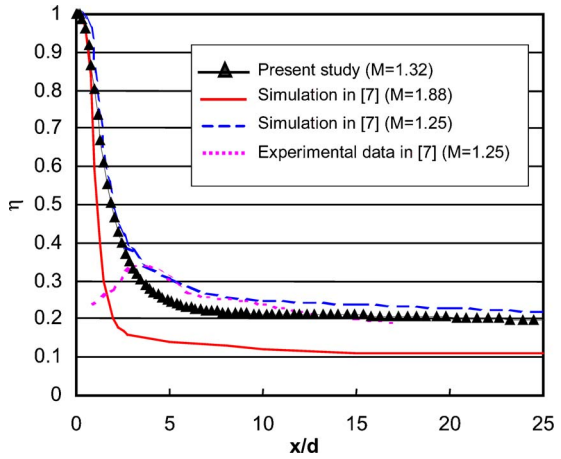

Fig. 12 Comparison to other studies (centerline cooling effectiveness of the round hole)

Validation of Numerical Results. Numerical results for single-phase air-film cooling are validated by comparing to data from other studies. Figure 12 shows the cooling effectiveness along the centerline of the round hole from different studies with various blowing ratios. The agreement is good in both the near and far fields. The discrepancy between the computational fluid dynamics (CFD) and experimental data for $x/d<5$ has been controversial and remains unresolved. There could be errors contributed by both CFD and experiments. The difficulty to achieve a true adiabatic wall condition near the cooling hole and preheating of the coolant in the experiment could result to a reduced film effectiveness. In computational simulation, the uncertainty in calculating the separated flow structure near the cooling hole may result in an over-predicted film effectiveness. Simulation in [7] included a plenum to account for the effect of flow inside the jet hole on film cooling, especially, close to the jet exit. It has been known that the plenum geometry could affect film cooling flow pattern and cooling performance. However, under the parameters of the current study, it seems that the plenum does not play a critical role under the parameters in this study if the plenum does not induce flow separation.

Effect of Mist Concentration. The effect of mist concentration is studied with a mist injection of 1%, 2%, and 5% of the coolant mass flow rate. Figure 13 shows the results in the 2D slot case. It can be seen that the cooling effectiveness increases as mist concentration increases. A mist of 5% can provide a cooling enhancement of 65% at $x/2b=30$. The increase is about linear when the concentration is low, but it slows down at high concentration (5%) where the cooling effectiveness is close to 0.9 for the 2D slot cooling. This high cooling effectiveness means that the temperature close to the cooling surface is low, and the droplet evaporation rate is reduced. When the mist concentration is low, higher concentration always means more latent heat is available to cool down almost the same amount of mainstream air. Therefore, a nearly linear relationship can be obtained if ignoring the effect of different main flow temperatures on evaporation. The average cooling effectiveness and mist cooling enhancement over the entire surface is listed in Table 1.

Effect of Droplet Size. The effect of droplet size on 2D slot mist film cooling is shown in Fig. 14 for droplet sizes of 5 μm, 10 μm, and 20 μm, respectively. It is seen that the smaller droplets produce better cooling because small droplets have larger surface to volume ratios and vaporize faster. Droplets of 20 μm make little difference to air-film cooling, at least within the $x/2b$ range under study. The cooling enhancement at $z/2b=30$ is 5% for droplets of 20 μm, and the average enhancement is only 2%. The result for

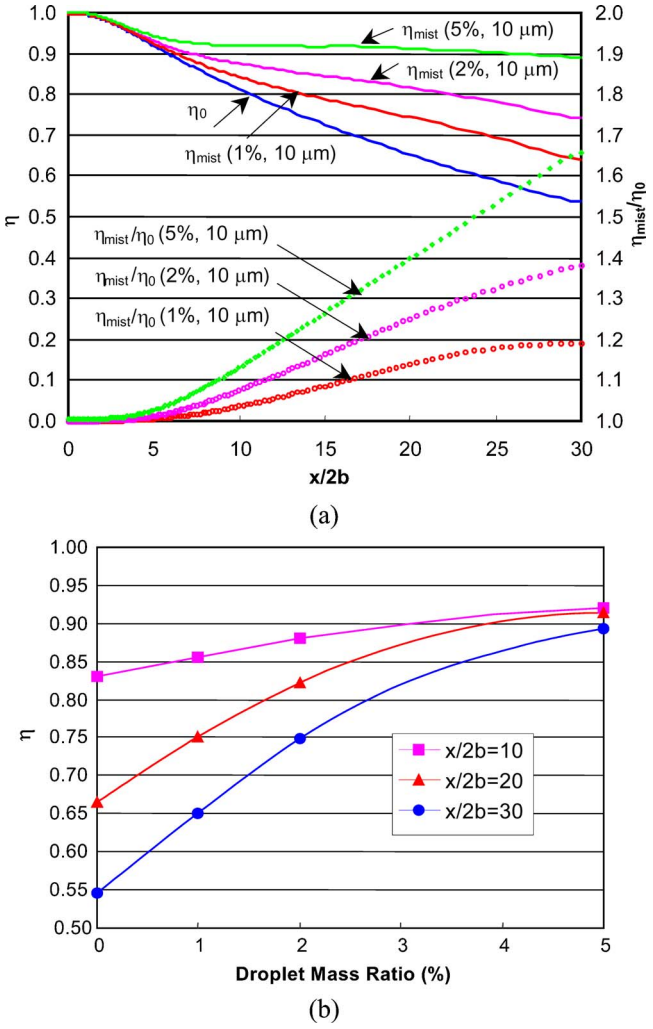

Fig. 13 Effect of mist concentration on adiabatic cooling effectiveness for a 2D slot film cooling

droplets of 50 μm shows <1% cooling enhancement; therefore, it goes into the same curve as the single-phase air-film cooling in the figure. Note the cooling effectiveness drops more quickly for the case with 5 μm droplets after $x/2b=22$ because most of the droplets have been evaporated by that time. Figure 15 shows the droplet trajectories predicted using a stochastic tracking method that considers the turbulent dispersion. The turbulent dispersion can bring the droplets toward the wall and thus improves cooling. As seen in Fig. 15, most of the 5 μm droplets evaporated before $x/2b=20$, whereas some of the 10 μm droplets can survive until the outlet. This numerical result is consistent with the analysis and estimation with Eq. (19). It can be concluded that a distributed size from 5 μm to 10 μm in real gas turbine applications will give an excellent enhancement on single-phase air-film cooling. Mist film cooling can be managed by manipulating both mist concentration and the droplet size.

Table 1 Cooling effectiveness and cooling enhancement averaged over the entire surface

Mist concentration (10 μm)	0%	1%	2%	5%
Maximum enhancement	0	19%	38%	65%
Average effectiveness	0.747	0.804	0.855	0.925
Average η_{mist}/η_0	1	1.076	1.145	1.238

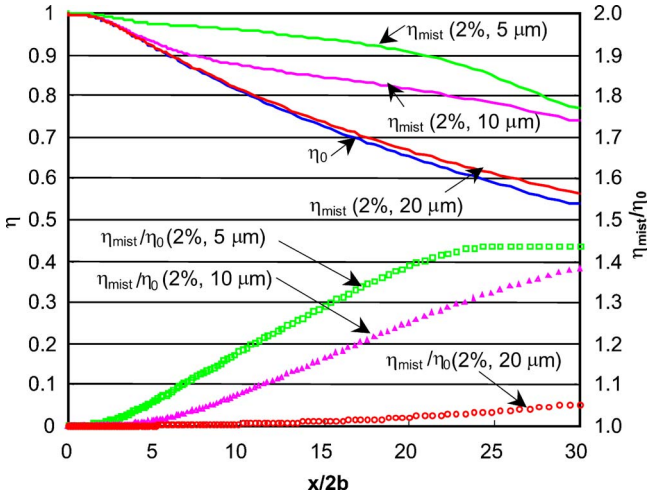

Fig. 14 Effect of droplet size on adiabatic cooling effectiveness for a 2D slot film cooling

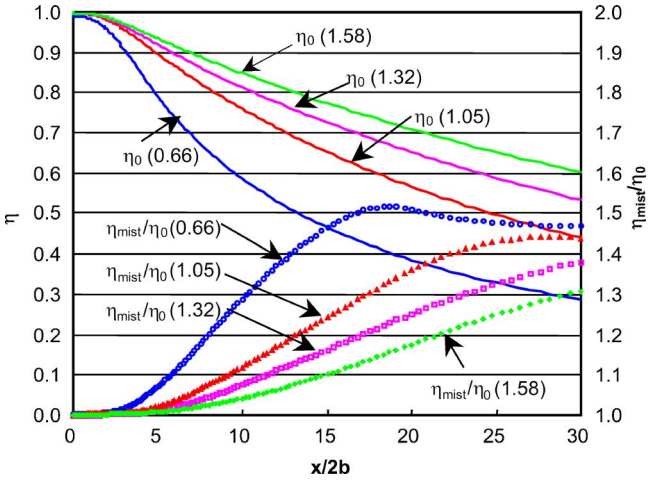

Fig. 16 Effect of mist injection on the slot jet air film cooling with different blowing ratios

Effect of Blowing Ratio. To achieve the best film-cooling performance, different blowing ratios might be used depending on cooling geometries and other parameters. Figure 16 shows the results with four different blowing ratios from 0.66 to 1.58 for the 2D slot case. To obtain different blowing ratios, the velocity of the coolant jet is changed while the mainstream flow remains the same. Mist concentration in all these cases is 2%, and the droplet diameter is 10 μm. It can be seen that the single-phase cooling effectiveness itself is a function of the blowing ratio. Under the settings of the current study, the cooling effectiveness increases when the blowing ratio increases, which can be simply due to more cooling flow being provided to protect the surface. However, the enhancement of mist film cooling reduces when the blowing ratio increases. The maximum cooling enhancement at a blowing ratio of 0.66 is 52%; this value drops to 31% when the blowing ratio is 1.58. The cooing enhancements averaged over the entire surface for these two cases are 34% and 12%, respectively. This can be interpreted by the droplets moving further away from the wall at high blowing ratios. Therefore, mist film cooling performs better with smaller blowing ratios.

Effect of Blowing Angle. The effect of blowing angle on mist film cooling is shown in Fig. 17 by running the 2D slot cases. Film cooling with a 30 deg injection is slightly better than that with a 35 deg injection with and without mist. It can also be seen that the mist-cooling enhancement is almost identical for these two cases although the 35 deg case has a little better performance, especially at $x/2b > 25$.

Effect of Main Flow Temperature. Figure 18 shows the result of 2D slot film cooling with a mainstream temperature of 500 K. The blowing ratio changes from 1.3 to 1.6 due to reduced main flow density. It can be seen that the adiabatic film-cooling effectiveness without mist injection (η_0) increases slightly when the main flow temperature increases from 400 K to 500 K. The cooling with mist keeps about the same until $x/2b=15-20$. After that, the mist cooling enhancement becomes lower at higher main flow temperature. This can be interpreted as high-temperature mainstream absorbs more heat and makes the evaporation time shorter, and fewer droplets are left after $x/2b=20$. As seen in Eq. (19), higher temperature difference makes the evaporation time shorter. Increasing the mist flow rate from 2% to about 5% can make film-cooling effectiveness higher and more uniform at high mainstream temperature as shown in Fig. 18. Detailed studies are needed to explore mist film cooling in real operating conditions.

Concerns and Future Research

The objective of this study is to explore the concept of mist film cooling. Numerical simulation only provides a qualitative descrip-

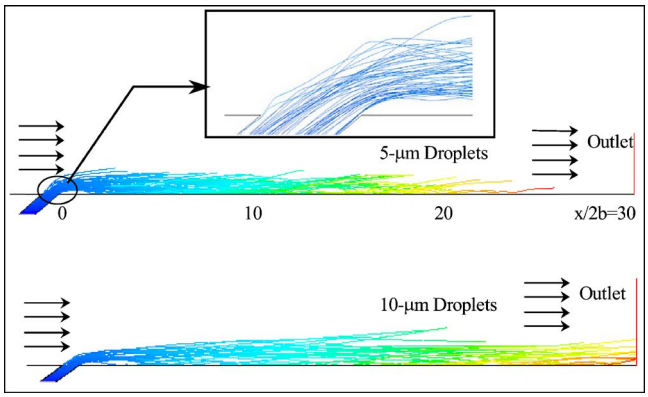

Fig. 15 Droplet trajectories predicted with stochastic tracking (2D slot case)

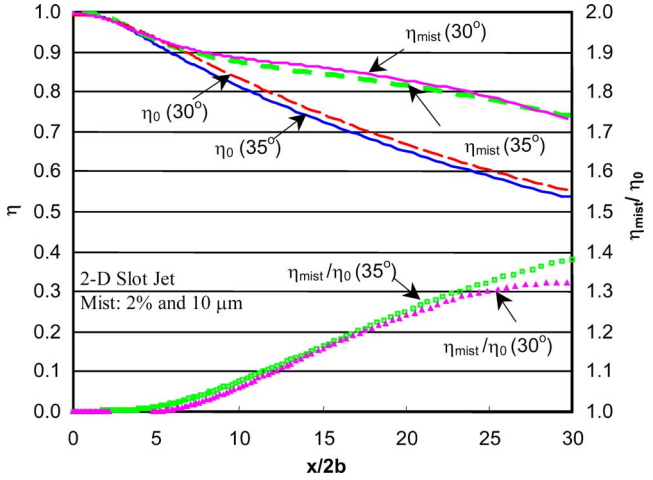

Fig. 17 Effect of mist injection on the slot-jet air film cooling with different blowing angles

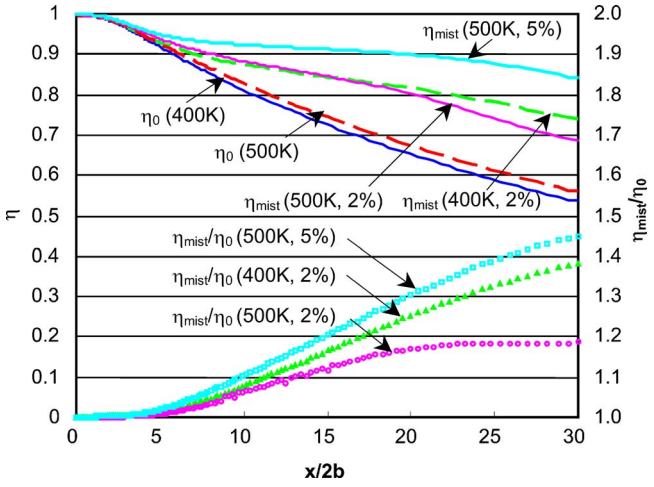

Fig. 18 Effect of mist film cooling with different mainstream temperatures

tion of the trend and effects of various parameters. Experiments are needed to verify the simulated results. In terms of the computational model, a more complicated model including heat transfer between the wall and droplets will be considered in the future. Models of collisions and coalescences will also be developed and incorporated into the future studies. Li et al. modeled the mist cooling [24] using the experimental data from [13] and reported the major contribution for mist-cooling enhancement was from the direct contact between droplets and the wall. In this paper, the direct droplet-wall contact heat transfer mechanism is not included; thus, the cooling results could be probably underpredicted. More realistic conditions with high temperature and high pressure will be considered in future studies. The major reservation of applying mist film cooling from gas turbine OEMs and users is the concern related to erosion and corrosion of water droplets on the heated surface. This task will be placed on metallurgists to find solutions.

Conclusions

Motivated to provide a significant improvement for cooling gas turbine hot-section components, this paper investigates the potential of film-cooling enhancement by injecting mist into the coolant. Three different holes are used, which include a 2D slot, a round hole, and a diffusion hole. Parametric studies have been performed with 2D slot cases. The conclusions from numerical simulation and parametric studies are as follows:

- By injecting mist into the coolant, the performance of air-film cooling can be improved significantly. Film cooling with a 2% mist can increase the cooling effectiveness about 30–50% for both 2D and 3D cases.
- The results reveal the benefit of mist film cooling by significantly enhancing cooling downstream of $x/2b$ (or x/d) >15, where the single-phase film cooling is less effective.
- Cooling enhancement has been shown to prevail in all three geometrical arrangements in the study. The maximum spanwise enhancement is ~50% for both the round-hole jet and the fan-shaped-hole jet.
- Higher mist concentration can result in higher cooling enhancement. For a 2D slot jet, 5% mist with 10 μm droplets can provide a cooling enhancement of 65% at $x/2b=30$, which makes the overall cooling effectiveness reach above 0.9.
- Based on 2D cases, smaller droplets show a higher effectiveness if the concentration is high enough. Cooling enhancement drops from 43% to 5% when droplet size changes from 5 μm to 20 μm under the conditions studied in this paper.
- The results of 2D cases show that mist film cooling performs better with smaller blowing ratio. With 2% mist, the maximum cooling enhancement can reach 52% with a blowing ratio of 0.66. The cooling effectiveness decreases as the blowing ratio increases.
- Mist cooling enhancement of 2D slot jet with a blowing angle of 30 deg is slightly (1–2%) lower than with a blowing angle of 35 deg at $x/2b<25$. The difference becomes bigger (7–8%) downstream at $x/2b=30$.
- Mainstream at high temperature absorbs the droplets quickly and, thus, makes the cooling enhancement low. The cooling enhancement reduces from 38% to 18% when the main flow temperature increases from 400 K to 500 K for a 2D slot case. The low performance at high main flow temperature can be compensated by using a higher mist concentration.

Acknowledgment

This study is supported by the Louisiana Governor's Energy Initiative via the Clean Power and Energy Research Consortium (CPERC) and administrated by the Louisiana Board of Regents.

Nomenclature

b = slot width (m)
C = concentration (kg/m^3)
c_p = specific heat (J/kg K)
D = mass diffusion coefficient (m^2/s)
d = diameter (m)
F = force (N)
k = turbulence kinetic energy (m^2/s^2)
k_c = mass transfer coefficient (m/s)
h = convective heat transfer coefficient (W/m^2 K)
h_{fg} = latent heat (J/kg)
M = blowing ratio, $(\rho u)_c/(\rho u)_g$
m = mass (kg)
Nu = Nusselt number, hd/λ
P = pressure (N/m^2)
Pr = Prandtl number, ν/α
Re = Reynolds number, ud/ν
S = source term
Sc = Schmidt number (ν/D)
Sh = Sherwood number ($k_c d/D$)
T = temperature (K, °F)
t = time (s)
u = streamwise velocity component (m/s)
v = spanwise velocity component (m/s)
x,y,z = coordinates

Greek

α = thermal diffusivity (m^2/s)
ε = turbulence dissipation rate (m^2/s^3)
η = adiabatic film cooling effectiveness, $(T_g-T_{aw})/(T_g-T_c)$
λ = heat conductivity (W/m K)
μ = dynamic viscosity (kg/m s)
ν = kinematic viscosity (m^2/s)
ρ = density (kg/m^3)
τ = stress tensor (kg/m s^2)

Subscript

aw = adiabatic wall
c = coolant or jet flow
g = hot gas/air
p = particle or droplet
t = turbulent

0 = values for air film cooling without mist
∞ = values far away from droplets

References

[1] Eriksen, V. L., and Goldstein, R. J., 1974, "Heat Transfer and Film Cooling Following Injection Through Inclined Tubes," ASME J. Heat Transfer, **96**, pp. 239–245.

[2] Goldstein, R. J., Eckert, E. R. G., and Burggraf, F., 1974, "Effects of Hole Geometry and Density on Three-Dimensional Film Cooling," Int. J. Heat Mass Transfer, **17**, pp. 595–607.

[3] Jia, R., Sunden, B., Miron, P., and Leger, B., 2003, "Numerical and Experimental Study of the Slot Film Cooling Jet With Various Angles," *Proc. ASME Summer Heat Transfer Conference*, ASME, New York, pp. 845–856.

[4] Kwak, J. S., and Han, J. C., 2003, "Heat Transfer Coefficients and Film-Cooling Effectiveness on a Gas Turbine Blade Tip," ASME J. Heat Transfer, **125**, pp. 494–502.

[5] Wang, T., Chintalapati, S., Bunker, R. S., and Lee, C. P., 2000, "Jet Mixing in a Slot," Exp. Therm. Fluid Sci., **22**(1), pp. 1–17.

[6] Bell, C. M., Hamakawa1, H., and Ligrani, P. M., 2000, "Film Cooling From Shaped Holes," ASME J. Heat Transfer, **122**, pp. 224–232.

[7] Brittingham, R. A., and Leylek, J. H., 2002, "A Detailed Analysis of Film Cooling Physics: Part IV—Compound-Angle Injection With Shaped Holes," ASME J. Turbomach., **122**, pp. 133–145.

[8] Chaker, M., Meher-Homji, C. B., and Mee, M., 2002, "Inlet Fogging of Gas Turbine Engines—Part A: Fog Droplet Thermodynamics, Heat Transfer and Practical Considerations," *ASME Proc. of Turbo Expo 2002*, Vol. 4, ASME, New York, pp. 413–428.

[9] Petr, V., 2003, "Analysis of Wet Compression in GT's," *Energy and the Environment—Proc. of International Conference on Energy and the Environment*, Vol. 1, WIT Press, Southampton, UK, pp. 489–494.

[10] Nirmalan, N. V., Weaver, J. A., and Hylton, L. D., 1998, "An Experimental Study of Turbine Vane Heat Transfer With Water-Air Cooling," ASME J. Turbomach., **120**(1), pp. 50–62.

[11] Guo, T., Wang, T., and Gaddis, J. L., 2000, "Mist/Steam Cooling in a Heated Horizontal Tube, Part 1: Experimental System, Part 2: Results and Modeling," ASME J. Turbomach., **122**, pp. 360–374.

[12] Guo, T., Wang, T., and Gaddis, J. L., 2001, "Mist/Steam Cooling in a 180° Tube Bend," ASME J. Heat Transfer, **122**, pp. 749–756.

[13] Li, X., Gaddis, J. L., and Wang, T., 2003, "Mist/Steam Cooling by a Row of Impinging Jets," Int. J. Heat Mass Transfer, **46**, pp. 2279–2290.

[14] Li, X., Gaddis, J. L., and Wang, T, 2003, "Mist/Steam Heat Transfer With Jet Impingement Onto a Concave Surface," ASME J. Heat Transfer, **125**, pp. 438–446.

[15] Dittmar, J., Schulz, A., and Wittig, S., 2003, "Assessment of Various Film-Cooling Configurations Including Shaped and Compound Angle Holes Based on Large-scale Experiments," ASME J. Turbomach., **125**(1), pp. 57–64.

[16] *Fluent Manual, Version 6.1.22*, 2003, Fluent, Inc., Lebanon.

[17] Launder, B. E., and Spalding, D. B., 1972, *Lectures in Mathematical Models of Turbulence*, Academic Press, London.

[18] Wolfstein, M., 1969, "The Velocity and Temperature Distribution of One-Dimensional Flow With Turbulence Augmentation and Pressure Gradient," Int. J. Heat Mass Transfer, **12**, pp. 301–318.

[19] Li, X., and Wang, T., 2005, "Effects of Various Modeling Schemes on Mist Film Cooling Simulation," *Proc. of ASME International Mechanical Engineering Congress & Exposition*, Orlando, ASME, New York, ASME Paper No. IMECE 2005–81780.

[20] Ranz, W. E., and Marshall, W. R., Jr., 1952, "Evaporation From Drops, Part I," Chem. Eng. Prog., **48**, pp. 141–146.

[21] Ranz, W. E., and Marshall, W. R., Jr., 1952, "Evaporation From Drops, Part II," Chem. Eng. Prog., **48**, pp. 173–180.

[22] Kuo, K. Y., 1986, *Principles of Combustion*, Wiley, New York.

[23] Wang, T., Li, X., and Pinninti, V., 2004, "Simulation of Mist Transport for Gas Turbine Inlet Air Cooling," Proc. of ASME International Mechanical Engineering Congress & Exposition, Anaheim, ASME, New York, ASME Paper No. IMECE04–60133.

[24] Li, X., Gaddis, J. L., and Wang, T., 2001, "Modeling of Heat Transfer in a Mist/Steam Impinging Jet," ASME J. Heat Transfer, **123**, pp. 1086–1092.

Surface Deformation and Convection in Electrostatically-Positioned Droplets of Immiscible Liquids Under Microgravity

Y. Huo

B. Q. Li[1]
e-mail: li@mme.wsu.edu

School of Mechanical and Materials Engineering,
Washington State University,
Pullman, WA 99164

A numerical study is presented of the free surface deformation and Marangoni convection in immiscible droplets positioned by an electrostatic field and heated by laser beams under microgravity. The boundary element and the weighted residuals methods are applied to iteratively solve for the electric field distribution and for the unknown free surface shapes, while the Galerkin finite element method for the thermal and fluid flow field in both the transient and steady states. Results show that the inner interface demarking the two immiscible fluids in an electrically conducting droplet maintains its sphericity in microgravity. The free surface of the droplet, however, deforms into an oval shape in an electric field, owing to the pulling action of the normal component of the Maxwell stress. The thermal and fluid flow distributions are rather complex in an immiscible droplet, with conduction being the main mechanism for the thermal transport. The nonuniform temperature along the free surface induces the flow in the outer layer, whereas the competition between the interfacial surface tension gradient and the inertia force in the outer layer is responsible for the flows in the inner core and near the immiscible interface. As the droplet cools into an undercooled state, surface radiation causes a reversal of the surface temperature gradients along the free surface, which in turn reverses the surface tension driven flow in the outer layer. The flow near the interfacial region, on the other hand, is driven by a complimentary mechanism between the interfacial and the inertia forces during the time when the thermal gradient on the free surface has been reversed while that on the interface has not yet. After the completion of the interfacial thermal gradient reversal, however, the interfacial flows are largely driven by the inertia forces of the outer layer fluid. [DOI: 10.1115/1.2188460]

Keywords: galerkin finite element, boundary element, weighted residuals methods, immiscible droplet, undercooled state, maxwell stress, surface tension

Introduction

Levitated droplets provide a useful vehicle for the study of fundamentals governing solidification processes and for the measurement of thermophysical properties of high temperature melts. Various levitation techniques have been developed, among which electrostatic levitation is favored for certain applications [1–10]. The basic concept of the electrostatic levitation is sketched in Fig. 1(*a*). In essence, a droplet is positively charged and immersed in an electric field generated by two electrodes at different potentials. This electric field interacts with the charges impressed on the droplet to give rise to an electrostatic force, which acts in the same direction as the electric field. If an appropriate combination of the electric field and charges is chosen, the electrostatic force (or the Coulomb force) will be strong enough to support the weight of the droplet in normal gravity. In a microgravity environment, the concept of the electrostatic levitation is exploited to position the sample from drifting in space so that desirable experiments with the droplet can be carried out. A major advantage provided by microgravity is that a much larger sample can be used. This advantage is considered essential for experiments directed toward a better understanding of the physics controlling the solidification of monotectic alloys from immiscible melts [11], which are considered prossessing desired properties for automobile applications [12].

There have been published studies on the fundamental fluid dynamic behavior of droplets levitated in electric fields, which include the analyses of an inviscid oscillation of charged drops for simple electric field configuration and shape stability [3–5,13,14]. Information on transport phenomena in electrostatically levitated droplets also has been obtained for single-phase droplets levitated in electric fields [15–17]. It is now understood that being nonvortical, the electrostatic forces do not drive an internal flow in an electrically conducting sample. The flow in a droplet, however, may come from other sources. For example, under terrestrial conditions, natural convection occurs due to a temperature difference in the droplet. Since the droplet size is small, surface tension driven flow or Marangoni convection can become important for levitated droplets in both normal and micro gravity.

While understanding of the physics governing the convection in a droplet of single-phase liquid has been acquired through extensive numerical simulations and experimental measurements [15–17], there appears to have been little, if at all, on the droplet behavior of immiscible liquids. Experience with immiscible droplets suggests that internal convection plays a crucial role in recoalescence during monotectic alloy formation [7]. Our understanding of thermal convection in these immiscible droplets, in particular, the convection in the regions near the immiscible interface, is rather limited, despite the importance of the subject. This hinders the development of appropriate procedures for designing

[1]To whom correspondence should be addressed.

Contributed by the Heat Transfer Division of ASME for publication in the JOURNAL OF HEAT TRANSFER. Manuscript received December 3, 2004; final manuscript received November 30, 2005. Review conducted by Yogesh Jaluria.

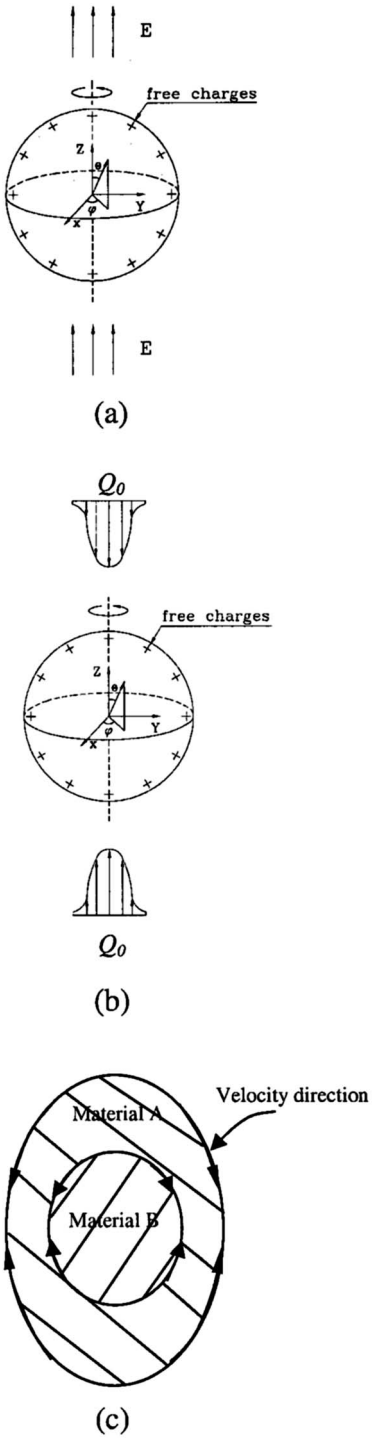

Fig. 1 Schematic representation of a positively charged melt droplet levitated in an electrostatic field: (*a*) levitation mechanism, (*b*) a two-laser-beam heating arrangement, and (*c*) two-fluid structure under the heat arrangement in (*b*)

and interpreting experiments with these droplets. The analyses presented in this paper further indicate that the knowledge of the flow in the immiscible droplets cannot be simply derived from our extensive knowledge of Marangoni convection associated with free surface only.

This paper presents a numerical study of the droplet deformation and fluid flow phenomena in electrostatically positioned droplets of immiscible liquids, both being electrically conducting, under microgravity. The intention is to establish a fundamental understanding of the basic mechanisms governing the interfacial fluid flow in the immiscible fluids and its possible relation to the convection driven by the Marangoni forces near the free surface. For this purpose, the Navier-Stokes equation is solved using the finite element method along with the thermal balance equation. Both the steady state and transient developments of the thermal and fluid flow fields in the droplets are studied, the latter being of direct relevance to the design of undercooling conditions that would be required for fundamental solidification studies. In developing the computational algorithms, the boundary element method is used for the solution of the electrostatic field distribution, and is coupled with the weighted residuals method for an iterative solution of the equilibrium free surface shapes of the levitated droplet. Numerical simulations are carried out for various immiscible liquid droplets electrostatically positioned under microgravity.

Governing Equations

Let us consider an electrostatically levitated droplet schematically represented in Fig. 1. The droplet under consideration is electrically conducting and is placed in a uniform electrostatic field generated by placing two electrodes far apart. For an electrically conducting droplet, a constant potential is established on the surface of the droplet because the electric field inside the droplet is identically zero by the Gauss law. The combination of the non-uniform charge distribution along the surface with a self-induced electric field local to the charges gives rise to a non-uniform electric surface force acting in the outward unit normal direction. The balance of this force with others acting on the droplet determines the equilibrium shape of the droplet [15–17]. The electric surface force, however, is non-vorticial in nature and is incapable of driving a flow in the droplet. For microgravity applications, the electric forces are used for the purpose of positioning the droplet at a fixed location.

In practice, laser beams are applied to melt the sample and/or heat it up to a designated temperature. Figure 1(*b*) shows a heating arrangement that uses two laser beams impinging on the two pole regions. Laser heating is in general non-uniform, because either the heating intensity in the beam is the Gaussian type or the heating arrangement is non-uniform or both. This non-uniform heating causes a surface tension gradient along the surface of a droplet, which is responsible for the Marangoni convection in the droplet. Convective flows in an immiscible droplet can be complex and different flow patterns may occur depending upon the applied conditions. Figure 1(*c*) sketches one type of the possible fluid structures when the heating arrangement in Fig. 1(*b*) is applied.

(a) Governing equations for the electric potential distribution. A complete description of the electrically induced surface deformation and thermally driven fluid flow phenomena in a droplet requires the solution of the coupled Maxwell and Navier-Stokes equations, along with the energy balance equation. In theory, electrical charges move in an external electric field and also are transported by flow convection. The dimensionless number that characterizes these effects is the electric Reynold number Re_{el}, which is the ratio of the time scale for charge convection by flow and that for charge relaxation by ohmic conduction [18]. For metal and semiconductor melts under practical conditions, the electric Reynolds number is on an order of 10^{-17}, which suggests that the convective transport of surface charges are negligible and the electric field distribution may be calculated as if the liquid droplet were solid [15,18,19]. Consequently, the solution of the Maxwell equations can be decoupled from the Navier-Stokes and thermal balance equations.

The above discussion further implies that for the problem under consideration, the electric field can be derived from an electric potential, $\mathbf{E}=\nabla\cdot\Phi$. Moreover, by the Gauss law, the electric potential is constant in an electrically conducting droplet. Thus the

vector Maxwell equations are simplified to a scalar partial differential equation governing the distribution of the electric potential outside the droplet,

$$\nabla^2\Phi = 0 \quad \in \Omega_2 \tag{1}$$

$$\Phi = \Phi_0 \quad \in \Omega_1 \cap \Omega_2 \tag{2}$$

$$\varepsilon_0 \mathbf{n}_1 \cdot \nabla\Phi = -\sigma_e \quad \in \Omega_1 \cap \Omega_2 \tag{3}$$

$$\oiint_{\partial\Omega_1\cap\partial\Omega_3} \sigma_e ds = -\oiint_{\partial\Omega_1\cap\partial\Omega_3} \varepsilon_0 \mathbf{n}_1 \cdot \nabla\Phi ds = Q \quad \in \Omega_1 \cap \Omega_2 \tag{4}$$

$$\Phi = -E_0 R\cos\theta \quad R \to \infty \tag{5}$$

In the above, the electric potential outside the droplet Φ is governed by Eq. (1), while the Gauss law is stated mathematically by Eq. (2). Equation (3) dictates the jump condition for the electric field along the droplet surface, a manifestation of a well-known fact that charges are distributed only on the surface of a conducting body. The law of charge conservation is described by Eq. (4), where Q is the total free charge applied on the droplet, which is zero for the problem under consideration for microgravity applications. Note that Eq. (4) is required to determine the constant potential Φ_0. Equation (5) states the electric potential condition at infinity, which basically means that the electrodes are placed far away from the droplet.

(b) Governing equations for droplet deformation. Deformation of a free surface or a fluid-fluid interface is determined by the force balance along the surface. For an electrostatically levitated melt droplet, the deformation is calculated by the following balance equations:

$$\mathbf{n}_1 \cdot \overline{\sigma_1} \cdot \mathbf{n}_1 + p_0 - \mathbf{n}_1 \cdot \mathbf{T}_E \cdot \mathbf{n}_1 = 2H\gamma \quad \in \Omega_1 \cap \Omega_2 \tag{6}$$

$$\mathbf{n}_3 \cdot \overline{\sigma_3} \cdot \mathbf{n}_3 - \mathbf{n}_3 \cdot \overline{\sigma_1} \cdot \mathbf{n}_3 = 2H\gamma \quad \in \Omega_1 \cap \Omega_3 \tag{7}$$

$$\int_{\Omega_1+\Omega_3} dV = V_0 \quad \in \Omega_1 \cup \Omega_3 \tag{8}$$

$$\int_{\Omega_1+\Omega_3} z dV = z_c \quad \in \Omega_1 \cup \Omega_3 \tag{9}$$

Here Eq. (6) states the balance of the hydrodynamic, Maxwell and surface tension stresses along the normal direction, which determines the free surface shape of the droplet. Equation (7) describes the balance of the surface tension stresses along the normal direction on the interfacial surface between the immiscible melt metals. The constraints of the volume conservation (Eq. (8)) and the center of the mass (Eq. (9)) of the electrostatically levitated droplet are needed to determine the pressure constant and the position of the droplet.

(c) Governing equations for the computation of thermal/fluids. For microgravity applications, the buoyancy effect may be neglected. Thus. the equations for the fluid flow and thermal fields may be written as follows:

$$\nabla \cdot \mathbf{u}_j = 0 \quad \in \Omega_1 \cup \Omega_3 \tag{10}$$

$$\rho\frac{\partial \mathbf{u}_j}{\partial t} + \rho\mathbf{u}_j \cdot \nabla\mathbf{u}_j = -\nabla p_j + \nabla \cdot \eta_j(\nabla\mathbf{u}_j + (\nabla\mathbf{u}_j)^T) \quad \in \Omega_1 \cup \Omega_3 \tag{11}$$

$$\rho_j C_{p_j}\frac{\partial T_j}{\partial t} + \rho_j C_{p_j}\mathbf{u}_j \cdot \nabla T_j = \nabla \cdot k_j \nabla T_j \quad \in \Omega_1 \cup \Omega_3 \tag{12}$$

where the subscript $j=1$ refers to the outer fluid of the droplet and $j=3$ to the inner core fluid. The solution of the above equations may be obtained by applying the appropriate boundary conditions,

$$-k\mathbf{n}_1 \cdot \nabla T_1 = \varepsilon\sigma_s(T_1^4 - T_\infty^4) + \mathbf{n}_1 \cdot \hat{\mathbf{r}}_l Q_o e^{-r_l^2/a_l^2} \quad \in \Omega_1 \cap \Omega_2 \tag{13}$$

$$\mathbf{u} \cdot \mathbf{n}_1 = 0 \quad \in \Omega_1 \cap \Omega_2 \tag{14}$$

$$\mathbf{t}_1 \cdot \overline{\sigma_1} \cdot \mathbf{n}_1 = \frac{d\gamma_1}{dT}\mathbf{t}_1 \cdot \nabla T_1 \quad \in \Omega_1 \cap \Omega_2 \tag{15}$$

$$\mathbf{u}_1 = \mathbf{u}_3 \quad \in \Omega_1 \cap \Omega_3 \tag{16}$$

$$T_1 = T_3 \quad \in \Omega_1 \cap \Omega_3 \tag{17}$$

$$\mathbf{t}_3 \cdot \overline{\sigma_3} \cdot \mathbf{n}_3 - \mathbf{t}_3 \cdot \overline{\sigma_1} \cdot \mathbf{n}_3 = \frac{d\gamma_3}{dT}\mathbf{t}_3 \cdot \nabla T \quad \in \Omega_1 \cap \Omega_3 \tag{18}$$

In Eq. (13), the absorption coefficient is factored into Q_o and $\hat{\mathbf{r}}_l$ the unit vector of laser beam pointing outward from the origin of the laser, i.e., $\mathbf{n}\cdot\hat{\mathbf{r}}_l \leqslant 0$. Equations (15)–(18) represent the fact that the flow along the free and interfacial surfaces of the droplet is induced by surface tension force if it is a function of temperature.

It is noted that in the above formulations, the effect of a surrounding gas is neglected. The liquid droplet is generally processed under a vacuum condition, although recently attempts have been made to process in an inert gas environment. For the latter case, it is estimated that the surrounding inert gas contributes about 3% or less to the Marangoni convection [17].

Method of Solution

The numerical algorithms for the solution of the above governing equations are divided into two parts: 1) the droplet deformation calculations and 2) the thermal and fluid flow calculations. The detailed verification of these methods was discussed in previous publications [9,10,15–17] and thus only an outline is given below.

1) Droplet deformation calculations. For practical applications, droplet deformation is essentially axisymmetric and viscous forces make a negligible contribution. Thus, the electric and droplet deformation calculations may be decoupled from the thermal and fluid calculations [16]. The procedures for the computation of electrically induced droplet deformation are detailed in our previous publications [15–17] and thus only an outline of the methodology is given here. Since the electric field inside the droplet is zero, only the potential distribution outside the droplet needs to be solved for. For the problem under consideration, the boundary element method should be the method of choice, since it requires a discretization of the droplet boundary only, thereby resulting in considerable computational savings [13]. The needed boundary integral can be obtained from the classical Green's theorem [19],

$$C(\mathbf{r}_i)\Phi'(\mathbf{r}_i) + \oint_{\partial\Omega_2} \Phi'(\mathbf{n}\cdot\nabla G)rd\Gamma + \oint_{\partial\overline{\Omega}_2} \Phi'(\mathbf{n}\cdot\nabla G)rd\Gamma = \oint_{\partial\Omega_2} G(\mathbf{n}\cdot\nabla\Phi')rd\Gamma + \oint_{\partial\overline{\Omega}_2} G(\mathbf{n}\cdot\nabla\Phi')rd\Gamma \tag{19}$$

where $\Phi' = \Phi + Er\cos\theta$, $\partial\Omega_2$ designates the surface of the droplet and $\partial\overline{\Omega}_2$ denotes the boundary at infinity. The Green function, G, and its normal derivative are calculated by the following expressions written for a cylindrical coordinate system [19]:

$$G(\mathbf{r}_i,\mathbf{r}) = \frac{4}{\sqrt{(r_i+r)^2 + (z-z_i)^2}}K(\kappa) \tag{20}$$

$$\frac{\partial G}{\partial n} = \frac{4}{\sqrt{(r+r_i)^2+(z-z_i)^2}}\left\{\frac{n_r}{2r}[E(\kappa)-K(\kappa)] - \frac{n_r(r-r_i)+n_z(z-z_i)}{(r-r_i)^2+(z-z_i)^2}E(\kappa)\right\} \quad (21)$$

where κ is the geometric parameter calculated by

$$\kappa^2 = \frac{4r_i r}{(r_i+r)^2+(z_i-z)^2} \quad (22)$$

Using the asymptotic properties of the functions G and Φ' [10], Eq. (19) is simplified to a boundary integral that involves only the surface of the droplet, $\partial\Omega_2$. Following the standard boundary element discretization, noticing that the potential on the surface is a constant and substituting $\Phi=\Phi'-Er\cos\theta$ into the resultant equation, one obtains the final matrix form for the unknowns on the surface of the droplet,

$$\mathbf{H}\{\Phi_0\} = -\mathbf{G}\left\{\frac{\partial\Phi}{\partial n}\right\} + E\mathbf{G}\left\{\frac{\partial z}{\partial n}\right\} - \mathbf{H}E\{z\} \quad (23)$$

where **H** and **G** are the coefficient matrices involving the integration of $\partial G/\partial n$ and G over a boundary element. To complete the solution, Eq. (4) is discretized and solved along with the above equation to obtain the surface distribution of $\partial\Phi/\partial n$ and the constant Φ_0.

For droplet shape calculations, the normal stress balance equation (Eq. (6)) along the droplet surface is solved using the Weighted Residuals method. Written in a spherical coordinate system, which is more convenient for the calculations, the weighted residuals approach leads to the following integral representation of the force equilibrium along the surface:

$$\int_0^\pi \left\{\frac{RR_\theta\frac{d\psi_i}{d\theta}+\psi_i(2R^2+R_\theta^2)}{\gamma\frac{}{\sqrt{R^2+R_\theta^2}}} + R^2\psi_i\left(P_o-\frac{\varepsilon_0(\mathbf{n}\cdot\nabla\Phi)^2}{2}\right)\right\}\sin\theta d\theta = 0 \quad (24)$$

The variables R and R_θ are calculated by

$$R=\sum_{i=1}^{Ne}\psi_i R_i \text{ and } R_\theta=\sum_{i=1}^{Ne}R_i\frac{d\psi_i}{d\zeta}\frac{d\zeta}{d\theta} \quad (25)$$

where R_i is the discretized surface coordinate and ψ_i is the boundary shape function. In arriving at Eq. (24), the dynamic pressure and viscous contribution has been neglected since their contributions are small for practical levitation conditions [15]. The constraints of the volume conservation and the center of the mass of the electrostatically levitated droplet are needed to determine the droplet shape and position. The two constraints are expressed as

$$\frac{1}{a_d^3}\int_0^\pi R^3\sin\theta d\theta = 2 \quad (26)$$

$$\frac{3}{8a_d^3}\int_0^\pi R^4\cos\theta\sin\theta d\theta = z_c \quad (27)$$

where z_c is the center of mass. The free surface may be discretized into N elements and Eqs. (24), (26), and (27) are integrated numerically. The final results are expressed as a set of algebraic equations, which are then solved for the unknowns R_i, K, and z_c [19],

$$\mathbf{KX}=\mathbf{F} \quad (28)$$

where the unknown vector includes the surface coordinates of the free surface [10].

It is noted that for microgravity applications, $z_c=0$, in Eq. (27) and also the immiscible interface remains spherical; this will be discussed in the Results and Discussion section.

2) Thermal and fluid flow calculations. With the droplet shape known, the momentum and energy equations (i.e., Eqs. (10)–(12)) for the thermal and fluid flow fields along with the boundary conditions are solved using the Galerkin finite element method. In essence, the computational domain is first divided into finite elements. With each element, the dependent variable **u**, P, and T are interpolated by the shape functions, ϕ, ψ, and θ,

$$\mathrm{u}^i(x,t)=\phi^T U^i(t) \quad P(x,t)=\psi^T P(t) \quad T(x,t)=\theta^T T(t)$$

where the $U^i(t)$, $P(t)$, and $T(t)$ are the column vectors of element nodal point unknowns. The matrix form of the finite element discretized equations for the thermal and fluid flow fields may be written as follows:

$$\begin{bmatrix}\mathbf{M}&\mathbf{0}&\mathbf{0}\\ \mathbf{0}&\mathbf{0}&\mathbf{0}\\ \mathbf{0}&\mathbf{0}&\mathbf{N}_T\end{bmatrix}\begin{bmatrix}\dot{\mathbf{U}}\\ \dot{\mathbf{P}}\\ \dot{\mathbf{T}}\end{bmatrix}+\begin{bmatrix}\mathbf{A}(\mathbf{U})+\mathbf{K}&-\mathbf{C}&\mathbf{0}\\ -\mathbf{C}^{\mathbf{T}}&\mathbf{0}&\mathbf{0}\\ \mathbf{0}&\mathbf{0}&\mathbf{D}_T(\mathbf{U})+\mathbf{L}_T\end{bmatrix}\begin{bmatrix}\mathbf{U}\\ \mathbf{P}\\ \mathbf{T}\end{bmatrix} = \begin{bmatrix}\mathbf{F}\\ \mathbf{0}\\ \mathbf{G}_T\end{bmatrix} \quad (29)$$

where the standard finite element coefficient matrices are calculated by

$$\mathbf{M}=\int_{\Omega_m}\phi\phi^T dV \quad \mathbf{N}_T=\int_{\Omega_m}\rho C_p\theta\theta^T dV$$

$$\mathbf{L}_T=\int_{\Omega_m}k\nabla\theta\cdot\nabla\theta^T dV \quad \mathbf{A}(\mathbf{U})=\int_{\Omega_m}\rho\phi\mathbf{u}_m\cdot\nabla\phi^T dV$$

$$\mathbf{D}_T(\mathbf{U})=\int_{\Omega_m}\rho C_p\theta\mathbf{u}_k\cdot\nabla\theta^T dV \quad \mathbf{G}_T=-\int_{\partial\Omega_1\cap\partial\Omega_2}q_T\theta ds$$

$$\mathbf{C}_j=\int_{\Omega_m}\hat{j}\cdot\nabla\phi\psi^T dV$$

$$\mathbf{F}_j=\int_{\partial\Omega_1\cap\partial\Omega_2}\hat{j}\cdot\overline{\sigma_1}\cdot\mathbf{n}\phi ds+\int_{\partial\Omega_1\cap\partial\Omega_3}\hat{j}\cdot(\overline{\sigma_3}-\overline{\sigma_1})\cdot\mathbf{n}\phi ds$$

$$\mathbf{K}_{ij}=\left(\int_{\Omega_m}\eta\nabla\phi\cdot\nabla\phi^T dV\right)\delta_{ij}+\int_{\Omega_m}\eta(\hat{i}\cdot\nabla\phi)(\hat{j}\cdot\nabla\phi^T)dV$$

where $m=1, 3$. The assembled global matrix equations are stored in the skyline form and solved using the Gaussian elimination method [15,17]. The transient term is set to zero for steady-state calculations, however.

Results and Discussion

The computational model developed above enables the prediction of the electric field distribution outside a droplet, the Maxwell stress distribution along the surface of the droplet, the shape of the droplet, and the temperature distribution and thermally-driven internal convection in the droplet. A selection of computed results is presented for some immiscible droplets being considered for microgravity applications. Unless otherwise indicated, the computations used the physical properties and parameters in Table 1. It is noted that Rayleigh predicted a critical charge above which a charged drop becomes unstable and starts to disintegrate into smaller droplets [20] and this criterion is easily satisfied for microgravity applications. For the results presented below, a total of 48 linear boundary elements was used for the electric potential calculations and 24 quadratic boundary elements for free surface deformation calculations. The thermal and fluid flow calculations

Table 1 Thermophysical properties used for computations

Parameters	Al	In	Fe	Pb	Co	Si
T_{melt} (K)	934	429.6	1809	600	1766	1685
ρ (kg/m^3)	2385	7023	7015	10678	7760	2510
$\mu\times10^3$ (kg/m s)	1.3	1.89	5.5	2.65	4.2	0.94
γ (N/m)	0.914	0.556	1.872	0.468	1.873	0.865
$d\gamma/dT\times10^4$ (N/m K)	−3.5	−0.9	−4.9	−1.3	−4.9	−1.3
K (W/m K)	95.37	42	78.2	19.9	96.0	138.5
C_P (J/kg K)	1080	259	795	135	590.0	1040
$\mathrm{Pr}\times10^2$	1.47	1.17	5.59	1.80	2.57	0.71
$\alpha\times10^6$	37.03	23.09	14.02	13.80	20.97	53.06

used 264 9-node elements, with the penalty formulation for pressure, and the density of the mesh was increased near the free surface to ensure accuracy. A convergence criterion of 1×10^{-4} was set for relative error associated with the unknowns for free surface shapes, temperature, and velocity. Different meshes and different mesh distributions were also used to check the mesh dependency. The final mesh used for the computations is shown in Fig. 2. It is determined such that any further refinement of the mesh produces an error smaller than 0.1% (relative to the final mesh).

1) Droplet deformation. As sketched in Fig. 1(*c*), there are two interfaces associated with an immiscible droplet. The outer surface is a free surface that separates the droplet from free space. The inner interface demarks the two immiscible fluids. Analyses are made to understand the reaction of these interfaces to an imposed electric field, which is used to position the droplet under microgravity.

We first consider the behavior of the inner interface. It is known that when an electric conductor is placed in an electric field, electric charges are induced on its surface. These charges induce an electric field inside the droplet just opposite to the applied field so that the total inside field is identically zero. This is the renowned Gaussian law of electrostatics, which requires that the whole droplet be at the equal potential and the surface charges appear only on the free (or outer) surface of the droplet. This implies that the Maxwell stress along the immiscible interface is zero and the inner interface shape is completely determined by the balance of the hydrodynamic forces along the interface face, or the balance of the surface effect (surface tension times the curvature) by the pressure difference between the two liquids. Thus under microgravity and with the viscous forces neglected under practical conditions, the interface remains spherical and is immune to the electric field outside the droplet. This is illustrated by curve *a* in Fig. 3. It is worthy noting that, from the above discussion, the electric effect will not come into play even when the droplet is levitated electrostatically under normal gravity. Of course, when gravity is present, the interface shape should be determined by the balance of the interfacial surface tension and the buoyancy force on the inner fluid, which results from the density difference between the two fluids.

We next consider the behavior of the outer surface, which is much different. Because of the induced surface charges, the normal component of the Maxwell stress, or the electric force, experiences a jump across the free surface. The force is non-uniformly distributed along the surface, which combines with the surface tension to determine the equilibrium shape of the free surface of the droplet. Two sets of shape deformation calculations are shown as curves *c* and *d* in Fig. 3 for two different applied electric fields, along with the non-deformed free surface shape denoted by curve *b*. Inspection of curve *c* indicates that the droplet deforms into an oval shape under the combined action of an applied electric field and surface tension in microgravity. The surface charge density

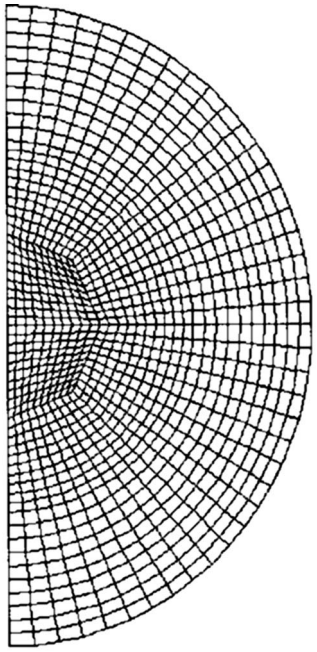

Fig. 2 Boundary element and finite element mesh for numerical computation

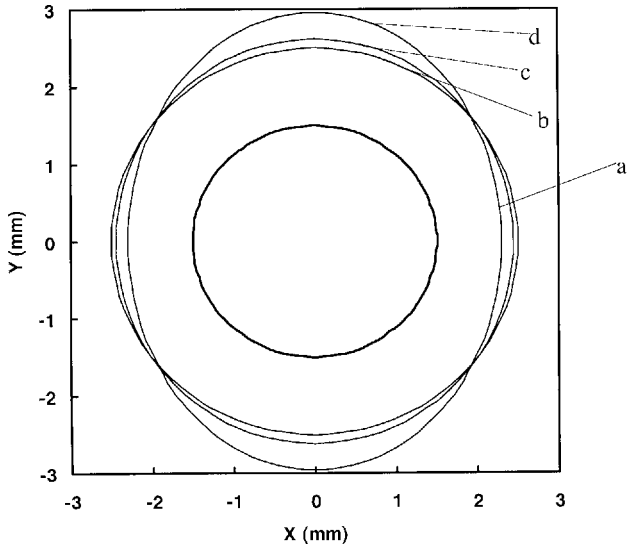

Fig. 3 Computation of free and interfacial surface of an Al-Pb droplet in microgravity: (*a*) interfacial surface shape ($r_i/r_0=0.6$); (*b*) undeformed free surface of liquid sphere; (*c*) $E_0=1.5\times10^6$ (V/m) and $Q=0$ (C); (*d*) $E_0=2.5\times10^6$ (V/m) and $Q=0$ (C)

increases from the equator region to the two pole regions, with the positive charges on the upper half surface and the negative charges on the lower half. The charges interact with the applied, upward-point electric field to produce the electric forces that tend to pull the droplet apart, thereby resulting in the oval shape. A stronger electric field induces stronger electric forces and hence a larger free surface deformation (see curve *d*). It is marked here that the symmetric deformation is a consequence of microgravity. Though not shown, under normal gravity, the deformation is asymmetric and the gravity force will cause the droplet free surface to deform into a blob with the pointy portion aligned along the gravity direction. The electric field effect, however, remains the same.

2) Steady-state temperature and flow fields. As stated earlier, the Maxwell stress only has a component normal to the surface of the droplet and is zero inside. Because it is non-vortical in nature, the stress does not induce internal flow in the droplet. However, the laser heating of the droplet generates a non-uniform temperature distribution both inside and along the surface of the droplet. This temperature variation along the free surface and the interface of the two immiscible fluids gives rise to non-uniform thermocapillary forces that drive the recirculating fluid flows in both liquids.

Figure 4 summarizes the possible different thermal and flow patterns inside the immiscible droplets electrostatically positioned in microgravity. Here A-B (e.g., Si-Co) means that the outer layer of the droplet is A (i.e., Si) and the inside core is A (i.e., Co); this convention will be used hereafter unless otherwise indicated. The droplet shapes are calculated based on the condition given in Table 2. The deformation of the droplet is a result of the balance between the electric and surface tension forces along the droplet surface, which differs from droplet to droplet, as shown in Fig. 4. The temperature and the velocity distributions along the free surface and along the immiscible interface are shown in Figs. 5 and 6, respectively.

Analyses are made to understand the underlying physics that governs these complex thermal and fluid field distributions in these droplets. Let us start with the thermal fields. A feature common to these cases is that the temperature field is symmetric with respect to the equator plane, a mere consequence of the laser beams being applied at the north and south pole regions of the droplets. A higher temperature exists near the laser heating spot and decreases along the fee surface and inside toward the equator plane. Examination of the temperature contour distributions in these droplets illustrates that the thermal energy transport inside these droplets are dominant by conduction mechanism and convection plays a minor role. This is a manifestation of the small Prandtl number Pr associated with these liquid metal droplets (see Table 1). It is further noticed that in the case of Pb-Fe, the temperature contours are distorted somewhat more severely than those in other cases, which is attributed to a relatively larger Pr number of Pb and Fe.

We now turn our attention to the thermally induced fluid flow phenomena inside the droplets. First the flow motion in the outer liquid layer is considered. As the temperature decreases from the pole region to the equator plane, the surface tension force increases accordingly. Along the droplet surface, a fluid particle experiences a surface force gradient and is dragged from the low to the high force region, thereby causing the melt to flow from the pole to the equator regions. At the equator plane, the fluid particle is forced inward into the droplets and finds a way back to the low force region to satisfy the mass conservation, thereby forming a visible recirculating flow insider the outer fluid layer. This surface tension effect is common in all six cases shown in Fig. 4.

The flow distributions near the interface region and insider the inner fluid core, however, display very complex patterns and differ from case to case. While a detailed flow distribution depends on both thermal and physical properties and applied conditions, the complex fluid flow patterns are attributed to a combined effect of the interfacial thermocapillary forces and the inertia in the outer

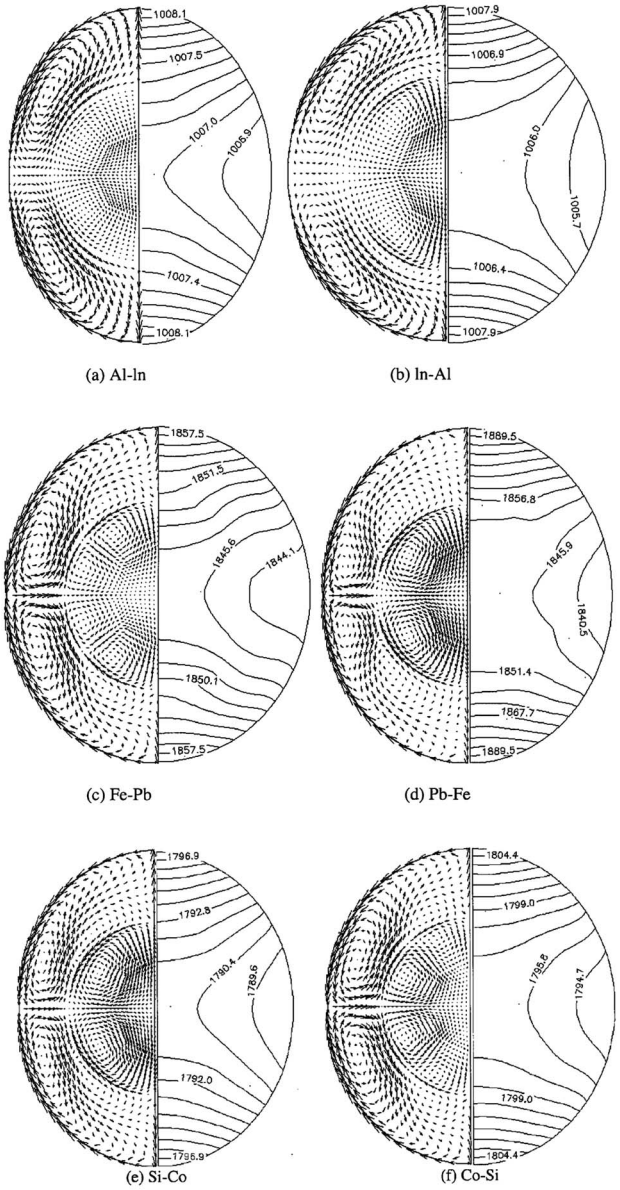

Fig. 4 Steady-state fluid flow and temperature distribution in the droplet ($r_i/r_o=0.6$) for some immiscible materials

fluid layer. Similar to the Marangoni force on the free surface, the interfacial thermocapillary force increases also with a decrease in temperature along the interface and pulls the fluid steam from the high to the low temperature region (see Figs. 5(*b*) and 6(*b*)). The interfacial force acts as an interfacial momentum source that drives the flow in both fluids. On the other hand, the flow resulting from the free surface Marangoni force produces an inertia that superimposes upon the interface and counterbalances the effect from the thermocapillary force. It is this competing mechanism that drives the flow near the interface and the flow inside the core of the droplet.

In the case of Al-In, a strong flow driven by the free surface Marangoni force provides a strong inertia near the immiscible interface and almost completely overpowers the interfacial thermocapillary force, thereby resulting in a very weak flow in the inner fluid core (see Fig. 4(*a*)). Exchanging the inside and outside fluids gives rise to a weaker flow in the outer layer. Thus a visible recirculating flow appears in the inner fluid (see Fig. 4(*b*) and Fig. 6). Perhaps, this competing mechanism for the internal flows is

Table 2 Parameters and some calculated results

Parameters	Al-In	In-Al	Fe-Pb	Pb-Fe	Co-Si	Si-Co	Si-Co	Si-Co
$E\times10^{-6}$ (V/m)	2.5	1.0	2.5	1.5	2.5	2.0	2.0	2.0
$Q_0\times10^{-5}$ (W/m^2)	1.0	1.0	11	11	10	10	10	10
a_d (mm)	2.5	2.5	2.5	2.5	2.5	2.5	2.5	2.5
a_1 (mm)	1.85	1.85	1.85	1.85	1.85	1.85	1.85	1.85
a_{di}/a_{do}	0.6	0.6	0.6	0.6	0.6	0.6	0.9	0.4
V_{maxo} (outer surface) (cm/s)	2.44	0.89	7.72	9.17	7.01	5.69	3.90	6.15
V_{maxi} (inner surface) (cm/s)	0.32	0.22	2.48	3.74	2.68	2.36	3.00	1.09
ΔT K (outer surface)	1.40	2.60	16.20	59.90	11.8	8.90	10.3	8.80
ΔT K (inner surface)	0.47	0.58	7.32	8.89	3.24	3.06	7.64	1.33
Ma_i	3.82	3.82	69.73	69.73	18.39	18.39	72.28	12.58
Ma_o	25.45	13.41	264.9	529.8	164.8	58.45	67.12	57.34
Re_o	111.9	82.68	246.2	923.7	323.8	379.8	260.3	410.5

most revealing in the results shown in Fig. 4(*c*). There are four strong recirculating eddies that comprise the entire flow field, with two in the outer and two in the inner fluids. The largest and yet strongest eddy occurs in the outer layer near the equator, which is driven by the free surface Marangoni forces. The eddy in the inner fluid near equator is clearly the consequence of the inertia force dominating the interfacial surface tension effect. In the region near the immiscible interface from the pole ($\theta=\pm\pi/2$) to ($\theta=\pm\pi/4$), the interfacial surface gradient shows its strongest effect and overpowers the inertia force from the outer fluid layer. It provides the major momentum force that drives the two recirculating loops in the region. When the two fluids switched in their positions in the droplet, the interfacial surface force gradient becomes even more effective in driving the fluid motion near the immiscible interface. This is evident in Fig. 6(*d*) in that the inner

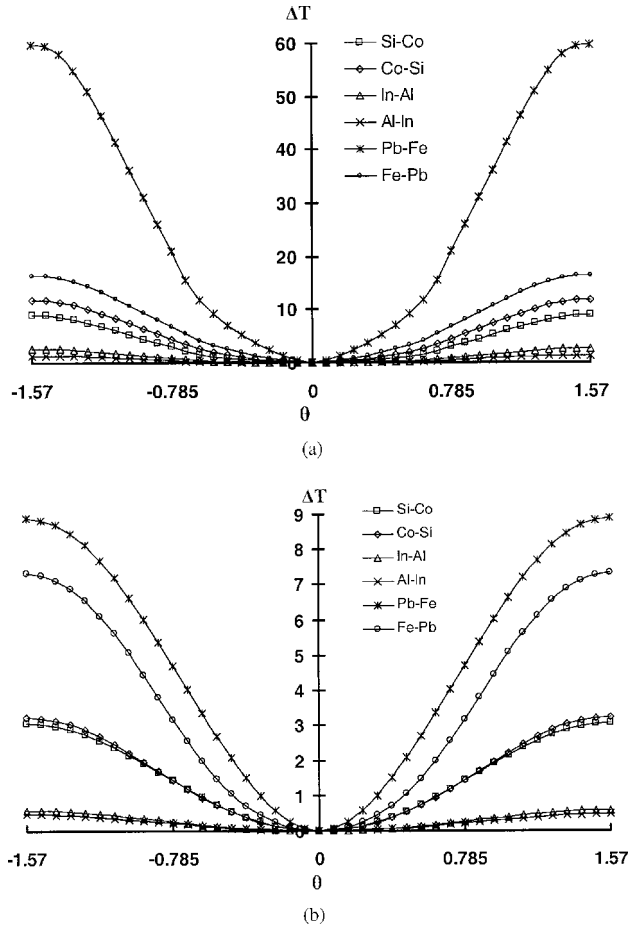

Fig. 5 Steady state temperature distribution ($\Delta T=T-T_{smin}$, where T_{smin} is the minimum surface temperature) along the free surface (*a*) and the interface between the two immiscible liquid metals (*b*). The surface is measured from south ($\theta=-\pi/2$) to north ($\theta=\pi/2$) pole.

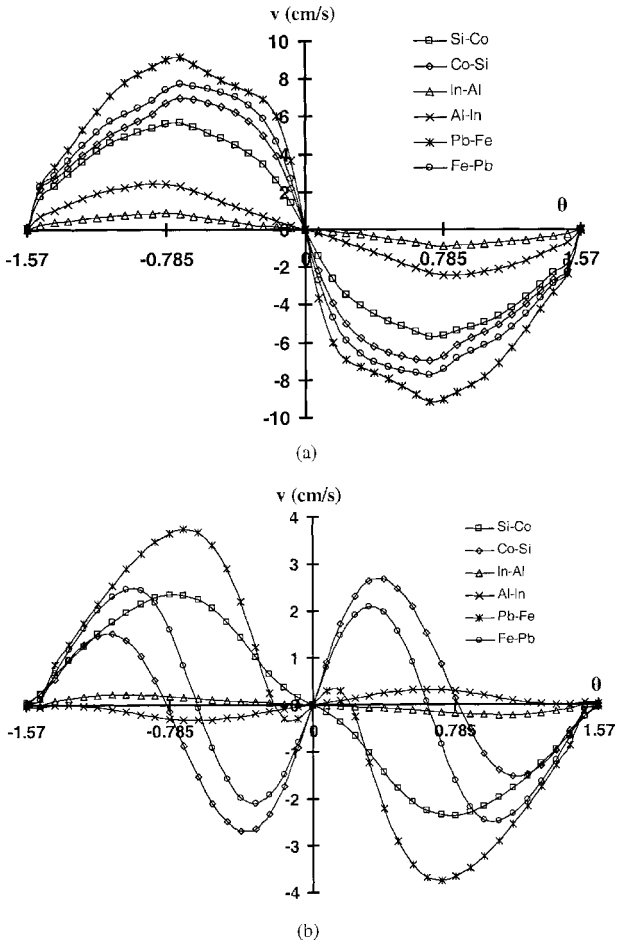

Fig. 6 Steady state fluid flow distribution along the free surface boundary (*a*) and the interface between the two immiscible liquid metals (*b*). The angle θ is measured from ($\theta=-\pi/2$) to ($\theta=\pi/2$). The velocity is positive in the clockwise direction and negative in the counter clockwise direction.

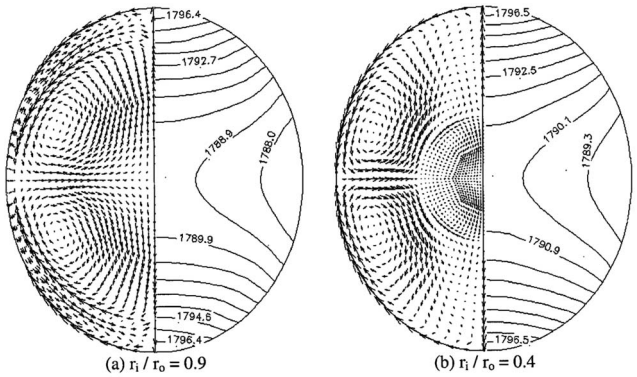

Fig. 7 Steady-state fluid flow and temperature distribution in the Si-Co droplet with different radius ratios

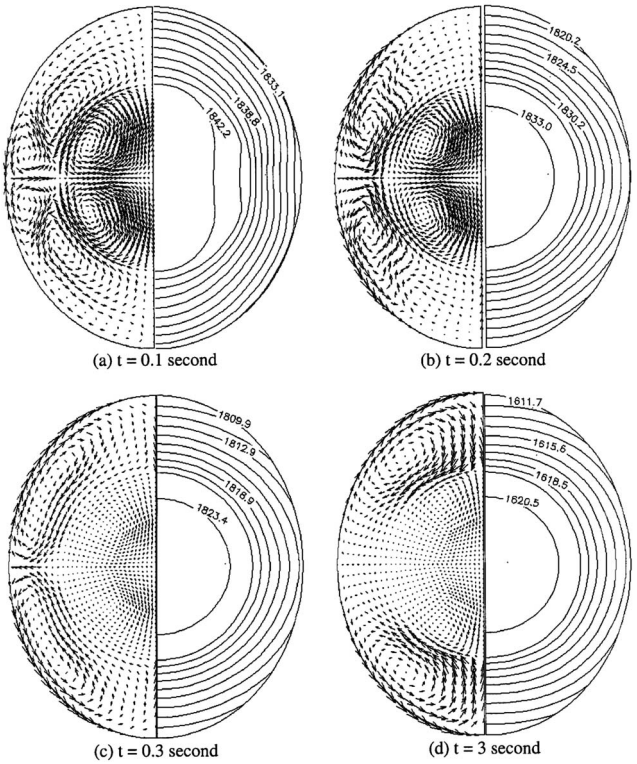

Fig. 8 Transient fluid flow and temperature distributions in a Pb-Fe droplet after the heating lasers are turned off

fluid is now completely covered by one eddy, which is apparently a consequence of the interfacial force induced eddy engulfing the weak inner flow eddy from near the equator plane. The same can be said for the thermal and fluid flow fields in Figs. 4(*f*) and 4(*e*), respectively. As expected, this competing mechanism between the interfacial surface force gradient and outer flow inertia can cause a variety of different flow conditions.

The flow pattern, the velocity intensity, and the thermal field distribution inside the droplets depend upon various parameters, as discussed above. These fluid dynamics and thermal characteristics are also affected by the ratio of the outer and inner fluid volumes. Two of these cases are shown in Fig. 7 for the Si-Co immiscible melt droplets with two different volumes of fluids. Comparison of Fig. 7 with Fig. 4(*e*) shows that the interfacial thermocapillary force becomes much stronger when the ratio of the inner radius over the outer is reduced. Indeed, Fig. 7(*a*) suggests that the flow insider the inner fluid shows an overwhelmingly strong effect from the interfacial surface tension gradient. This contrasts with the case of Fig. 7(*b*), which shows that the effect of the interfacial thermocapillary force is essentially suppressed by the momentum from the outer layer fluid, when the inner-outer radius ratio is reduced to 0.4. This effect is obviously attributed to the fact that a much higher surface temperature gradient exists along the immiscible interface, because of the improved heat conduction due to the increased ratio of the inner over outer radius.

3) Evolution of fluid flow and temperature fields. Knowledge of the decay of both temperature and velocity fields in a levitated droplet of the immiscible metals, as it cools into an undercooling region, is crucial for the design of microgravity experiments for the study of solidification fundamentals. In practice, when the levitation is stabilized and the sample is heated to a desired temperature, the laser beams are turned off and the sample is allowed to cool below the melting point of one of the two fluids by radiation. The computational methodology discussed above may be applied to predict the dynamic development of transient thermal and fluid flow fields in electrostatically positioned droplets as they undergo undercooling. The Pb–Fe droplets are selected for discussion in this study, and the analysis should be applicable to other cases as well. The transient calculations began with the initial ($t=0$) velocity and temperature fields shown in Fig. 4(*d*).

Figure 8 illustrates a set of snapshots of the time evolving velocity and temperature fields in the Pb–Fe droplet when the laser power is switched off and the droplet is allowed to cool for about 3 s. At this point, the temperature drops below the melting point of iron. The time development of the detailed temperature and velocity distributions both along the free surface and the immiscible interface are shown in Figs. 9 and 10. The twofold symmetry with respect to the equator plane is apparently a consequence of the initial fields and thus does not need an elaboration.

Cross examination of Figs. 8–10 reveals some of the most interesting features associated with this complex evolving thermal and fluid flow phenomena as the droplet cools into an undercooling region. First, the temperature drops very rapidly over $t=0$ to $t=0.1$ (s) after the laser power is turned off and the decrease continues afterwards but at a slower pace. At $t=0.1$ (s), the outer surface temperature difference between the pole ($\theta=\pm\pi/2$) and the equator has decreased by about 30 times, which compares with a factor of 5 for a drop in the surface inner temperature difference (also see Fig. 5). On the free surface, the temperature gradient is completely reversed at about $t=0.2$ (s), with the temperature at the pole now being smaller than that at the equator. In comparison, the reversal takes about 0.3 (s) along the immiscible interface. This change in the temperature distribution may be explained by the fact that thermal radiation is stronger near the pole where temperature is high and thus the temperature reversal starts there. As the change in the thermal field needs time to propagate into the inside of the droplet, there exists a delay in the temperature reversal at the immiscible interface. After the reversal is completed, the temperature gradient direction remains the same along both the free surface and the interface. This dynamic evolution of the thermal field is largely attributed to thermal conduction and surface radiation, and the convection effect is relatively weak or minimal, as evident by the small Prandlt number of the melts. This change in the thermal field is responsible for the complex evolving fluid flow field in the droplet, as shown in Fig. 8.

Figure 8(*a*) shows that at $t=0.1$ (s), the four-loop structure remains unchanged despite a significant drop in temperature. This is because the surface tension force gradient is unchanged. The large drop in the temperature, however, causes a reduction in the velocity magnitude, as is evident by comparing Figs. 7 and 10, where the velocity distribution along the free and inter surfaces are plotted. At some time close to $t=0.2$ (s), a reversal of the temperature gradient along the free surface occurs, which in turn causes a

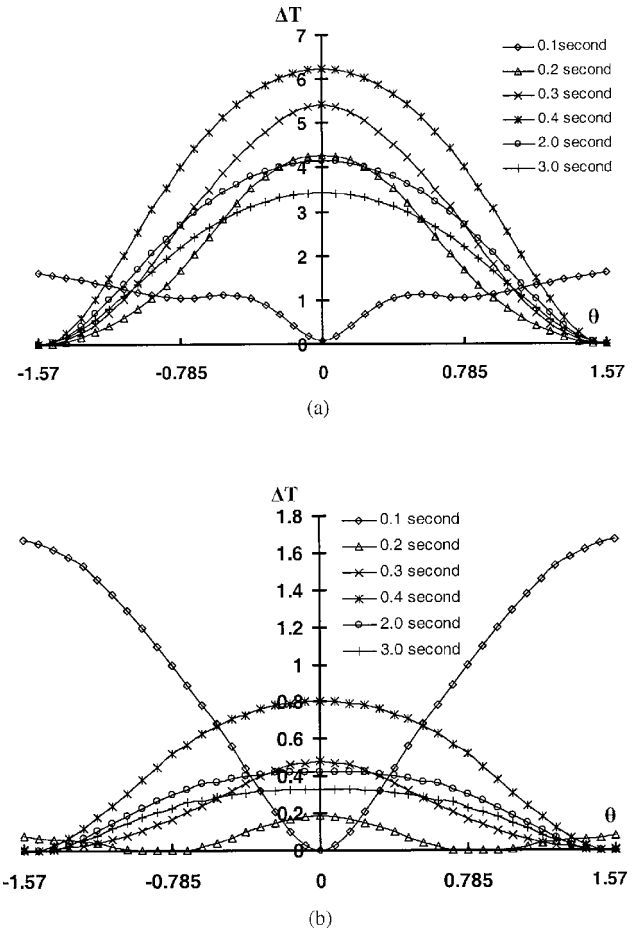

Fig. 9 Transient temperature distribution ($\Delta T = T - T_{min}$) along the surface from ($\theta = -\pi/2$) to ($\theta = \pi/2$): (*a*) free surface and (*b*) the immiscible interface (Pb-Fe)

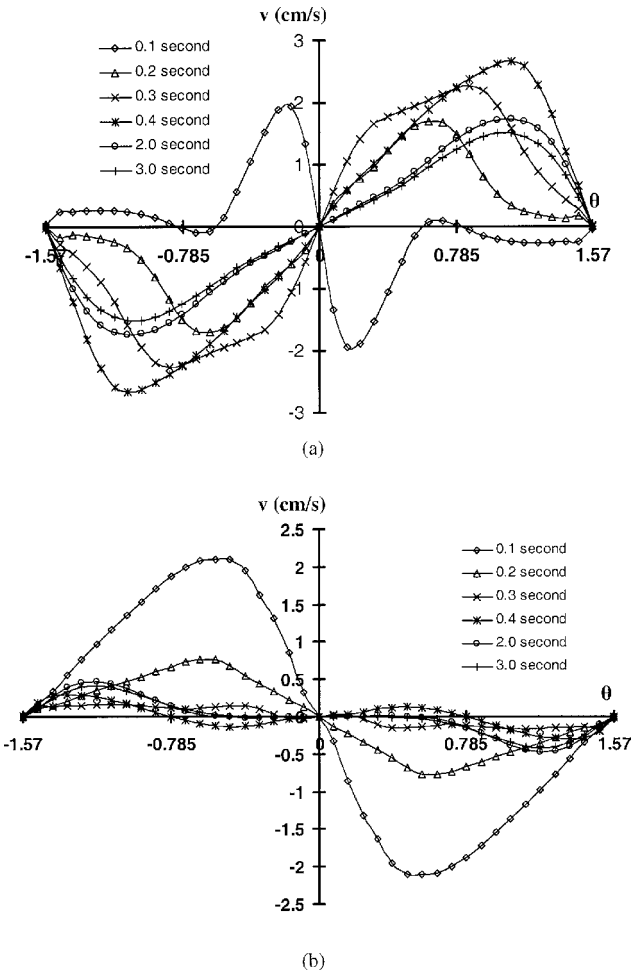

Fig. 10 Transient fluid flow distribution along the surface from ($\theta = -\pi/2$) to ($\theta = \pi/2$): (*a*) free surface and (*b*) the immiscible interface (Pb-Fe). The velocity is positive in the clockwise direction and negative in the counter clockwise direction.

corresponding reversal of the surface tension force gradient, with a higher pulling force now at the pole. Consequently, the fluid stream along the free surface now flows from the equator plane to the poles (see Fig. 8(*b*)), thereby causing the outer fluid eddy near the equator to reverse its rotation. At this point, however, the interfacial surface force gradient still remains the same in direction, that is, it intends to drive the flow from the pole to the equator region. Thus, in the near interfacial region, the outer flow inertia force complements the interfacial surface force gradient, thereby giving rise to the fluid pattern as shown in Fig. 8(*b*). As the evolution continues, the interface gradually completes its temperature reversal. Then the inertia force starts competing with the interface surface force in driving the fluid flow near the interfacial region. Figures 8(*c*) and 8(*d*) reveal that the outer flow inertia force becomes more powerful from $t = 0.3$ (s) onwards and is mainly responsible for the flow near the immiscible interface region. This means that the flow in both the immiscible fluids of the droplet comes primarily from the free surface Marangoni effect and the interfacial surface force plays a negligible role.

Concluding Remarks

This paper has presented a numerical study of the free surface deformation and Marangoni convection in electrically conducting immiscible droplets electrostatically-positioned under microgravity. The computational methodology entails the use of the boundary element method for the solution of the electrostatic field outside the droplets, which is coupled with the weighted residuals method for solving the unknown free surface shapes along the droplet free surfaces. The temperature and fluid flow fields, in both transient and steady states, are solved using the Galerkin finite element method. It is shown that the inner interface demarking the two immiscible fluids in an electrically conducting droplet is immune to the applied electrostatic field and maintains its sphericity in microgravity. The free surface, however, deforms into an oval shape, which is determined by the balance of the Maxwell stress and the surface tension. The thermal and fluid flow field distributions are rather complex in an immiscible droplet. The thermal transport is by heat conduction and convection plays only a minor role. The flow near the free surface is driven by the well-known Marangoni convection mechanism, which causes the fluid particle to move from the high to low temperature regions. The flow inside the inner fluid and near the immiscible interface, however, is driven by a competing mechanism between the thermally-induced interfacial surface tension gradient and the inertia force associated the outer fluid layer. During cooling into an undercooled state, the surface temperature gradients along the free surface experience a reversal, as a result of surface radiation, which results in a reversal of the surface flow. During the time between the surface thermal gradient reversals along the free and the interfacial surfaces, the flow near the interfacial region is driven by a complimentary mechanism between the interfacial and the inertia forces. After the interfacial thermal gradient reversal is completed, however, the interfacial flows are predominantly driven by the inertia forces of the outer layer fluid.

Acknowledgment

Financial support of this work by NASA (Grant No. NNM04AA17G) is gratefully acknowledged.

Nomenclature

a_d, a_{di}, a_{do} = radius of a sphere, inner radius of a droplet, and outer radius of a droplet
$C(r_i)$ = geometric coefficient resulting from boundary integral formulation
C_p = heat capacity
$\mathbf{E}, E_0$ = electric field, applied electric field
$\mathbf{F}$ = Force vector from numerical formulation
G = Green function
H = mean curvature
$\hat{i}$ = Unit vector of ith component
k = thermal conductivity
$\mathrm{Ma}_i, \mathrm{Ma}_0$ = inner, outer Marangoni numbers $\mathrm{Ma}_i = (\partial\gamma/\partial T)(T_{\min} - T_{\max})\rho C_p a_{di}/\mu k$, $\mathrm{Ma}_o = (\partial\gamma/\partial T)(T_{\min} - T_{\max})\rho C_p a_{do}/\mu k$
$\mathbf{n}(n_r, n_z)$ = outward unit normal, its r and z components
p = pressure
p_o = hydrostatic pressure constant
Pr = Prandtl number, $\mathrm{Pr} \equiv \mu C_p k$
Q = net charge on the droplet
Q_c = critical charge
Q_o = laser beam heat flux constant
$\mathbf{r}, \hat{\mathbf{r}}, \mathbf{r}$ = point vector, unit vector, and r coordinate
R = distance measured from the center of the unformed droplet
Re_0 = Reynolds number, $\mathrm{Re}_0 = \rho V_{\max,o} a_{do}/\mu$
$\mathrm{Re}_{\mathrm{el}}$ = electric Reynolds number, $\mathrm{Re}_{\mathrm{el}} = (\epsilon_0/\sigma)V_{\max}/a_{do}$
$\mathbf{t}$ = tangential vector
T, T_∞, T_r = temperature, temperature of surroundings, reference temperature
T_E = Maxwell stress
$T_{\max}, T_{\min}$ = maximum and minimum temperatures
ΔT = difference between $T_{\max}$ and $T_{\min}$
$\mathbf{T}_E$ = $\mathbf{T}_E = [(\mathbf{n}\cdot\nabla\Phi)^2/2]\mathbf{nn}$ the Maxwell stress tensor
$V_{\max}, V_{\max,0}$ = maximum velocity, maximum velocity of the outer layer
$\mathbf{u}$ = velocity
$\hat{z}$ = unit vector of z direction
z = z coordinate
z_c = center of mass along the z axis

Greek Symbols

β = thermal expansion coefficient
ϵ_0 = permittivity of free surface or region designated by Ω_2
ϵ = emissivity
∇ = gradient operator
φ_{AB} = mass diffusivity coefficient
ϕ = shape function of velocity
Φ = electric potential
γ = surface tension
κ = geometric parameter for elliptical functions
η = molecular viscosity
ρ = density
θ = shape function of temperature
ψ = shape function of pressure
ξ = shape function of molar concentration
σ = electrical conductivity
σ_e = surface charge distribution
σ_s = Stefan-Boltzmann constant
$\underline{\sigma}$ = stress tensor
Ω = computational domain

Subscripts

d = droplet
i = the ith point
l = laser beam
1 = outer layer region inside the droplet
2 = region outside the droplet
3 = inner layer region inside the droplet

Superscripts

i = the ith component
T = matrix transpose
1 = outer layer region inside the droplet
2 = region outside the droplet
3 = inner layer region inside the droplet

References

[1] Trinh, B., and Wang, T. G., 1982, "Large-Amplitude Free and Driven Drop-Shape Oscillations: Experimental Observation," J. Fluid Mech., **122**, pp. 315–338
[2] Zong, J. H., Li, B. Q., and Szekely, J., 1992, "The Electrodynamic and Hydrodynamic Phenomena in Magnetically-Levitated Droplets, Part I, Steady State Behavior," Acta Astronaut., **26**(6), pp. 435–439
[3] Rhim, W. K., Chung, S. K., Barber, D., Man, K. F., Gutt, G., and Rulison, A., 1993, "An Electrostatic Levitator for High-Temperature Containerless Materials Processing in l-g," Rev. Sci. Instrum., **64**(10), pp. 2961–2965.
[4] Rhim, W. K., 1997, Private Communication, Jet Propulsion Laboratory, California Institute of Technology, Pasadena, CA.
[5] Rhim, W. K., 1997, "Thermophysical Property Measurements of Molten Semiconductors," in Microgravity Materials Science Conference, Huntsville, AL, pp. 427–433.
[6] Taylor, G. I., 1966, "Studies in Electrodynamics," Proc. R. Soc. London, Ser. A, **291**, pp. 159–171.
[7] Torza, S., Cox, R. G., Mason, S. G., 1971, "Electrohydrodynamic Deformation and Burst of Liquid Drops," Philos. Trans. R. Soc. London, Ser. A, **269**, p. 295.
[8] Ajayi, O. O., 1978, "A Note on Taylor's Electrohydrodynamic Theory," Proc. R. Soc. London, Ser. A, **364**, pp. 499–505.
[9] Song, S. P., Li, B. Q., 1998, "Coupled Boundary/Finite Element Analysis of Magnetic Levitation Processes: Free Surface Deformation and Thermal Phenomena," ASME J. Heat Transfer, **120**, pp. 492–503.
[10] Song, S. P., and Li, B. Q., 1999, "Coupled Boundary/Finite Element Solution of Magnetothermal Problems," Int. J. Numer. Methods Eng., **44**, pp. 1055–1077.
[11] Kolbe, M., Reutzel, S., Patti, A., Egry, I., Ratke, L., and Herlach, D. M., 2004, "Undercooling and Demixing of Cu-Co Melts in the Tempus Facility during Parabolic Flight," in *Multiphase Phenomena and CFD Modeling and Simulation in Materials Processing*, L. Nastac and B. Q. Li, eds. TMS, PA, pp. 55–64.
[12] Ratke, L., and Diefenbach, S., 1995, "Liquid Immiscible Alloys," Mater. Sci. Eng., R., **R15**, pp. 263–347.
[13] Adornato, P. M., and Brown, R. A., 1983, "Shape and Stability of Electrostatically Levitated Drops," Proc. R. Soc. London, Ser. A, **389**, pp. 101–122.
[14] Feng, J. Q., and Beard, K. V., 1990, "Small-Amplitude Oscillations of Electrostatically Levitated Drops," Proc. R. Soc. London, Ser. A, **430**, pp. 133–154.
[15] Song, S. P., Li, B. Q., 2000, "Free Surface Shapes and Thermal Convection in Electrostatically Levitated Droplets," Int. J. Heat Mass Transfer, **43**, pp. 3589–3606.
[16] Song, S. P., and Li, B. Q., 2001, "A Hybrid Boundary/Finite Element Method for Simulating Viscous Flows and Shapes of Droplets in Electric Fields," Int. J. Comput. Fluid Dyn., **15**, pp. 293–308.
[17] Huo, Y., and Li, B. Q., 2004, "Three-Dimensional Marangoni Convection in Electrostatically Positioned Droplets under Microgravity," Int. J. Heat Mass Transfer, **47**, pp. 3533–3547.
[18] Feng, J. Q., 1999, "Electrohydrodynamic Behavior of a Drop Subjected to a Steady Uuniform Electric Field at Finite Electric Reynolds Number," Proc. R. Soc. London, Ser. A, **455**, pp. 2245–2269J.
[19] Jackson, D., 1975, Classical Electrodynamics, (2nd ed.), Wiley, New York.
[20] Rayleigh, J. W. S., 1882, "On the Equilibrium of Liquid Conducting Mass Charged With Electricity," Philos. Mag., **14**, pp. 184–186.

Height Effect on Heat-Transfer Characteristics of Aluminum-Foam Heat Sinks

W. H. Shih
Research Assistant

W. C. Chiu
Research Assistant

W. H. Hsieh
Professor
e-mail: imewhh@ccu.edu.tw

Department of Mechanical Engineering,
National Chung Cheng University,
Chia-Yi, Taiwan, R.O.C.

This study investigates and demonstrates the two conflicting effects of the height on the cooling performance of aluminum-foam heat sinks, under the impinging-jet flow condition. In addition, the nonlocal thermal equilibrium phenomena are also investigated. When the H/D (the height to diameter ratio) of the aluminum-foam heat sinks is reduced from 0.92 to 0.15, the Nusselt number of aluminum-foam heat sinks is found to first increase and then decrease. The increase in the Nusselt number is caused by the increased percentage of the cooling air reaching the top surface of the waste-heat generation block, resulting from the reduced flow resistance. The decrease in the Nusselt number is mainly caused by the reduction in the heat-transfer area between the cooling air and the solid phase of the aluminum-foam heat sink. As the porosity and pore density decrease, the Nusselt number increases and the convective heat transfer is enhanced. The correlation between the Nusselt and Reynolds numbers for each of the 15 samples studied in this work is reported. For samples with a $H/D > 0.31$, the temperature difference between the solid and gas phases of aluminum-foam heat sinks decreases with the increase of the distance from the heated surface. The non-local thermal equilibrium regime is observed to exist at low Reynolds number and small dimensionless height. On the other hand, for samples with a $H/D \leqslant 0.31$, the temperature difference first increases and then decreases with the increase of the distance from the heated surface; the maximum temperature difference is located at $z/H \fallingdotseq 0.25$ and is independent of the Reynolds number.
[DOI: 10.1115/1.2188461]

Keywords: porous material, aluminum foam, nonlocal thermal equilibrium, Nusselt number, convective heat transfer, height effect

Introduction

In the convective cooling processes of electronic components with metal-foam heat sinks, the waste heat generated by the electronic components passes through the metal foam, and then mostly dissipates in a convective manner into the air (a small part of waste heat is transferred to the air by means of radiation). The increase in height of metal-foam heat sinks will increase the gas-solid interfacial heat-transfer area and result in a better cooling performance. On the other hand, the increase in height of porous heat sinks will increase the flow resistance, reduce the percentage of the cooling gas reaching the heated surface and result in a worse cooling performance. Considering these two conflicting effects of height increase, it is evident that there must be a height for the best cooling performance of a particular type of the metal-foam heat sink.

In the past, most of the studies on metal-foam heat sinks were devoted to the investigation of enhanced heat-transfer characteristics, with little emphasis on the effect of flow resistance on the heat-transfer performance. Chao and Li [1] reported a significant improvement in power dissipation when a commercial pin-fin sink was replaced with an aluminum-foam heat sink under forced convective cooling condition. Chou and Yang [2] also showed that the overall heat-transfer coefficient of aluminum foam with 91.4% porosity was reported to be 25% higher than that for a conventional finned array at an air speed of 3.6 m/s. In the work of Lee et al. [3], a dissipating power of 100 W for a 1 cm^2 chip with an aluminum metal-foam heat sink and a low-power muffin fan was demonstrated. Izadpanah et al. [4] showed that the effect of natural convection is negligible, and that forced convection is the main mechanism of heat transfer over the range of operating conditions in their investigation.

The effect of flow resistance on the cooling performance of metal-foam heat sinks has rarely been studied. Seo et al. [5] reported that when the air is flowing in a channel half filled with an aluminum-foam heat sink, there is only 28–37% of the air flowing through the aluminum-foam heat sink due to higher flow resistance of the aluminum-foam heat sink. When the percentage of the air flowing through the aluminum-foam heat sink is increased, the heat-transfer performance is also increased.

The thermal analysis of metal-foam heat sinks has started to receive a fair amount of attention recently in theoretical studies [6–8]. The analyses of the local thermal equilibrium (LTE) condition in porous media (Sozen and Vafai [9], Amiri and Vafai [10], Hwang and Chao [11], Hwang et al. [12], Hsieh and Lu [13]) have shown that the assumption of LTE usually leads to an unacceptable error, due to the large difference in their thermal conductivities. The necessity of considering the temperature difference between the solid metal foam and the air has been demonstrated by various theoretical and numerical studies as discussed above. However, the experimental measurement of the temperature difference of the gas and the solid phases in order to further investigate these phenomena and provide data for model validation has rarely been carried out.

Recently, Hsieh et al. [14] performed an experimental study to measure the Nu, and the temperature distributions of the gas and the solid phases at the circumferential edge of six types of aluminum-foam heat sinks under forced convective cooling conditions. The effects of the porosity and the pore density of aluminum foam, and the air velocity on Nu and the temperature distributions, were also investigated in this work. In addition, the existence of a non-local thermal equilibrium (NLTE) condition

Contributed by the Heat Transfer Division of ASME for publication in the JOURNAL OF HEAT TRANSFER. Manuscript received November 30, 2004; final manuscript received October 12, 2005. Review conducted by Suresh V. Garimella.

Table 1 Properties of aluminum foam used in this study

Sample No.	PPI (pore/inch)	Porosity	Mean pore diameter, d_p (m)	Equivalent spherical diameter, D_p (m)	K[a] (W/m K)	H (mm)	H/D
1-1	10	0.92	1.19×10^{-3}	1.59×10^{-4}	5.89	60	0.92
1-2	10	0.92	1.19×10^{-3}	1.59×10^{-4}	5.89	20	0.31
2-1	20	0.87	8.27×10^{-4}	1.85×10^{-4}	8.32	60	0.92
2-2	20	0.87	8.27×10^{-4}	1.85×10^{-4}	8.32	50	0.77
2-3	20	0.87	8.27×10^{-4}	1.85×10^{-4}	8.32	40	0.62
2-4	20	0.87	8.27×10^{-4}	1.85×10^{-4}	8.32	30	0.46
2-5	20	0.87	8.27×10^{-4}	1.85×10^{-4}	8.32	20	0.31
2-6	20	0.87	8.27×10^{-4}	1.85×10^{-4}	8.32	15	0.23
2-7	20	0.87	8.27×10^{-4}	1.85×10^{-4}	8.32	10	0.15
3-1	20	0.94	8.14×10^{-4}	8.49×10^{-5}	4.95	60	0.92
3-2	20	0.94	8.14×10^{-4}	8.49×10^{-5}	4.95	20	0.31
4-1	20	0.96	8.00×10^{-4}	5.26×10^{-5}	3.55	60	0.92
4-2	20	0.96	8.00×10^{-4}	5.26×10^{-5}	3.55	20	0.31
5-1	40	0.94	6.85×10^{-4}	7.14×10^{-5}	4.50	60	0.92
5-2	40	0.94	6.85×10^{-4}	7.14×10^{-5}	4.50	20	0.31

[a]Reference 19.

within the aluminum-foam heat sink was discussed as well, based on the deduced temperature difference between the gas and the solid phases of aluminum-foam heat sinks. The height effect on the heat-transfer characteristics, however, was not discussed in their work.

In the cooling process of aluminum-foam heat sinks, the heat-transfer area and the flow resistance are the two main factors that influence the heat-transfer performance. Following the study of Hsieh et al. [14], this study systematically changes the height of the aluminum-foam heat sinks to investigate the height effect on the cooling performance. At the same time, the effects of the porosity and the pore density of aluminum foam, as well as the air velocity on Nu and the solid- and gas-temperature distributions are investigated experimentally. In addition, the existence of a NLTE condition within the aluminum-foam heat sink is discussed based on the deduced temperature differences between the gas and the solid phases of the aluminum-foam heat sinks.

Materials and Methods

Five types of aluminum-foam heat sinks (Duocel®, Alloy 6101, ERG Materials and Aerospace Corporation), as shown in Table 1, are used in this study. Figure 1 is the micrograph of an aluminum-foam heat sink, showing the dimensions and axes. Samples 1, 3 and 5 are used for studying the pore-density effect, and samples 2, 3, and 4, for the porosity effect. In order to study the influence of the height of aluminum-foam heat sinks on the heat-transfer characteristics, samples 2-1–2-7 were made of the same aluminum foam but with different dimensionless heights. All other samples have two different dimensionless heights, $H/D=0.92$ and 0.31. The measurement of the mean pore diameter (d_p) and the equivalent spherical diameter (D_p) was achieved according to the method used in Refs. [15,16].

Figure 2 shows the schematic diagram of the experimental apparatus used in this study for the measurement of heat-transfer characteristics of aluminum-foam heat sinks. The flow straightener within the inlet air pipe (diameter=65 mm, length=50 mm) consists of stacked foam sponges. At the inlet of the aluminum foam, the temperature and pressure of the air are measured with a *k*-type thermocouple and a pressure transducer (Validyne pressure transducer, 0.5% accuracy), respectively, to determine the condition of the inlet air.

Each aluminum-foam heat sink is composed of a piece of aluminum foam and a base plate. The diameter of the aluminum foam is 65 mm. The base plate is made of 3-mm-thick aluminum. During the tests, the waste heat is generated by a waste-heat generating block, which consists of a 20-mm-thick circular copper plate with a diameter of 65 mm and an electric heating tape, which is attached to the bottom of the copper plate as shown in

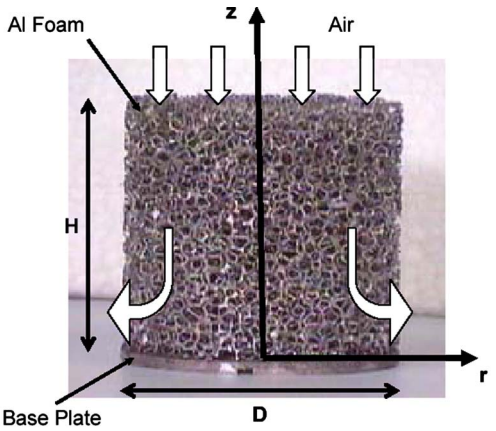

Fig. 1 A photo of the aluminum-foam heat sink showing the dimensions and axes (sample 1-1, 10 PPI, $\varepsilon=0.92$, $H=60$ mm, $D=65$ mm)

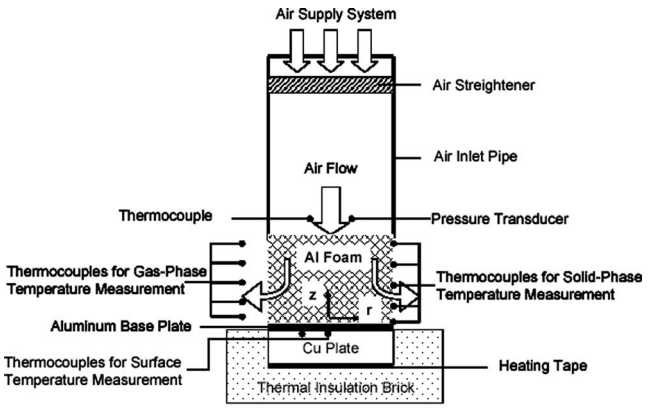

Fig. 2 Experimental apparatus for the measurements of heat transfer characteristics of aluminum-foam heat sinks

Fig. 2. Three thermocouples for the measurement of temperature are placed in the groves at the top surface of the copper plate. Two thermocouples are installed in positions symmetric to the center of the copper plate, and on a radius of 30 mm from the center. The third one is also installed 30 mm away from the center but at a 90° angle to the other two thermocouples. Due to the highly conductive nature of the copper plate, the measured temperatures from the three thermocouples are within 0.15%, and therefore, the values of temperatures reported later in this paper are the average temperatures measured from the three thermocouples. For that reason, the deduced Nusselt number based on this average number represents the overall thermal performance of aluminum-foam heat sinks.

In measuring the solid- and gas-phase temperatures of the heat sink, six *k*-type thermocouples are positioned at equal spacing along a *z*-direction line, 0.1 cm away from the perimeter of the aluminum foam. These thermocouples measure the temperature profile of the air exiting the aluminum foam. Another set of six *k*-type thermocouples are silver glued (also at equal spacing in the *z* direction) at the perimeter of the solid-phase portion (aluminum portion) of the aluminum foam, for measuring the solid-phase temperature. The diameter of the insulated thermocouple wire is 1 mm. In silver gluing the thermocouple to an aluminum-foam heat sink, the silver epoxy (Loctite Corporation, 3880, thermal conductivity=4 W/m K) is applied to the contacting area between the thermocouple and the aluminum-foam heat sink after they have been positioned in contact with each other on a working plate. Afterwards, the silver epoxy is cured by putting the working plate with the thermocouple and the aluminum-foam heat sink in a furnace (Lindberg/Blue M) and going through a curing temperature cycle (heating at 8°C/min until 150°C, maintaining at 150°C for 40 min, and then cooling in the furnace). Based on the post-test examination, the thickness of the silver epoxy is observed to be less than 0.1 mm. The associated interface thermal resistance is estimated to be about 4°C/W. By considering the heat losses through the thermocouple wire and the insulation layer, the heat transfer across the silver epoxy interface is about 8×10^{-4} W. The temperature measurement error based on the estimated interface thermal resistance and heat transfer across the silver epoxy interface is about 3×10^{-3}°C. During a test, the amount of air flow is regulated by a valve, and the flow is straightened by the flow straightener installed in the air inlet pipe before entering the test section. With the valve in the open position, the power is turned on to the heating tape, and the heat conducts to the porous heat sink through the copper plate. The readings of the thermocouples, used to measure solid- and gas-phase temperatures, are recorded when the steady-state condition has been reached. The power to the heating tape is then turned off, and the flow rate of the air is increased so as to cool down the porous heat sink until it reaches the ambient temperature. This procedure is repeated for all samples of porous heat sink at each flow rate. For examining the repeatability of the experiments, the tests are repeated three times at each flow rate for samples 1 and 5. A good agreement is found in these tests at each air flow rate. The maximum difference in the measurement of the solid- and gas-phase temperature between these repeated tests for samples 1 and 5 is 4.8% and Nu, 2.4%. Due to the demonstrated good repeatability of the experiments, one test is performed for the other samples at each flow rate.

In this study, the Nu defined below is measured experimentally

$$\mathrm{Nu}_{Dp} = \frac{hD_p}{k} \tag{1}$$

and

$$h = q/[A(T_{\mathrm{Cu}} - T_{in})] \tag{2}$$

where h is the convective heat transfer coefficient, D_p the equivalent spherical diameter of porous media, k the effective thermal conductivity of the aluminum foam, q the waste-heat transfer rate, A the base area of the aluminum-foam heat sink, T_{Cu} the surface temperature of the waste-heat generating block (i.e., the surface of copper plate), and T_{in} the temperature of the inlet air. In this paper, the Nusselt number is defined in order to evaluate the ratio of the convective heat transfer to the conductive heat transfer (including the conduction through the air and the aluminum) of the aluminum-foam heat sink. The effective thermal conductivity used in this study is a property evaluating the ability of the aluminum foam to conduct the heat through the gas (air) and solid (aluminum) phases of the aluminum foam under a no flow condition. Thus, following the works by Bhattacharya and Mahajan [17] and Calmidi and Mahajan [18], the effective thermal conductivity, including the contributions from the conductivity of both the air and the aluminum, is used in Eq. (1) to calculate the Nusselt number. The effective thermal conductivity of the aluminum foams is calculated from the correlation developed by Calmidi and Mahajan [19]. The correlation was obtained by averaging the heat transfer through the complex structure of the aluminum foam, and verified experimentally. The aluminum foams used in this work and Calmidi and Mahajan [19], were supplied by the same corporation. The accuracy of the correlation is 3.6%.

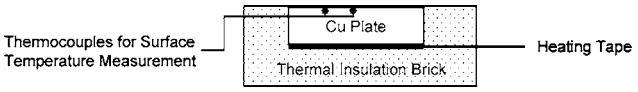

Fig. 3 Apparatus for measuring heat loss

In determining the convective heat transfer coefficient h, Eq. (2) is used with the substitution of the measured *Ts*. In Eq. (2), q is the waste-heat transfer rate, and is equal to the subtraction of heat loss through the thermal insulation brick from the heat generated by the heating tape. The heat loss through the thermal insulation brick is a function of the temperature difference between the top surface of the waste-heat generating block and the ambient, obtained by the following procedures [14].

Figure 3 shows the experimental apparatus for the measurement of heat loss through the insulation brick at different $(T_{\mathrm{Cu}}-T_\infty)$, where T_{Cu} is the top surface temperature of the copper plate and T_∞ is the temperature of the ambient [14]. The experimental apparatus is the same as the one used for Nu measurement described above, except that the aluminum-foam heat sink is removed from the apparatus. As shown in Fig. 3, the heating tape is powered by a dc power supply. A FLUKE Hydra Series II records the top-surface temperature of the copper plate *Ts* and the ambient temperature T_∞. The copper plate and the heating tape are placed within the thermal insulation bricks made of alumina ($Al_2O_3+Si_2O_2+Fe_2O_3$, bulk density $\leqslant$0.9 g/cm^3, porosity $\leqslant$0.8, thermal conductivity at 350°C$\leqslant$0.314 W/m°C). The temperatures of the top surface of the copper plate and the ambient are both measured under natural convection and steady-state condition. The heat loss through the insulation brick at different $(T_{\mathrm{Cu}}-T_\infty)$ is calculated by the equations given below

$$q_{\mathrm{Loss}} = q_{in} - q_{\mathrm{Natural}} \tag{3}$$

$$q_{in} = IV \tag{4}$$

$$q_{\mathrm{Natural}} = \bar{h}A(T_{\mathrm{Cu}} - T_\infty) \tag{5}$$

where q_{loss} is the heat loss through the alumina brick to the ambient; q_{Natural} is the heat transfer through natural convection from the top surface of the copper plate to the ambient; $\bar{h}$ is the average natural convective heat transfer coefficient at the top surface of the copper plate [20]; A is the top surface area of the copper plate; T_{Cu} is the top-surface temperature of the copper plate, which ranges from 317 to 380 K in this study; T_∞ is the temperature of the ambient; q_{in} is the power generated by the heating tape; I and

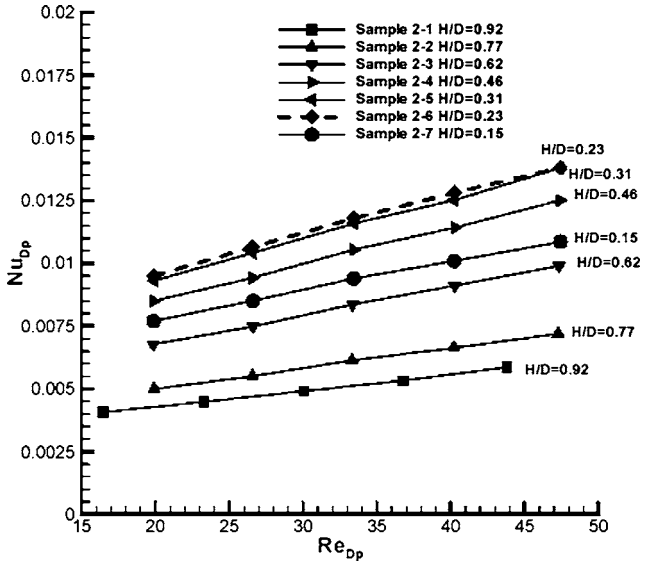

Fig. 4 Effect of Reynolds number on the Nusselt number for samples 2-1–2-7

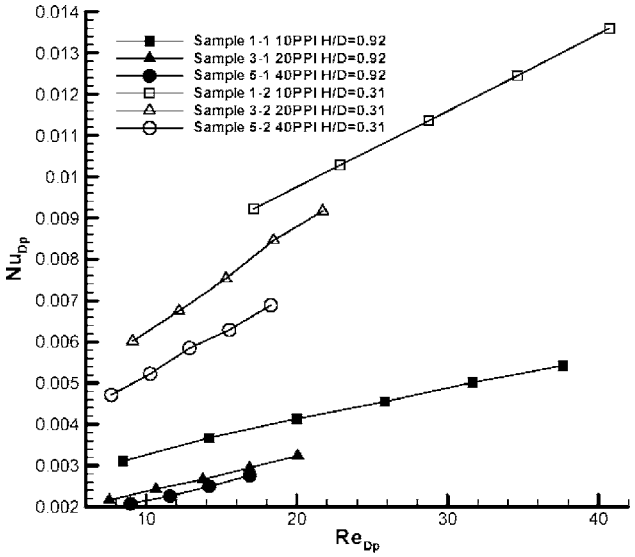

Fig. 5 Effect of Reynolds number on Nu for heat sinks with different pore densities and heights

V are the input dc current and voltage, respectively. The correlation between heat loss and temperature difference of the copper plate and ambient deduced from the experimental data is

$$q_{\text{loss}} = 1.26 \times 10^{-7}(T_{\text{Cu}} - T_\infty)^3 - 3.9 \times 10^{-6}(T_{\text{Cu}} - T_\infty)^2 + 7.61 \times 10^{-2}(T_{\text{Cu}} - T_\infty) + 0.179 \quad (6)$$

The standard error of the estimate of the correlation [21] is less than 5.8%. When estimating the heat loss through the heat insulation brick, the measured Ts and T_∞ during an experiment of the Nu measurements are substituted into Eq. (3). The result shows that the heat loss is a function of the temperature difference between the top surface of the waste-heat generating block and the ambient. The heat loss is about 6.6–10% of the input power.

The uncertainties of the experimental apparatus used in this experiment are obtained from the apparatus suppliers. Temperature reader (Fluke Hydra II) has an uncertainty of ±0.45 K. The flow meter calibrated by the manufacturer has a volumetric flow accuracy of ±0.05%. The power supply has a current uncertainty of ±0.2%. The size precision is ±0.02 mm. The uncertainty of the thermocouple, which is calibrated with a resistance temperature detector (RTD) (Omega PR-11, accuracy: ±0.35 K at 273.15–373.15 K), is ±0.25%. The uncertainties of deduced data are determined with the t distribution under a confident level of 0.95 [22,23]. The degree of freedom is determined by the number of test data. The uncertainty of the temperature measurement is ±1.34%–2.42%. The pressure measurement has an uncertainty of ±3.3%. The power measurement has an uncertainty of ±0.1%. The uncertainty of the velocity is about ±3.8%–15.8%. The uncertainties for the Reynolds number and heat transfer coefficient are ±3.0%–15.4% and ±11.3%–12.3%, respectively.

Results and Discussion

To analyze the heat transfer phenomena of aluminum-foam heat sinks for electrical devices, this work experimentally measures the temperature distribution of air and aluminum foam, and the surface temperature of the waste-heat generating block. The Nusselt number and dimensionless temperatures are deduced from the measured data.

Figure 4 shows the effect of the Reynolds number on the Nusselt number for samples 2-1–2-7. The definitions of the Reynolds number is given as

$$\text{Re}_{Dp} = \frac{\rho U D_p}{\mu} \quad (7)$$

In the heat-transfer process of aluminum-foam heat sinks, the decrease in height of a heat sink will decrease the gas-solid interfacial heat-transfer area and result in a worse cooling performance. On the other hand, the increase in the height of the heat sink would increase the flow resistance and force the cooling air to go radially outwards, exiting from the heat sink. This would reduce the percentage of the cooling air reaching the top surface of the waste-heat generation block, resulting in a worse cooling performance. Samples 2-1–2-7 are the same aluminum-foam heat sinks with different dimensionless heights. In Fig. 4, it is noted that the Nusselt number increases with the decrease of the dimensionless height of aluminum—foam heat sinks until $H/D=0.23$, and then the Nusselt number decreases. The increase in the Nusselt number is caused by the increased percentage of the cooling air reaching the top surface of the waste-heat generation block, resulting from the reduced flow resistance. The decrease in the Nusselt number is mainly caused by the reduction in the heat-transfer area between the cooling air and the solid phase of the aluminum-foam heat sink. For this particular sample, it is evident that the dimensionless height for the maximum cooling performance is at $H/D=0.23$. It is also evident that the Nusselt number increases as the Reynolds number increases due to the higher mass flow rate taking away more heat.

Figure 5 shows the effect of the Reynolds number on Nu for heat sinks with different pore densities and two different dimensionless heights, $H/D=0.92$ and 0.31.

The results in Fig. 5 show that the Nusselt number increases with the increase in the Reynolds number and the decrease in the pore density. The decrease of the dimensionless height will increase the Nusselt number about 2.2–2.9 times due to the decreased flow resistance as the dimensionless height decreases. Figure 6 shows the effect of the Reynolds number on Nu for heat sinks with different porosities and two different dimensionless heights, $H/D=0.92$ and 0.31. From Fig. 6, it is noted that the Nusselt number increases with the increase in the Reynolds number and the decrease in porosity. The decrease in dimensionless height will increase the Nusselt number about 2.1–2.9 times due to the decreased flow resistance as the dimensionless height decreases.

Based on the experimental results shown in Figs. 4–6 a corre-

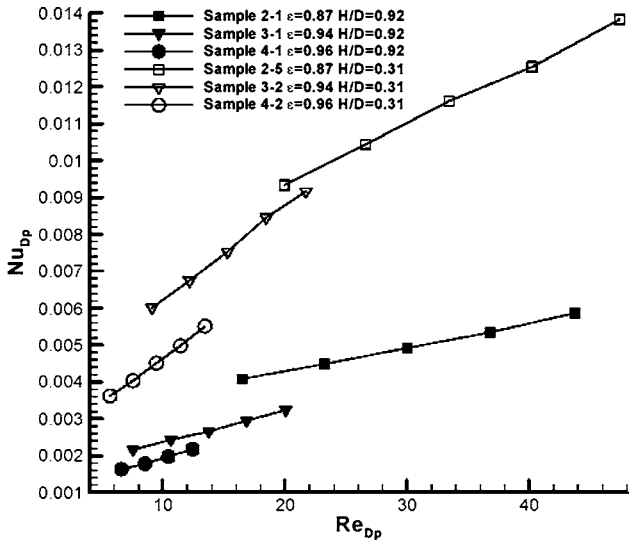

Fig. 6 Effect of Reynolds number on Nu for heat sinks with different porosities and heights

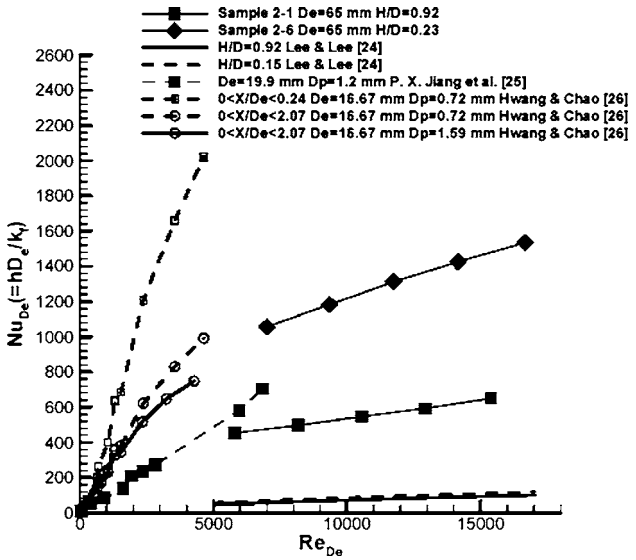

Fig. 7 Comparison of Nu_{De} from the present study, Lee and Lee [24], Jiang et al. [25], and Hwang and Chao [26]

lation between the Nusselt and Reynolds numbers for each sample is obtained by a least-square fitting method. The correlation is expressed in the form of the following equation

$$\mathrm{Nu}_{Dp} = a\,\mathrm{Re}_{Dp}^{b} \tag{8}$$

The coefficients, a and b, of Eq. (9) are tabulated in Table 2. The standard error of estimate, S_e, is defined as [21]

$$S_e = \sqrt{\sum_{i}^{n} (\mathrm{Nu}_i - \mathrm{Nu}_{pred,i})^2/(n-2)} \tag{9}$$

where n is the number of data point, $n-2$ is the degree of freedom, Nu_i the ith data point of measured Nusselt number, and $\mathrm{Nu}_{pred,i}$ the calculated Nusselt number by Eq. (8). The result shows that the fit is in good agreement with measured Nu.

In order to demonstrate the enhanced heat transfer by the metal foams, the comparison of the results from this work and the results of air impinging on a flat surface by Lee and Lee [24] is given in Fig. 7. In addition, the results from the studies of the forced convective heat transfer in sintered porous plate channels [25,26] are also compared in Fig. 7. The correlation between the average Nusselt number and the Reynolds number for the impinging jet is shown as follows [24]

$$\mathrm{Nu}_{De} = 0.203\,\mathrm{Re}_{De}^{0.635}\,(H/D_e)^{-0.0968} \tag{10}$$

Following the notation used in [24], the Nusselt and the Reynolds numbers in Fig. 7 are based on the hydraulic diameter and gas conductivity, as shown in the following

$$\mathrm{Nu}_{De} = \frac{hD_e}{k_f} \tag{11}$$

$$\mathrm{Re}_{De} = \frac{\rho U D_e}{\mu} \tag{12}$$

The results in Fig. 7 show that the use of metal foams would enhance the heat transfer significantly. The Nusselt number with metal foams is about 6.5–20.4 times larger than that with an impinging jet alone. The dependence of Nu_{De} on Re_{De} is similar for both studies; the Nu_{De} increases with the increase of Re_{De}. On the other hand, the effect of the height is different. For an impinging jet, the Nu_{De} increases monotonically with the decrease of the height of the jet (as indicated by Eq. (9)). For this particular type of aluminum-foam heat sink discussed in Fig. 7, the Nu_{De} has a maximum value at $H/D=0.23$ as shown in Fig. 4.

Figure 7 also shows the comparison of the results from the present study and the studies of the forced convective heat transfer in sintered porous plate channels [25,26]. As shown in Fig. 7, though the flow pattern and materials are different, the measured Nu_{De} is in the same order of magnitude. The Nu_{De} for sintered porous plate channels shows a higher Re_{De} dependence than that for the axisymmetric aluminum-foam heat sink of this work.

In order to investigate the local thermal equilibrium phenomena of aluminum-foam heat sinks, the temperatures of the solid and gas phases at the perimeter of the heat sinks are measured at different Reynolds numbers. The results are shown in Figs. 8(*a*) and 8(*b*). The dimensionless temperatures of the solid and gas phases are defined, respectively, as

$$\theta_s = \frac{T_s - T_{in}}{\dot{q}H/k} \tag{13}$$

Table 2 Coefficients of the correlations between Nu_{Dp} and Re_{Dp} (*: from Ref. [21])

Sample No.	$\mathrm{Nu}_{Dp}=a\mathrm{Re}_{Dp}^{b}$		
	a	b	S_e^*
1-1	1.34×10^{-3}	3.81×10^{-1}	7.60×10^{-5}
1-2	2.49×10^{-3}	4.56×10^{-1}	1.45×10^{-4}
2-1	1.38×10^{-3}	3.77×10^{-1}	1.03×10^{-4}
2-2	1.36×10^{-3}	4.30×10^{-1}	6.44×10^{-5}
2-3	1.75×10^{-3}	4.47×10^{-1}	1.00×10^{-4}
2-4	2.17×10^{-3}	4.52×10^{-1}	1.34×10^{-4}
2-5	2.35×10^{-3}	4.56×10^{-1}	1.49×10^{-4}
2-6	2.58×10^{-3}	4.34×10^{-1}	5.61×10^{-5}
2-7	2.31×10^{-3}	3.99×10^{-1}	6.58×10^{-5}
3-1	9.04×10^{-4}	4.20×10^{-1}	5.60×10^{-5}
3-2	1.96×10^{-3}	5.00×10^{-1}	1.15×10^{-4}
4-1	9.04×10^{-4}	4.20×10^{-1}	5.60×10^{-5}
4-2	1.96×10^{-3}	5.00×10^{-1}	1.15×10^{-4}
5-1	7.53×10^{-4}	4.55×10^{-1}	4.52×10^{-5}
5-2	1.88×10^{-3}	4.44×10^{-1}	7.25×10^{-5}

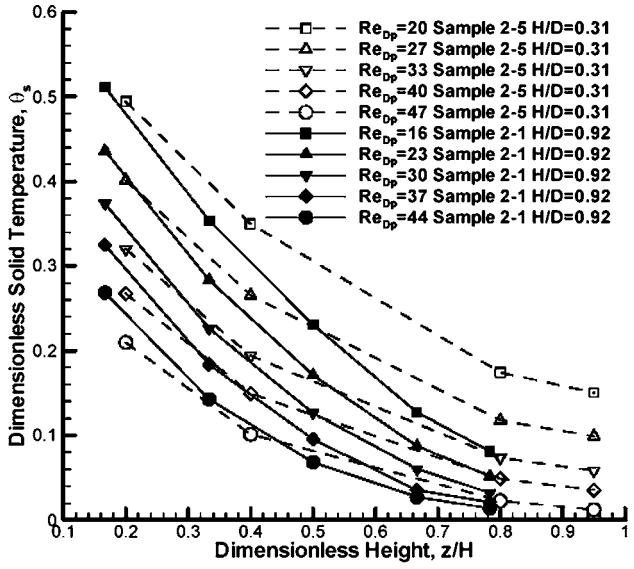

(*a*)

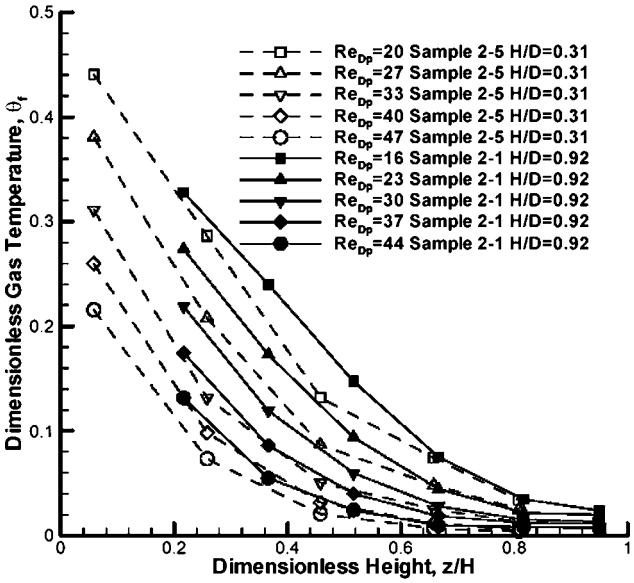

(*b*)

Fig. 8 (*a*) Effect of Reynolds number on the distributions of dimensionless solid temperature of samples 2-1 and 2-5. (*b*) Effect of Reynolds number on the distributions of dimensionless gas temperature of samples 2-1 and 2-5.

$$\theta_f = \frac{T_f - T_{in}}{\dot{q}H/k} \tag{14}$$

In Figs. 8(*a*) and 8(*b*), the dimensionless solid and fluid temperatures are noted to decrease with the increase of the Reynolds number and the distance away from the heated base plate. Near the air inlet (where $z/H=1$), the dimensionless gas temperatures of samples 2-1 and 2-5, as shown in Fig. 8(*b*) are very close to the inlet air temperature under different Reynolds numbers. On the other hand, the dimensionless solid-phase temperature of sample 2-1 ($H/D=0.92$) as shown in Fig. 8(*a*) is lower than that of sample 2-5 ($H/D=0.31$). This is caused by the dimensionless height difference of these two samples. Sample 2-1 is much longer than Sample 2-5, and the heat is carried away before it reaches the top of the aluminum foam, resulting in the temperature at the top of sample 2-1 being very close to the air inlet temperature, and lower than that of sample 2-5.

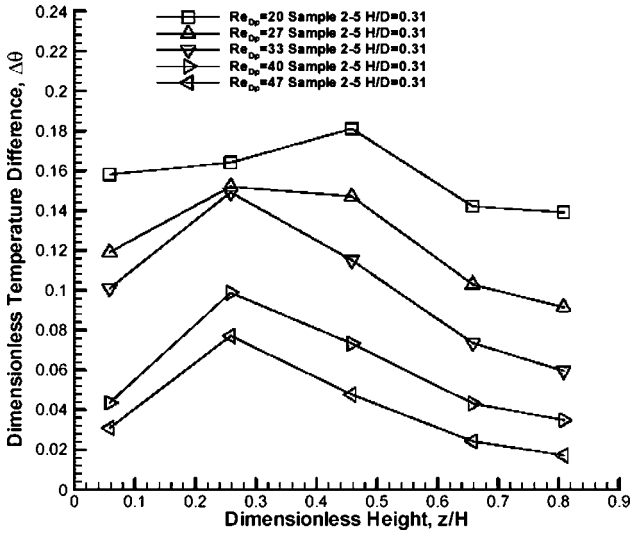

Fig. 9 Effect of Reynolds number on the distributions of dimensionless temperature difference of sample 2-5

Since the heat is conducted to the aluminum-foam heat sink from the heated base plate, the heat exchange between the solid and the gas phases can be investigated by observing the temperature difference near the base plate. The effect of the Reynolds number on the distribution of the dimensionless temperature difference of sample 2-5 is shown in Fig. 9. The definition of the dimensionless temperature difference is given below

$$\Delta\theta = \theta_s - \theta_f \tag{15}$$

From Fig. 9, we can find that the temperature difference decreases with the increase of the Reynolds number. There is a maximum temperature difference located at $z/H=0.25$ or 0.45. This indicates that the non-local thermal equilibrium condition is very significant at this location.

Figure 10 shows the height effect on the distribution of dimensionless temperature difference. When the dimensionless height of the sample is less than or equal to 0.31, it is noted that there is a maximum temperature difference located at $0.25<z/H<0.45$. At

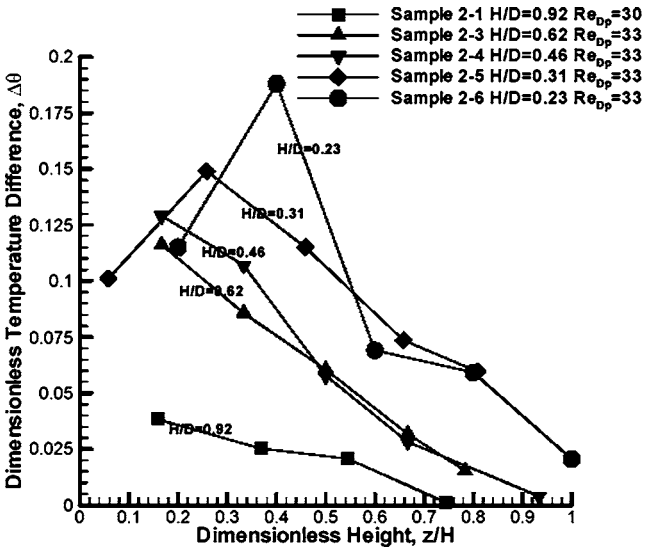

Fig. 10 Height effect on the distribution of dimensionless temperature difference

the boundary between the aluminum foam and the aluminum base plate, the temperatures of the solid phase of the aluminum foam and the air should be theoretically equal to the surface temperature of the aluminum base plate, and are very close to each other. This is due to the continuous temperature boundary condition at the surface and the uniform temperature distribution of the aluminum base plate caused by its highly conductive nature. As the distance from the surface of the aluminum base plate is increased, the air velocity is increased. The increased air velocity would increase both the local mass flux of the air and the convective heat-transfer coefficient between the solid phase of the aluminum foam and the air. The rate of increase of the mass flux (which is linearly proportional to the velocity) is, however, larger than that of the convective heat-transfer coefficient between the solid phase of the aluminum foam and the air (which is usually proportional to the velocity raised to a power less than one). This would result in a lower air temperature and an increased temperature difference between the solid phase of the aluminum foam and the air, though the heat transfer between the solid phase and the air increases. The temperature difference between the solid phase of the aluminum foam and the air would reach a maximum as the distance from the surface of the aluminum base plate is further increased, and then the temperature difference starts to decrease caused by the reduced temperature of the solid phase as its heat is taken away by the air.

In Fig. 10, the non-monotonic variation of temperature difference can be clearly observed from the measured data for the sample with a dimensionless height equal to 0.31 or 0.25. It is also observed that the location of the maximum temperature moves closer to the surface of the aluminum base plate as the dimensionless height of the sample increases. Due to the insufficient spatial resolution of the temperature measurement for samples with a dimensionless height larger than 0.31 in this study (temperature measurements are conducted at six locations spaced equally along the z direction), the detailed temperature distributions near the surface were not obtained and the nonmonotonic variation of temperature difference was not observed for these samples in Fig. 10.

The Reynolds number and the spatial location are the two main factors affecting the local thermal equilibrium condition between the solid and the air. Figures 11(a) and 11(b) show the effects of these two factors on the difference of dimensionless temperatures for samples 2-1 and 2-5, respectively. It can be seen that the temperature difference decreases with the increase in the Reynolds number and the dimensionless height for sample 2-1. On the other hand, there is a maximum temperature difference at $z/H=0.25$ for sample 2-5 as shown in Figs. 9 and 10. In modeling the heat-transfer processes of porous materials, according to [27], the effect of a non-local thermal equilibrium between the solid and the fluid should be considered when the temperature difference between the two phases exceeds 5%, and the assumption of a local thermal equilibrium is no longer valid. According to this 5% temperature difference, the boundary between the local thermal equilibrium regime and the non-local thermal equilibrium regime is plotted in Figs. 11(a) and 11(b). For sample 2-1, it is noted that the local thermal equilibrium regime is located at the high Reynolds number and large dimensionless height (top/right) portion of the figures, and that the non-local thermal equilibrium regime is located at the low Reynolds number and small dimensionless height (bottom/left) portion of the figures. For sample 2-5, the non-local thermal equilibrium regime occupies most of the region in Fig. 11(b).

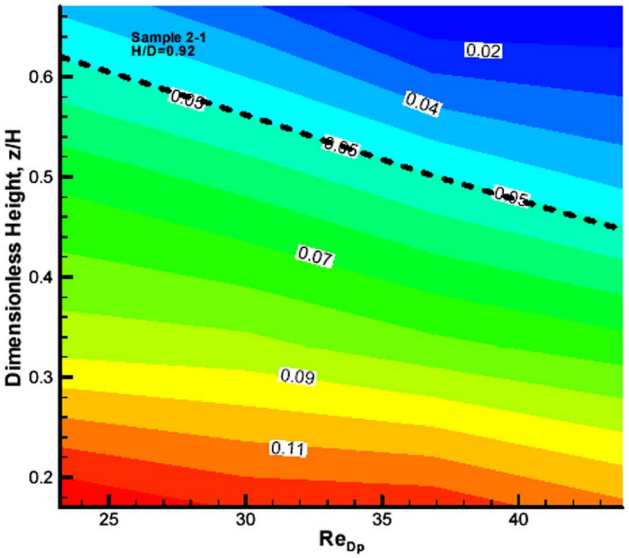

Fig. 11 (*a*) Effects of the Reynolds number and the height on the dimensionless temperatures difference for sample 2-1. (*b*) Effects of the Reynolds number and the height on the dimensionless temperature difference for sample 2-5.

Summary and Conclusions

This study investigates and demonstrates the two conflicting effects of the height on the cooling performance of aluminum-foam heat sinks, under the impinging-jet flow condition. Results indicate that the decrease in the height of aluminum-foam heat sink would first increase and then decrease the cooling performance of the aluminum-foam heat sink. On the one hand, the increase in the cooling performance is caused by the increased percentage of the cooling air reaching the top surface of the waste-heat generation block, resulting from the reduced flow resistance. On the other hand, the decrease in the cooling performance is mainly caused by the reduction in the heat-transfer area between the cooling air and the solid phase of the aluminum-foam heat sink. Though many theoretical studies have demonstrated the importance and necessity in considering the non-local thermal equilibrium phenomenon for simulating the heat transfer of porous materials, experimental data are rare in the literature. This work provides the much needed experimental data of the temperature difference between the gas and the solid phases for better understanding the non-local thermal equilibrium phenomenon and for validating theoretical models. For samples with a dimensionless height >0.31, the non-local thermal equilibrium regime was observed to exist at the low Reynolds number and small dimen-

sionless height. On the other hand, for samples with a dimensionless height ≤ 0.31, the non-local thermal equilibrium regime existed at most of the Reynolds numbers and at any height.

Acknowledgment

This paper represents part of the study results obtained by the work supported by the National Science Council of Taiwan, R.O.C. under Contract No. NSC-90-2212-E-194-038.

Nomenclature

D = pipe diameter of the air inlet pipe and diameter of aluminum-foam heat sink, m
D_P = equivalent spherical diameter of porous media, m
De = hydraulic diameter, m
d_p = mean pore diameter, m
h = mean convective heat transfer coefficient, $W/m^2\text{-}°C$
H = height of the test section, m
k = effective thermal conductivity, $W/m\text{-}°C$
n = number of data points
Nu = nusselt number
PPI = pores per inch
q = waste heat transfer rate, W
$\dot{q}$ = heat flux through the bottom of aluminum-foam heat sink
r = position along r direction, m
Re = Reynolds number
S_e = standard error of estimate
T = temperature, K
U = average entrance velocity, m/s
z = position along axial direction, m

Greek Symbols

μ = viscosity
ε = porosity
Δ = difference

Subscripts

air = air properties
e = estimate
f = fluid
in = inlet condition
I = electric current, A
s = solid
V = voltage
W = wall
∞ = ambient condition

References

[1] Chao, C.-H., and Li, J.-M., 1998 "Foam-Metal Heat Sinks for Thermal Enhanced BGA Package Applications," *The 11th International Symposium on Transport Phenomena ISTP-II*, Hsinchu, Taiwan, Vol. 4, pp. 23–29.
[2] Chou, S.-F., and Yang, C.-H., 1993, "Heat Transfer Characteristics of Aluminum Foam Metal," *Proceedings of Sixth International Symposium on Transport Phenomena in Thermal Engineering*, Seoul, Korea, pp. 709–714.
[3] Lee, Y. C., Zhang, W., Xie, H., and Mahajan, R. L., 1993, "Cooling of a FCHIP Package With 100 W, 1 cm^2 Chip," *Proceedings of the 1993 ASME Int. Elec. Package Conf.*, Vol. 1, ASME, New York, pp. 419–423.
[4] Izadpanah, M. R., Muller-Steinhagen, H., and Jamialahmadi, M., 1998, "Experimental and Theoretical Studies of Convective Heat Transfer in a Cylindrical Porous Medium," Int. J. Heat Fluid Flow, **19**, pp. 629–635.
[5] Seo, Y. K., Jin, W. P., and Byung, H. K., 2003, "Thermal Performance of Aluminum-Foam Heat Sinks by Forced Air Cooling," IEEE Trans. Compon. Packag. Technol., **26**, pp. 262–267.
[6] Calmidi, V. V., 1998, "Transport Phenomena in High Porosity Fibrous Metal Foams," Ph.D. thesis, Department of Mechanical Engineering, University of Colorado.
[7] Antohe, B. V., Lage, J. L., and Price, D. C., 1996, "Numerical Characterization of Micro Heat Exchangers Using Experimentally Tested Porous Aluminum Layers," Int. J. Heat Fluid Flow, **17**, pp. 594–603.
[8] Lage, J. L., and Weinert, A. L. D. C., 1996, "Numerical Study of a Low Permeability Microporous Heat Sink for Cooling Phased-Array Radar Systems," Int. J. Heat Mass Transfer, **39**, pp. 3633–3647.
[9] Sozen, M., and Vafai, K., 1993, "Longitudinal Heat Dispersion in Porous Beds With Real Gas Flow," J. Thermophys. Heat Transfer, **7**, pp. 153–157.
[10] Amiri, A., and Vafai, K., 1994, "Analysis of Dispersion Effects, and Non-Thermal-Equilibrium, Non-Darcian, Variable Porosity Incompressible Flow Through Porous Media," Int. J. Heat Mass Transfer, **37**, pp. 939–954.
[11] Hwang, G. J., and Chao, C. H., 1994, "Heat Transfer Measurement, and Analysis for Sintered Porous Channel," J. Heat Transfer, **116**, pp. 456–464.
[12] Hwang, G. J., Wu, C. C., and Chao, C. H., 1995, "Investigation of Non-Darcian Forced Convection in an Asymmetric Heated Sintered Porous Channel," J. Heat Transfer, **117**, pp. 725–732.
[13] Hsieh, W. H., and Lu, S. F., 2000, "Heat-Transfer Analysis, and Thermal Dispersion in Thermally-Developing Region of a Sintered Porous Metal Channel," Int. J. Heat Mass Transfer, **43**, pp. 3001–3011.
[14] Hsieh, W. H., Wu, J. Y., Shih, W. H., and Chiu, W. C., 2004, "Experimental Investigation of Heat-Transfer Characteristics of Aluminum-Foam Heat Sinks," Int. J. Heat Mass Transfer, **47**, pp. 5149–5157.
[15] Richardson, J. T., Peng, Y., and Remue, D., 2000, "Properties of Ceramic Foam Catalyst Supports: Pressure Drop," Appl. Catal., A, **204**, pp. 19–32.
[16] Liu, J. F., Wu, W. T., Chiu, W. C., and Hsieh, W. H., 2006, "Measurement, and Correlation of Friction Characteristic of Flow Through Foam Matrixes," Exp. Therm. Fluid Sci., **30**, pp. 329–336.
[17] Bhattacharya, A., and Mahajan, R. L., 2002, "Finned Metal Foam Heat Sinks for Electronics Cooling in Forced Convection," J. Electron. Packag., **124**, pp. 155–163.
[18] Calmidi, V. V., and Mahajan, R. L., 2000, "Forced Convection in High Porosity Metal Foams," J. Heat Transfer, **122**, pp. 557–565.
[19] Calmidi, V. V, and Mahajan, R. L., 1999, "The Effective Conductivity of High Porosity Fibrous Metal Foams," J. Heat Transfer, **121**, pp. 466–471.
[20] Incropera, F. P., *Introduction to Heat Transfer*, 3rd ed. Wiley, New York, p. 462.
[21] Freund, J. E., and Simon, G. A., 1970, Statistics-A First Course, 6th ed., Prentice–Hall, Engelwood Cliffs, NJ., p. 455.
[22] Kline, S. J., and McClintock, F. A., 1953, "Describing the Uncertainties in Single Sample Experiments," Mech. Eng. (Am. Soc. Mech. Eng.), **75**, pp. 3–8.
[23] Benediet, R. P., 1984, *Fundamentals of Temperature, Pressure, and Flow Measurements*, Wiley, New York.
[24] Lee, J., and Lee, S.-J., 1999, "Stagnation Region Heat Transfer of a Turbulent Axisymmetric Jet Impinging," Exp. Heat Transfer, **12**, pp. 137–156.
[25] Jiang, P.-X., Li, M., Lu, Y.-J., Yu, L. Ren, Z.-P., 2004, "Experimental Research on Convection Heat Transfer in Sintered Porous Plate Channels," Int. J. Heat Mass Transfer, **47**, pp. 2085–2096.
[26] Hwang, G. J., and Chao, C. H., 1994, "Heat Transfer Measurement, and Analysis for Sintered Porous Channels," J. Heat Transfer, **116**, pp. 456–464.
[27] Vafai, K., and Sozen, M., 1990, "Analysis of Energy, and Momentum Transport for Fluid Flow Through a Porous Bed," J. Heat Transfer, **112**, pp. 690–699.

Modeling of Heat Transfer in Low-Density EPS Foams

R. Coquard
Centre Scientifique et Technique du Bâtiment (CSTB),
24 rue Joseph Fourier,
38400 Saint Martin d'Hères, France
e-mail: r.coquard@cstb.fr

D. Baillis
Centre Thermique de Lyon (CETHIL),
UMR CNRS 5008,
Domaine Scientifique de la Doua, INSA de Lyon,
Bâtiment Sadi Carnot,
9 rue de la physique,
69621 Villeurbanne CEDEX, France
e-mail: dominique.baillis@insa-lyon.fr

Expanded polystyrene (EPS) foams are one of the most widely used thermal insulators in the building industry. Owing to their very low density, both conductive and radiative heat transfers are significant. However, only few studies have already been conducted in the modeling of heat transfer in this kind of medium. This is due to their complex porous structure characterized by a double-scale porosity which has always been ignored by the previous works. In this study, we present a model of one-dimensional steady state heat transfer in these foams based on a numerical resolution of the radiation-conduction coupling. The modeling of the conductive and radiative properties of the foams takes into account their structural characteristics such as foam density or cell diameter and permits us to study the evolution of their equivalent thermal conductivity with these characteristics. The theoretical results have been compared to equivalent thermal conductivity measurements made on several EPS foams using a flux-meter apparatus and show a good agreement. [DOI: 10.1115/1.2188464]

Keywords: EPS foams, equivalent thermal conductivity, radiation/conduction coupling, radiative properties

1 Introduction

Among all the different porous media used for the building thermal insulation, expanded polystyrene (EPS) foams are the most widely sold after glass wools. They represent approximately 25% of the total building insulation market. Indeed, they are very convenient to manipulate due to their mechanical properties (lightness and stiffness), relatively cheap, and have good thermal performances. They are generally classified among the cellular materials but their porous structure is, in fact, more complex than a simple cellular matrix. This structure is characterized by a double-scale porosity as a result of their production process. Owing to their very low density comprised between 10 and 30 kg/m^3, both conductive and radiative transfers are significant, leading to a coupling between these two modes of heat transfer.

Numerous studies have dealt with radiative and conductive heat transfer through porous materials as reported by Baillis and Sacadura [1]. Fibrous materials have been the most widely studied. We can cite as examples, the work of Lee [2], Jeandel et al. [3] on silica fibers, Milos and Marschall [4] on rigid fibrous ceramic insulation or Milandri [5]. Other researchers worked on glass foams (Fedorov and Viskanta [6]), carbon foams (Baillis [7]) packed beds (Kaviany and Singh [8], Kamiuto [9], Coquard and Baillis [10]), cellular foams (Glicksman et al. [11]) or metallic foams (Calmidi and Mahajan [12]). However, only few studies have already been conducted in the modeling of heat transfer in EPS foams.

Glicksman et al. [11] proposed a general study of radiative and conductive transfer through cellular foam insulation but they only consider materials with homogeneous cellular structure composed of cells struts and windows and with densities much greater than EPS foams. Kuhn et al. [13] studied more precisely heat transfer through EPS foams but they also considered that their cellular structure is homogeneous and thus, neglected the influence of macroscopic porosities. Moreover, this study was especially interested in EPS foams with relatively high density and did not show good agreements with experimental measurements for foams with lower densities. Finally, Quenard et al. [14] proposed another simple model which takes into account more precisely the real porous structure of EPS foams and, noticeably, their double-scale porosity for the conduction calculation. All of these studies neglected the coupling between radiative and conductive transfer and used Fourier's law and Rosseland approximation to treat conductive and radiative transfer, respectively. Moreover, they always considered that the cellular material forming the foam is made of dodecahedric cells.

In the present study, we propose a new approach to treat the total heat transfer in low density EPS foams based on a numerical resolution of the conduction-radiation coupling. The modeling of the radiative and conductive properties, required for the numeric calculation, take into account the particular structure of EPS foams, notably their double scale porosity. Moreover, our model permits us to analyze the influence of the shape of the cells forming the cellular materials contained in EPS beads, as we both take into account dodecahedric and cubic shapes. First, we describe the particular porous structure of EPS foams. Then, we present precisely the model proposed. Thereafter, the results of our model are analyzed in order to investigate the evolution of the thermal performances of the foam with its structural parameters. Finally, we check the validity of these theoretical results by comparing the equivalent thermal conductivity of several EPS foams, measured by a guarded hot plate apparatus, with those predicted by our model.

2 Description of the Structure of EPS Foams

As was explained before, expanded polystyrene foams are generally classified among the cellular materials. However, contrary to other foams like polyurethane (PU) foams, their structure is more complex than a simple cellular matrix. This particular structure is directly due to their production process.

Indeed, EPS foams are made from weakly porous cellular polystyrene beads containing pentane as expanding agent. At the beginning of the process, the diameter of these spherical beads is lower than 1 mm and they are perfectly independent from each other. They are expanded first (preexpansion) by simply injecting steam in order to noticeably increase their porosity. Thereafter, they are placed in a closed container and undergo a second expansion. During this second expansion, they are compressed together and thus deformed, and mechanical bonds are created between neighboring beads. At the end of the second expansion, the material is presented in the form of a unique rigid porous piece from

Contributed by the Heat Transfer Division of ASME for publication in the JOURNAL OF HEAT TRANSFER. Manuscript received March 21, 2005; final manuscript received November 4, 2005. Review conducted by Jose L. Lage.

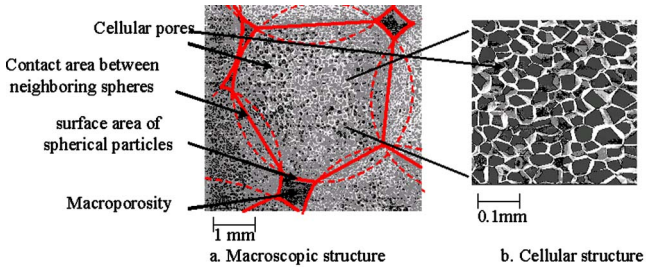

Fig. 1 SEM photographs representing macro and microporosity of EPS foams

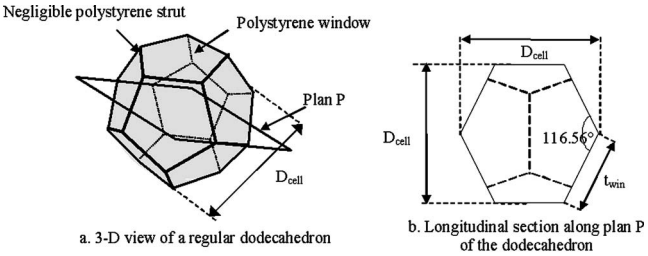

Fig. 2 Illustration of the morphology of dodecahedric cells

which slabs can be cut up and used for the thermal insulation of walls. The diameter of the beads at the end of the second expansion is between 3 and 6 mm.

As a result of this production process, EPS foams are characterized by a double-scale porosity. Indeed, as shown on the photograph of Fig. 1, the porous structure of EPS foams is not homogeneous and is, in fact, composed of two different types of pores:

- cellular pores with regular shape, contained in the beads,
- pores with irregular shape, formed during the second expansion of the cellular beads corresponding to the interparticle space.

The order of magnitude of the size of the pore contained in the beads is approximately 100 μm, whereas it is approximately 1 to several mm for the pores formed during the second expansion. Then, subsequently, we will use the terms "microporosity" and "macroporosity," respectively, to make a distinction between the two types of pores.

The macroporosity $\varepsilon_{\text{interbead}}$ due to the interparticle space formed during the second expansion varies between 4% and 10% for the standard EPS foams. Generally, the lower the density of the foam is, the lower the macroporosity is. The diameter D_{bead} of the compressed beads is relatively homogeneous in the foam and we will assume afterwards that all the beads in a given foam have the same diameter.

The characteristic macroscopic structure of the EPS foams could be accurately reproduced by considering that the foam is an arrangement of overlapping spherical particles representing the compressed beads. The distance d between the center of two neighboring particles is shorter than their diameter. This distance depends on the expansion rate of the beads during the second expansion and is related to the macroporosity $\varepsilon_{\text{interbead}}$. The contact area between two neighboring particles is assumed perfectly plane and is located on the intersection plane of the two spheres as shown in Fig. 1.

We can check in this figure that the morphology of the arrangement of spherical particles obtained perfectly matches the macroscopic structure of real EPS foam. In particular, the shape of the macropores is well reproduced.

As regards the cellular medium contained in the compressed beads, its porosity $\varepsilon_{\text{cell}}$ is very high and varies approximately between 97% and 99%. The shape and the size of the cells are relatively homogeneous as can be seen in Fig. 1(b). Therefore, we will assume subsequently that all the cells belonging to the same foam have the same dimensions.

Most of the previous researchers who dealt with the internal morphology of EPS foams like Quenard et al. [14] and Kuhn et al. [13] assumed that the cellular medium has a dodecahedral shape (see Fig. 2). Thus, each cell is composed of 12 pentagonal windows of polystyrene joined by their edge. The cellular material is then perfectly closed. Owing to the high porosity of the cellular medium, the thickness of the faces is negligible when compared to their size. We will make the same assumption as Kuhn et al. [13] and consider that this thickness is constant all over the surface area of the windows. Finally, in lots of cellular materials, one can notice the presence of heaps of matter at the junction of two cellular faces like in PU foams. These so-called "cells struts" are thicker than the faces. Kuhn et al. [13] and Quenard et al. [14] took them into account for evaluating the conductive and radiative properties of their EPS foams. However, in the case of low-density EPS foams, as a result of the very high porosity of the cellular medium, they are very small and we can neglect them. Thus, the entire polymer is supposed to be contained in the pentagonal windows.

To quantify the dimensions of the cells, we use the parameter D_{cell}, called the mean cell diameter, corresponding to the distance between two opposite windows of the same cell (see Fig. 2). The volume V_{dode} of the cell is related to this diameter by the following relation

$$V_{\text{dode}} \approx 0.427 \times D_{\text{cell}}^3 \tag{1}$$

The height t_{win} of the pentagonal windows forming the cells (see Fig. 2) is also related to D_{cell}

$$t_{\text{win}} = \frac{D_{\text{cell}}}{2 \times \sin\left(\frac{116.56°}{2}\right)} \approx \frac{D_{\text{cell}}}{1.7013} \tag{2}$$

Assuming that the entire polymer is contained in the cell windows, it is then possible to express the thickness h of these windows according to the mean cell diameter and the porosity $\varepsilon_{\text{cell}}$ of the cellular medium. Indeed, the surface area S_{win} of one window is: $S_{\text{win}} \approx 0.72654 \times t_{\text{win}}^2$.

Moreover, given that each cell is composed of 12 identical faces, each of these windows being shared with one neighboring face, there are finally six windows for one cell. And then

$$(1 - \varepsilon_{\text{cell}}) = \frac{6 \times S_{\text{win}} \times h}{V_{\text{dode}}} \Leftrightarrow h \approx 0.2836 \times (1 - \varepsilon_{\text{cell}}) \times D_{\text{cell}} \tag{3}$$

In real EPS foams, the cells forming the porous medium in the beads are not rigorously dodecahedrons but have rather irregular and random shapes composed of pentagonal, quadrilateral, or hexagonal faces. Their shape is then more complex than the dodecahedron model and could not be perfectly described from a unique cell shape. However, in order to investigate the influence of the morphology of cellular medium on the thermal properties of EPS foams, we will also consider, subsequently, the case of cellular medium made of cubic cells. The cells are then composed of six square faces. The mean cell diameter is noted D_{cube} and the relation expressing the cell volume and the height, the surface area and the thickness of the windows is replaced by

$$V_{\text{cube}} = D_{\text{cube}}^3;\ t_{\text{win}} = D_{\text{cube}};\ S_{\text{win}} \approx D_{\text{cube}}^2 \quad \text{and}$$
$$(1 - \varepsilon_{\text{cell}}) = \frac{3 \times V_{\text{fen}}}{V_{\text{cube}}} \Leftrightarrow h = \frac{(1 - \varepsilon_{\text{cell}}) \times D_{\text{cube}}}{3} \tag{4}$$

In conclusion, our representation of the porous structure of EPS foams is entirely described using four different structural characteristics:

- the mean bead diameter D_{bead} of the beads
- the macroporosity $\varepsilon_{\text{interbead}}$ or the distance d between the center of two touching beads
- the mean cell diameter D_{cell}
- the porosity of the cellular medium $\varepsilon_{\text{cell}}$

Generally, one prefers to use the density ρ_{EPS} of the foam instead of the porosity $\varepsilon_{\text{cell}}$ given that it could be measured directly contrary to $\varepsilon_{\text{cell}}$ which must be determined from the measured density ρ_{EPS} and interbead porosity $\varepsilon_{\text{interbead}}$. Indeed, we have

$$\rho_{\text{EPS}} = (1-\varepsilon_{\text{cell}}) \times (1-\varepsilon_{\text{interbeads}}) \times \rho_{\text{PS}}$$

$$\Leftrightarrow \varepsilon_{\text{cell}} = 1 - \frac{\rho_{\text{EPS}}}{\rho_{\text{PS}}} \times (1-\varepsilon_{\text{interbeads}})^{-1} \tag{5}$$

3 Modeling of the One-Dimensional Coupled Heat Transfer

In the building insulation industry, people are usually interested in the total heat flux passing through a slab submitted to a one-dimensional steady-state heat transfer in Cartesian coordinates Indeed, this configuration corresponds to the thermal conditions encountered by the insulator during its use. Thus, in the rest of the paper, we will only consider this kind of heat transfer.

3.1 Numerical Resolution of the Energy Equation. As was previously explained, in low-density porous materials, given that conductive and radiative heat transfer are both dependent on the temperature distribution in the medium, there is a coupling between these two modes of heat transfer. This coupling is governed by the energy equation explaining the thermal equilibrium in the material. For a one-dimensional steady-state heat transfer, this equation is

$$\frac{\delta q_c}{\delta z} + \frac{\delta q_r}{\delta z} = 0 \tag{6}$$

In the model retained, we assume that the conductive heat transfer follows a diffusion law. Thus, the conductive flux is related to the temperature by an analytical relation

$$q_c = -K_c(T) \,.\, \frac{\delta T}{\delta z} \quad \text{and}$$

$$\frac{\delta q_c}{\delta z} = -K_c(T) \,.\, \frac{\delta^2 T}{\delta z^2} - \frac{\delta K_c}{\delta z} \,.\, \frac{\delta T}{\delta z} \approx -K_c(T) \,.\, \frac{\delta^2 T}{\delta z^2} \tag{7}$$

The energy equation can be reformulated

$$K_c(T) \,.\, \frac{\delta^2 T}{\delta z^2} = \frac{\delta q_r}{\delta z} \tag{8}$$

This equation can be solved numerically by an iterative process using the control volume method. The principle of this method is to divide the slab thickness in elementary control volumes. The temperature of the medium at the center of each volume has to be calculated in order to know the temperature distribution in the medium. The iterative process goes on as follows. First, an initial temperature distribution in the medium is chosen, for example, linearly dependent on the z coordinates. Using this initial temperature distribution, the radiative problem is solved and the radiative heat flux divergence $\delta q_r/\delta z$ is calculated in each control volume. A new temperature distribution is then calculated from this heat flux divergence distribution in order to satisfy the energy Eq. (8). From this new temperature distribution, the radiative problem is solved again, a new radiative heat flux divergence distribution is calculated…and so on. The previous process is repeated until the relative difference between the temperature distribution obtained for two successive iterations is lower than a very small value criteria equal to 10^{-8}, synonymous with convergence. The total heat flux passing through the slab could then be computed in each control volume by adding the conductive and radiative heat flux.

As we can see, to solve the conduction-radiation coupling, one has to be able to solve the radiative heat transfer problem, that is, to compute the radiative transfer divergence distribution from a known temperature distribution.

3.2 Numerical Resolution of the Radiative Transfer Equation. Radiative heat transfer in low-density porous medium is a relatively complex problem given that it takes into account not only the emission, absorption but also the scattering of radiation by the porous material. Then, contrary to the conductive heat transfer, the radiative heat flux could not be related to the temperature distribution by a simple analytical expression. It is thus necessary to solve the radiative transfer equation (RTE) governing the spatial and angular distribution of monochromatic radiation intensity $I_\lambda(z,\mu)$ in the medium. For a one-dimensional heat transfer with azimuthal symmetry, this equation is expressed by

$$\mu \frac{\delta I_\lambda(z,\mu)}{\delta z} = -\beta_\lambda I_\lambda(z,\mu) + \kappa_\lambda I_\lambda^0(T) + \frac{\sigma_\lambda}{2} \int_{-1}^{1} \phi_\lambda(\mu' \to \mu) I_\lambda(z,\mu') d\mu' \tag{9}$$

and the boundary conditions

$$I_\lambda(0,\lambda>0) = E_{\text{hot},\lambda} I_\lambda^0(T_c) + 2 \,.\, (1-E_{\text{hot},\lambda}) \,.\, \int_0^1 I(0,-\mu')\mu' d\mu'$$

$$I_\lambda(0,\lambda<0) = E_{\text{cold},\lambda} I_\lambda^0(T_f) + 2 \,.\, (1-E_{\text{cold},\lambda}) \,.\, \int_0^1 I(l,\mu')\mu' d\mu' \tag{10}$$

σ_λ, κ_λ and $\beta_\lambda = \sigma_\lambda + \kappa_\lambda$ characterize the ability of the medium to scatter, absorb, and attenuate the radiation with wavelength λ $\Phi_\lambda(\mu_{\text{inc}} \to \mu_{\text{sca}})$ characterizes the probability, for a radiation incident in direction $\mu_{\text{inc}} = \cos\theta_{\text{inc}}$, to be scattered in an elementary solid angle around the direction $\mu_{\text{sca}} = \cos\theta_{\text{sca}}$

Several numerical methods can be used to solve the RTE. For example, we can cite the spherical harmonics method, the zone method of HOTTEL or the ray-tracing methods. However, the discrete ordinates method (DOM) is the most frequently used and gives accurate results. In our study, we use it. The DOM is based on a spatial discretization of the slab thickness and an angular discretization of the space. The angular discretization allows replacing the angular integrals by finite summations over n_d discrete directions with given weighting factors w_j. The spatial discretization must be the same as the one used for the numerical resolution of the energy equation. The DOM has already been explained in numerous previous publications as Ref. [15] (Siegel and Howell), for example, and we will not describe it here more precisely. The accuracy of the results is entirely dependent on the angular discretization. We then choose a very fine discretization dividing the 180° (2π radians) in 180 directions of 1° and whose weighting factors are proportional to the solid angle they encompass.

Theoretically, the RTE has to be solved for the entire wavelengths and the radiative heat flux divergence distribution is computed by integrating the contributions of each wavelength

$$\frac{\delta q_r}{\delta z}(z) = \int_0^\infty \kappa_\lambda \left[4\pi \,.\, I_\lambda^0(z) - 2\pi \sum_{j=1}^{n_d} I_{\lambda,j}(z) \,.\, w_j \right] . \, d\lambda \tag{11}$$

where the subscript j refers to the j^{th} discrete direction.

In practice, to save computational time and memory usage, the spectral integration is made by considering that the intensity field in the slab is constant in N wavelength bands covering the entire wavelengths. Then we have

$$\frac{\delta q_r}{\delta z} = \sum_{k=1}^{N} \kappa_k \,.\, \left[4\pi \,.\, I_k^0 - 2\pi \sum_{i=1}^{n_d} w_i \,.\, I_k \right]$$

$$\text{where: } I_k = \int_{\Delta\lambda_k} I_\lambda \,.\, d\lambda \tag{12}$$

where the subscript k refers to the k^{th} band and $\Delta\lambda_k$ is the width of the k^{th} band.

3.3 Modeling of the Radiative and Conductive Properties of EPS Foams. In order to solve the energy equation as well as the RTE, and then evaluate the total heat transfer, the effective thermal conductivity K_{EPS} and the monochromatic radiative properties σ_λ, κ_λ, β_λ and $\Phi_\lambda(\mu_{\text{inc}} \rightarrow \mu_{\text{sca}})$ of EPS foams have to be determined. In the following paragraphs we present the model developed in order to evaluate these properties.

3.3.1 Determination of the Effective Thermal Conductivity. The effective thermal conductivity K_{EPS} of porous materials strongly depends on the thermal conductivity of each of its constituents as well as on the morphology of the porous structure. In the case of EPS foams, the constituents are air (thermal conductivity K_{air}) and polystyrene polymer (thermal conductivity K_{PS}). The internal structure is characterized by two different types of pores which differ in size and shape (see Fig. 1). To take into account this specific structure, we choose the approach proposed by Quenard et al. [14] which divided EPS foams in three different phases with varying thermal conductivities. One phase corresponds to the macroporosity of air and the two other phases to the cellular materials contained in the beads. Indeed, the authors noticed a difference between the porosity and cell size of the cellular medium located at the center of the beads and those located at the periphery. Thus, they make a distinction between these two regions of the beads. However, in the case of EPS foams with low density, we have analyzed several scanning electron microscopy (SEM) photographs of the cellular medium and we did not note a perceptible difference. Then, we will assume that the cellular material is homogeneous in the beads and then that EPS foams can be divided in only two phases: a gaseous phase and a cellular phase. The effective thermal conductivity resulting from the interaction of the two phases can be estimated by the model of De Vries [16] which assumes that one phase constitutes a continuous medium (cellular phase), whereas the other phase is dispersed in spherical inclusions which do not interact with each other. We then have

$$K_{\text{EPS}} = \frac{(1-\varepsilon_{\text{interbeads}}) \,.\, K_{\text{cell}} + G^{\text{air}} \,.\, \varepsilon_{\text{interbeads}} \,.\, K_{\text{air}}}{(1-\varepsilon_{\text{interbeads}}) + G^{\text{air}} \,.\, \varepsilon_{\text{interbeads}}}$$

$$\text{where } G^{\text{air}} = \frac{1}{[1 + 1/3 \times (K_{\text{air}}/K_{\text{cell}} - 1)]} \tag{13}$$

The thermal conductivity of the cellular medium K_{cell} depends on the conductivity of air and polystyrene and the cellular porosity $\varepsilon_{\text{cell}}$, and is calculated by the correlation of Glicksman which is commonly used

$$K_{\text{cell}} = \varepsilon_{\text{cell}} \,.\, K_{\text{air}} + K_{\text{PS}} \,.\, (1-\varepsilon_{\text{cell}}) \,.\, \frac{(2-f_s)}{3} \tag{14}$$

where f_s, the proportion of polymer in the cell struts, is equal to 0 for EPS foams.

The values of the thermal conductivity of air and polystyrene used are

$$\left.\begin{aligned} K_{\text{PS}} = 0.16 \text{ W/m/K and } \quad & K_{\text{air}} = 0.02624 + 7.94.10^{-5} \times (T-300) \text{ W/m/K when } T > 300 \text{ K} \\ & K_{\text{air}} = 0.02624 + 7.58.10^{-5} \times (T-300) \text{ W/m/K when } T < 300 \text{ K} \end{aligned}\right\} \tag{15}$$

3.3.2 Modeling of the Monochromatic Radiative Properties of EPS Foams. Like the effective thermal conductivity, the radiative properties of EPS foams are closely related to the properties of its constituents but also to their porous structure. It is then necessary to take into account as accurately as possible the real morphology of EPS foams and especially the presence of macroscopic pores which could represent 10% of the total volume. We, thus, propose an innovative model to determine the extinction, absorption and scattering coefficients and the scattering phase functions. It is divided in two stages:

- First, we focus on the equivalent radiative properties of the cellular material contained in the beads alone.
- Then, the properties of the entire foam are calculated by assimilating the foam to an arrangement of overlapping spherical particles containing an homogeneous absorbing and scattering medium with known radiative properties.

3.3.2.1 Equivalent radiative properties of the cellular medium. The principle of most of the methods designed to compute the equivalent radiative properties of porous media is to divide the porous structure into particles whose shape and size permit the reproduction of the internal structure of the porous material. For example, the radiative properties of fibrous materials are generally computed assuming that the medium is constituted of randomly or non-randomly oriented infinite circular cylinders representing the fibers. Indeed, under the assumption of independent scattering, the equivalent radiative properties of the porous medium could be calculated by adding the radiative characteristics of each particle present in an elementary volume. These radiative characteristics are: the absorption cross section $C_{a,\lambda}(\text{m}^2)$, the scattering cross section $C_{s,\lambda}(\text{m}^2)$, the extinction cross section $C_{e,\lambda} = C_{a,\lambda} + C_{s,\lambda}(\text{m}^2)$ and the scattering phase function $\Phi_\lambda(\theta)$.

In our study, the radiative properties of the cellular medium contained in the beads are computed assuming that it is made of a cloud of randomly oriented cell windows which scatter radiation independently. The hypothesis of randomly oriented particles could appear a bit surprising given that the orientation and location of the windows belonging to a same dodecahedric or cubic cell are not independent of each other. However, we have already pointed out the fact that the shape and location of the cells in real EPS foams are quite irregular and random. This is the reason why it seems to us more judicious to make this assumption. Given the very high porosity of the cellular material, we will consider the independent scattering hypothesis as valid. In their study on EPS foams, Kuhn et al. [13] used a similar approach.

We apply the approach previously described to cellular materials with pentagonal and square cell windows. In order to compute the radiative characteristics of a particle, it is theoretically necessary to consider a plane, monochromatic wave incident upon this particle and apply Maxwell's equation. This has been done ana-

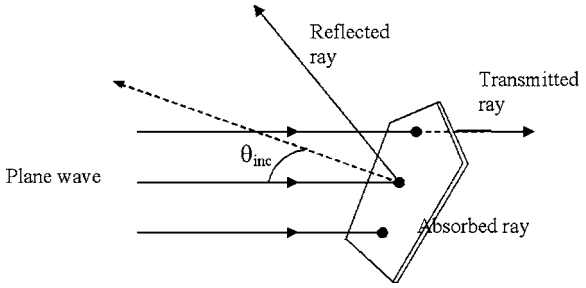

Fig. 3 Illustration of the interaction of a plane wave with a pentagonal window

lytically for spheres, cylinders, and spheroids by Mie. However, this is very complicated for particles with complex shapes and needs numerical method. Fortunately, when certain criterions are satisfied, some limiting analytical solutions give accurate results. Noticeably, when the particle size parameter $x=\pi.D/\lambda$ is very large, one can apply the geometric optics laws and the diffraction theory. As was previously noticed, the mean diameter of the cells contained in EPS beads is generally comprised between 100 and 300 μm, and then the height t_{win} is close to or greater than 100 μm. Whereas the infrared wavelengths radiations at the origin of the radiative heat transfer at ambient temperature are close to 10 μm. Thus, the geometric optics and diffraction approximation could be used to treat the radiation/matter interaction for the particles considered. Furthermore, the influence of diffraction on the radiative heat transfer is usually neglected. Indeed, the diffraction phase function for particles with a very large size parameter is predominantly oriented in the forward direction and diffracted rays are very close to transmitted rays. We then assume, here, that, for radiative heat transfer calculations, diffraction can be treated as transmission and that the radiation/matter interaction can be treated using the Fresnel relations.

We have checked the validity of the previous assumption for square or pentagonal windows oriented normally to the plane wave by comparing the radiative characteristics stemming from the geometric optics approximation with the results of a numerical method developed by Draine and Flatau [17]. This software facilitates the numerical solving of the Maxwell's equation for particles with various shapes using the disrete dipole approximation (DDA) method and has been the subject of numerous validations which guarantee its accuracy. With regards to the cross sections, the comparison shows that the geometric optics approximation leads to errors lower than 5% for windows with t_{win} as small as 30 μm. The scattering phase function given by the DDA for pentagonal or square windows oriented normally to the plane wave also proves to be very close to the phase function of the geometric optics. In the rest of the study we will assume that these conclusions are valid whatever the orientation of the windows.

When the geometric optics approximation is valid and the diffraction neglected, the absorption and scattering cross sections are computed by multiplying the cross section of the particle by its absorptivity and reflectivity calculated by the Fresnel relations. Given that the particles forming the cellular material are supposed to be randomly oriented, their radiative characteristics have to be calculated by integrating over all the possible incident directions of the plane wave. To compute these properties we developed a method based on a ray-tracing procedure, illustrated in Fig. 3. Pentagonal or square windows are illuminated by rays representing the plane wave. For each ray, the angle θ_{inc} between the plane wave and the normal to the surface of the window is randomly chosen using random numbers *Ran* in order to respect the incidence probability which is proportional to the incident solid angle $d\Omega_{inc}=2\pi\sin(\theta_{inc})d\theta_{inc}$. We then have

$$\frac{\int_0^{\theta_{inc}}\sin(\theta)d\theta}{\int_0^{\pi/2}\sin(\theta)d\theta}=Ran\Leftrightarrow\cos\theta_{inc}=Ran\Leftrightarrow\theta_{inc}=\cos^{-1}(Ran) \tag{16}$$

For each incident ray, the reflectance R_{win}, the absorbance A_{win}, and the transmittance Tr_{win} are determined. A new random number *Ran* is chosen and

- If $Ran>1-A_{win}$, the variable, the ray is absorbed and the variable *Abs* is incremented of S_{win}, the normal cross section of the window
- If $1-A_{win}>Ran>R_{win}$, the ray is transmitted through the window
- If $Ran<R_{win}$, the ray is reflected and the variables *Sca* and $E(\theta)$ are incremented of S_{win} and 1, respectively. θ refers to the angle between the incident and reflected directions. In practice, the repartition is discretized for $\theta_0=0°$, $\theta_1=1°$, $\ldots.\theta_{180}=180°$. Then, all the rays reflected with an angle θ comprised between $\theta_i-0.5°$ and $\theta_i+0.5°$ are regrouped in $\mathbf{E}(\theta_i)$. Owing to the very high porosity of the cellular medium, the thickness h of the windows is very small and is comparable to the radiation wavelengths. Therefore, in order to compute A_{win}, R_{win} and Tr_{win}, we must use the thin film optic laws stemming from the Fresnel relations and which take into account the interference effects. These relations are well described in Ref. [18] (Brewster). For dielectrics like polystyrene, we have

$$R_{win}=R_{12}+T_{12}R_{21}T_{21}e^{-i\times2\tilde{\beta}}+T_{12}R_{21}^3T_{21}e^{-i\times4\tilde{\beta}}+\cdots=\frac{R_{12}+R_{21}e^{-i\times2\tilde{\beta}}}{1+R_{12}R_{21}e^{-i\times2\tilde{\beta}}} \tag{17}$$

$$Tr_{win}=T_{12}T_{21}e^{-i\times\tilde{\beta}}+T_{12}R_{21}^2T_{21}e^{-i\times3\tilde{\beta}}+\cdots=\frac{T_{12}T_{21}e^{-i\times\tilde{\beta}}}{1+R_{12}R_{21}e^{-i\times2\tilde{\beta}}}; \tag{18}$$

$$A_{win}=1-R_{win}-T_{win} \tag{19}$$

with

$$\tilde{\beta}=\frac{2\pi\times\tilde{n}\times h\times\cos(\theta_{ref})}{\lambda};\quad\sin(\theta_{ref})=\frac{\sin(\theta_{inc})}{n};$$

$$R_{12}=\frac{(|r_{12\parallel}|^2+|r_{12\perp}|^2)}{2}=R_{21};$$

$$T_{12}=1-R_{12}=T_{21};\quad r_{12\parallel}=\frac{n\cos(\theta_{inc})-\cos(\theta_{ref})}{n\cos(\theta_{inc})+\cos(\theta_{ref})}$$

$$r_{12\perp}=\frac{\cos(\theta_{inc})-n\cos(\theta_{ref})}{\cos(\theta_{inc})+n\cos(\theta_{ref})} \tag{20}$$

Moreover, the windows reflect rays specularly and then $\theta=\pi-2\times\theta_{inc}$.

For a great number of rays, N_{rays}, the cross sections and phase function integrated over all the incident directions are given by

$$\langle C_a\rangle=\frac{Abs}{N_{rays}};\quad\langle C_s\rangle=\frac{Sca}{N_{rays}};\quad\langle C_e\rangle=\frac{Abs+Sca}{N_{rays}}\quad\text{and}$$

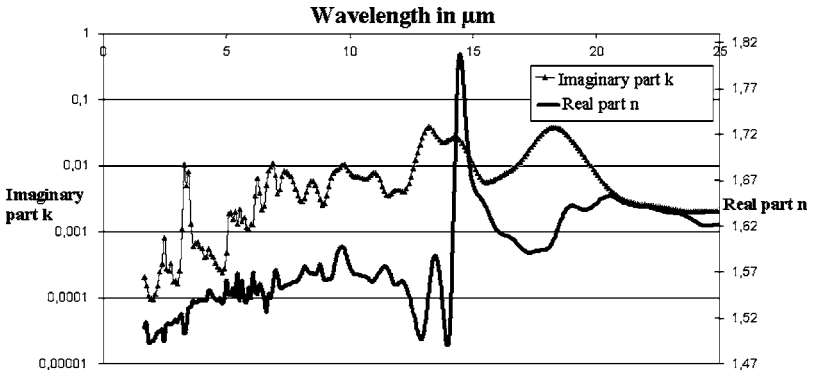

Fig. 4 Variation of the refractive index of polystyrene with the I/R radiation wavelength

$$\langle \phi_{\text{part}}(\theta_i) \rangle = \frac{4\pi \,.\, E(\theta_i)}{N_{\text{rays}} \,.\, d\omega(\theta_i)} = \frac{4 \times E(\theta_i)}{N_{\text{rays}} \,.\, \sin(\theta_i) \times \dfrac{\pi}{90}} \tag{21}$$

The phase function is then normalized in order to have

$$\frac{1}{4\pi} \sum_{i=0}^{180} \langle \phi_{\text{part}}(\theta_i) \rangle \times 2\pi \sin(\theta_i) d\theta_i = 1 \tag{22}$$

In practice, the number of rays used must be sufficiently important so that the results are practically independent of its value. For all the computations made, we have $N_{\text{rays}} = 10^6$.

Given that the cellular medium is only constituted by windows, its radiative properties could be determined from the radiative characteristics of the particles by

$$\kappa_{\text{cell}} = N_{\text{part}} \times \langle C_{a,\lambda} \rangle; \quad \sigma_{\text{cell}} = N_{\text{part}} \times \langle C_{s,\lambda} \rangle;$$

$$\beta_{\text{cell}} = \kappa_{\text{cell}} + \sigma_{\text{cell}} \quad \text{and} \quad \phi_{\text{cell}}(\theta) = \langle \phi(\theta) \rangle \tag{23}$$

where N_{part} is the number of particles per unit volume of cellular medium.

For dodecahedric cells, there are six windows per cell and then

$$N_{\text{part}} = \frac{6}{V_{\text{cell}}} \approx \frac{14.06}{D_{\text{cell}}^3} \tag{24}$$

For cubic cells, there are three windows per cell and

$$N_{\text{part}} = \frac{3}{V_{\text{cell}}} = \frac{3}{D_{\text{cell}}^3} \tag{25}$$

To carry the computation of R_{win}, A_{win} and Tr_{win}, the complex refractive index $\tilde{n} = n - ik$ of the polystyrene used in EPS foams has to be known. We have determined this index for infrared (I/R) wavelength using an identification method based on transmittance and reflectance measurements on thin(50 μm in thickness) and thick(600 μm in thic kness) polystyrene films made from melted EPS foams. This method computes the value of n and k minimizing the difference between experimental and theoretical transmittances and reflectances. The variation of the refractive index with the wavelength is shown in Fig. 4.

Owing to the working range of the spectrometer used for the transmittance and reflectance measurements, we could only compute the refractive index for wavelength comprised between 2 and 25 μm. For higher wavelengths, we assume that the real and imaginary part of the refractive index are constant and equal to the average values

$$\overline{n}_{\lambda>25\ \mu\text{m}} = \frac{\displaystyle\int_{2\ \mu\text{m}}^{25\ \mu\text{m}} n_\lambda \,.\, L_\lambda^0(300\ \text{K})}{\displaystyle\int_{2\ \mu\text{m}}^{25\ \mu\text{m}} L_\lambda^0(300\ \text{K})} \quad \text{and}$$

$$\overline{k}_{\lambda>25\ \mu\text{m}} = \frac{\displaystyle\int_{2\ \mu\text{m}}^{25\ \mu\text{m}} k_\lambda \,.\, L_\lambda^0(300\ \text{K})}{\displaystyle\int_{2\ \mu\text{m}}^{25\ \mu\text{m}} L_\lambda^0(300\ \text{K})} \tag{26}$$

This approximation does not have a strong influence on the accuracy of the results given that, at ambient temperature (300 K), approximately 84% of the radiant energy emitted by a blackbody concerns wavelength comprised between 2 and 25 μm.

We have computed the variation of $\kappa_{\text{cell},\lambda}$, $\sigma_{\text{cell},\lambda}$, $\beta_{\text{cell},\lambda}$ and $\Phi_{\text{cell},\lambda}(\theta)$ with the radiation wavelength for cellular materials with different morphologies using the identified refractive index. Some results are illustrated in Fig. 5 where the variation of the extinction coefficient $\beta_{\text{cell},\lambda}$ and scattering albedo $\omega_{\text{cell},\lambda} = \sigma_{\text{cell},\lambda}/\beta_{\text{cell},\lambda}$ are depicted for dodecahedric cellular media with $D_{\text{cell}} = 200$ μm and with various cellular porosities. This figure shows that the radiation/matter interaction is dominated by scattering given that $\omega_{\text{cell},\lambda}$ is generally close to one except for some wavelength belonging to a polystyrene absorption peak. We can also check that the radiative properties are a function of the polystyrene optical properties and the morphology of the medium as well.

3.3.2.2 Radiative properties of the entire foam. Once the radiative properties of the cellular medium have been determined, the foam is assimilated to a random arrangement of spherical overlapping particles containing an homogeneous absorbing and scattering medium whose equivalent radiative properties are those of the cellular material. We have already shown that this representation is very close to the real macroscopic structure of EPS foams. The porosity and the particle diameter of the arrangement must, respectively, be equal to the interbead porosity $\varepsilon_{\text{interbead}}$ and the mean bead diameter D_{bead} of the EPS foam studied. The arrangement of spheres representing the foam is generated using the same procedure as the one presented in Ref. [10] (Coquard and Baillis) and the properties of the entire foam are computed using a method similar to that presented by Coquard and Baillis for packed beds of opaque [10] or semi-transparent spheres [19]. The principle of the method is illustrated on Fig. 6.

First, a ray-tracing procedure is applied in a spherical domain of the arrangement much larger than D_{bead}. The paths of rays, starting in random points of the bed and with random starting

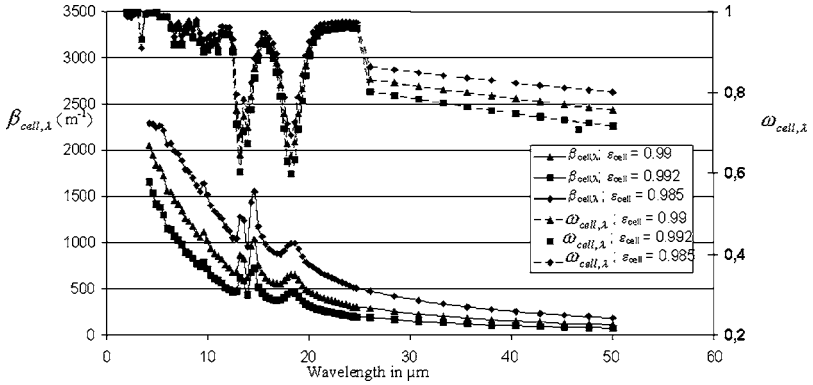

Fig. 5 Evolution of the extinction coefficient and scattering albedo with the radiation wavelength for different cellular medium with D_{cell}=200 μm

directions, are tracked until they leave the spherical domain centered on the starting point (Fig. 2). Each ray can be scattered one or several times or absorbed by the cellular medium contained in the EPS beads before leaving the spherical domain with an angle θ'. It could also pass through the sphere without being intercepted. The distance **dist** covered by the ray in the cellular medium contained in the beads before being intercepted is strongly dependent on the extinction coefficient β_{cell} and is calculated using random numbers $Ran(0<D<1)$

$$dist = -Ln(Ran)/\beta_{cell} \tag{27}$$

The probability for the intercepted rays to be scattered by the cellular medium in the beads is equal to ω_{cell}, whereas the probability for it to be absorbed is equal to $(1-\omega_{cell})$. If the ray is scattered, the scattering angle θ is determined from the scattering phase function $\Phi_{cell}(\theta)$ using random numbers by computing the value of θ which satisfies the relation:

$$\frac{\int_0^{\theta} \Phi_{cell}(\alpha)\sin(\alpha)d\alpha}{\int_0^{\pi} \Phi_{cell}(\alpha)\sin(\alpha)d\alpha} = Ran \tag{28}$$

The ray-tracing procedure permits to compute three variables entirely describing the radiative behavior of the packed bed of EPS beads. The three variables correspond to the proportion of starting energy traveling through the spherical domain without being either absorbed or scattered, the proportion leaving after one or several scatterings inside the particles and the angular repartition of this latter energy. The traveling of the rays through the absorbing and scattering medium representing the cellular material is dictated by the radiative properties κ_{cell}, σ_{cell}, β_{cell} and $\Phi_{cell}(\theta)$. Second, an identification procedure determines the equivalent radiative properties κ_λ, σ_λ, β_λ and $\Phi_\lambda(\theta)$ of the homogeneous semi-transparent medium that best match the radiative behavior of the arrangement of spheres previously characterized. For more details about the method, one can consult the paper [19] (Coquard and Baillis).

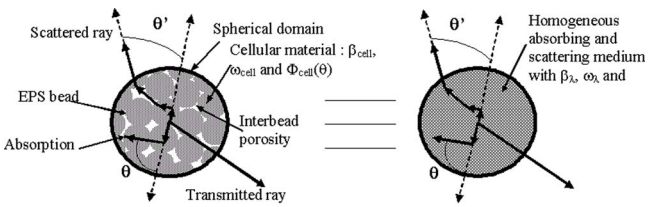

Fig. 6 Principle of the method computing the radiative properties of the arrangement of EPS beads

4 Results

The model previously presented has been applied to several fictive EPS foams with different values of the structural characteristics ρ_{EPS}, D_{bead}, $\varepsilon_{interbead}$ and D_{cell} covering the whole ranges of variation observed for usual EPS foams. These results permit us to investigate the influence of each of these characteristics on the total one-dimensional heat flux transferred through a slab of EPS foam with the idea of optimizing their thermal performances during their production process.

Finally, in order to test the accuracy of our model and the validity of our conclusions, we have compared the predicted and measured equivalent thermal conductivity of several commercial EPS foams.

4.1 Evolution of the Theoretical Equivalent Thermal Conductivity. In order to quantify the performances of thermal insulators, people working in the building insulation industry use a characteristic called "equivalent thermal conductivity" (noted K_{equ}). This equivalent conductivity is simply equal to heat flux density passing through a slab of materials multiplied by its thickness and divided by the temperature difference between the hot and cold boundaries. These hot and cold boundaries generate the heat transfer. The temperatures of the boundaries used for the theoretical calculations are T_{cold}=303 K and T_{cold}=288 K; the slab thickness 1 is equal to 40 mm and the emissivities $E_{hot,\lambda}$ and $E_{cold,\lambda}$ of the boundaries are gray and equal to 0.9.

The spatial discretization used for the calculations divides the slab thickness in n_z=30 volumes using the Tchebycheff grid for which

$$\Delta z_j = \frac{1}{2} \times l \times \left[\cos\left(\frac{(j-1)\pi}{n_z}\right) - \cos\left(\frac{j\pi}{n_z}\right) \right] \quad \text{for } i = 1, \ldots, n_z \tag{29}$$

This grid provides narrower volumes near the boundary and is well suited to our problem.

The angular discretization chosen has 90 directions regularly covering the whole range of angular directions from θ=0 deg to θ=180 deg. The discretized directions are then: θ_i =0,2,4,6$\cdots$86 deg, 88,92,94,$\ldots$,180 deg for i=1,$\ldots$,90. Each discretized direction encompasses all the directions comprised between θ_i−1 deg and θ_i+1 deg except the directions i=1, i=45, i=46 and i=90, which, respectively, encompass the directions

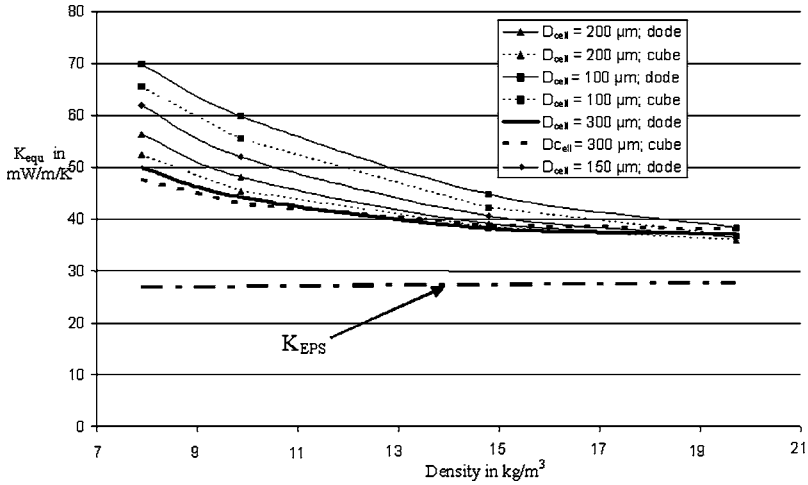

Fig. 7 Evolution of the equivalent conductivity with the density for different mean cell diameter

comprised between 0 and 1 deg, 87 and 90 deg, 90 and 93 deg and 179 and 180 deg. The directing cosines μ_i are determined by: $\mu_i = \cos(\theta_i)$. The weighting factors w_i are proportional to the solid angle of each direction

$$\begin{aligned} w_i &= |\cos(\theta_i - 1\ \text{deg}) - \cos(\theta_i + 1\ \text{deg})| && \text{for } i = 2, \ldots, 44 \text{ and } i = 46, \ldots, 89 \\ w_i &= |\cos(0\ \text{deg}) - \cos(1\ \text{deg})| && \text{for } i = 1 \\ w_i &= |\cos(87\ \text{deg}) - \cos(90\ \text{deg})| && \text{for } i = 45 \\ w_i &= |\cos(90\ \text{deg}) - \cos(93\ \text{deg})| && \text{for } i = 46 \\ w_i &= |\cos(179\ \text{deg}) - \cos(180\ \text{deg})| && \text{for } i = 90 \end{aligned} \tag{30}$$

In order to check that the spatial and angular discretizations used give accurate results for the resolution of the radiation/conduction coupling, we have compared the total heat flux calculated for several media with known conductive and radiative properties with the exact values given in the literature by Yuen and Wong [20]. We noticed that the relative difference is lower than 0.5% whatever the properties of the fictitious medium and the temperature and emissivities of the boundaries.

As regards the spectral discretization, given that the identification of the radiative properties of the entire foam using the ray-tracing procedure (Coquard et Baillis [19]) is time consuming, we opted for a six band discretization. For each band, the radiative properties of the entire foam have been identified using the mean radiative properties of the cellular material. We checked that the number of wavelength bands is sufficient to obtain accurate results. The radiative properties of the foam are assumed constant in each band. The discretization chosen is delimited as follows

1. $\lambda_1 = 2\ \mu\text{m} < \lambda < \lambda_2 = 8\ \mu\text{m}$
2. $\lambda_2 = 8\ \mu\text{m} < \lambda < \lambda_3 = 12\ \mu\text{m}$
3. $\lambda_3 = 12\ \mu\text{m} < \lambda < \lambda_4 = 15\ \mu\text{m}$
4. $\lambda_4 = 15\ \mu\text{m} < \lambda < \lambda_5 = 20\ \mu\text{m}$
5. $\lambda_5 = 20\ \mu\text{m} < \lambda < \lambda_6 = 25\ \mu\text{m}$
6. $\lambda_6 = 25\ \mu\text{m} < \lambda < \lambda_7 = 100\ \mu\text{m}$

The wavelengths lower than 2 μm and greater than 100 μm are neglected as they represent less than 0.1% of the radiant energy emitted by the blackbody at ambient temperature.

The equivalent conductivity calculations have been conducted for EPS foams with structural properties ρ_{EPS}, D_{cell}, $\varepsilon_{interbead}$ and D_{beads} varying, respectively, from 8 to 20 kg/m^3, 100 to 300 μm, 2–13% and 3 to 6 mm. Moreover, the results are given for dodecahedric and cubic cells.

4.1.1 Influence of the Foam Density. The evolution of the equivalent thermal conductivity with the foam density is depicted in Fig. 7 for foams with a mean bead diameter $D_{bead} = 4$ mm, an interbead porosity $\varepsilon_{interbead} = 6.1\%$ and different mean cell diameter D_{cell}. Thus, it is the cellular porosity alone that varies. The results obtained with the hypothesis of dodecahedric cells are referenced as "dode," whereas the one obtained for cubic cells is noted as "cube." We also represent on the same figure the evolution of the effective thermal conductivity K_{EPS} predicted by the model in order to illustrate the relative contributions of conduction and radiation to the total heat transfer. This effective thermal conductivity only depends on the density of the material.

The results show that the foam density has a strong influence on the equivalent conductivity of low-density EPS foams whatever the size and the shape of the cells. The lighter the foam is, the worse its thermal performances are. This conclusion is well known by people working in the building insulation industry who often have to find a compromise between light, and then cheap but weakly effective insulating materials and heavier (and more expensive) but more effective ones. One can also remark that at the same time, given the very high porosity of the material, the effective thermal conductivity K_{EPS} of the foam only increases imper-

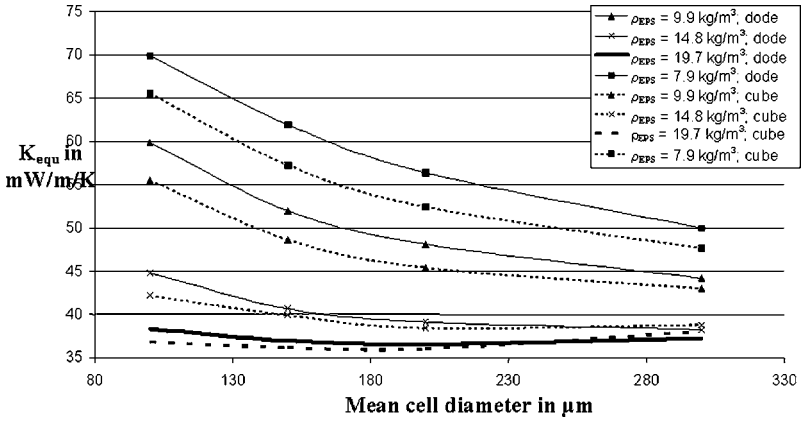

Fig. 8 Evolution of the equivalent conductivity with the mean cell diameter for different densities

ceptibly and stays close to the thermal conductivity of air. Then, it reveals that the increase of the equivalent conductivity of EPS foams with decreasing density is entirely due to an increase of the radiant energy propagating through the medium. This could be intuitively explained by the fact that when foam gets lighter, the particles preventing the radiation from propagating in the medium are less opaque and the radiation/matter interaction is less pronounced. Radiative heat transfer then becomes relatively important and could represent more than 50% of the total flux passing through the slab for foams lighter than 10 kg/m^3. Moreover, as the effective conductivity of EPS foams varies only very slightly with the density, we can conclude that all the variations of the equivalent conductivity K_{equ} with different parameters are only due to variations of the radiative contribution.

The decrease of K_{equ} with increasing density is not linear and is more rapid for very light foams. One could also notice that the influence of the shape of the cells is non-negligible given that the equivalent conductivities stemming from the cubic cells assumption are lower than those obtained considering dodecahedric cells. This is due to the difference between Eqs. (3) and (24), and Eqs. (4) and (25) which are valid for dodecahedric and cubic cells, respectively. However, the relative difference for the equivalent thermal conductivity is always lower than 7%.

4.1.2 Influence of the Mean Cell Diameter. The theoretical results obtained using the same parameters as those presented in the previous paragraph are now depicted in Fig. 8 in order to show the influence of the mean cell diameter on the thermal performances of the EPS foams.

As can be noticed, the diameter of the cells forming the cellular medium contained in the beads also has a substantial influence on the equivalent thermal conductivity of the EPS foam. However, the variations of K_{equ} with D_{cell} are not the same for foams with different densities. Then, for very low-density EPS foams ($\rho_{EPS} < 10$ kg/m^3), the results show that in the range of cell diameter studied ($100\ \mu m < D_{cell} < 300\ \mu m$), the equivalent conductivity decreases rapidly when the diameter D_{cell} increases. For example, for EPS foams of approximately 8 kg/m3, the theoretical equivalent conductivity varies from 65 to 48 mW/m/K when the cell diameter goes from 100 to 300 μm. We can also remark that the decrease of K_{equ} is slower when the cells are large.

On the other hand, when the density of the foam is greater than a fixed value, we can notice that there is an optimal cell diameter lower than 300 μm for which the equivalent conductivity of the foam slab is minimal. This optimal cell size depends on the foam density as well as on the morphology of the cell considered. Then, for foams of 14.8 and 19.7 kg/m^3 in density, the optimal cell diameter is approximately 300 and 200 μm for dodecahedric cells and 250 and 200 μm for cubic cells. Actually, there is an optimal cell size whatever the density of the foam but for very light foams, this diameter is very large and greater than the diameter commonly observed in commercial EPS foams.

4.1.3 Influence of the Mean Bead Diameter. The influence of the bead diameter on the thermal performances of EPS foams has been studied for foams with interbead porosity $\varepsilon_{interbead} = 6.1\%$ made of cells of 200 μm in diameter and with densities varying from 7.9 to 14.8 kg/m^3. We take into account both dodecahedric and cubic cells. Figure 9 illustrates the results.

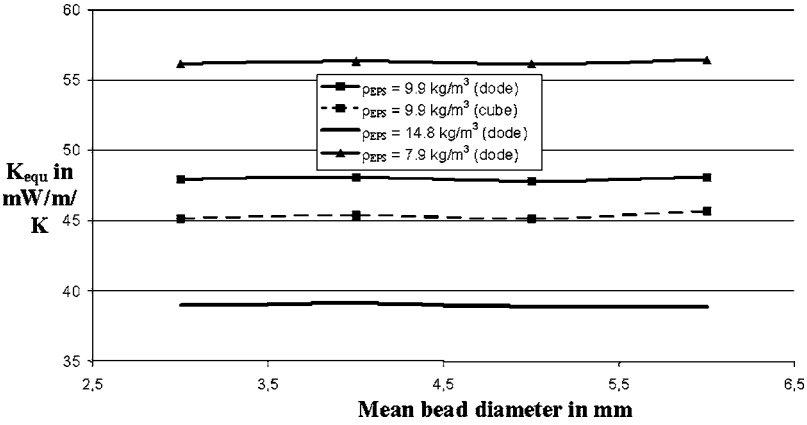

Fig. 9 Evolution of the equivalent conductivity with the mean bead diameter

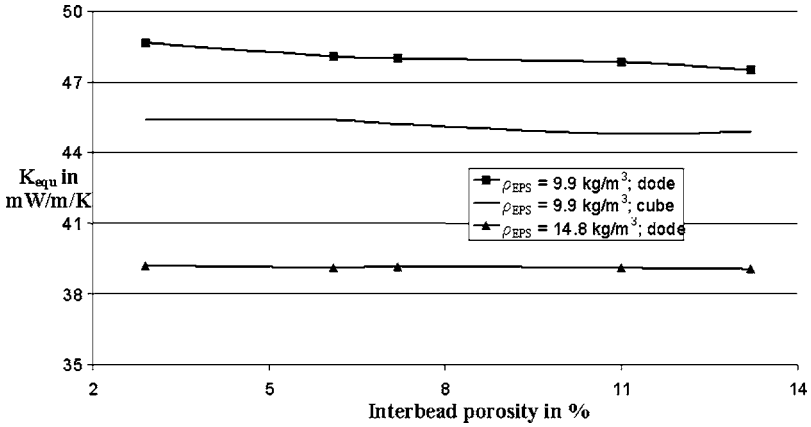

Fig. 10 Evolution of the equivalent conductivity with the interbead porosity

We notice that the influence of the bead diameter on the insulating performances of the foam is almost null as we do not observe any significant variation of the equivalent thermal conductivity when D_{bead} varies from 3 to 6 mm. This parameter actually has antagonistic influences on the extinction coefficient and scattering phase function which tend to cancel each other.

4.1.4 Influence of the Interbead Porosity. As regards the influence of the interbead porosity, the study has been conducted for foams made of beads of 4 mm in diameter and of cells of 200 μm, the density of the foam being constant. The calculations were made for different densities and considering dodecahedric and cubic cells. These variations are depicted in Fig. 10.

Figure 10 shows that the influence of the interbead porosity is relatively weak compared to that of density or cell diameter. However, we notice that the equivalent conductivity of EPS foams tends to decrease when $\varepsilon_{interbead}$ increases, all other parameters being unchanged. For example, for foams of 9.9 kg/m^3 in density, K_{equ} goes from 48.7 to 47.5 mW/m/K when the interbead porosity goes from 2.9% to 13.2%. This remark is valid for either dodecahedric or cubic cells and especially for foams of relatively high equivalent thermal conductivity. For foams with higher density ($\geqslant$15 kg/m^3), for which radiative heat transfer is weak, the influence of $\varepsilon_{interbead}$ is almost imperceptible.

4.1.5 Conclusions. The study on the variation of K_{equ} with the structural parameters has revealed that the most important characteristics are the foam density and the mean diameter of the cells contained in the beads. The results of the model show that the lighter the foam is, the larger the equivalent conductivity is. They also indicate that for low-density EPS foams, it could be interesting to obtain large cell size in order to optimize their insulating performances. Indeed, other computations have shown that the optimal mean cell diameter is beyond 300 μm. For heavier foams, the required cell diameter is lower and is in the region of 200 μm for foams of 20 kg/m^3 in density. Furthermore, the theoretical results also permit us to conclude that the size of the compressed beads has almost no influence on equivalent thermal conductivity. Finally, it also turns out that the theoretical insulating performances of EPS foams weakly improve when their interbead porosity increases. The following classification summarizes the importance of each parameter:

1. Foam density
2. Mean cell diameter
3. Interbead porosity
4. Mean bead diameter

4.2 Experimental Validation of the Theoretical Model. The model presented in this study has been made in order to take into account as faithfully as possible the characteristics of EPS foams. However, some assumptions have been made to simplify the problem especially during the modeling of the radiative properties (geometric optics hypothesis, assuming no struts, unique cell size…). Then, in order to check the accuracy of the theoretical results, we have compared the equivalent thermal conductivities predicted by the model with experimental measurements made on seven usual EPS foam slabs using the flux meter apparatus of the Centre Scientifique et Technique du Bâtiment (CSTB). The apparatus consists of:

- a cold plate and a hot plate sandwiching the slabs of EPS foams (thickness 1) which are maintained at two different temperatures by a thermostated bath of water;
- two flux meter measuring the heat flux $\dot{Q}_{hot}$ and $\dot{Q}_{cold}$ at the two plates; and
- two thermocouples measuring the temperature T_{cold} and T_{hot} of the two plates.

The position of the cold plate (placed at the bottom of the apparatus) and hot plate (placed at the top of the apparatus) is chosen to avoid measurement errors due to convection phenomenon when the hot plate is placed at the bottom of the apparatus. Moreover, the apparatus is insulated in order for the thermal losses to be negligible. The measurements are made by placing the slab between the two plates and waiting for the steady state which can be considered reached when the sum of the heat flux density at the two plates does not vary anymore. The measured equivalent conductivity is then obtained by the relation

$$K_{eq} = \frac{(\dot{Q}_{hot} + \dot{Q}_{cold})/2}{T_{hot} - T_{cold}} \cdot l \tag{31}$$

The apparatus has been calibrated and the relative uncertainty on the equivalent thermal conductivity measured has been evaluated by the CSTB to 5%. The emissivities of the two plates are: $E_{cold,\lambda} = E_{hot,\lambda} = 0.9$.

The structural parameters of the foam slabs have been determined using characterization techniques developed by the CSTB and are summarized in Table 1.

The theoretical calculations have been made using the discretizations previously specified. The comparison of the theoretical and experimental equivalent thermal conductivities is illustrated in Fig. 11 where we have depicted their variations according to the foam density.

First, we notice that there is a relatively good agreement between experimental and theoretical results. The worst theoretical results are found for slab No. 2 for which the relative difference between predicted and measured equivalent conductivities is 11%

Table 1 Structural characteristics of the foam slabs

Slab number	ρ_{EPS} in kg/m^3	D_{cell} in μm	D_{bead} in mm	$\varepsilon_{interbead}$	Thickness l in mm	T_{hot} (K)	T_{cold} (K)
1	8.7	200	5.6	6.1%	61.5	304.3	287.8
2	11.25	150	5.3	5.1%	50.8	304.1	287.7
3	12.8	160	5.1	7.1%	50.4	304	287.8
4	14.6	180	3.6	11.0%	49	304.6	287.8
5	12.5	110	4	13.2%	60.1	304.2	287.8
6	13.2	180	3.8	14.2%	49	303.9	287.8
7	17	80	3.2	8.1%	49.2	304	287.8

when dodecahedric cells are considered and 6% for cubic cells. For the other slabs the maximal relative difference is 9% and 4% for dodecahedron and cube. We can also remark that the theoretical models generally tend to overestimate the equivalent conductivity whatever the characteristics of the slab. Moreover, the predictions are more accurate when we consider cubic cells instead of dodecahedron. Besides, the cubic cells assumption always gives very accurate results.

It seems that the relative difference between predicted and measured values is related to the density of the foam and that the lighter the foam is, the less accurate the results are. However, as regards slab No. 7, although it is the densest slab, the theoretical results are worse than for the other slabs. This could be explained by the fact that, for this slab, the mean cell diameter is relatively weak (80 μm) and thus that the geometric optics approximation is less accurate. Moreover, we also noticed during the structural characteristics measurement that the size of the cells contained in the beads is relatively dispersed and that it was difficult, for this foam, to evaluate a mean cell diameter.

One can also remark that, the theoretical observations concerning the influence of the density are confirmed by experimental results as there is a regular decrease of the measured equivalent conductivity when the foam density increases, except for slab Nos. 5 and 7 which have a relatively weak mean cell diameter. For these two slabs, the equivalent conductivity is greater than the average experimental evolution deducted from the experimental results of the other foams which have mean cell diameters close to each other. This observation confirms the previous theoretical remarks concerning the influence of D_{cell} on K_{equ} which have shown that small cells tend to enhance radiative heat transfer. Experimental results for slabs Nos. 5 and 7 are then in perfect agreement with theoretical conclusions for dodecahedric cells and cubic cells as well.

5 Conclusions

Although they are commonly used in the building industry as a thermal insulator, expanded polystyrene foams have not been the subject of numerous thermal studies. Moreover, all the previous works which tried to model the heat transfer in this kind of material have assimilated their porous structure to a homogeneous cellular matrix, and then, have neglected the presence of macroscopic porosities generated during the second expansion and compression of the polystyrene beads. Furthermore, the earlier studies were not particularly interested in EPS foams with very low densities (<15 kg/m^3) and calculated the total heat transfer neglecting the coupling between conduction and radiation and using the Rosseland approximation to treat the radiative transfer.

In the present paper, we propose a new model designed to predict conductive and radiative coupled heat transfer in low-density EPS foams. The radiation/conduction coupling is solved using numerical resolution methods of the energy equation and radiative transfer equation. The models used for the prediction of conductive and radiative properties try to take into account as faithfully as possible the real morphology of EPS foams. To do that, we use a representation of the porous structure which reproduces the double-scale porosity of this medium. Moreover, the cells forming the cellular materials contained in the beads can be either dodecahedric or cubic which allow us to analyze the influence of the cell shapes on the thermal behavior of the foam. Cubic windows have been proved to be more appropriate for EPS foams.

The theoretical results permit us to investigate the influence of the parameter characterizing the micro and macrostructure on the equivalent thermal conductivity of EPS foams and show that the density and mean cell diameter are the most influential one. The influence of macroporosity has been proved to be negligible. The conclusions drawn could be very useful for industrials who want to optimize the insulating performances of EPS foams during their

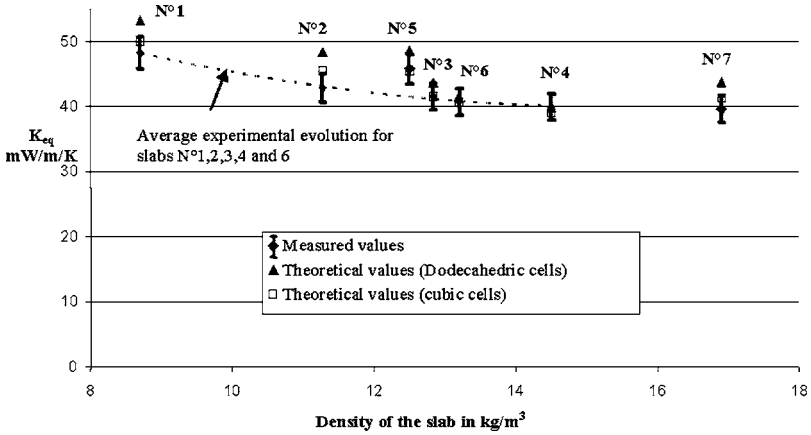

Fig. 11 Evolution of the theoretical and experimental equivalent conductivities with the foam density

production process. The validity of the theoretical model has been checked by comparing the predicted equivalent thermal conductivities of several foams to measured values. The accuracy of the theoretical results proved to be quite satisfactory.

Nomenclature

A = absorbance
C = cross section (m^2)
D = mean diameter (m)
$d\Omega_{inc}$ = solid angle around incident direction (str)
E = emissivity
V = volume in m^3
f_s = fraction of polymer in the cell struts
h = thickness of the cell windows (m)
$I(z,\mu)$ = radiation intensity at point of z abscissa in direction μ ($W/m^2/Str$)
$I^0(T)$ = radiation intensity of the blackbody at temperature T ($W/m^2/Str/\mu m$)
K = conductivity (W/m/K)
l = thickness of the foam slab
$\tilde{n}$ = $n-ik$: complex refractive index of polystyrene
N_{part} = number of particle per unit volume (m^{-3})
n_z = number of volume for the spatial discretization
n_d = number of directions for the angular discretization
q_r = radiative heat flux density (W/m^2)
q_c = conductive heat flux density (W/m^2)
$\dot{Q}_{hot}$ = total heat flux density at the hot plate (W/m^2)
$\dot{Q}_{cold}$ = total heat flux density at the cold plate (W/m^2)
R = reflectance
Ran = random number
S = surface area (m^2)
T = temperature (K)
Tr = transmittance
t = height in m
w = weighting factors of the discretized directions
x = size parameter of the particle
z = coordinate along the axis parallel to the thermal heat transfer (m)

Greek

β = extinction coefficient (m^{-1})
ε = porosity
$\varepsilon_{interbead}$ = porosity due to the macroscopic pores generated during the compression of beads
ρ = density (kg/m^3)
σ = scattering coefficient (m^{-1})
κ = absorption coefficient (m^{-1})
$\Phi(\mu' \rightarrow \mu) = \Phi(\theta)$ = scattering phase function
θ = angle (rad)
ω = scattering albedo
λ = radiation wavelength (μm)

Subscripts

a = absorption
s = scattering
e = extinction
part = of the particle
cell = of the cellular material contained in the beads
bead = of the beads
cold = of the cold boundary
hot = of the hot boundary
air = of air
EPS = of the EPS foam
PS = of the polystyrene polymer
eq = equivalent
part = of the particle
win = of the cell windows
λ = monochromatic value
inc = incident
sca = scattered
ref = reflected

References

[1] Baillis, D., and Sacadura, J. F., 2000, "Thermal Radiation Properties of Dispersed Media: Theoretical Prediction and Experimental Characterization," J. Quant. Spectrosc. Radiat. Transf., **67**, pp. 327–363.
[2] Lee, S. C., 1989, "Effect of Fibre Orientation on Thermal Radiation in Fibrous Media," Int. J. Heat Mass Transfer, **32**(2), pp. 311–319.
[3] Jeandel, G., Boulet, P., and Morlot, G., 1993, "Radiative Transfer Through a Medium of Silica Fibres Oriented in Parallel Planes," Int. J. Heat Mass Transfer, **36**(2), pp. 531–536.
[4] Milos, F. S., and Marschall, J., 1997, "The Calculation of Anisotropic Extinction Coefficients for Radiation Diffusion in Rigid Fibrous Ceramic Insulations," Int. J. Heat Mass Transfer, **40**(3), pp. 627–634.
[5] Milandri, A., 2000, "Détermination des Paramètres Radiatifs d'un Isolant Fibreux: Théorie de Mie, Oscillateur De LORENTZ Et Méthodes Inverses" Ph.D. thesis, Université de Nancy I.
[6] Fedorov, A. G., and Viskanta, R., 2000, "Radiation Characteristics of Glass Foams," J. Am. Ceram. Soc., **83**(11), pp. 2769–2776.
[7] Baillis, D., Raynaud, M., and Sacadura, J. F., 2000, "Determination of Spectral Radiative Properties of Open Cell Foam. Model Validation," J. Thermophys. Heat Transfer, **14**(2), pp. 137–143.
[8] Kaviany, M., and Singh, B. P., 1992, "Modelling Radiative Transfer in Packed Beds," Int. J. Heat Mass Transfer, **35**(6), pp. 1397–1405.
[9] Kamiuto, K., Iwamoto, M., Nishimura, T., and Sato, M., 1991, "Albedos and Asymmetry Factors of the Phase Function for Packed-spheres Systems," J. Quant. Spectrosc. Radiat. Transf., **46**(4), pp. 309–316.
[10] Coquard, R., and Baillis, D., 2004, "Radiative Characteristics of Opaque Spherical Particles Beds: A New Method of Prediction," J. Thermophys. Heat Transfer, **18**(2), pp. 178–186.
[11] Glicksman, L., Schuetz, M., and Sinofsky, M., 1987, "Radiation Heat Transfer in Foam Insulation," ASME J. Heat Transfer, **109**, pp. 809–812.
[12] Calmidi, V. V., and Mahajan, R. L., 1999, "The Effective Thermal Conductivity of High Porosity Fibrous Metal Foams" ASME J. Heat Transfer, **121**, pp. 466–471.
[13] Kuhn, J., Ebert, H. P., Arduini Schuster, M. P., Buttner, D., and Fricke, J., 1992, "Thermal Transport in Polystyrene and Polyurethanes Foam Insulations," Int. J. Heat Mass Transfer, **35**(7), pp. 1795–1801.
[14] Quenard, D., Sallee, H., Menneteau, F. D., and Giraud, D., 1996, "Heat Transfer in the Packings of Cellular Pellets: Microstructure and Apparent Thermal Conductivity," *Proc. 14th European Conference on Thermophysical Properties*, Lyon, France.
[15] Siegel, R., and Howell, J. R., 1992, "Thermal Radiation Heat Transfer," 3rd ed., Hemisphere, Washington, DC.
[16] De Vries, D. A., 1975, "Heat Transfer in Soils," in *Heat and Mass Transfer in the Biosphere* by De Vries, D. A., and Afgan, N. H., Wiley, New York, pp. 5–18.
[17] Draine, B. T., and Flatau, P. J., 1994, "Discrete Dipole Approximations for Scattering Calculations," J. Opt. Soc. Am. A, **11**, pp. 1491–1499.
[18] Brewster, Q., 1992, *Thermal Radiative Transport and Properties*, 1st ed., Wiley, New York, Vol. 1.
[19] Coquard, R., and Baillis, D., 2004, "Radiative Characteristics of Beds of Spheres Containing an Absorbing and Scattering Medium," J. Thermophys. Heat Transfer, **18**(2), pp. 178–186.
[20] Yuen, W. W., and Wong, L. W., 1980, "Heat Transfer by Conduction and Radiation in a One-Dimensional Absorbing, Emiiting and Anisotropically-Scattering Medium" ASME J. Heat Transfer, **102**, pp. 303–307.

Fully Developed Heat Transfer to Fluid Flow in Rectangular Passages Filled With Porous Materials

A. Haji-Sheikh
Department of Mechanical and Aerospace Engineering,
The University of Texas at Arlington,
Arlington, TX 76019-0023

This is a theoretical and numerical study of fully developed forced convection in various rectangular ducts. Each duct is filled with porous materials and the Brinkman model describes the laminar fluid flow inside this fully saturated porous passage. A Fourier series solution provides the exact solution for the velocity field. Also, a Fourier series solution can produce the temperature profile for a condition of constant energy input per unit length. This includes two different wall conditions: a uniform wall temperature at any axial location and a locally uniform heat flux over the boundary. The case of constant wall temperature over the entire passage is also accommodated using a special analytical/numerical solution. [DOI: 10.1115/1.2188507]

Keywords: duct flow, porous media, fully developed, forced convection, rectangular ducts

1 Introduction

A study of flow in rectangular porous passages is of interest in a variety of heat transfer applications such as electronic cooling. The fundamentals of steady flow in porous media are reported in [1–4]. Recently, comprehensive studies of heat transfer in developing sections of porous plate channels and circular tubes are reported in the literature, e.g, [5–9].

This paper studies the fully developed temperature fields in rectangular channels with classical boundary conditions. These boundary conditions for free flow in rectangular ducts are well documented in the literature. For the locally constant wall heat flux at the boundaries, Sparrow and Siegel [10] studied the variations of the heat transfer coefficient in rectangular ducts. Another model that has been studied considers the heat flux per unit length to be uniform while maintaining a uniform temperature along the perimeter of the ducts [11,12]. This later case is designated as H1 and the locally constant wall heat flux case [10] is the H2 case. Finally, the constant wall temperature case is designated as the T case in this work. For the T case, the data for free flow though rectangular passages are available in [12]. A summary of these data from [10–12] is in Table 1. Later, they are compared with the corresponding data from this study.

This study assumes the Brinkman model applies to unidirectional flow in a duct. This would provide the velocity field for a given porous passage. For a rectangular duct, an exact series solution is possible. Also, it is possible to obtain exact series solutions for both H1 and H2 cases. The computed Nusselt numbers for these two cases are remarkably different. The computation of temperature field under the locally constant wall temperature condition is also acquired using a series solution while the eigenvalues are computed numerically.

2 Velocity Field in a Rectangular Channel

For a steady and hydrodynamically fully developed flow passing through an impermeable rectangular channel, shown in Fig. 1, the Brinkman momentum equation is

$$\mu_e\left(\frac{\partial^2 u}{\partial y^2}+\frac{\partial^2 u}{\partial z^2}\right)-\frac{\mu}{K}u-\frac{\partial p}{\partial x}=0 \tag{1}$$

with a constant pressure gradient $\Phi=-\partial p/\partial x$. In this equation, the effective viscosity is μ_e, the fluid viscosity is μ, and the permeability is K. Using a in Fig. 1 as the characteristic length, Eq. (1), in dimensionless form, becomes

$$\left(\frac{\partial^2 \overline{u}}{\partial \overline{y}^2}+\frac{\partial^2 \overline{u}}{\partial \overline{z}^2}\right)-\frac{1}{M\,\mathrm{Da}}\overline{u}+1=0 \tag{2}$$

where $\overline{y}=y/a$, $\overline{z}=z/a$, $M=\mu_e/\mu$, $\overline{u}=\mu_e u/(\Phi a^2)$, and $\mathrm{Da}=K/a^2$ is the Darcy number. The boundary conditions are $\overline{u}=0$ at $\overline{y}=\pm 1$ and at $\overline{z}=\pm\overline{b}=\pm b/a$ while $\partial\overline{u}/\partial\overline{y}=0$ at $\overline{y}=0$ and $\partial\overline{u}/\partial\overline{z}=0$ at $\overline{z}=0$.

The formulation of velocity distribution begins by selecting a functional relation of the form

$$\overline{u}=\sum_{n=1}^{\infty}\sum_{m=1}^{\infty}a_{mn}\cos(\beta_n\overline{y})\cos(\gamma_m\overline{z}) \tag{3}$$

that satisfies the specified boundary conditions at $y=0$ and $z=0$ shown in Fig. 1. Using the boundary conditions at $y=a$ and $z=b$, one obtains $\beta_n=(n-1/2)\pi$ and $\gamma_m=(m-1/2)\pi/\overline{b}$. The substitution of $\overline{u}$ from Eq. (3) in Eq. (2) provides the relation

$$\sum_{n=1}^{\infty}\sum_{m=1}^{\infty}a_{mn}\left(\beta_n^2+\gamma_m^2+\frac{1}{M\,\mathrm{Da}}\right)\cos(\beta_n\overline{y})\cos(\gamma_m\overline{z})=1 \tag{4}$$

Multiplying both sides of Eq. (4) by $\cos(\beta_i\overline{y})\cos(\gamma_j\overline{z})$, integrating over $\overline{y}$ from 0 to 1 and integrating over $\overline{z}$ from 0 to $\overline{b}=b/a$, and following the application of the orthogonality condition the value of a_{mn} is

$$a_{mn}=\frac{4(-1)^{m+n}}{\overline{b}\beta_n\gamma_m\left(\beta_n^2+\gamma_m^2+\frac{1}{M\,\mathrm{Da}}\right)} \tag{5}$$

Upon substitution of a_{mn} from Eq. (5) in Eq. (3), the following relation provides the velocity distribution:

Contributed by the Heat Transfer Division of ASME for publication in the JOURNAL OF HEAT TRANSFER. Manuscript received June 1, 2005; final manuscript received December 1, 2005. Review conducted by Bengt Sunden.

Table 1 Computed limiting values of Nu_D for the H1, H2 and T cases

	H1 Case		H2 Case		T Case	
b/a	Ref. [11]	Eq. (11*b*)	Ref. [10]	Eq. (26)	Ref. [12]	Eq. (34)
1	3.61	3.608	3.09	3.087	2.98	2.978
2	4.12	4.123	3.02	3.019	3.39	3.392
3	4.79	4.795	—	2.961	3.96	3.958
4	5.33	5.331	2.93	2.933	4.44	4.440
6	—	6.049		2.913	—	5.138
8	6.49	6.490	2.90	2.907	5.60	5.594
10	—	6.785	2.90	2.906	—	5.908
∞	8.235	8.235	—	2.906	7.54	7.541

$$\overline{u} = \sum_{n=1}^{\infty}\sum_{m=1}^{\infty} \frac{4(-1)^{m+n}\cos(\beta_n \overline{y})\cos(\gamma_m \overline{z})}{\overline{b}\beta_n\gamma_m\left(\beta_n^2+\gamma_m^2+\frac{1}{M\,\mathrm{Da}}\right)} \tag{6}$$

Next, the average velocity U, defined by the relation

$$U = \frac{1}{ab}\int_{y=0}^{a}\int_{z=0}^{b} u dz dy$$

leads to the average reduced velocity, by using $\overline{u}$ from Eq. (6) instead of u

$$\overline{U} = \sum_{n=1}^{\infty}\sum_{m=1}^{\infty} \frac{4}{(\overline{b}\beta_n\gamma_m)^2\left(\beta_n^2+\gamma_m^2+\frac{1}{M\,\mathrm{Da}}\right)} \tag{7}$$

Equations (6) and (7) provide the value of $u/U=\overline{u}/\overline{U}$ for inclusion in the energy equation. In these relations, the quantity $1/(M\mathrm{Da})$ would vanish when the passage is free from porous materials, since $M\,\mathrm{Da}\to\infty$.

3 Solution of the Energy Equation

The general solution of the energy equation includes the thermal entry region and the thermally fully developed condition. However, the emphasis of this presentation is to investigate the latter case. The energy equation, under a fully developed thermal condition, for the rectangular passages, is

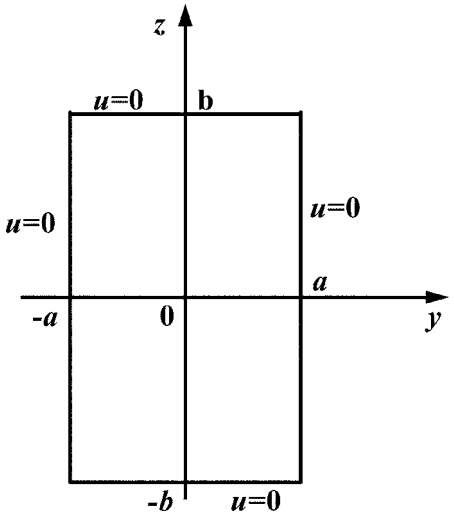

Fig. 1 The coordinate system and dimensions for a rectangular passage

$$k\left(\frac{\partial^2 T}{\partial y^2}+\frac{\partial^2 T}{\partial z^2}\right) = \rho c_p u\frac{\partial T}{\partial x} \tag{8a}$$

Once temperature and velocity distributions are available, the relation

$$T_b = \frac{1}{ab}\int_{y=0}^{a}\int_{z=0}^{b}\left(\frac{u}{U}\right)T dz dy \tag{8b}$$

defines the bulk temperature T_b.

For flow through porous passages, three types of boundary conditions are studied. They are H1 type and H2 type with constant $\partial T/\partial x$ and locally constant wall temperature with $\partial T/\partial x$ monotonically reducing throughout the passage. For free flow through rectangular channels with locally constant wall heat flux, the solution to this problem by Sparrow and Siegel [10] is available using the method of weighted residuals. Also for free flow, other heat transfer information is available in Table 9-2 of Ref. [11] and in Table 32 of Ref. [12].

3.1 The H1 Solution. This special solution considers uniform energy input per unit length of a passage while maintaining a wall temperature $T_w(x)$ that depends only on the axial coordinate x. This case is expected when the walls of a passage are orthotropic with a relatively high thermal conductivity in the directions perpendicular to the x axis. If the average heat flux is designated as $\overline{q_w}$, the aforementioned condition requires that $\partial T/\partial x=\partial T_b/\partial x=\overline{q_w}C/(c_p\rho UA)$. After inserting this value of $\partial T/\partial x$ in Eq. (8*a*) and then replacing T using the relation $T=T_w+\theta(\overline{q_w}a/k)$, it becomes

$$\left(\frac{\partial^2\theta}{\partial\overline{y}^2}+\frac{\partial^2\theta}{\partial\overline{z}^2}\right)=\left(\frac{4a}{D_h}\frac{u}{U}\right)=\left(\frac{4a}{D_h}\frac{\overline{u}}{\overline{U}}\right) \tag{9}$$

where $\overline{y}=y/a$, $\overline{z}=z/a$, and $D_h=4A/C=4ab/(a+b)$ is the hydraulic diameter. The solution of Eq. (9) is obtainable from the relation

$$\theta(\overline{y,z}) = \frac{1}{\overline{U}}\sum_{n=1}^{\infty}\sum_{m=1}^{\infty} c_{mn}\cos(\beta_n\overline{y})\cos(\gamma_m\overline{z}) \tag{10a}$$

where $\overline{U}$ is defined in Eq. (7). Next, the function θ from Eq. (10*a*) and the dimensionless velocity ratio $\overline{u}/\overline{U}$ from Eqs. (6) and (7) should be substituted in Eq. (9). Then, the application of orthogonality condition yields

$$c_{mn} = -\left(\frac{4a}{D_h}\right)\frac{a_{mn}}{\beta_n^2+\gamma_m^2} \tag{10b}$$

Based on the definition of the heat transfer coefficient $h=\overline{q_w}/(T_w-T_b)$ and the definition of $\theta_b=(T_b-T_w)/(\overline{q_w}a/k)$, one gets $ha/k=1/\theta_b$. Moreover, the substitution of θ from Eq. (10) into the dimensionless form of Eq. (8*b*) leads to a relation

$$\theta_b = \sum_{n=1}^{\infty}\sum_{m=1}^{\infty}\frac{a_{mn}c_{mn}}{4\overline{U}^2} \tag{11a}$$

for the bulk temperature. Therefore, the Nusselt number is obtainable using the relation

$$\mathrm{Nu}_D = hD_h/k = (D_h/a)/\theta_b \tag{11b}$$

Figure 2 shows the values of Nu_D plotted as a function $\omega=1/\sqrt{M\,\mathrm{Da}}$. Each line in Fig. 2 corresponds to a different $\overline{b}=b/a$ value. A selected set of Nu_D values, for different b/a and M Da, are in Table 2. For comparison with the available data, the limiting values of Nu_D as M Da goes to ∞ are in Column 3 of Table 1 and they agree well with those from [11].

3.2 The H2 Solution. This solution assumes a locally uniform wall heat flux over the entire surfaces of a rectangular pas-

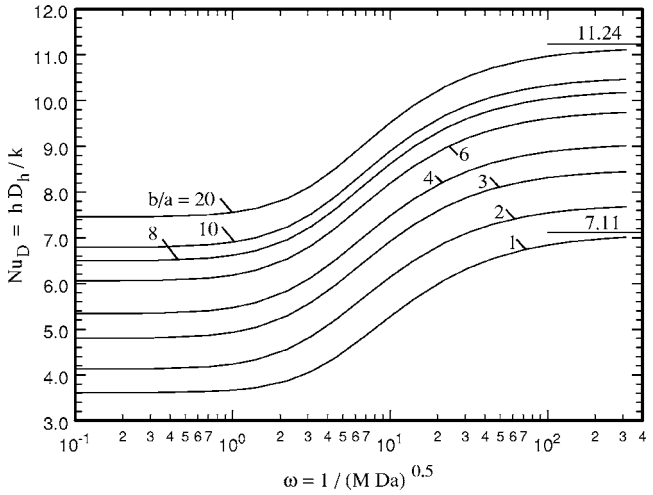

Fig. 2 Average Nusselt number, for the H1 case, as a function of *M* Da, for different values of *b*/*a*

sage. Equation (8*a*), following substitution for $T=\theta(q_w a/k)$ and $\partial T/\partial x=\partial T_b/\partial x=q_w C/(c_p\rho UA)$, in the dimensionless space, becomes

$$\left(\frac{\partial^2\theta}{\partial\bar{y}^2}+\frac{\partial^2\theta}{\partial\bar{z}^2}\right)=\left(\frac{4a}{D_h}\frac{u}{U}\right) \tag{12a}$$

subject to the boundary conditions

$$\left.\frac{\partial\theta}{\partial\bar{y}}\right|_{\bar{y}=1}=\left.\frac{\partial\theta}{\partial\bar{z}}\right|_{\bar{z}=\bar{b}}=1 \quad \text{and} \quad \left.\frac{\partial\theta}{\partial\bar{y}}\right|_{\bar{y}=0}=\left.\frac{\partial\theta}{\partial\bar{z}}\right|_{\bar{z}=0}=0 \tag{12b}$$

where $D_h=4A/C=4ab/(a+b)$ is the hydraulic diameter, $\bar{y}=y/a$, and $\bar{z}=z/a$. After substitution for D_h, Eq. (12*a*) becomes

$$\left(\frac{\partial^2\theta}{\partial\bar{y}^2}+\frac{\partial^2\theta}{\partial\bar{z}^2}\right)=\left(\frac{a+b}{b}\right)\frac{u}{U}=\left(1+\frac{1}{\bar{b}}\right)\frac{u}{U} \tag{13}$$

where $\bar{b}=b/a$. A needed transformation that makes the boundary conditions homogeneous introduces an interesting special solution and it is presented a priori.

3.2.1 A Special Solution. The exact series solution of Eq. (13) is based on an auxiliary solution for slug/plug flow when $u/U=1$. This auxiliary solution of Eq. (13) is designated as $\theta^*(\bar{y},\bar{z})$ and satisfies the equation

$$\left(\frac{\partial^2\theta^*}{\partial\bar{y}^2}+\frac{\partial^2\theta^*}{\partial\bar{z}^2}\right)=\left(1+\frac{1}{\bar{b}}\right) \tag{14a}$$

The solution of Eq. (14*a*) subject to the boundary conditions

$$\left.\frac{\partial\theta^*}{\partial\bar{y}}\right|_{\bar{y}=1}=\left.\frac{\partial\theta^*}{\partial z}\right|_{\bar{z}=\bar{b}}=1 \quad \text{and} \quad \left.\frac{\partial\theta^*}{\partial\bar{y}}\right|_{\bar{y}=0}=\left.\frac{\partial\theta^*}{\partial z}\right|_{\bar{z}=0}=0$$

is

$$\theta^*=\frac{\bar{y}^2}{2}+\frac{\bar{z}^2}{2\bar{b}}+\text{constant} \tag{14b}$$

The constant in this solution represents θ^* at $x=y=0$ and could be replaced with $\theta^*(0,0)$.

By definition, the bulk temperature for slug flow is

$$\theta_b^*=\frac{1}{\bar{b}}\int_{\bar{y}=0}^{1}\int_{\bar{z}=0}^{\bar{b}}\theta^*d\bar{z}d\bar{y}=\int_{\bar{y}=0}^{1}\int_{\bar{z}=0}^{\bar{b}}\left[\frac{\bar{y}^2}{2}+\frac{\bar{z}^2}{2\bar{b}}+\theta^*(0,0)\right]d\bar{z}d\bar{y}$$
$$=\frac{1+\bar{b}}{6}+\theta^*(0,0) \tag{15a}$$

Moreover, the average wall temperature for slug flow is

$$\theta_{w,\text{ave}}^*=\frac{1}{1+\bar{b}}\left[\int_0^1\theta^*(\bar{y},1)d\bar{y}+\int_0^{\bar{b}}\theta^*(1,\bar{z})d\bar{z}\right]$$
$$=\frac{1}{1+\bar{b}}\left[\int_0^1\left(\frac{\bar{y}^2}{2}+\frac{\bar{b}}{2}\right)d\bar{y}+\int_0^{\bar{b}}\left(\frac{1}{2}+\frac{\bar{z}^2}{2\bar{b}}\right)d\bar{z}\right]+\theta^*(0,0)$$
$$=\frac{1+6\bar{b}+\bar{b}^2}{6(1+\bar{b})}+\theta^*(0,0) \tag{15b}$$

The difference between Eqs. (15*a*) and (15*b*) is

Table 2 Nusselt number for H1 case at different values of *b*/*a* and *M* Da

M Da	$b/a=1$	$b/a=2$	$b/a=4$	$b/a=6$	$b/a=8$	$b/a=10$	$b/a=\infty$
∞	3.6080	4.1233	5.3311	6.0495	6.4904	6.7850	8.2353
10	3.6141	4.1353	5.3468	6.0644	6.5044	6.7982	8.2439
2	3.6384	4.1815	5.4056	6.1204	6.5569	6.8481	8.2775
1	3.6678	4.2355	5.4715	6.1831	6.6162	6.9047	8.3182
0.5	3.7240	4.3330	5.5851	6.2918	6.7198	7.0044	8.3952
0.2	3.8741	4.5666	5.8419	6.5406	6.9611	7.2400	8.5968
0.1	4.0773	4.8433	6.1347	6.8299	7.2466	7.5225	8.8612
0.05	4.3729	5.2004	6.5080	7.2045	7.6210	7.8964	9.2301
0.02	4.8722	5.7398	7.0680	7.7724	8.1932	8.4712	9.8155
0.01	5.2760	6.1428	7.4828	8.1946	8.6197	8.9006	10.2586
0.005	5.6570	6.5048	7.8519	8.5701	8.9993	9.2830	10.6543
0.002	6.0854	6.8952	8.2460	8.9704	9.4038	9.6903	11.0762
0.001	6.3424	7.1221	8.4729	9.2005	9.6362	9.9243	11.3183
0.0005	6.5442	7.2966	8.6464	9.3763	9.8136	10.1028	11.5029
0.0002	6.7389	7.4623	8.8103	9.5421	9.9808	10.2711	11.6768
0.0001	6.8431	7.5500	8.8967	9.6294	10.0688	10.3597	11.7682
0.00005	6.9195	7.6138	8.9594	9.6927	10.1327	10.4239	11.8344
0.00002	6.9892	7.6716	9.0161	9.7500	10.1904	10.4819	11.8943
0.00001	7.0250	7.7012	9.0452	9.7792	10.2199	10.5116	11.9249
0	7.1135	7.7740	9.1164	9.8511	10.2923	10.5844	12.0000

$$\theta^*_{w,\text{ave}} - \theta^*_b = \frac{T_{w,\text{ave}} - T_b}{q_w a/k} = \frac{2}{3}\left(\frac{\overline{b}}{1+\overline{b}}\right) \tag{16}$$

Using the definition $\text{Nu}_D = hD_h/k$, where $D_h = 4A/C$, the heat transfer coefficient h is obtainable from the relation

$$\text{Nu}_D = \frac{hD_h}{k} = \frac{q_w a/(T_{w,\text{ave}} - T_b)}{k}\left(\frac{D_h}{a}\right) = \frac{3}{2}\left(\frac{1+\overline{b}}{\overline{b}}\right)\left(\frac{4ab}{a+b}\right)\frac{1}{a} = 6 \tag{17}$$

It is interesting to note that Nu_D is a constant for slug flow through rectangular passages, independent of the aspect ratios.

This exact and simple result introduces another interesting phenomenon. The Nusselt number is $\text{Nu}_D = 12$ for slug flow between two parallel plates having uniform heat flux; however, it is equal to 6 for rectangular passages for all b/a values. An examination of the thermal entrance solution shows that the entrance region increases as b/a increases and it approaches infinity as b/a goes to infinity. This indicates that there is a singularity at infinity where Nu_D goes from 12 to 6. In general, for the H2 case, the thermally fully developed solution may become unattainable when b/a is very large. Therefore, when b/a is relatively large, one should examine the thermal entrance solution before using the fully developed thermal condition.

3.2.2 General Solution. The following temperature solution uses the computed value of the velocity from Eq. (6). The parameter $M\,\text{Da}$ affects the temperature field by appearing within the coefficient a_{mn} as given by Eq. (5) and in $\overline{u}$, Eq. (6). Therefore, the following temperature solution depends on the $M\,\text{Da}$ values through the velocity field u/U. To acquire a solution for Eq. (13), one can subtract Eq. (14*a*) from Eq. (13) and the result is

$$\left[\frac{\partial^2(\theta-\theta^*)}{\partial\overline{y}^2} + \frac{\partial^2(\theta-\theta^*)}{\partial\overline{z}^2}\right] = \left(\frac{4a}{D_h}\frac{u}{U}\right) - \left(1+\frac{1}{\overline{b}}\right) \tag{18a}$$

In this equation, the parameter $\theta-\theta^*$ is designated as a new function ψ and it leads to a transformation

$$\theta(\overline{y},\overline{z}) = \theta^*(\overline{y},\overline{z}) + \psi(\overline{y},\overline{z}) \tag{18b}$$

while Eq. (14*b*) provides the function $\theta^*(\overline{y},\overline{z})$. Since the function θ^* satisfies the specified nonhomogeneous boundary conditions for Eq. (14*a*), then, the transformed dimensionless temperature ψ must satisfy the equation

$$\left(\frac{\partial^2\psi}{\partial\overline{y}^2} + \frac{\partial^2\psi}{\partial\overline{z}^2}\right) = \left(\frac{4a}{D_h}\frac{u}{U}\right) - \left(1+\frac{1}{\overline{b}}\right) = -\left(1+\frac{1}{\overline{b}}\right)\left(1-\frac{\overline{u}}{\overline{U}}\right) \tag{19a}$$

subject to the homogeneous boundary conditions of the second kind

$$\left.\frac{\partial\psi}{\partial\overline{y}}\right|_{\overline{y}=1} = \left.\frac{\partial\psi}{\partial\overline{z}}\right|_{\overline{z}=\overline{b}} = \left.\frac{\partial\psi}{\partial\overline{y}}\right|_{\overline{y}=0} = \left.\frac{\partial\psi}{\partial\overline{z}}\right|_{\overline{z}=0} = 0 \tag{19b}$$

The next task is to find a solution for Eq. (19*a*). The following solution of Eq. (19*a*):

$$\psi(\overline{y},\overline{z}) = \sum_{n=0}^{\infty}\sum_{m=0}^{\infty} c_{mn}\cos(n\pi\overline{y})\cos(m\pi\overline{z}/\overline{b}) \tag{20}$$

satisfies the homogeneous boundary conditions given by Eq. (19*b*). The substitution of ψ from Eq. (20) into Eq. (19*a*) produces the relation

$$\sum_{n=0}^{\infty}\sum_{m=0}^{\infty} c_{mn}(1-\delta_{0,m+n})[(n\pi)^2 + (m\pi/\overline{b})^2]\cos(n\pi\overline{y})\cos(m\pi\overline{z}/\overline{b}) = \left(1+\frac{1}{\overline{b}}\right)\left(1-\frac{\overline{u}}{\overline{U}}\right) \tag{21}$$

The quantity $(1-\delta_{0,m+n})$, containing the Kronecker delta, indicates that the constant term c_{00} drops out following the differentiation when $m=0$ and $n=0$. Since this series in Eq. (21) is not complete, the solution is valid within a constant. The use of orthogonality condition yields the coefficients c_{mn}

$$c_{mn} = \frac{(2-\delta_{0,n})(2-\delta_{0,m})}{\overline{b}[(n\pi)^2 + (m\pi/\overline{b})^2]}\int_{\overline{y}=0}^{1}\int_{\overline{z}=0}^{\overline{b}}\left(1+\frac{1}{\overline{b}}\right)\left(1-\frac{\overline{u}}{\overline{U}}\right) \times \cos(n\pi\overline{y})\cos(m\pi\overline{z}/\overline{b})\,d\overline{z}\,d\overline{y}. \tag{22}$$

Then, the solution for ψ is

$$\psi = c_{00} + \sum_{n=0}^{\infty}\sum_{m=0}^{\infty}\frac{(2-\delta_{0,n})(2-\delta_{0,m})(1-\delta_{0,m+n})}{\overline{b}\pi^2[n^2 + (m/\overline{b})^2]} \times \left(1+\frac{1}{\overline{b}}\right)\Lambda_{mn}\cos(n\pi\overline{y})\cos(m\pi\overline{z}/\overline{b}) \tag{23a}$$

where

$$\Lambda_{mn} = \int_{\overline{y}=0}^{1}\int_{\overline{z}=0}^{\overline{b}}\left(1-\frac{\overline{u}}{\overline{U}}\right)\cos(n\pi\overline{y})\cos(m\pi\overline{z}/\overline{b})\,d\overline{z}\,d\overline{y} = \sum_{i=1}^{\infty}\sum_{j=1}^{\infty}\frac{\overline{b}(-1)^{(i+j)}(i-1/2)(j-1/2)a_{ij}/\overline{U}}{\pi^2[n^2-(i-1/2)^2][m^2-(j-1/2)^2]} \tag{23b}$$

and

$$a_{ij} = \frac{4(-1)^{i+j}}{\overline{b}\beta_i\gamma_j[\beta_i^2 + \gamma_j^2 + 1/(M\,\text{Da})]} \tag{23c}$$

with $\beta_i = (i+1/2)\pi$ and $\gamma_j = (j+1/2)\pi/\overline{b}$. Therefore, having the temperature solution $\theta(\overline{y},\overline{z}) = \theta^*(\overline{y},\overline{z}) + \psi(\overline{y},\overline{z})$ in hand, the values of $\theta_{w,\text{ave}}$ and θ_b are also known by explicit relations

$$\theta_b = c_{00} + \sum_{n=0}^{\infty}\sum_{m=0}^{\infty}\frac{(2-\delta_{0,n})(2-\delta_{0,m})(1-\delta_{0,m+n})}{\overline{b}\pi^2[n^2+(m/\overline{b})^2]}\left(1+\frac{1}{\overline{b}}\right)\Lambda_{mn}^2 + \sum_{i=1}^{\infty}\sum_{j=1}^{\infty}\left\{\frac{2(-1)^{(i+j)}[-8+\pi^2(1-4j+4j^2)]}{(2j-1)(2i-1)^3\pi^4} + \frac{2(-1)^{(i+j)}[-8+\pi^2(1-4j+4j^2)]}{(2i-1)(2j-1)^3\pi^4}\right\}\frac{a_{ij}}{\overline{U}} \tag{24}$$

and

$$\theta_{w,\text{ave}} = c_{00} + \sum_{n=0}^{\infty}\sum_{m=0}^{\infty}\frac{(2-\delta_{0,n})(2-\delta_{0,m})(1-\delta_{0,m+n})}{\pi^2\overline{b}[n^2+(m/\overline{b})^2]\overline{U}} \times \Lambda_{mn}[\delta_{0,m}(-1)^n + \delta_{0,n}(-1)^m] + \frac{1/6 + \overline{b} + \overline{b}^2/6}{1+\overline{b}} \tag{25}$$

As stated earlier, the difference $\theta_{w,\text{ave}} - \theta_b = T_{w,\text{ave}}/(q_w a/k) - T_b/(q_w a/k)$ provides the average Nusselt from the relation

$$\text{Nu}_D = \frac{hD_h}{k} = \left(\frac{q_w}{T_{w,\text{ave}} - T_b}\right)\frac{D_h}{k} = \left(\frac{q_w a/k}{T_{w,\text{ave}} - T_b}\right)\frac{D_h}{a} = \frac{D_h/a}{\theta_{w,\text{ave}} - \theta_b} \tag{26}$$

All computations for H1 and H2 cases were performed using MATHEMATICA [13]. These data are gathered from the exact series

Table 3 Nusselt number for H2 case at different values of *b*/*a* and *M* Da

M Da	*b*/*a*=1	*b*/*a*=2	*b*/*a*=4	*b*/*a*=6	*b*/*a*=8	*b*/*a*=10
∞	3.0874	3.0192	2.9326	2.9126	2.9074	2.9061
10	3.0924	3.0303	2.9526	2.9363	2.9329	2.9326
2	3.1123	3.0731	3.0268	3.0231	3.0257	3.0290
1	3.1364	3.1228	3.1083	3.1167	3.1251	3.1317
0.5	3.1824	3.2120	3.2440	3.2690	3.2854	3.2966
0.2	3.3053	3.4219	3.5266	3.5754	3.6030	3.6206
0.1	3.4717	3.6632	3.8128	3.8746	3.9081	3.9291
0.05	3.7144	3.9645	4.1382	4.2055	4.2411	4.2631
0.02	4.1259	4.4046	4.5778	4.6416	4.6747	4.6949
0.01	4.4606	4.7263	4.8824	4.9383	4.9671	4.9846
0.005	4.7777	5.0121	5.1441	5.1905	5.2142	5.2286
0.002	5.1357	5.3180	5.4166	5.4506	5.4679	5.4783
0.001	5.3512	5.4948	5.5709	5.5969	5.6101	5.6180
0.0005	5.5206	5.6305	5.6878	5.7072	5.7170	5.7229
0.0002	5.6843	5.7589	5.7973	5.8103	5.8168	5.8207
0.0001	5.7721	5.8268	5.8547	5.8641	5.8689	5.8717
0.00005	5.8363	5.8760	5.8963	5.9030	5.9064	5.9085
0.00002	5.8948	5.9204	5.9337	5.9380	5.9402	5.9415
0.00001	5.9247	5.9429	5.9527	5.9558	5.9573	5.9583
0	6	6	6	6	6	6

solution with a high degree of precision and they agree well with other data from earlier studies. To enhance the computational speed for small *M* Da values, the data for H2 case were also computed using a FORTRAN program.

A sample of numerical data using Eq. (26) for different *M* Da values are prepared and presented in Table 3. For comparison with data from Sparrow and Siegel [10] when *M* Da=∞, the Nusselt number for different aspect ratios are computed using Eq. (26) and they are in Column 5 of Table 1. They show the Nusselt number reduces and assumes an asymptotic value of 2.906 as *b*/*a* increases.

Figure 3 shows the variation of the Nusselt number Nu_D as a function of $\omega=1/\sqrt{M\,Da}$ for different values of $\bar{b}=b/a$. As in the H1 case, the data clearly indicate an increase in the value of the Nusselt number as ω increases, while *M* Da decreases. Also, as ω increases, the data in Fig. 3 indicate that the Nu_D values asymptotically approach the value of 6 obtained when *M* Da=0, for all aspect ratios.

3.3 Constant Temperature Solution. For a porous passage with constant wall temperature, $\partial T/\partial x$ in Eq. (8*a*) depends on *x*, *y*, and *z*. Therefore, the extended method of weighted residual [7] is a suitable mathematical tool. As discussed in [7] the temperature solution can have the form

$$T(y,z;x)=\sum_{m=1}^{N} B_m \Psi_m(y,z) e^{-\lambda_m^2 x} \tag{27}$$

where

$$\Psi_m=\sum_{j=1}^{N} d_{mj} f_j(y,z) \tag{28}$$

The functions $f_j(y,z)$ for $j=1,2,\ldots,N$ are to be selected so that they satisfy the homogeneous boundary conditions of the first kind along the surface of the ducts. Among many suitable $f_j(y,z)$ functions, the following is selected [7]:

$$f_j=(a^2-y^2)(b^2-z^2)y^{2(m_j-1)}z^{2(n_j-1)}, \quad \text{for } j=1,2,\ldots,N. \tag{29}$$

As described in [7], in the matrix form, the relation

$$\mathbf{A}+\lambda^2\mathbf{B}=0 \tag{30}$$

provides the eigenvalues wherein the members of matrix **A** are

$$a_{ij}=-\int_A k_e \nabla f_i(\mathbf{y},z)\cdot\nabla f_j(\mathbf{y},z)\,dA$$

$$\text{for } i=1,2,\ldots,N \quad \text{and} \quad j=1,2,\ldots,N \tag{31}$$

and the members of matrix **B** are

$$b_{ij}=\int_A \rho c_p u(y,z) f_i(y,z) f_j(y,z)\,dA$$

$$\text{for } i=1,2,\ldots,N \quad \text{and} \quad j=1,2,\ldots,N \tag{32}$$

As shown in these relations, the matrices **A** and **B** are symmetric [7]. The symbolic software MATHEMATICA [13] was used to compute the eigenvalues from the relation

$$\mathbf{B}^{-1}\mathbf{A}+\lambda^2\mathbf{I}=0 \tag{33}$$

As *x* goes to infinity, the first eigenvalue provides the Nusselt number for the fully developed thermal condition; this limiting Nusselt number is obtainable from the relation

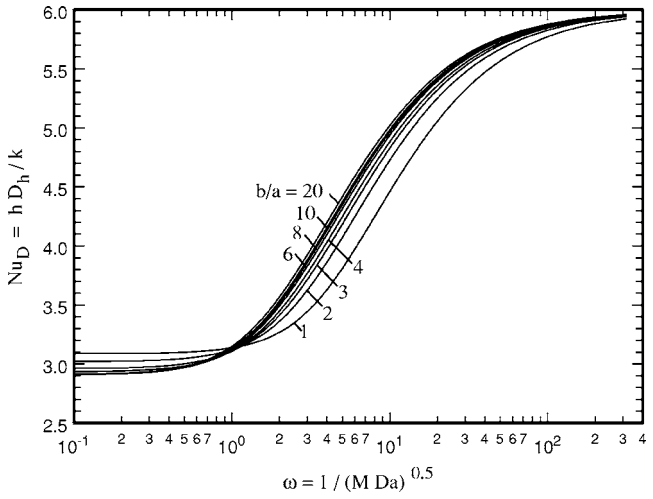

Fig. 3 Average Nusselt number, for the H2 case, as a function of *M* Da, for different values of *b*/*a*

Table 4 Nusselt number for T case at different values of *b*/*a* and *M* Da

M Da	*b*/*a*=1	*b*/*a*=2	*b*/*a*=4	*b*/*a*=6	*b*/*a*=8	*b*/*a*=10	*b*/*a*=∞
∞	2.978	3.392	4.441	5.138	5.594	5.908	5.908
10	2.982	3.401	4.455	5.152	5.607	5.920	5.920
2	2.999	3.436	4.507	5.204	5.656	5.966	5.966
1	3.019	3.476	4.564	5.261	5.709	6.016	6.016
0.5	3.058	3.549	4.659	5.354	5.797	6.100	6.100
0.2	3.163	3.720	4.863	5.553	5.989	6.285	6.285
0.1	3.303	3.917	5.080	5.768	6.201	6.495	6.495
0.05	3.506	4.162	5.339	6.031	6.464	6.758	6.758
0.02	3.834	4.507	5.701	6.402	6.842	7.133	7.133
0.01	4.082	4.743	5.947	6.656	7.100	7.399	7.399
0.005	4.297	4.937	6.149	6.866	7.315	7.618	7.618
0.002	4.513	5.127	6.343	7.065	7.517	7.824	7.824
0.001	4.632	5.227	6.443	7.167	7.622	7.931	7.931
0.0005	4.718	5.301	6.518	7.246	7.704	8.015	8.015
0.0002	4.794	5.365	6.580	7.310	7.770	8.082	8.082
0.0001	4.830	5.396	6.608	7.340	7.801	8.115	8.115
0.00005	4.858	5.419	6.639	7.373	7.836	8.151	8.151
0.00002	4.876	5.435	6.655	7.390	7.854	8.169	8.169
0.00001	4.893	5.441	6.661	7.403	7.861	8.176	8.176
0	4.935	5.483	6.711	7.453	7.920	8.238	8.238

$$\mathrm{Nu}_D = hD_h/k_e = \left(\frac{D_h}{2a}\right)^2 \lambda_1^2 \tag{34}$$

Table 4 shows the computed values of Nu_D for selected aspect ratios b/a and M Da values. Moreover, Fig. 4 is prepared to demonstrate the variation of Nusselt number as a function of $1/\sqrt{M\,\mathrm{Da}}$ as M Da decreases. For free flow through rectangular passages, the computed Nu_D values, using Eq. (34), are in Column 7 of Table 1 and they compare with those from [12] in Column 6. The asymptotic behaviors of Nu_D for slug flow are in the last row of Table 4. As $M\,\mathrm{Da}\to 0$, the classical heat conduction yields $\lambda_1^2 = (\pi/2)^2[1+(a/b)^2]$ and it provides the data in the last row of Table 4 following its substitution in Eq. (34).

4 Discussion

The data in Figs. 2–4 reveal the limiting conditions for the heat transfer to fluids passing through these rectangular passages filled with saturated porous materials. The first rows in these tables provide the Nusselt number for free flow, when M Da$=\infty$. The last rows are the Nusselt numbers for slug flow $u/U=1$, when M Da $=0$. For the H1 case, when $M\,\mathrm{Da}\to 0$, Table 2 shows different asymptotic values for Nu_D at each $\bar{b}$. These limiting values are consistent with the data directly computed for the slug flow. The last column in Table 2 provides the Nusselt number for parallel plate channels, as $\bar{b}$ goes to infinity. The number of terms needed to assure the convergence of Eq. (11*a*) and accuracy of data in Table 2 increases as b/a increases and as M Da becomes small, see Eq. (5).

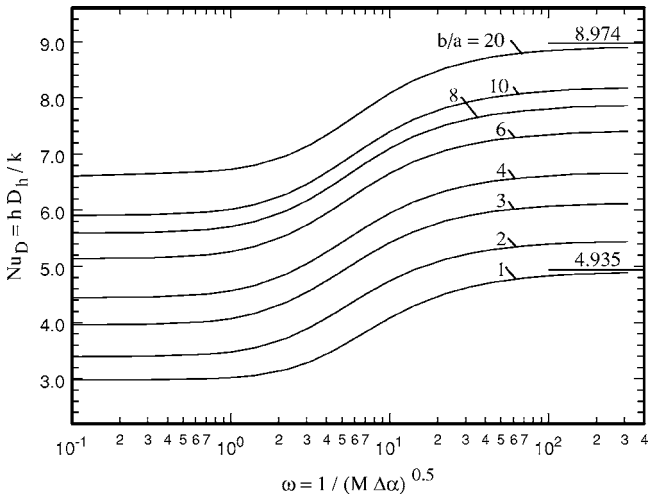

Fig. 4 Average Nusselt number, for the T case, as a function of *M* Da, for different values of *b*/*a*

For the H2 case, the data for all aspect ratios approach a constant value of 6. Indeed, the data in Table 3 show that the deviations from 6 become small for M Da values of 10^{-5} or less. This represents an interesting difference between H1 case and H2 case where Nu_D has different values as $M\,\mathrm{Da}\to 0$. As $\bar{b}$ goes to infinity, the fully developed Nusselt number values for the H2 case should approach those given for the H1 case in Table 2. Similar to the H1 case, the number of terms needed to assure the convergence of Eq. (24) depends on the values of b/a and M Da. Since Eq. (24), with Λ_{mn} from Eq. (23*b*), contains four summations, each data in Table 3 required a considerably larger computation time in comparison to that for the H1 case.

Under thermally fully developed condition, the exact series solutions for the H1 and H2 can provide results with any desirable degree of accuracy. In contrast, for the T case, matrix inversions are needed for determining the eigenvalues. A series solution with a large number of eigenvalues increases the size of matrices **A** and **B** and the round-off error can become substantial during matrix inversion. Therefore, it is necessary to show the convergence behavior of this type of solution. A test of this series solution shows a reasonably rapid convergence when M Da is relatively large. As an example, when $b/a=1$ and $M\,\mathrm{Da}=10^{-1}$, the solution using 10, 15, 21, and 28 eigenvalues produced $\mathrm{Nu}_D=3.3031$, 3.3032, 3.3033, and 3.3033. Indeed the actual difference between the last two entries was less than 0.001%. However, as M Da decreases, more eigenvalues are needed to get a reasonably accurate solution. As the number eigenvalues increases, the algebraic steps would require a higher degree of precision in order to avoid relatively large round-off errors. As an illustration, when $M\,\mathrm{Da}=10^{-5}$, using 36, 55, and 78 eigenvalues produced $\mathrm{Nu}_D=4.860$, 4.882, and 4.893 while the corresponding value for slug flow is 4.935. Accordingly, the entries in Table 4 are expected to have smaller errors as M Da increases. Similar to Table 2, the first row in Table 4 is for free flow, the last row is for slug flow, and the last column is for the parallel plate channels.

5 Conclusion

For hydrodynamically fully developed flow, the velocity in rectangular passages is readily available as a function of y and z. However, in the thermal entrance region, the computation of the heat transfer coefficient becomes more demanding since temperature depends on x, y, and z. Accordingly, the common practice is to obtain the entrance heat transfer data using an approximate numerical technique. Therefore, these acquired data can serve as a tool to verify the accuracy of the entrance flow solutions when the thermal condition becomes fully developed.

An exact solution for the fully developed temperature field in a rectangular duct filled with porous material is obtainable for H1 and H2 cases using the classical separation of variable technique. The solutions, for the cases studied, indicate higher Nu_D values as M Da decreases. The value of the Nusselt number, for the H2 case, increases by a factor that approaches 2 as M Da decreases. Moreover, the definition of the Nusselt number includes the effective thermal conductivity k. The increase in k becomes substantial when the porous matrix is composed from metal foam with a relatively high thermal conductivity. In such a case, the effective thermal conductivity can become significantly larger than that for the fluid, e.g., air. This can lead to a significant enhancement of the heat transfer coefficient for applications such as electronic cooling.

Nomenclature

A = area, m^2
a = duct dimension, m, see Fig. 1
a_{mn} = coefficients
b = duct dimension, m, see Fig. 1
C = circumference, m
c_{mn} = coefficients
c_p = specific heat, J/kg K
Da = Darcy number, $\mathrm{K/H}^2$
D_h = hydraulic diameter, m
h = average heat transfer coefficient, $\mathrm{W/m}^2\,\mathrm{K}$
i,j = indices
K = permeability, m^2
k = effective thermal conductivity
M = μ_e/μ
m,n = indices
Nu_D = Nusselt number hD_h/k_e
p = pressure, Pa
q_w = wall heat flux, $\mathrm{W/m}^2$
$\overline{q_w}$ = circumferentially averaged wall heat flux, $\mathrm{W/m}^2$
T = temperature, K
T_w = wall temperature, K
U = average velocity, m/s
$\overline{U}$ = average value of $\overline{u}$
u = velocity, m/s
$\overline{u}$ = $\overline{u}=\mu u/(\Phi H^2)$
x = axial coordinate, m
y,z = coordinates, m
$\overline{y},\overline{z}$ = y/a and z/a

Greek

β_j = eigenvalues
γ_j = eigenvalues
θ = dimensionless temperature
θ^* = θ for slug flow, see Eq. (14*a*)
μ = fluid viscosity, $\mathrm{N\,s/m}^2$
μ_e = effective viscosity, $\mathrm{N\,s/m}^2$
ρ = density, $\mathrm{kg/m}^3$
Φ = $-\partial p/\partial x$
Ψ = reduced temperature solution, see Eq. (19*a*)
ω = $1/\sqrt{M\ \mathrm{Da}}$

Subscripts

b = bulk
w = wall

References

[1] Nield, D. A., and Bejan, A., 1999, *Convection in Porous Media*, 2nd ed., Springer-Verlog, New York.
[2] Kaviany, K., 1991, *Principles of Heat Transfer in Porous Media*, Springer-Verlag, New York.
[3] *Handbook of Porous Media*, 2000, K. Vafai, ed., Marcel Dekker, New York.
[4] Nield, D. A., Kuznetsov, A. V., and Xiong, M., 2002, "Effect of Local Thermal Non-equilibrium on Thermally Developing Forced Convection in a Porous Medium," Int. J. Heat Mass Transfer **45**(25), pp. 4949–4955.
[5] Haji-Sheikh, A., Minkowycz, W. J., and Sparrow, E. M., 2004, "Green's Function Solution of Temperature Field for Flow in Porous Passages," Int. J. Heat Mass Transfer, **47**(22), pp. 4685–4695.
[6] Haji-Sheikh, A., Minkowycz, W. J., and Sparrow, E. M., 2004, "A Numerical Study of the Heat Transfer to Fluid Flow through Circular Porous Passages," Numer. Heat Transfer, Part A, **46**(10), pp. 929–956.
[7] Haji-Sheikh, A., Sparrow, E. M., and Minkowycz, W. J., 2005, "Heat Transfer to Flow Through Porous Passages Using Extended Weighted Residuals Method–A Green's Function Solution," Int. J. Heat Mass Transfer, **48**(7), pp. 1330–1349.
[8] Nield, D. A., Kuznetsov, A. V., and Xiong, M., 2003, "Thermally Developing Forced Convection in a Porous Medium: Parallel Plate Channel With Walls at Uniform Temperature, With Axial Conduction and Viscous Dissipation Effects," Int. J. Heat Mass Transfer **46**(4), pp. 643–651.
[9] Kuznetsov, A. V., Nield, D. A., and Xiong, M., 2003, "Thermally Developing Forced Convection in a Porous Medium: Circular Ducts With Walls at Constant Temperature, With Longitudinal Conduction and Viscous Dissipation Effects," Transp. Porous Media, **53**(3), pp. 331–345.
[10] Sparrow, E. M., and Siegel, R., 1959, "A Variational Method for Fully Developed Laminar Heat Transfer in Ducts," J. Heat Transfer, **81**(2), pp. 157–167.
[11] Kays, W. M., and Crawford, M. E., 1993, *Convective Heat and Mass Transfer*, McGraw-Hill, New York.
[12] Kays, W. M., and Perkins, H. C., 1973, "Forced Convection, Internal Flow in Ducts," Sec. 7, *Handbook of Heat Transfer*, W. M. Rohsenow, and J. P. Hartnett, eds., McGraw-Hill, New York.
[13] Wolfram, S., 1999, *The Mathematica Book*, 4th ed., Cambridge University Press, Cambridge, UK.

Heat Transfer in a Surfactant Drag-Reducing Solution—A Comparison With Predictions for Laminar Flow

Paul L. Sears
e-mail: psears@nrcan.gc.ca

Libing Yang

Natural Resources Canada,
CANMET Energy Technology Centre-Ottawa,
1 Haanel Drive,
Nepean, ON K1A 1M1, Canada

Heat transfer coefficients were measured for a solution of surfactant drag-reducing additive in the entrance region of a uniformly heated horizontal cylindrical pipe with Reynolds numbers from 25,000 to 140,000 and temperatures from 30 to 70°C. *In the absence of circumferential buoyancy effects, the measured Nusselt numbers were found to be in good agreement with theoretical results for laminar flow. Buoyancy effects, manifested as substantially higher Nusselt numbers, were seen in experiments carried out at high heat flux.* [DOI: 10.1115/1.2188462]

Keywords: heat transfer, drag-reducing additive, surfactant, buoyancy effects, laminar flow

1 Introduction

Research on the properties of drag-reducing (DR) agents in aqueous solutions generally has, as its aim, the use of these materials to reduce pumping costs or increase system capacity in district heating systems. Drag-reducing agents may also find application in smaller installations, such as building hydronic heating systems. The properties of the solutions are such that flow friction may be reduced by 80% compared with that expected in water. Heat transfer is also affected, being severely compromised in some forms of heat exchanger [1].

Drag-reducing agents function at Reynolds numbers of about 10,000–100,000. Turbulent flow would be expected in this range, and other authors have described the conditions as turbulent, even though measured drag may be much lower than expected for fully turbulent flow [2,3]. The reductions in drag and heat transfer caused by surfactants are ascribed to damping of the turbulence by micelles that form in the solutions. The detailed mechanisms by which drag reducing agents inhibit heat and momentum transfer have also been studied by direct numerical simulation [4] and laser Doppler velocimetry coupled with measurement of temperature fluctuation [5].

Our work is proceeding in two main areas: testing the fundamental properties of solutions of drag-reducing agents in well controlled but relatively artificial situations and using them in conventional heating system circuits. For the first task, a test loop was constructed in which heat transfer coefficients were measured between an electrically heated tube and the liquid flowing within. Measured results in turbulence-suppressed flow for heat transfer in the entrance region were then compared with a theoretical model obtained through a detailed literature search. This paper describes the results of this work.

2 Experimental Setup

A schematic diagram of the drag-reducing experimental loop is shown in Fig. 1. Thin-walled Inconel pipe was selected for the test section because of its higher electrical resistivity compared with stainless steel. The pipe in the test section was 17.5 mm ID (internal diameter), with a wall thickness of 0.89 mm. The remaining pipe in the test loop was the stainless steel with the same ID.

Testing was undertaken using a closed loop piping system. A variable speed pump was installed to circulate the test fluid. The test section was 3.5 m long and located downstream of a 6 m (342 diameter) straight segment of piping to ensure fully developed flow at the entrance of the test section. A long length of straight pipe was also installed after the variable speed pump, although previous research [1,6,7] suggested that this may not have been necessary since the use of a centrifugal pump did not cause noticeable degradation effects to surfactant solution. The entire test loop was thermally insulated in order to reduce heat loss from the system to the atmosphere. Heat transfer was measured under constant heat flux conditions. The heat source used was a dc power generator with a maximum 10 kWe output. Calibration of the voltage and current measurement indicated the output power was accurate to within ±5%. The test section was electrically insulated from the rest of the stainless steel loop by two Teflon gasket connections. A tank having a volume of 28 L was installed as a reservoir and temperature fluctuation damper for the test fluid. The test fluid itself was cooled using city water via a brazed plate heat exchanger.

Instruments in the test loop were interfaced with a Honeywell controller and data acquisition system using PlantScape software that enabled the control to be automated. A conventional PID (proportional, integral, derivative) control loop was used to control the test fluid temperature leaving the heat exchanger at the desired value by adjusting the city water cooling flow through the plate heat exchanger by means of a pneumatically controlled valve. A second PID controller was introduced to control the electrical power input to the test section. A third PID controller was used to control the pump speed, and thus set the fluid velocity. The set points of these three controlled values could be adjusted through a remote computer.

Three resistance temperature detectors (RTDs) were inserted through the pipe and into the test fluid to measure the bulk temperature: one 6 m upstream of the test section, one at the inlet of the plate heat exchanger, and one at the outlet of the plate heat exchanger.

Steiff [1] and Groth [8] stated that surfactant solution has little effect on the accuracy of magnetic flowmeters, while it may affect the performance of turbine, impeller and vortex-shedding flowmeters. For this reason, a Clorius magnetic volume and energy meter

Contributed by the Heat Transfer Division of ASME for publication in the JOURNAL OF HEAT TRANSFER. Manuscript received November 30, 2004; final manuscript received December 22, 2005. Review conducted by Phillip M. Ligrani.

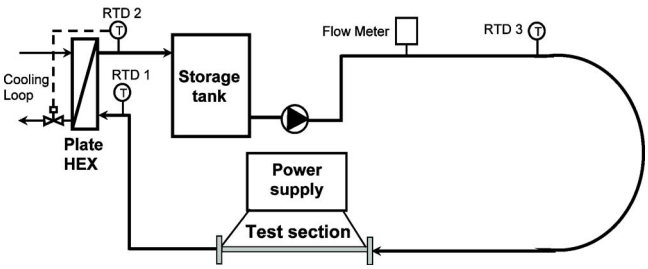

Fig. 1 Schematic diagram of experimental test loop

was used to measure the flow rate. The maximum capacity of the flowmeter was 3.6 m^3/h. Calibration of the flowmeter by Bellamy indicated that it was accurate to within ±0.5% [9].

Figure 2 shows a diagram of the experimental test section. The outer wall temperatures of the test pipe, needed for the heat transfer calculations, were measured by 16 surface platinum RTDs 7–195 diameters from the inlet. The surface RTDs were mounted on the top of the pipe. Three additional RTDs were mounted on the middle side of the pipe at 11.7, 41.8 and 122.0 diameters to compare the temperature difference between the top and side and thereby to evaluate buoyancy effects.

Each surface RTD was calibrated after connection to the Honeywell controller and data acquisition system. In this way, the offset found accounts for the errors introduced by RTD, wires and Honeywell acquisition system. The individual offset was used to correct readings of the corresponding RTD to compensate for the introduced errors. The standard deviation from the mean value of all surface RTDs after offset correction was 0.1°C, when the fluid was circulated at room temperature, 23°C, and high velocity, 3.0 m/s.

Sixteen pressure tap holes (2 mm diameter) were drilled and de-burred in the Inconel test section pipe 10–140 diam downstream of the test section inlet. Pressure taps were connected by clear plastic tubing to a pressure transducer calibrated to measure pressure differences up to 10 kPa. The connection was arranged to measure the pressure differences between points 1–2, 1–3, and up to 1–16. Each point could be read in turn by using isolation valves fitted to the plastic tubing. Manufacturer's specifications give the accuracy of the transducer as ±0.5% of full range.

Measured experimental data, including pressure drops, temperatures, electrical input power, and flow rate were recorded by the Honeywell data acquisition system and stored in the computer.

3 Experimental Material and Experimental Runs

The cationic surfactant used in the experiments was Ethoquad O/12 PG provided by Akzo Nobel Chemicals. This surfactant belongs to the N-alkyl quaternary ammonium family with a chemical name of N.N-bis(2-hydroxyethyl-N-methyl-9-octadecen-1-aminium) chloride. It is supplied in a 1,2-propanediol solvent. The DR solution contained a concentration of 2000 ppm surfactant

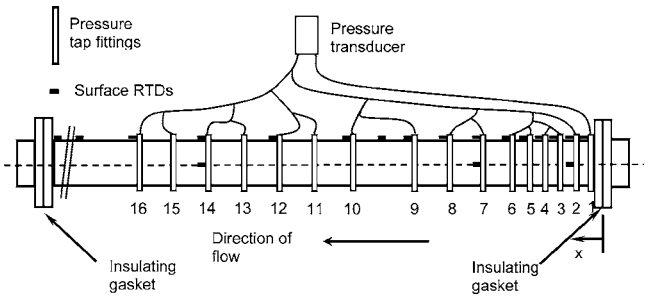

Fig. 2 Schematic diagram of experimental test section

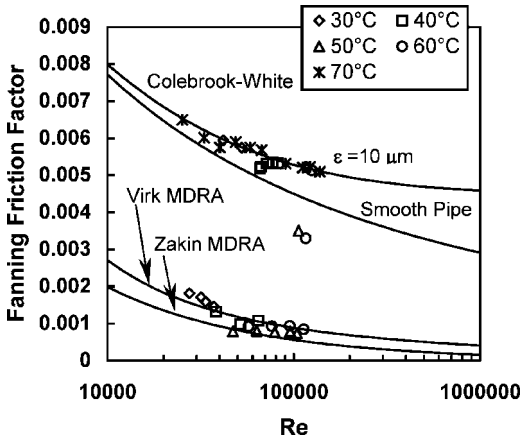

Fig. 3 Fanning friction factor versus solvent Reynolds number at various fluid temperatures for Ethoquad O/12 PG (2000 ppm)

plus 2000 ppm sodium salicylate (HOC_6H_4COONa) to provide salicylate counterion, in reverse osmosis purified water.

Experimental runs were carried out at temperatures from 30 to 70°C and fluid velocities from 0.56 to 3.5 m/s, thus straddling normal velocities of heat transfer liquids in pipes. The aim was to investigate the drag reduction and the heat transfer reduction behavior of the surfactant solution. The velocity increment was deliberately reduced in the range of transition from turbulence-suppressed region to turbulent region in order to find critical Reynolds number at each temperature. Three heat fluxes, 2.36, 4.72, and 23.6 kW/m^2 were applied in the experiments. The highest heat flux, 23.6 kW/m^2, was higher than the normal heat transfer rate in a plate heat exchanger in space heating application, but it is readily achievable in domestic hot water application. The solution was about four months old when these experimental runs were performed.

The reduction of drag that occurs in these solutions is believed to be a phenomenon of turbulent flow [2,3]. In this paper we describe this regime as turbulence suppressed, in order to distinguish it from the conditions under which drag-reducing effects disappeared and from true laminar flow.

4 Experimental Uncertainty

A propagation of error analysis was done to determine the uncertainty in the measured friction factor and Nusselt number. The uncertainty for the friction factor was within ±17%. The uncertainty for the Nusselt number in the turbulence-suppressed region was ranged from a low of ±5% at the highest heat flux ($23.6\ kW/m^2$) to a high of ±20% at the lowest heat flux ($2.36\ kW/m^2$). Because of small wall-to-bulk temperature difference in the turbulent flow region, only the high heat flux ($23.6\ kW/m^2$) was applied in the experiments when flow became fully turbulent. The uncertainty of the Nusselt number for this case was estimated at ±20% for Reynolds numbers up to 100,000. Beyond this point, the temperature difference was so small that errors increased rapidly.

5 Experimental Results

5.1 Drag Reduction. Based on pressure drop and flow rate measurements, it was possible to calculate Fanning friction factors and they are plotted versus Reynolds number in Fig. 3. Also plotted in Fig. 3 are Virk's [10] limiting maximum drag reduction asymptote (MDRA) for polymer Eq. (1) and Zakin's [11] MDRA for surfactant Eq. (2).

$$\frac{1}{f_f^{1/2}} = 19 \log_{10}(\mathrm{Re}\, f_f^{1/2}) - 32.4 \tag{1}$$

$$f_f = \frac{1.26}{4}\,\mathrm{Re}^{-0.55} \tag{2}$$

The drag reduction is based on the reference case given by the Colebrook–White equation [12] for a Newtonian fluid. Equation (3) is an explicit expression of the Colebrook–White equation developed by Chen [12], which is in good agreement with Colebrook–White with the maximum deviation being −0.39%. The Colebrook–White curve is also plotted in Fig. 3 as a reference

$$\frac{1}{f_f^{1/2}} = 3.48 - 1.7372 \ln\left(\frac{\varepsilon}{R_i} - \frac{16.2426}{\mathrm{Re}} \ln A\right) \tag{3}$$

where ε is the roughness of the pipe and

$$A = \frac{(\varepsilon/R_i)^{1.1098}}{6.0983} + \left(\frac{7.149}{\mathrm{Re}}\right)^{0.8981}$$

Calculating a Reynolds number to reflect the conditions of an experiment is somewhat problematic because the viscosity of the solution is shear dependent. The solvent (water) viscosity was therefore used in Reynolds number calculation for simplicity and availability. This method is quite common in drag-reduction or heat transfer calculations particularly for practical purposes, although it would be more appropriate to use measured viscosity when calculating the Reynolds and Prandtl numbers for drag-reducing solutions and especially for surfactants [2,13].

Figure 3 shows that at all temperatures except 70°C the friction factors follow Zakin's maximum drag-reduction asymptote until finally the drag reduction vanishes at high Reynolds number, where the critical wall shear stress is exceeded. During the transition from the turbulence-suppressed region to the turbulent region, the experimental friction factors lie between values predicted by Zakin's MDRA and Colebrook–White's curves. The experimental friction factors then fit very well with Colebrook–White's curve for Newtonian fluids assuming a pipe roughness (ε) of 10 μm. This may be taken to be the net effect of the roughness of the pipe and that caused by the pressure tap holes along the test section.

Many surfactants have been reported as having different available temperature ranges, over which their friction reducing properties are observed [14–17]. This range can also be observed in Fig. 3 for the DR surfactant (Ethoquad O/12 PG). The drag reduction is seen to increase with increasing temperature to a maximum at 50°C. Above this temperature the drag-reduction effect is diminished at 60°C and finally disappears at 70°C.

For theoretical analysis, Gasljevic [2] suggested that the drag-reduction effect be quantified by a relative reduction difference between laminar and turbulent flows. For practical purposes, however, the drag reduction is often defined as the difference between the values of friction factor for water and the surfactant solution at the same Reynolds number, divided by the value for water. This parameter compares directly the levels of friction with and without drag-reducing effects.

$$DR(\%) = \frac{f_w - f_s}{f_w} \times 100 \tag{4}$$

The above simple term was used in this study to calculate the percentage of drag reduction, since our interest was to identify the pressure drop or heat transfer reduced by the introduction of an additive in the solvent (water). The friction factor for the water was calculated by the Colebrook–White equation, Eq. (3), for fully developed turbulent flow with $\varepsilon = 10$ μm.

Figure 4 shows the drag reduction versus Reynolds number at different test temperatures. The results show that the drag reduction was between 70 and 85% before the critical wall shear stress was reached. This occurred at different Reynolds numbers for different fluid temperatures: about 40,000 at 30°C, 65,000 at 40°C and 100,000 at 50°C and 60°C. At these last two temperatures the drag reduction had not entirely disappeared at the highest Reynolds numbers achieved. The drag reduction disappeared completely at a fluid temperature of 70°C.

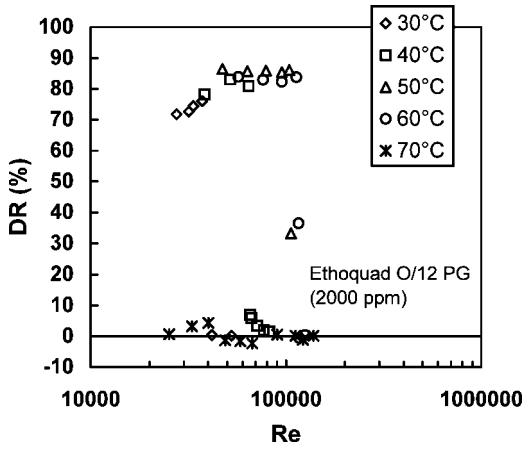

Fig. 4 Drag reduction as a function of solvent Reynolds number at various fluid temperatures

Experimental runs were repeated for several randomly selected temperatures and velocities eight months after the solution was prepared. It was found that there was only slight degradation (DR reduced approximately 3% on average) compared with the fresh solution. The experimental results also indicated good repeatability.

5.2 Heat Transfer Reduction. Heat transfer reduction for the drag-reducing surfactant solution was defined by

$$HTR(\%) = \frac{\mathrm{Nu}_w - \mathrm{Nu}_s}{\mathrm{Nu}_w} \times 100 \tag{5}$$

Based on the fluid bulk temperature and surface temperature measurements, it was possible to calculate the convective heat transfer coefficient and Nusselt number inside the pipe and thereby calculate the heat transfer reduction. The local Nusselt number at distance x along the test section was calculated by

$$\mathrm{Nu}_s = \frac{Q}{2\pi r_i L(T_{w,i} - T_{b,x})} \times \frac{D_i}{k} \tag{6}$$

The inner wall temperature, $T_{w,i}$, was calculated from the measured outer wall surface temperature by applying a zero heat flux boundary condition, i.e., all energy transferred to the inside of the tube. Calculations of heat losses under experimental conditions indicated that losses to the surroundings were less than 3% of the power applied even at the highest temperature used. The local bulk fluid temperature at distance x along the test section, $T_{b,x}$, was calculated from the inlet temperature measured by insertion RTD 3 (Fig. 1), applied heat flux and flow.

The Gnielinski correlation Eq. (7) was used in [12] as the basis of comparison for all the correlations for fully developed turbulent flow, because overall it was in best accord with the experimental data.

$$\mathrm{Nu} = \frac{(f_f/2)(\mathrm{Re} - 1000)\mathrm{Pr}}{1 + 12.7(f_f/2)^{1/2}(\mathrm{Pr}^{2/3} - 1)} \tag{7}$$

A simplified Gnielinski correlation [12] was used to calculate the Nusselt number for water, Nu_w.

$$\mathrm{Nu}_w = 0.012(\mathrm{Re}^{0.87} - 280)\mathrm{Pr}^{0.4} \tag{8}$$

The above correlation is for $1.5 \leqslant \mathrm{Pr} \leqslant 500$ and $3000 \leqslant \mathrm{Re} \leqslant 10^6$, where it agrees with Eq. (7) within ±10%.

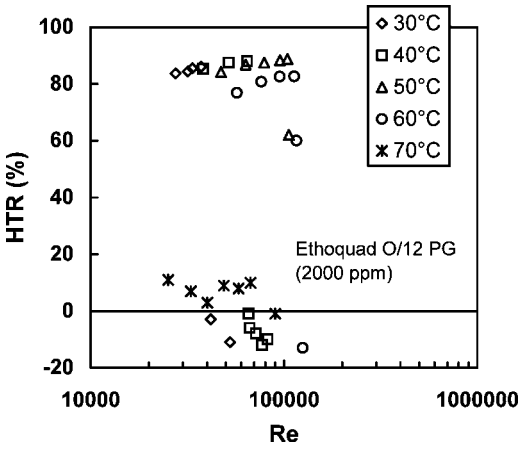

Fig. 5 Heat transfer reduction as a function of solvent Reynolds number at various fluid inlet temperatures. The heat flux was constant at 23.6 kW/m^2.

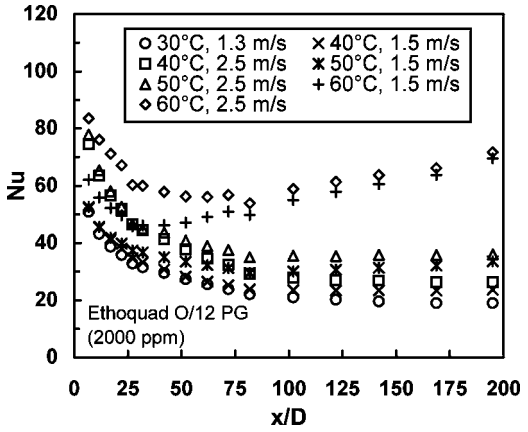

Fig. 6 Experimental Nusselt number as a function of axial distance at various fluid inlet temperatures and velocities in turbulence-suppressed region. The heat flux was constant at 23.6 kW/m^2.

Figure 5 shows the heat transfer reduction as a function of solvent Reynolds number at various fluid inlet temperatures. The Nusselt number of the surfactant was the mean of those calculated from the temperature measurements along the test pipe while the Nusselt number for water was calculated using Gnielinski's correlation Eq. (8).

Figure 5 indicates that the heat transfer reduction was between 80 and 90% before the critical wall shear stress was reached. The heat transfer reduction was greater than the drag reduction for experiments at lower Reynolds numbers (20,000–40,000), and comparable with it for Reynolds numbers of 50,000 up, which contrasts somewhat with the results of Gasljevic for Ethoquad T13, for which the heat transfer reduction was always significantly greater [2,18]. Heat transfer reduction and drag reduction both disappeared at 70°C. It should be noted that precision of measurement of the heat transfer reduction is much better for experiments where the flow is in the turbulence-suppressed region (where the heat transfer reduction is high) than in the turbulent region (where there is little or no heat transfer reduction). See Sec. 4.

5.3 Comparisons of Heat Transfer Results with Theoretical Model. The thermal entrance region is the length of pipe where the radial temperature profile is being established. In this experiment, it spanned the entire test section because of the turbulence-suppressed flow. Theoretical solutions for the thermal entrance region have usually been developed for Newtonian fluid with no circumferential buoyancy effect. In the turbulent region, empirical correlations have also been developed based on the experimental results from work using Newtonian fluid.

Gasljevic et al. [19] found two effects of buoyancy under turbulence-suppressed flow conditions: a distortion of the temperature profile (or circumferential variation of local convective heat transfer), and a change in the average Nusselt number compared with the flow without buoyancy. The local variation in the fluid density is seen to lead to a secondary flow pattern, which is superimposed on the main axial flow. These buoyancy effects are larger at the same GrPr number than those observed with Newtonian fluids. Gasljevic estimated that buoyancy effects may increase the Nusselt number for drag-reducing viscoelastic fluids to a level 50% greater than that of the expected theoretical value with no buoyancy effects, whereas only a 12% difference is expected under the same conditions for Newtonian fluids [19].

It is, therefore, of great interest to compare the Nusselt numbers for viscoelastic surfactant fluids with those calculated from theoretical models (or empirical correlations) for inelastic ones at similar heat and flow rate conditions.

5.3.1 Heat Transfer in Turbulence-Suppressed Region

5.3.1.1 Experimental heat transfer results. Figure 6 shows local Nusselt numbers obtained at various fluid inlet temperatures and velocities. The flow at the entrance to the test section was in the turbulence-suppressed region for each experiment with the exception of that carried out at 60°C and 2.5 m/s velocity. In this case, the flow was at the upper limit of the turbulence-suppressed region, and was already becoming turbulent.

For the lowest entrance temperatures (30 and 40°C), the Nusselt number decreased over the entire length of the test section. For higher entrance temperatures, it can be seen that the Nusselt number flattened and then began to rise after an initial fall. In general, one would expect these Nusselt numbers to decrease throughout the entrance region and then stabilize. The reason for the behavior observed here becomes evident when Fig. 7 is examined—when the wall temperature exceeds a little over 70°C, the heat transfer increases in such a way as to limit the wall temperature. The drag reducing agent ceases to function in the outermost layer of liquid, turbulent flow sets in in this layer, and

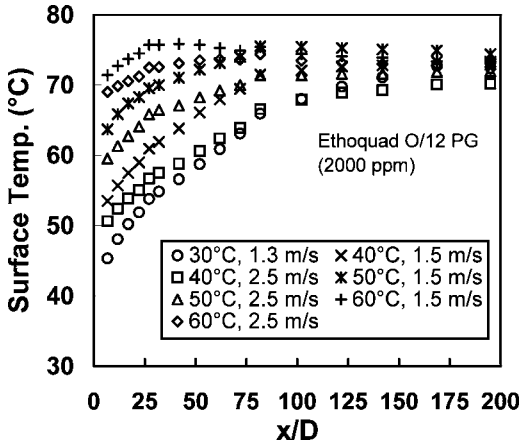

Fig. 7 Measured outer-wall surface temperatures along the test section at various fluid inlet temperatures and velocities in turbulence-suppressed region. The heat flux was constant at 23.6 kW/m^2.

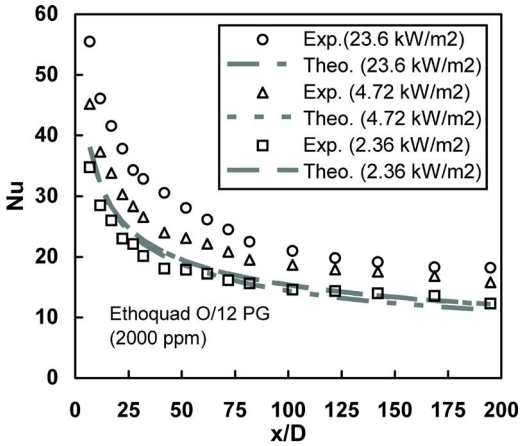

Fig. 8 Nusselt number as a function of axial distance at a fluid inlet temperature of 30°C and velocity of 1.5 m/s at various heat fluxes. Dashed lines are theoretical values.

Nusselt numbers rise.

Temperature measurements also showed that the wall-to-bulk temperature difference, at the end of the test section, ranged from 38.9°C at fluid inlet temperature 30°C, to 9.7°C at fluid inlet temperature 60°C with an applied heat flux of 23.6 kW/m^2. Over the length of the test section, the fluid bulk temperature increased by about 3.2°C at a velocity of 1.5 m/s and about 1.9°C at a velocity of 2.5 m/s with the same heat flux (23.6 kW/m^2).

5.3.1.2 Theoretical model. Differential equations are well known tools for modeling the heat transfer in laminar flow (for Newtonian fluids) in the entrance region of a semi-infinite pipe with constant wall heat flux. Analytical solutions do not exist, but the Nusselt number can be derived from summation of a series of terms (eigenvalues and constants) [20]. Based on Graetz-type and Leveque-type solutions for the constant heat flux thermal entrance length problem, the local Nusselt numbers can be computed from [20]:

For $x^* \leq 0.00005$

$$\mathrm{Nu} = 1.302x^{*(-1/3)} - 1 \tag{9}$$

For $0.00005 \leq x^* \leq 0.0015$

$$\mathrm{Nu}_x = 1.302x^{*(-1/3)} - 0.5 \tag{10}$$

For $x^* \geq 0.0015$

$$\mathrm{Nu}_x = 4.364 + 8.68(10^3 x^*)^{-0.506} e^{-41x^*} \tag{11}$$

where: $x^* = x/D_i/\mathrm{Re}\,\mathrm{Pr}$

5.3.1.3 Comparisons of heat transfer results. The Nusselt numbers (in the turbulence-suppressed region) calculated from the experimental data, Eq. (6), were then compared with those calculated by the theoretical equations, Eqs. (9)–(11). The Re and Pr numbers used for determining x^* required by Eqs. (9)–(11) were based on inner wall temperature at each temperature measuring location of the test section. It should be noted that the theoretical equations are for a Newtonian fluid with no buoyancy effect. Experimental runs with fluid inlet temperature 30°C at velocity of 1.5 m/s and three heat fluxes are compared in Fig. 8.

The difference between experimental and theoretical Nusselt number was always within ±12% at a heat flux of 2.36 kW/m^2 and from 17 to 32% at a heat flux of 4.72 kW/m^2. However, at the highest heat flux, 23.6 kW/m^2, the experimental Nusselt numbers were 40–60% higher than the theoretical values. Comparisons for other experimental runs at other velocities, with 23.6 kW/m^2 heat flux and 30°C fluid inlet temperature, show similar differences.

Table 1 Measured surface temperature difference between top and midside of test pipe at various heat fluxes

	ΔT (°C) = T_{top}-T_{side}		
	x/D=11.7	x/D=41.8	x/D=122.0
Heat Flux	30 °C, 1.5 m/s		
23.6 kW/m^2	0.2	2.0	6.4
4.72 kW/m^2	-0.1	0.6	0.6
2.36 kW/m^2	-0.1	0.5	0.2
	40 °C, 1.5 m/s		
23.6 kW/m^2	0.0	1.9	2.7
	50°C, 2.0 m/s		
23.6 kW/m^2	0.1	0.3	0.0
4.72 kW/m^2	0.1	0.4	0.6
	60°C, 1.5 m/s		
23.6 kW/m^2	0.0	0.5	0.0

The theoretical Nusselt values at different heat fluxes are similar, as shown in Fig. 8, therefore it is very difficult to distinguish the three gray dashed lines in the figure. This was because the three experimental conditions had identical velocity and inlet temperatures. Only the temperatures downstream differed, because of the different heat flux used in experiments. However, the experimental Nusselt numbers were reduced on reducing the heat flux.

5.3.1.4 Buoyancy effect on experimental heat transfer results. The higher experimental Nusselt number at the high heat flux (23.6 kW/m^2) is almost certainly due to the buoyancy effects discussed by Gasljevic et al. [19]. The local variations in the fluid density lead to a secondary flow pattern, which is superimposed on the main axial flow. Gasljevic [19] found a temperature difference of 1.8°C between top and bottom at a flow distance of 675 diameters and a bulk fluid temperature of 22°C. The average Nusselt number, calculated by three wall-to-bulk (top, middle and bottom) temperature differences, was 53% higher than its theoretical value (Nu=4.36) with no buoyancy effects [19].

In order to reduce the buoyancy effect on the measurements, the authors of [19] suggested using relatively low heat flux. If that is not convenient or feasible, a temperature sensor placed on the side of the pipe at the mid-elevation should be used, since it will give a good approximation of the average Nusselt number between top and bottom measurements.

For this reason, three RTDs were mounted at mid-elevation at 11.7, 41.8 and 122.0 diameters to investigate the buoyancy effect on our experiments. Table 1 shows the comparison of surface temperatures at various heat fluxes.

Table 1 shows that the temperature differences between the top and side were negligible near the entrance, even at high heat flux. However, the difference increased considerably with the axial distance at high heat flux and low fluid inlet temperature (30 and 40°C). One explanation is that the wall-to-bulk temperature difference increased with the axial distance and that the secondary flow pattern induced by the fluid density variations became stronger. For fluid inlet temperatures of 30 and 40°C at a heat flux of 23.6 kW/m^2, the surface temperature difference reached 6.4 and 2.7°C at 122 diameters, respectively. This temperature difference resulted in a calculated Nusselt number difference of 22.8% for 30°C and 10.2% for 40°C.

The surface temperature difference between the top and side was insignificant at $x/D=122$ at fluid inlet temperature of 50 and 60°C even with a high heat flux (23.6 kW/m^2). This was mainly because at this high heat flux the surface temperature exceeded 70°C at $x/D>80$ and the surfactant lost its drag reduction effects at this temperature. Consequently, turbulence (mixing) occurred near the wall area, which reduced the temperature difference.

Table 1 also indicates that the temperature difference between the top and midside is relatively small, all within 0.7°C, for the experiments performed at lower heat flux. This means the buoy-

ancy effect was reduced at low heat flux because the difference between the wall and bulk fluid temperature was also reduced. It was also observed, at low heat flux, that the surface temperature did not drop at $x/D>80$ since it was well below 70°C and the surfactant did not lose its drag reduction effect.

Based on the experimental results for Ethoquad T13/27, Gasljevic [19] found that the effects of buoyancy do not seem to be important for values of GrPr/Re less than about 3. However, the authors [19] pointed out that this criterion may have some limitation since only one fluid was used.

To test this criterion for the surfactant (Ethoquad O/12 PG) used in the current study, the GrPr/Re numbers were computed based on the experimental data for the three runs at 30°C and various heat fluxes shown in Fig. 8. The GrPr/Re number ranged from 8.8 to 29.7 at a heat flux of 23.6 kW/m^2 and from 1.9 to 6.2 at a heat flux of 4.76 kW/m^2 along the test section. For the heat flux of 2.36 kW/m^2, the GrPr/Re number was between 1.0 and 3.3 along the test section. The experimental Nusselt number for the last case had the best agreement with the theoretical value (with a difference within ±12%).

Similar comparisons were also made for experimental runs with fluid inlet temperature of 50°C. The experimental Nusselt numbers at a velocity of 2.0 m/s at a relatively low heat flux (4.72 kW/m^2) were from 18 to 36% higher than the theoretical ones (GrPr/Re number from 1.6 to 5.0). However, at high heat flux (23.6 kW/m^2), the experimental Nusselt numbers were 53–80% higher than the theoretical values for $0<x/D<80$ (GrPr/Re number from 7.3 to 15.3), and up to 148% higher at locations after 80 diameters ($GrPr/Re>16$). The high deviation after 80 diameters at high heat flux was again because the surfactant lost its drag reduction effects at 70°C and turbulence (mixing) occurred and the Nusselt number increased.

For experimental runs at 40 and 60°C, the experimental Nusselt numbers at high heat flux (23.6 kW/m^2) were also more than 50% higher than the theoretical ones when the drag-reducing solution was in the effective temperature range. In all these cases, the GrPr/Re number was well above 3.5 (typically 10–25) along the entire length of the test section. The results further support the criterion suggested by Gasljevic [19], that for values of GrPr/Re less than about 3 the effects of buoyancy are not important.

6 Conclusions

A series of experiments has been performed at various fluid inlet temperatures and velocities for drag-reducing surfactant Ethoquad O/12 PG solution (2000 ppm).

It was found that the drag reduction ranged from 70 to 85% before the critical wall shear stress was reached. The drag reduction increased with increasing fluid temperature and reached maximum effectiveness at 50°C. The drag reduction effect diminished at 60°C and finally disappeared at approximately 70°C. Along with the drag reduction, the heat transfer coefficients were also reduced. The experimental results showed that the heat transfer coefficient reduction was similar to or greater than the drag reduction. It ranged from 80 to 90%.

The Reynolds numbers at which these experiments were carried out are such that turbulent flow would be expected. Other authors have referred to such conditions as turbulent flow, and have indicated that the turbulence may be damped or partially suppressed by the action of the drag-reducing agent. It was nevertheless found that the heat transfer coefficients measured at low heat fluxes were well matched to the theoretical predictions for laminar flow (with a difference within ±12%). It would seem that the damping of the turbulence achieved by the drag-reducing additives is sufficient that the flow may, for practical purposes, be regarded as laminar as far as heat transfer is concerned. Recent work [4] has shown that turbulent heat transfer perpendicular to the wall is reduced to a small fraction of that expected for the fluid without drag reducing agent, and that the effect is most marked near the wall, where the temperature gradient is greatest. This is consistent with our results.

At high heat flux in this turbulence-suppressed flow, the experimental Nusselt numbers were more than 50% higher than the theoretical predictions. The higher Nusselt number was mainly a result of a buoyancy effect. The higher the heat flux, the stronger the buoyancy effect (higher GrPr/Re number) on the drag-reducing fluid. In order to reduce the buoyancy effect on the heat transfer measurements relatively low heat flux should be applied. For the current study it corresponded to GrPr/Re number less than 3.5, which supported the criterion suggested by Gasljevic [19] for evaluating the buoyancy effects.

Acknowledgment

The authors would like to gratefully acknowledge the support of this work by the Program on Energy Research and Development (PERD) of the Government of Canada and the donation of surfactant samples by Akzo Nobel (U.S.).

Nomenclature

- D = pipe diameter, m
- DR = drag reduction, %
- f = friction factor
- Gr = Grashof number based on diameter, $Gr=g\beta D^3\Delta T/\nu^2$
- HTR = heat transfer reduction, %
- h = heat transfer coefficient, $W/m^2\,K$
- k = thermal conductivity, W/m K
- L = pipe length, m
- Nu = Nusselt number, $Nu=h\cdot D_i/k$
- Pr = Prandtl number, $Pr=\nu/\alpha$
- Q = input electrical power, W
- R = radius of pipe, m
- Re = Reynolds number, $Re=u\cdot D_i/\nu$
- T = temperature, °C
- u = fluid velocity, m/s
- x = axial distance from pipe inlet, m

Greek Symbols

- α = thermal diffusivity, m^2/s
- ε = roughness of a pipe, m
- ν = kinematic viscosity, m^2/s

Subscripts:

- b = bulk
- f = Fanning
- i = inner
- s = surfactant
- w = water or pipe wall
- x = local

References

[1] Steiff, A., and Kloepper, K., 1996, "Application of Drag Reducing Additives in District Heating Systems," FED (Am. Soc. Mech. Eng.), **237**(2), pp. 235–242.

[2] Gasjevic, K., and Matthys, E. F., 1999, "Improved Quantification of the Drag Reduction Phenomenon Through Turbulence Reduction Parameters," J. Non-Newtonian Fluid Mech., **84**, pp. 123–130.

[3] Aguilar, G., Gasjevic, K., and Matthys, E. F., 2001, "Asymptotes of Maximum Friction and Heat Transfer Reductions for Drag-Reducing Surfactant Solutions," Int. J. Heat Mass Transfer, **44**, pp. 2835–2843.

[4] Yu, B., and Kawaguchi, Y., 2005, "DNS of Fully Developed Turbulent Heat Transfer of a Viscoelastic Drag-reducing Flow," Int. J. Heat Mass Transfer, **48**, pp. 4569–4578.

[5] Li, F. C., Kawaguchi, Y., and Hishida, K., 2005, "Structural Analysis of Turbulent Transport in a Heated Drag-Reducing Channel Flow with Surfactant Additives," Int. J. Heat Mass Transfer, **48**, pp. 965–973.

[6] Gasljevic, K., and Matthys, E. F., 1992, "Effect of Drag-Reducing Surfactant Solutions on Centrifugal Pumps Performance," AMD (Am. Soc. Mech. Eng.), **153**, Recent Advances in Non-Newtonian Flows, pp. 49–56.

[7] Park, S. R., 1996, "Pump and Temperature Effects on Flow Characteristics of

Drag Reducing Surfactants," FED (Am. Soc. Mech. Eng.), **237**(2), pp. 177–182.
[8] Groth, S., Steiff, A., and Weinspach, P., 1994, "Influence of Drag Reducing Additives on the Measurement Accuracy of Heat Meters," University of Dortmund, Dortmund, Germany.
[9] Bellamy, J., 2000, "Recovery of Surfactant-Induced Friction Reduction in a Closed Hot Water System," Masters thesis, Department of Chemical Engineering, University of Ottawa, Canada.
[10] Virk, P. S., Mickley, H. S., and Smith, K. A., 1970, "The Ultimate Asymptote and Mean Flow Structures in Tom's Phenomenon," ASME J. Appl. Mech., **37**, p. 488.
[11] Zakin, J. L., Myska, J., and Chara, Z., 1996, "New Limiting Drag Reduction and Velocity Profile Asymptotes for Nonpolymeric Additives Systems," AIChE J., **42**(12), pp. 3544–3546.
[12] Bhatti, M. S., and Shah, R. K., 1987, "Turbulent and Transition Flow Convective Heat Transfer in Ducts," S. Kakac, R. K. Shah, and W. Aung, (eds.), *Handbook of Single-Phase Convective Heat Transfer*, Wiley, New York, Chap. 4.
[13] Macêdo, E. N., Maneschy, C. E., and Quaresma, J. N. N., 2000, "Forced Convection in Thermally Developing Turbulent Flow in Drag-Reducing Fluids Within Circular Tubes," Int. J. Heat Mass Transfer, **43**(20), pp. 3785–3794.
[14] De Groot, M. C., and Kievit, E. A., 1996, "The Effect of Surfactant on Domestic Heat Exchangers for Hot Water Supply and Heat Flow Meters in D/H Systems," Advanced Energy Transmission Fluids for District Heating and Cooling, International Energy Agency Programme of Research, Development and Demonstration on District Heating and Cooling, No. N2: B1-B94.
[15] Bewerdorf, H. W., and Ohlendorf, D., 1988, "The Behaviour of Drag-Reducing Cationic Surfactant Solutions," Comput. Polym. Sci., **266**(10), pp. 941–953.
[16] Chou, L., and Zakin, J. L., 1989, *Proceedings of Fourth International Conference on Drag Reduction*, Davos, R.H.S. IAHR/AIRH, p. 141.
[17] Sugawara, H., Yamauchi, M., and Wakui, F., 2002, "A Study on Cationic Surfactants as Drag-Reducing Additives," Chem. Eng. Commun., **189**, pp. 1671–1683.
[18] Gasljevic, K., and Matthys, E. F., 1997, "Experimental Investigation of Thermal and Hydrodynamic Development Regions for Drag-Reducing Surfactant Solutions," ASME J. Heat Transfer, **119**, pp. 80–88.
[19] Gasljevic, K., Aguilar, G., and Matthys, E. F., 2000, "Buoyancy Effects on Heat Transfer and Temperature Profiles in Horizontal Pipe Flow of Drag-Reducing Fluids," Int. J. Heat Mass Transfer, **43** (2000), pp. 4267–4274.
[20] Shah, R. K., and Bhatti, M. S., 1987, "Laminar Convective Heat Transfer in Ducts," S. Kakac, R. K. Shah, and W. Aung, (eds.), *Handbook of Single-Phase Convective Heat Transfer*, Wiley, New York, Chap. 3.

Numerical Simulation of Flow Field and Heat Transfer of Streamlined Cylinders in Cross Flow

Zhihua Li

Jane H. Davidson
e-mail: jhd@me.umn.edu

Susan C. Mantell

Department of Mechanical Engineering,
University of Minnesota,
111 Church St., SE,
Minneapolis, MN 55455

The drag and convective heat transfer coefficients along the outer surface of lenticular and elliptical tubes with minor-to-major axis ratios of 0.3, 0.5, and 0.8 were determined numerically for cross-flow Reynolds numbers from 500 to 10^4. *The two-dimensional, unsteady Navier-Stokes equations and energy equation were solved using the finite volume method. Laminar flow was assumed from the front stagnation point up to the point of separation. Turbulent flow in the wake was resolved using the shear stress transport* k-ω *model. Local heat transfer, pressure and friction coefficients as well as the total drag coefficient and average Nusselt number are presented. The results for streamlined tubes are compared to published data for circular and elliptical cylinders. Drag of the elliptical and lenticular cylinders is similar and lower than a circular cylinder. Drag can be reduced by making the streamlined cylinders more slender. Drag is relatively insensitive to Reynolds number over the range studied. An elliptical cylinder with an axis ratio equal to 0.5 reduces pressure drop by 30–40% compared to that of a circular cylinder. The Nusselt numbers of lenticular and elliptical cylinders are comparable. The average Nusselt number of an elliptical or lenticular cylinder with axis ratio of 0.5 and 0.3 is 15–35% lower than that of a circular cylinder.* [DOI: 10.1115/1.2188463]

Keywords: heat transfer, pressure drop, lenticular, elliptical, cylinder, cross flow, subcritical flow

Introduction

The objective of the present study is to quantify the impact of shape on the drag coefficient and forced convection Nusselt number of streamlined tubes for cross flow in the subcritical flow regime. The motivation for the study arose as a result of the interest in developing a method to improve the performance of heat exchangers made of polymer tubes. Polymer heat exchangers are commonly used with corrosive fluids [1–4] and may compete with metal heat exchangers in diverse applications where weight is a concern or innovative shapes are desirable. Because of the relative ease of extruding polymer tubes into a variety of shapes, it is feasible to manufacture streamlined tubes, such as elliptical or lenticular tubes. In a prior paper [5] we developed a procedure to select the shape of the internal flow passage of such tubes considering the requirement to minimize deformation and to maintain the strain limit at 5%. In general, tubes with a non-uniform wall thickness distribution emerge as the best solution. We refer to such tubes as "shaped tubes." An example of a shaped tube with a circular inner flow passage and an elliptical outer profile is shown in Fig. 1. For such a tube, it is possible to determine the overall heat transfer by treating the shaped tube as a base circular tube to which longitudinal fin(s) are added to form the outer profile [6]. A shaped tube efficiency can then be used in the same manner as fin efficiency to determine the outside convective resistance once the average film coefficient for a constant temperature surface is known.

This numerical study provides the drag coefficient and average heat transfer coefficient of various elliptical and lenticular cylinders (Fig. 2) as functions of the minor-to-major axis ratio, termed λ_o, and the Reynolds number. Because only the exterior of the tubes is considered, the tubes were treated as solid bodies in the numerical analysis and are thus referred to as cylinders. A value of $\lambda_o=1$ represents a circular cylinder. The streamlined cylinders become more slender as λ_o is decreased. Because it is expected that heat exchangers will use very small diameter tubes, the range of Reynolds numbers was restricted to $500 \leqslant \mathrm{Re}_D \leqslant 10^4$. The characteristic length scale is the length of the minor axis, $D=2r_o$. This Reynolds number range was selected based on gas speeds less than 30 m/s and minor axis lengths of 1.5–4 mm. The results presented extend the prior work on ellipses to a wider range of shapes and lower Reynolds number and to our knowledge provide the first examination of the lenticular cylinder. Calculated drag coefficients and Nusselt numbers of the streamlined cylinders are compared with measured data for circular cylinders.

Prior Work

Although prior studies of the flow and temperature distribution of circular cylinders in cross flow abound in the literature, measurement of drag and heat transfer of individual noncircular cylinders in cross flow is limited to elliptical cylinders [7–10] primarily for $\mathrm{Re}_D \geqslant 10^4$, and for limited values of λ_o. In the subcritical flow regime, the prior studies considered minor-to-major axis ratio of 0.3 at $\mathrm{Re}_D=1.6\times10^4$ [10], 0.5 at $3000<\mathrm{Re}_D<4\times10^4$ [7,8], and 0.6 at $500<\mathrm{Re}_D<2886$ [9]. In general, these studies show the drag decreases as the ellipse is made more slender, i.e., $\lambda_o \rightarrow 0$. At $\mathrm{Re}_D \sim 10^4$, flow separation occurs at $\alpha=110$ to 140 deg, with α decreasing as λ_o is decreased [8]. For $\mathrm{Re}_D \geqslant 10^4$, the drag coefficient is estimated by [11]

Contributed by the Heat Transfer Division of ASME for publication in the JOURNAL OF HEAT TRANSFER. Manuscript received March 8, 2005; final manuscript received December 23, 2005. Review conducted by Louis C. Burmeister. Paper presented at the 2005 ASME Summer Heat Transfer Conference.

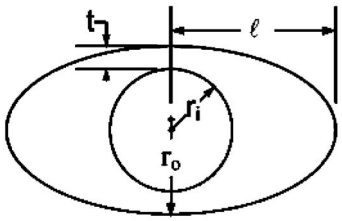

Fig. 1 Example of a "shaped" polymer tube. The outer surface of the tube is an ellipse. The inner flow passage is circular. The non-uniform wall is selected to minimize the conductive resistance across the wall and to prevent deformation and strain failure [5].

$$C_D = 0.015\left(1 + \frac{1}{\lambda_o}\right) + 1.1\lambda_o \tag{1}$$

This correlation indicates the drag of an ellipse with $\lambda_o = 0.5$ is 60% of that of a circular cylinder. Drag reductions may be less significant at lower Re because the boundary layer remains laminar prior to separation. For example, at $3000 < \mathrm{Re} < 4 \times 10^4$, the drag coefficient is reduced 20–40% for an elliptical cylinder with $\lambda_o = 0.5$ [8].

Heat transfer correlations developed for subcritical flow across an elliptical cylinder are also limited to a few geometries, namely $\lambda_o = 0.3$ and 0.5. As presented in Table 1, the prior studies have correlated the Nusselt number in the conventional form

$$\mathrm{Nu}_L = C\,\mathrm{Re}_L^m \tag{2}$$

with some variation in the choice of the characteristic length scale L [8,10,12,13]. In the present study, to facilitate a straightforward comparison of shapes, the length scale used in Re and Nu is the minor axis, D. Using this common length scale, the Nu_D of an elliptical cylinder with $\lambda_o = 0.5$ is 12% lower than that of a circular cylinder at $\mathrm{Re}_D = 5000$.

Numerical Method

The flow and temperature distributions across individual streamlined cylinders were modeled with FLUENT® assuming an unsteady two-dimensional flow. The flow was assumed to be in the direction of the major axis, i.e., with zero angle of attack, and a constant temperature boundary is assumed at the surface of the cylinder. The boundary layer over the cylinder was modeled by assuming a laminar zone from the front stagnation point at $\alpha = 0$ to $\alpha < 90°$, and a turbulent zone from $90° \leq \alpha \leq 180°$, using the shear stress transport (SST) k-ω model [14]. Increasing the laminar zone to $\alpha = 110°$, which is closer to the predicted angle of separation, had no effect on the calculated drag coefficient. This approach was taken after unsuccessful trials of fully laminar and turbulent models. The laminar models over predicted the size of the bubble in the wake. The turbulent models, including the standard k-ω model, the standard k-ω model, the SST k-ω model and the v2F model, under predicted drag, especially for slender ellipses, by as much as 30%. The combined laminar/turbulent approach produced local and average results that compare favorably to measured data.

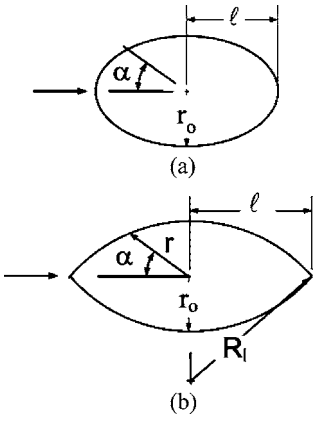

Fig. 2 Streamlined outer profile of (*a*) elliptical, and (*b*) lenticular tubes. The outer surface of a lenticular cylinder is formed by two symmetrically intersected arcs, each given by $(r\cos\alpha)^2+(r\sin\alpha+R_l-r_o)^2=R_l^2$, where and λ_o is the length ratio of the minor to major axis of the outer surface. A value of $\lambda_o = 1$ represents a circular cylinder. The cylinders become more slender as λ_o is decreased.

Table 1 Heat transfer correlations for cross flow over individual elliptical cylinders

Correlation	Length scale	Source
$\mathrm{Nu}_L = C\,\mathrm{Re}_L^m$ $10^3 < \mathrm{Re}_L < 10^5$ and $\lambda_o = 0.5$, $C = 0.344$, $m = 0.573$ at $\phi = 0°$ $C = 0.470$, $m = 0.537$ at $\phi = 15°$	$L = 2\ell$	[12]
$\mathrm{Nu}_L = C\,\mathrm{Re}_L^m$, $10^3 < \mathrm{Re}_L < 10^5$ and $\lambda_o = 0.3$ $C = 0.546$, $m = 0.539$ at $\phi = 0°$ $C = 0.839$, $m = 0.492$ at $\phi = 15°$	$L = 2\ell$	[10]
$\mathrm{Nu}_L = 0.27\,\mathrm{Re}_L^{0.6}\mathrm{Pr}^{0.37}\left(\frac{\mathrm{Pr}}{\mathrm{Pr}_w}\right)^{0.25}$	$L = 2\ell$	[8]
$10^3 \leq \mathrm{Re}_L \leq 10^4$, $\lambda_o = 0.5$, $\phi = 0$ $\mathrm{Nu}_L = 0.224\,\mathrm{Re}_L^{0.612}$, $10^3 < \mathrm{Re}_L < 10^4$, $\lambda_o = 0.5$, $\phi = 0$	$L = r_o + \ell$	[13]

The computational domain and boundary conditions are shown in Fig. 3; an elliptical cylinder is shown for illustration. The size of the domain ensured the boundaries did not affect vortex shedding or drag force. It has been suggested that the lateral boundary should be at least eight diameters from the center of a circular cylinder at $\mathrm{Re}_D = 100$ [15]. Because the present simulations involve higher Reynolds numbers, the lateral boundary was located 16 diameters from the center of the cylinder. The upstream and downstream boundaries were set to 16ℓ and 40ℓ, respectively, based on prior simulation of a circular cylinder [16].

At the inlet, uniform air velocity and temperature boundary conditions were imposed.

$$p = p_\infty; \quad u_x = u_\infty; \quad u_y = 0 \tag{3}$$

$$T_\infty = 300\ \mathrm{K} \tag{4}$$

The initial velocity and temperature fields were set equal to the uniform inlet condition. The inlet free stream turbulence intensity was set to 1%. A fully developed boundary condition was applied at the outlet.

$$\frac{\partial \xi}{\partial x} = 0, \quad \xi = u_x, u_y, T, p \tag{5}$$

Symmetry boundary conditions were applied at the lateral boundaries.

$$\frac{\partial \xi}{\partial y} = 0, \quad \xi = u_x, T, p \tag{6}$$

$$u_y = 0 \tag{7}$$

The no-slip boundary condition was applied at the isothermal cylinder wall.

$$u_{x,w} = u_{y,w} = 0 \tag{8}$$

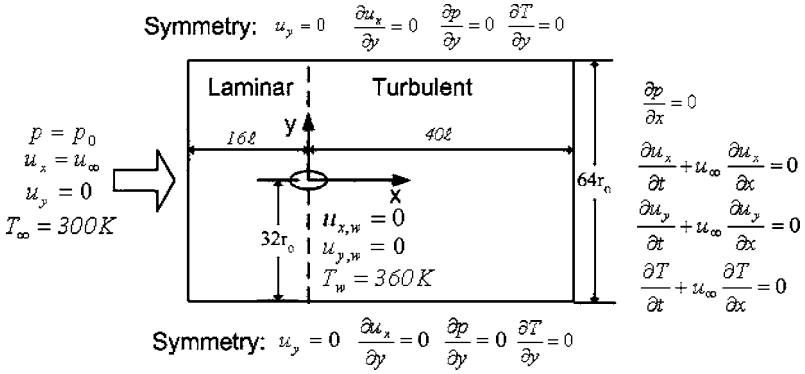

Fig. 3 Computational domain and boundary conditions of flow and heat transfer

$$T_w = 360\ \text{K} \tag{9}$$

The second-order upwind method was used for spatial discretization. Time derivatives were discretized using the second-order implicit method. The segregated solver was applied to solve the momentum equations and the energy equation. At each step, the momentum equations were first solved to obtain the velocity field. The pressure field was updated by solving the Poisson equation. The pressure field and the velocity field were coupled by the SIMPLEC method. After solving the continuity equation and momentum equations, the energy equation was solved to achieve a quasi-steady periodic solution. The integrated pressure force and heat transfer over the cylinder surface were monitored as a function of time at each Re_D. The steady-periodic state was achieved when the variation in the oscillating amplitudes of the pressure force and heat transfer rate was less than 1%.

The computational domain was meshed using GAMBIT [17] with unstructured triangular meshes using a pave method except inside the boundary layer where a quadratic mesh was used (Fig. 4). The boundary layer thickness before separation was estimated by a theoretical formulation [8]. The inlet and outlet boundaries were meshed into 32 grid points. The upper and lower boundaries were meshed into 150 grid points. The cylinder wall was meshed into 60 grid points. Thirty layers of quadratic meshes were attached inside the boundary layer. The radial thickness of the first mesh layer was $5\times10^{-5}r_o$. The mesh was increased by a factor of 1.3 in the radial direction. The total thickness of the attached quadratic meshes was $0.45r_o$. The number of nodes used is shown in Table 2 for an elliptical cylinder with $\lambda_o=0.5$. For each cylinder, the mesh was refined at $\text{Re}_D=500$ and 10^4 until the variations of the time averaged values of C_D and Nu_D were less than 2.5%. Based on the comparison in Table 2, 23,670 nodes were applied for the elliptical cylinder with $\lambda_o=0.5$. A similar analysis was conducted for each shape. The number of nodes applied was 34,058 and 44,030 for elliptical cylinders with $\lambda_o=0.3$ and 0.8, respectively. For lenticular cylinders, 44,663, 30,242, and 22,128 nodes were used in simulations of flow for $\lambda_o=0.3$, 0.5 and 0.8, respectively.

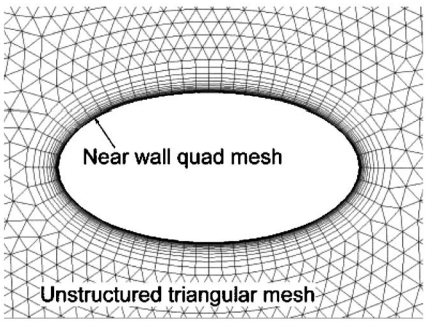

Fig. 4 Triangular and quad meshes for flow over an individual elliptical cylinder

Large time steps were applied initially to reach a steady-periodic solution efficiently. At that point, the time step was selected based on the expected vortex shedding frequency in the wake area [18–21]. For each shape, 100 time steps were performed per period. The time step was selected to assure convergence of the total drag over the range of Reynolds number considered.

Analysis

The primary results of interest are the steady periodic overall drag coefficient and average Nusselt number. Local values of friction coefficient, pressure coefficient and Nusselt number were compared to prior experimental data to validate the computational approach. The time averaged value of variable $f(t)$ at the steady-periodic state is given by

$$\overline{f} = \frac{\int_{t=t_0}^{t_1} f(t)dt}{t_1 - t_0} \tag{10}$$

where t_1-t_0 is ten times the vortex shedding period.

Flow Field. Local pressure and friction coefficients as well as total drag were computed. The local pressure coefficient is defined as

$$C_{p,\alpha} = \frac{\overline{p_\alpha} - p_\infty}{\frac{1}{2}\rho u_\infty^2} \tag{11}$$

where $\overline{P_\alpha}$ is the time-averaged local pressure on the cylinder surface with an angular coordinate of α measured from the front stagnation point and the reference pressure $p_\infty=p_0-\rho u_\infty^2/2$, where p_0 is the stagnation pressure. The local friction coefficient is defined as

Table 2 Test of grid independence for an ellipatical cylinder with $\lambda_o=0.5$

λ_o	Re_D	Number of nodes	C_D	Nu_D
0.5	500	23,670	0.81	9.6
		79,090	0.81	9.5
	10^4	23,670	0.60	48.1
		79,090	0.59	48.1

$$C_{f,\alpha} = \frac{\overline{\tau_w}}{\frac{1}{2}\rho u_\infty^2} \tag{12}$$

The wall shear stress was evaluated from the normal velocity gradient at the cylinder wall.

$$\tau_w(t,\alpha) = \left. \mu \frac{\partial u(t,\alpha)}{\partial n} \right|_w \tag{13}$$

The drag coefficient, C_D, is the sum of the time-averaged pressure coefficient and time-averaged friction coefficients.

$$C_D = C_p + C_f \tag{14}$$

where

$$C_p = \frac{\overline{F_p}}{A_\perp \frac{\rho u_\infty^2}{2}} \tag{15}$$

and

$$C_f = \frac{\overline{F_f}}{A_\perp \frac{\rho u_\infty^2}{2}} \tag{16}$$

The projected area of the cylinder is perpendicular to the direction of flow; $A_\perp = 2r_o$, assuming cylinders of unit length. Total pressure force and wall shear stress were determined by integration over the surface of the cylinder

$$F_p(t) = \int_0^{2\pi} \rho_\alpha(t,\alpha) r_\alpha \cos\alpha \, d\alpha \tag{17}$$

$$F_f(t) = \int_0^{2\pi} \tau_w(t,\alpha) r_\alpha \sin\alpha \, d\alpha \tag{18}$$

Heat Transfer. Local and average Nusselt numbers were determined. The local Nusselt number is given by

$$\mathrm{Nu}_{D,\alpha} = \frac{-\int_{t_0}^{t_1} 2r_o \left(\frac{\partial T(t,\alpha)}{\partial n} \right)_w dt}{t_1 - t_0}. \tag{19}$$

The average heat transfer coefficient and Nusselt number over the surface are

$$\overline{h} = \frac{\overline{Q}}{A_{\mathrm{HT}}(T_w - T_w)} \tag{20}$$

and

$$\mathrm{Nu}_D = \frac{\overline{h} \cdot 2r_o}{k_\infty} \tag{21}$$

where heat transfer rate Q was reported in FLUENT as a function of time. The heat transfer surface areas, A_{HT}, for elliptical and lenticular cylinders of unit length are given by Eqs. (22) and (23), respectively.

$$A_{\mathrm{HT},e} = \pi(r_o + \ell) \tag{22}$$

$$A_{\mathrm{HT},1} = 4R \arcsin\left(\frac{\ell}{R}\right) \tag{23}$$

Results

The presentation which follows is structured first to validate the numerical approach and second to highlight the effects of shape, both geometry and length ratio, λ_o, on drag and heat transfer.

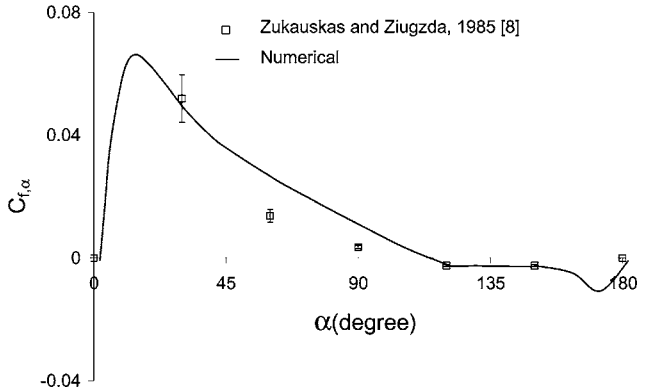

Fig. 5 Comparison of predicted local friction coefficient with experiment [8] for an elliptical cylinder with $\lambda_o = 0.5$ at $\mathrm{Re}_D = 3200$

Validation of Numerical Approach. The numerical approach was assessed by comparing local and average values of drag coefficient and Nusselt number to prior data for an ellipse with $\lambda_o = 0.5$. The local friction coefficient is presented in Fig. 5. The overall drag coefficient is plotted as a function of Re_D in Fig. 6. Local and average Nusselt numbers are shown in Figs. 7 and 8.

In Fig. 5 the numerical and measured [8] instantaneous values of $C_{f,\alpha}$ at $\mathrm{Re}_D = 3200$ are compared. The measured data were obtained for a free stream turbulence intensity of 0.3%. The error bars in the graph are based on estimates in [8]. The overall trends in the predicted and measured data are similar. The predicted separation point at $\alpha = 112$ deg (the angle at which $C_{f,\alpha} = 0$) agrees well with reported values of 110–140 deg [8]. The behavior of the friction drag coefficient after separation reflects the development of vortices in the wake. The change in the friction coefficient near 180 deg is due to an increase in the magnitude of vorticity. The vortices in the wake are not symmetric and thus the location of the inflection point will change over about 10 deg with time. As will be shown later in the discussion of Fig. 9, the skin friction drag for the Reynolds number range of interest is much less than form drag.

In Fig. 6, the numerical drag coefficient is compared to measured values [7,8] for $500 \leqslant \mathrm{Re}_D \leqslant 1.2 \times 10^4$. There is some scatter in the data, and the numerical results fall within the measured values. The data and numerical model indicate the drag coefficient is relatively insensitive to Re_D in this range.

The steady periodic local Nusselt numbers are plotted in Fig. 7 for $\mathrm{Re}_D = 3074$. These values are averages over one shedding pe-

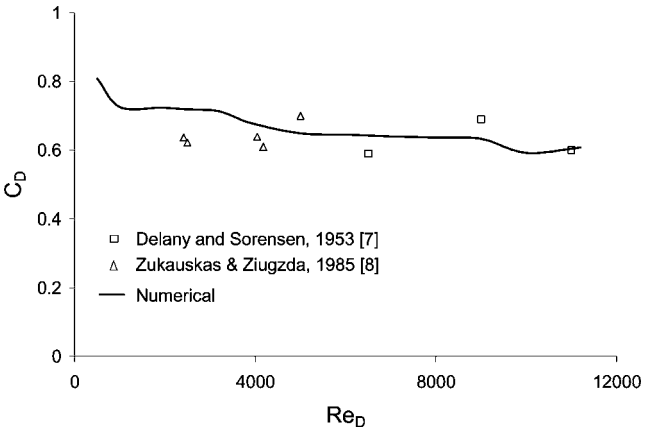

Fig. 6 Comparison of numerical drag coefficient with experiment [7,8] for an elliptical cylinder with $\lambda_o = 0.5$

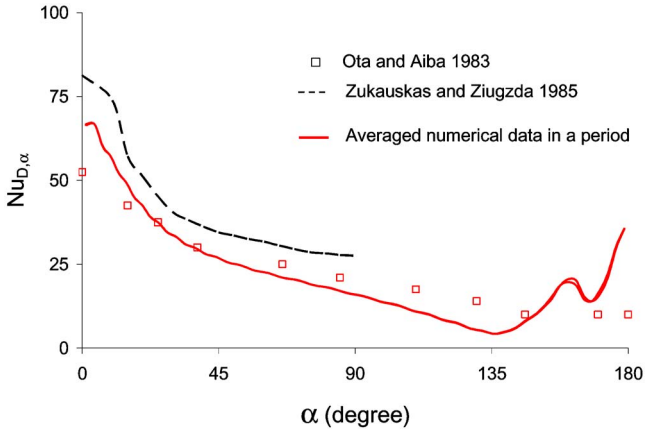

Fig. 7 Comparison of predicted local Nusselt number with experiment [12] and an empirical correlation [8] for an elliptical cylinder with $\lambda_o=0.5$ at $Re_D=3074$

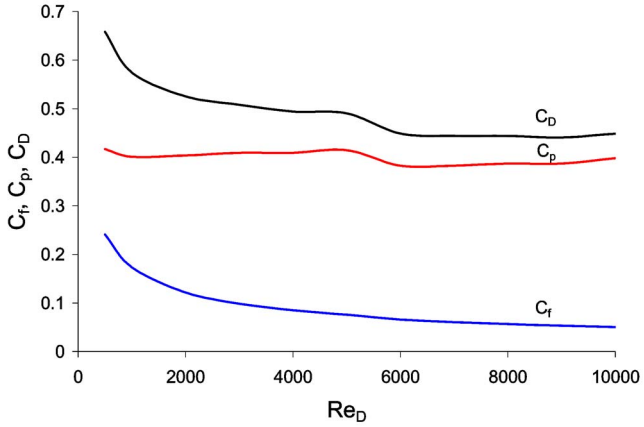

Fig. 9 Friction, pressure and drag coefficient of an elliptical cylinder with $\lambda_o=0.3$

riod and do not exhibit the oscillations of vortex shedding. The numerical average Nusselt number is compared with an empirical correlation [8] and data obtained with a constant heat flux boundary condition [12]. The predicted values are close to the measured data, which are about 20% lower than the correlation developed by Zukauskas and Ziugzda [8].

In Fig. 8, the average Nusselt number for $500 \leqslant Re_D \leqslant 10^4$ is compared to empirical correlations developed for an ellipse with $\lambda_o=0.5$ (see Table 1). The numerical Nusselt number falls within the range of values predicted with the empirical correlations [8,12,13].

Parametric Study. Attention is first turned to the effect of streamlined cylinder shape, both geometry and length ratio, λ_o, on the drag coefficient. Numerical results for elliptical and lenticular cylinders with $\lambda_o=0.3$, 0.5 and 0.8 at $500 \leqslant Re_D \leqslant 10^4$ are compared to experimental data for circular cylinders ($\lambda_o=1$). The results are interpreted to determine the conditions under which the shaped tube is feasible from the perspective of reducing drag in laminar cross flow.

Figure 9 shows the friction, pressure and total drag coefficients versus Re for an elliptical cylinder with $\lambda_o=0.3$. The plot illustrates the importance of form drag as opposed to friction drag even for the most streamlined ellipse considered. The value of C_p is two to eight times the value of C_f depending on the value of Re. The overall drag coefficient is not a strong function of Re but there is a slight downward trend in drag coefficient as Re is increased from 500 to 10,000. The trends shown in this figure are similar for the other length ratios and the lenticular cylinder.

Figure 10 shows the effect of geometry (ellipse, lenticular or circular cylinder) and λ_o on the overall drag coefficient. The numerical data are best correlated for $5000 \leqslant Re_D \leqslant 10^4$ by

$$C_{D,e} = (0.112 \pm 0.009)\lambda_o^{2.6\pm0.5} \ln Re_{D,e} + (0.41 \pm 0.04) \quad (24)$$

for elliptical tubes with $R^2=0.9919$ and

$$C_{D,l} = (0.120 \pm 0.006)\lambda_o^{2.2\pm0.4} \ln Re_{D,l} + (0.46 \pm 0.05) \quad (25)$$

for lenticular cylinders with $R^2=0.9945$. The drag coefficients of the elliptical and lenticular cylinders are similar. The impact of Re within the range considered is insignificant for both streamlined geometries. The value of C_D decreases as the cylinders are slenderized, i.e., λ_o is decreased. For example, for an elliptical cylinder, C_D at $\lambda_o=0.3$ is 25% lower than that at $\lambda_o=0.5$ and 60% lower than the circular cylinder [22]. The decrease in drag coefficient is attributed to a delay of separation as λ_o is decreased (Table 3). Significant reductions in drag compared to that of the circular cylinder are possible for $\lambda_o \leqslant 0.5$. To illustrate this point, consider elliptical and lenticular cylinders with $\lambda_o=0.5$ at $Re_D=5000$; drag is reduced by 37%, and 31%, respectively, compared to the circular cylinder.

Next, consider the effect of shape on heat transfer. Although the streamlined cylinders provide a reduction in drag, the average

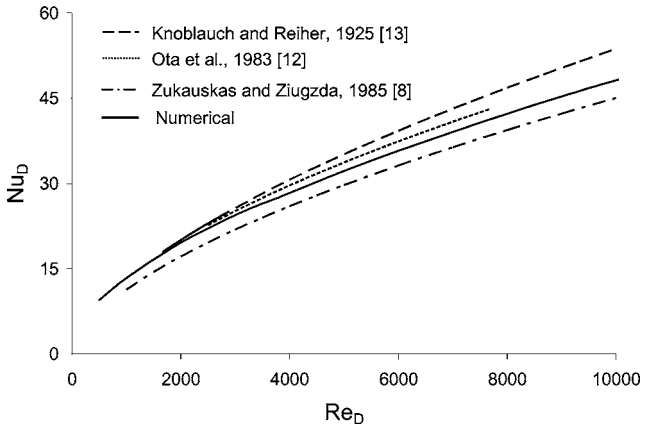

Fig. 8 Comparison of predicted average Nusselt number with empirical correlations [8,12,13] for an elliptical cylinder with $\lambda_o=0.5$

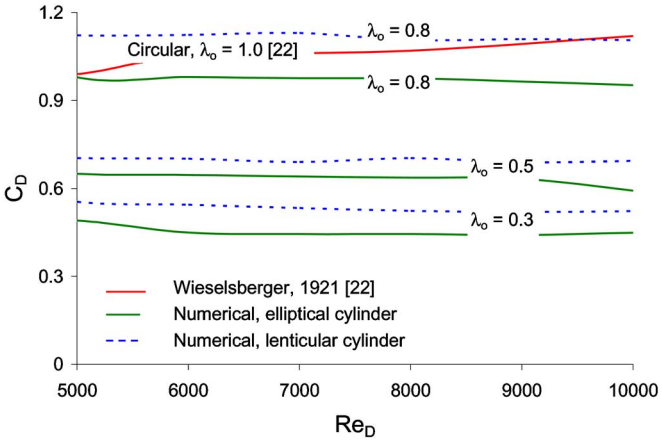

Fig. 10 Comparison of drag coefficients of elliptical, lenticular and circular cylinders. The drag coefficient of a circular cylinder is calculated from correlation of [22].

Table 3 Angle of separation for circular, elliptical and lenticular cylinders with $\lambda_o=0.3$, 0.5, and 0.8 at $500 \leqslant Re_D \leqslant 10^4$

Shape	λ_o	Angle of separation (degree)
Circular	1.0	80 (measured by [8])
Elliptical	0.3	155–135[a]
	0.5	130–100
	0.8	110–90
Lenticular	0.3	145–110
	0.5	130–95
	0.8	110–90

[a]The angle of separation increases slightly as Re is increased. For example, for an ellipse with $\lambda_o=0.3$, separation occurs at 155 deg at $Re_D=500$ and 135 deg at $Re=10^4$.

Nusselt number is expected to be lower than that for a circular cylinder. The potential benefit of added surface area depends on the material and geometry. For cylinders with non-uniform wall thickness, heat transfer is expressed in terms of a shaped tube efficiency χ, which depends solely on Biot number, based on the length of material added to a base circular tube, and a dimensionless length, $\lambda_o=r_o/\ell$ [6]. The shaped tube efficiency is used in the same manner as a fin efficiency to determine the outside convective resistance.

$$R_{th,o}=\frac{1}{\chi\overline{h}_o A_o} \tag{26}$$

The average heat transfer coefficient for a constant temperature surface can be obtained from the present simulations. The predicted average Nusselt number for elliptical and lenticular cylinders is plotted along with that for a circular cylinder at $500 \leqslant Re_D \leqslant 10^4$ in Fig. 11. The numerical results are best correlated for the elliptical cylinder by

$$Nu_{D,e}=(0.37\pm0.03)\lambda_{o,e}^{0.4\pm0.1}\,Re_{D,e}^{0.554\pm0.008} \tag{27}$$

with a coefficient of determination $R^2=0.9992$, and for the lenticular cylinder by

$$Nu_{D_o,l}=(0.3\pm0.1)\lambda_{o,l}^{0.46\pm0.06}\,Re_{D,l}^{0.60\pm0.05} \tag{28}$$

with $R^2=0.9817$. The elliptical cylinder correlation is nearly identical to that reported in literature [8,10,12]. Nu_D increases with increasing λ_o. An elliptical cylinder with $\lambda_o=0.5$ has a 16% higher heat transfer coefficient than that one with $\lambda_o=0.3$. At $\lambda_o=0.8$, the predicted Nusselt number reaches that of a circular cylinder whose diameter equals the length of the minor axis ($D=2r_o$).

Conclusion

The numerical simulations of the drag and heat transfer across elliptical and lenticular cylinders in cross flow for $500 \leqslant Re_D \leqslant 10^4$ provide generalized expressions for drag coefficient and average Nusselt number for a range of profiles. Compared to circular cylinders, the streamlined tubes result in a delay of separation and thus increasing reductions in form drag as the cylinders are made more slender, i.e., λ_o is decreased. There is no substantial difference in the drag over elliptical or lenticular cylinders with the same value of λ_o. Compared with a circular tube, the drag coefficient is reduced by 30–40% by the use of an elliptical tube or lenticular tube with $\lambda_o=0.5$. The numerical results are well correlated in the forms given in Eqs. (24) and (25).

General Nusselt number correlations were developed for constant surface temperature cylinders. As with drag coefficient, the average convective heat transfer coefficient is similar for elliptical and lenticular cylinders for a fixed value of λ_o. This similarity is based on using a common length scale based on the diameter of the cylinder perpendicular to the flow, i.e., the length of the minor axis. The Nusselt number increases with increasing λ_o and is lower than measured values for a circular cylinder. The numerical results are well correlated in the forms given in Eqs. (27) and (28).

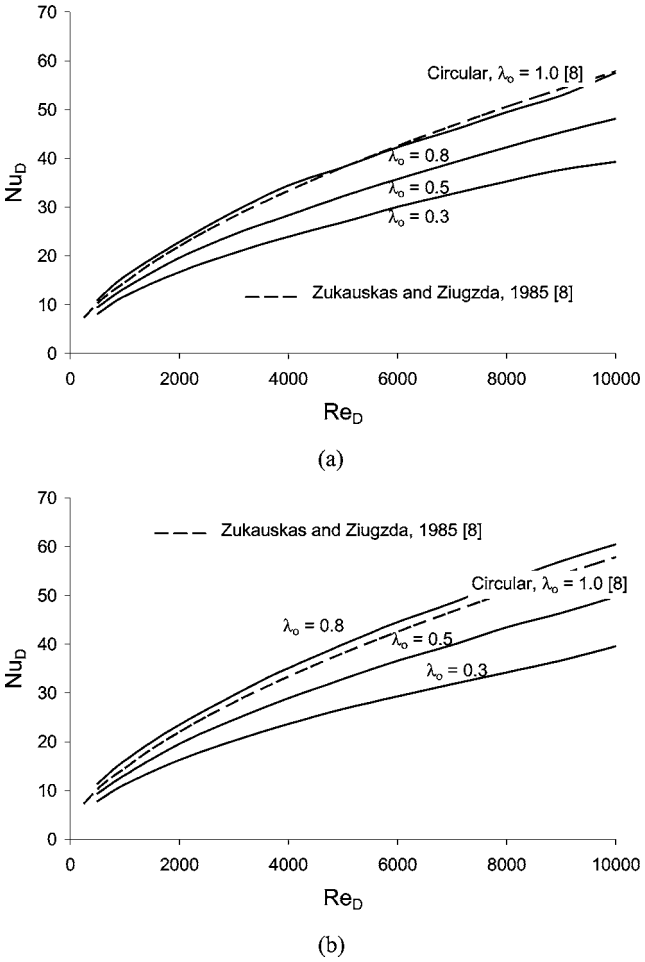

Fig. 11 Average Nusselt number of streamlined cylinders with $\lambda_o=0.3$, 0.5, and 0.8 at $500 \leqslant Re_D \leqslant 10^4$, (*a*) elliptical, (*b*) lenticular. The Nusselt number of the circular cylinder is calculated from correlations provided by [8].

Although the results presented here for individual cylinders cannot be directly extended to banks of tubes, the general finding that streamlined tubes have lower drag coefficients and lower average heat transfer coefficients than do circular cylinders is anticipated to apply to tube banks. The effect of pitch-to-diameter ratio on drag and heat transfer for tube banks requires additional study.

Acknowledgment

The authors are indebted to Professor Krishnan Mahesh at the University of Minnesota who helped guide the selection of numerical method. The financial support of the U.S. National Science Foundation through Grant No. DMII-0084765, the University of Minnesota Graduate School Dissertation Fellowship, and the University of Minnesota Supercomputing Institute are acknowledged. The contents of the paper are solely attributed to the authors.

Nomenclature

A_{HT} = heat transfer surface area of cylinders, per unit length, m^2

$A_\perp$ = projected are of the cylinder in the direction perpendicular to flow, m^2

Bi = Biot number, $Bi=\overline{h}r_o/k_w$

C_D = drag coefficient
C_f = friction coefficient
C_p = pressure coefficient
D = length of the minor axis, $D=2r_o$, m
F_p = pressure force, N
F_f = friction force, N
h = convective heat transfer coefficient, $W/m^2 K$
k = thermal conductivity, W/m K
ℓ = length of the semi-major axis, m
Nu = Nusselt number
P = fan pumping power, W
Pr = Prandtl number of the fluid, evaluated at the fluid bulk temperature
Pr_w = Prandtl number of the fluid, evaluated at the tube wall surface temperature
p = pressure, Pa
Q = heat transfer rate, W
R^2 = coefficient of determination
R_1 = arc radius of the lenticular cylinder, m
Re = Reynolds number
r = radial coordinate, m
r_i = radius of inside circular channel, m
r_o = length of outside semi-minor axis, m
T = temperature, K
t = time, s
u = velocity, m/s
V = volumetric flow rate, m^3/s

Greek Symbols

α = angle measured from the front stagnation point, degree
χ = shaped tube efficiency
ε = tube effectiveness, Eq. (29)
ϕ = angle of attack, degree
λ_o = outside tube length ratio of the minor-to-major axis, $\lambda_o=r_o/\ell$
λ_t = length ratio of the wall thickness at $\alpha=90°$ to the outside minor axis, $\lambda_t=t/r_o$
τ_w = wall shear stress, N/m^2
ψ = performance effectiveness, defined as the ratio of heat transfer rate to fan pumping power of an individual elliptical to that of a circular tube, Eq. (34)

Superscript

$\bar{}$ = overbar indicates time-averaged quantity

Subscript

c = refers to a circular cylinder
e = refers to an elliptical cylinder
L,D = refers to characteristic length
l = refers to a lenticular cylinder
o = refers to value at cylinder outer surface
w = refers to value at the cylinder wall
x,y = refer to values at x and y direction
α = refers to values at angle α
∞ = refers to free stream

References

[1] Bigg, D. M., Stickford, G. H., and Talbert, S. G., 1989, "Applications of Polymeric Materials for Condensing Heat Exchangers," Polym. Eng. Sci., **29**(16), pp. 1111–1116.
[2] Davidson, J. H., Oberreit, D., Liu, W., and Mantell, S. C., 1999, "Are Plastic Heat Exchangers Feasible for Solar Water Heaters? Part I: A Review of the Technology, Codes and Standards, and Commercial Products," ASME/KSME/JSME/ASHRAE/JSES International Renewable and Advanced Energy Systems for the 21st Century, CD-ROM, RAES99-7683, Maui, Hawaii.
[3] El-Dessouky, H. T., and Ettouney, H. M., 1999, "Plastic/Compact Heat Exchangers for Single-Effect Desalination Systems," Desalination, **122**(2–3), pp. 271–289.
[4] Jachuck, R. J. J., and Ramshaw, C., 1994, "Process Intensification: Polymer Film Compact Heat Exchanger (PFCHE)," Chem. Eng. Res. Des., **72**(A2), pp. 255–262.
[5] Li, Z., Mantell, S. C., and Davidson, J. H., 2005, "Mechanical Analysis of Streamlined Tubes with Nonuniform Wall Thickness for Heat Exchangers," J. Strain Anal. Eng. Des., **40**(3), pp. 275–285.
[6] Li, Z., Davidson, J. H., and Mantell, S. M., 2004, "Heat Transfer Enhancement Using Shaped Polymer Tubes: Fin Analysis," J. Heat Transfer, **126**(2), pp. 211–218.
[7] Delany, N., and Sorensen, N., 1953, "Low Speed Drag of Cylinders of Various Shapes," NACA Technical Note, Report No. 3038.
[8] Zukauskas, A., and Ziugzda, J., 1985, *Heat Transfer of a Cylinder in Crossflow*, Hemisphere, 150.
[9] Badr, H. M., Dennis, S. C. R., and Kocabiyik, S., 2001, "Numerical Simulation of the Unsteady Flow Over an Elliptic Cylinder at Different Orientations," Int. J. Opt. Comput., **37**(8), pp. 905–931.
[10] Ota, T., and Nishiyama, H., 1984, "Heat Transfer and Flow Around an Elliptic Cylinder," Int. J. Heat Mass Transfer, **27**(10), pp. 1771–1779.
[11] Hoerner, S. F., 1965, *Fluid-Dynamic Drag*, Hoerner Fluid Dynamics, Midland Park, NJ.
[12] Ota, T., Aiba, S., Tsuruta, T., and Kaga, M., 1983, "Forced Convection Heat Transfer from an Elliptic Cylinder of Axis Ratio 1:2," Bull. JSME, **26**(212), pp. 262–267.
[13] Knoblauch, O., and Reiher, H., 1925, "Waermeuebertragung," Handbuch der Experimentalphysik, W. Wien and F. Harms, eds., **9**(1), p. 189.
[14] Menter, F. R., 1994, "Two-Equation Eddy-Viscosity Turbulence Models for Engineering Applications," AIAA J., **32**(8), pp. 1598–1605.
[15] Behr, M., Hastreiter, D., Mittal, S., and Tezduyar, T. E., 1995, "Incompressible Flow Past a Circular Cylinder: Dependence of the Computed Flow Field on the Location of the Lateral Boundaries," Comput. Methods Appl. Mech. Eng., **123**(1–4), pp. 309–316.
[16] Reichel, C., and Strohmeier, K., 2003, "Circular Cylinder Exposed to Cross Flow Fluid Forces-Parameters of Influence-Limits of Numerical Models," *ASME Pressure Vessels and Piping Conference, American Society of Mechanical Engineers*, Cleveland, OH, pp. 35–44.
[17] Abdulhadi, M., 1989, "Boundary Layer Calculations on Cylinders of Rankine-Oval Sections," Trans. Can. Soc. Mech. Eng., **13**(3), pp. 65–68.
[18] Knauss, D. T., John, J. E. A., and Marks, C. H., 1976, "Vortex Frequencies of Bluff Cylinders at Low Reynolds Numbers," J. Hydronaut., **10**(4), pp. 121–126.
[19] Ratliff, C. L., 1992, "Vortex Shedding Frequencies of Elliptical Cylinders in the Irregular Reynolds Number Region," *Winter Annual Meeting of the American Society of Mechanical Engineers*, 8–13 Nov. ASME, New York, NY, Anaheim CA, pp. 53–60.
[20] Modi, V. J., and Dikshit, A. K., 1975, "Near Wakes of Elliptic Cylinders in Subcritical Flow," AIAA J., **13**(4), pp. 490–497.
[21] Modi, V. J., and Wiland, E., 1970, "Unsteady Aerodynamics of Stationary Elliptic Cylinders in Subcritical Flow," AIAA J., **8**(10), pp. 1814–1821.
[22] Wieselsberger, E., 1921, "Neuere Feststellungen über die Gesetze des Flüssigkeits- und Luftwiderstandes," Phys. Z., **22**, pp. 321–328.

Film-Cooling Efficiency in a Laval Nozzle Under Conditions of High Freestream Turbulence

Valery P. Lebedev

Vadim V. Lemanov

Victor I. Terekhov
e-mail: terekhov@itp.nsc.ru

Kutateladze Institute of Thermophysics,
Russian Academy of Sciences,
Siberian Division,
630090, Lavrent'ev Ave., 1,
Novosibirsk, Russia

In the present work we experimentally examined the effect of enhanced freestream turbulence on the film-cooling efficiency in an axisymmetric supersonic nozzle. A considerable reduction in the film-cooling efficiency was observed with increasing level of flow turbulence, both in the subsonic and supersonic parts of the Laval nozzle. For instance, an increase in the freestream turbulence number from 0.2% to 15% resulted in more than twofold deterioration of film-cooling efficiency. A similar decrease of film-cooling efficiency was also observed under off-design flow conditions. At the same time, the increase in the freestream turbulence number had almost no effect on the recovery factor and on the distribution of static pressure over the length of the nozzle. The Kutateladze-Leont'ev asymptotic theory of gas cooling films was used to generalize the experimental data for nozzle flows with allowance for flow nonisothermality, compressibility, longitudinal pressure gradient, and high freestream turbulence number. [DOI: 10.1115/1.2188508]

1 Introduction

Film cooling is widely used in protecting the working surfaces of apparatus against high-temperature or aggressive flows. By now, ample data concerning this matter have been accumulated; these data were summarized in several reviews (see [1–5]). Thermal protection presents an especially challenging problem in Laval nozzles, the most heat-beat components of high-speed turbines [5–7], and rocket engines [2,3]. Distinctive features of nozzle flows are their considerable acceleration in the convergent part of the nozzle, high level of heat fluxes in the nozzle throat, and effects due to flow compressibility in the supersonic part of the nozzle. A numerical study of nozzle flows presents rather a complex problem [5,8] because, here, effects due to the laminar-turbulent transition, relaminarization of the turbulent boundary layer under high pressure gradients, high freestream turbulence, and compressibility must be taken into account. Another feature that additionally hampers simulation studies in this area is the change in the type of transfer equations for the transonic region of the flow. For all these reasons, an experimental study of film-cooling efficiency in high-turbulence Laval-nozzle flows remains a topical problem.

Flow turbulization is known to have a profound effect on the friction and on heat-transfer processes in near-wall flows [9,10]. The turbulence number in turbomachine cascades can run into 35% [5,9]. Under gradientless conditions, enhanced turbulence results in substantial deterioration of film-cooling efficiency [4,5,11–16].

Film cooling in Laval nozzles is a multiparametric problem involving the interaction of a high-turbulence external flow with a wall jet under the action of steamwise gradient of flow velocity and compressibility. Moreover, the acceleration of the nozzle flow drastically modifies the distribution of velocity fluctuations over the length of the nozzle compared to the flow in a cylindrical pipe [17–19]. The above features of flows in film-cooled axisymmetric nozzles are expected to have an effect on the distribution of the efficiency factor.

Available works on film cooling in Laval nozzles (see, for instance, [20–22]), in which experiments were performed under conditions of low freestream turbulence, have revealed a profound effect of steamwise acceleration and compressibility of the flow on the efficiency factor.

There are many reported studies on film cooling in high-turbulence flows produced by gas-turbine cascades [4–6,10]; yet, almost no data were reported on protective properties of high-turbulence films in nozzle flows [18]. The most complex cases of film-cooled nozzles include off-design discharge regimes, with compression shocks entering the supersonic part of the nozzle. For low-turbulent flows, such regimes were experimentally examined in [7,23]. The authors of [7,23] showed that compression shocks cause intense mixing of the protective film flow and, therefore, decrease the efficiency factor. No such data were obtained for conditions with high main-flow turbulence.

In the present study, we experimentally examined the film-cooling efficiency in an axisymmetric supersonic Laval nozzle under various freestream turbulence numbers in design and off-design regimes. The experimental results were compared to data on the film-cooling efficiency in cylindrical pipes under identical thermal and gas-dynamic conditions at the inlet to the channel. This allowed us to directly determine the influence of the above-indicated factors on film-cooling efficiency.

2 Experimental Setup and Procedure

The experiments were performed in an open-type wind tunnel facility. The working gas was compressed air. The diagram of the test section is shown in Fig. 1(*a*). The major components here are turbulizer 1, settling-chamber convergent part 2, partition 3, injection chamber 4, and Laval nozzle 6. The flow compression ratio in the convergent part 2 is $n=7.2$. The film flow was injected into the main flow out of the injection chamber 4 through an annular tangential slot of height $s=2$ mm. The partition 3, which separated the main flow and the wall jet flow, was made of caprolone. The thickness of the partition was 0.2 mm.

The geometry of the Laval nozzle is depicted in Fig. 1(*c*). The supersonic nozzle 6, whose wall thickness is 12–16 mm, was made of textolite. The semi-angle of convergence of the subsonic part of the nozzle is 30 deg, and the semi-vertex angle of divergence of its supersonic part is 6 deg. The inlet and outlet diameters of the nozzle are $D_0=80$ mm and $D_A=50$ mm, and the nozzle-throat diameter is $D_k=20$ mm. The length of the nozzle is $L=212$ mm. To avoid flow separation and the formation of stagnant zones, the nozzle contour at the entrance to the nozzle was

Contributed by the Heat Transfer Division of ASME for publication in the JOURNAL OF HEAT TRANSFER. Manuscript received July 16, 2005; final manuscript received November 11, 2005. Review conducted by Phillip M. Ligrani.

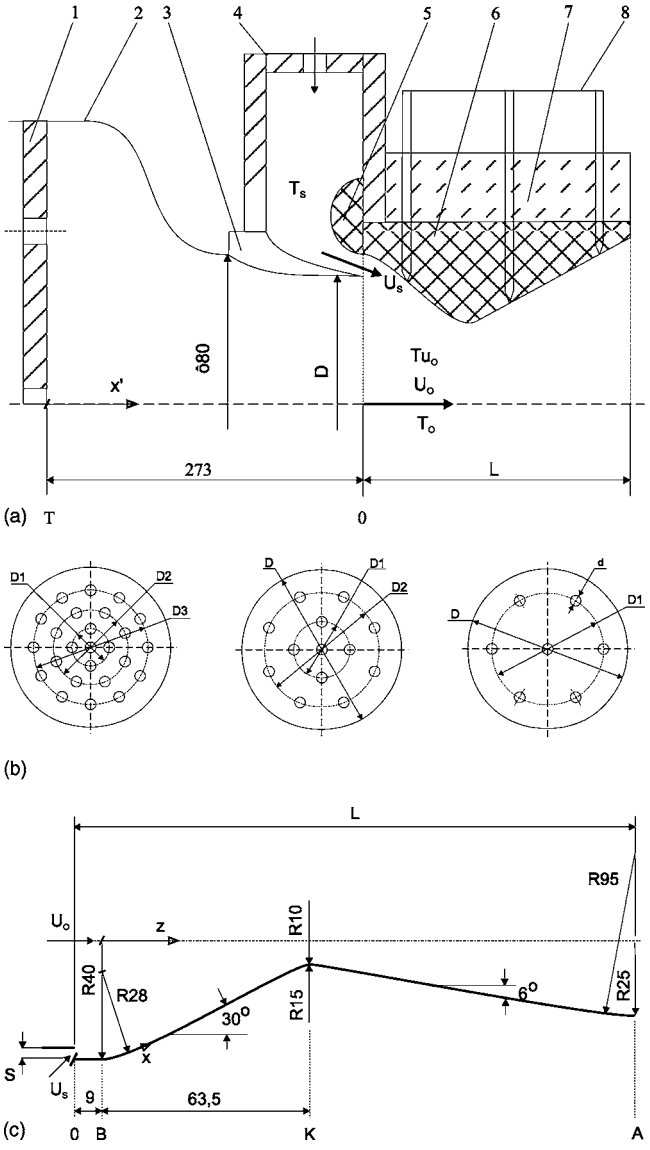

Fig. 1 (*a*) Schematic of the test section: 1—turbulizer, 2—convergent part of the settling-chamber, 3—partition, 4—injection chamber, 5—fairing, 6—test section, 7—thermal insulation, and 8—thermocouples; (*b*) turbulence generators (T in (a)); (*c*) geometry of the Laval-nozzle contour

rounded off with radius $r=0.7\times R_1=28$ mm; in the nozzle-throat section, the rounding-off radius was $r=1.5\times R_k=15$ mm.

To turbulize the main flow, turbulence generators were used, prepared as disks with drilled holes. A schematic of the turbulizers is shown in Fig. 1(*b*). The turbulizers were fabricated strictly observing the recommendations given in [9]. The thickness of the steel disks was 4 mm, and their diameter was $D=219$ mm. The diameter of the holes was $d=10$ mm. Various freestream turbulence numbers were obtained with disks having different numbers of holes. Uniform profiles of flow velocity and turbulence intensity at the exit plane of the slot were obtained due to the compression of the flow in the convergent part 2. The measured energy spectra of velocity fluctuations displayed no local peaks. The fluctuations were isotropic within 20%. The integral streamwise turbulence scale was $L=6$–10 mm at $Tu_0=7$–15% and $L=5$ mm at $Tu_0=0.2\%$. The turbulence number Tu_0 at the inlet to the nozzle was 0.2% in the case without a turbulizer. With turbulizers having 25, 13, and 7 holes, freestream turbulence numbers of 7%, 12%, and 15% were obtained.

The range of stagnation pressure in the experiments was as follows: the stagnation pressure at the inlet to the nozzle in the design flow regime was $p_0=7.2\times10^5$ Pa; in the presence of compression shocks, this pressure decreased to $p_0=2\times10^5$ Pa. The injection parameter was $m=0.1$–0.3. The turbulence number of the flow at the inlet to the channel was $Tu_0=0.2$–15%. The main-flow temperature and the injected-flow temperature were $T_0=292$ K and $T_s=360$ K, respectively. The flow velocity at the inlet to the nozzle was $U_0=15$ m/s, and the Mach number at the nozzle exit plane in the design regime was $M=3.4$. The adiabatic-wall temperature was measured by chromel-copel thermocouples prepared from 0.2 mm dia wire. The holes for tapping the static pressure over the length of the nozzle were 0.4 mm dia. The mean and pulsating flow velocities in the subsonic part of the nozzle and in the cylindrical pipe were measured with the help of a DISA 55M two-wire anemometric system. To measure the temperatures, pressures, velocities, turbulence numbers, and other flow quantities, an automated data acquisition and processing system was used [22–24]. The basic errors in the experiment were as follows: temperature, 0.2–3%;pressure, 0.5–2.5%; flow velocity, 0.3–4%, mean-square velocity fluctuations, 3–8%; and film-cooling efficiency, 3–10%.

3 Inlet Conditions

First of all, we examined the dynamic characteristics of the flow at the inlet to the test section. The measured fields of the mean and pulsating flow velocity at the slot exit plane showed that the injected flow was uniform within 2–5% and 6–10% in terms of the mean and pulsating velocity, respectively. The profiles of flow velocity in the boundary layer at the Reynolds number $Re_0=8\times10^6$ in the slot exit plane are shown in Figs. 2(*a*) and 2(*b*) for the minimum and maximum turbulence number. The same figure shows the power function [2]

$$\frac{U}{U_m}=A(n)\left(\frac{y}{\delta^{**}}\right)^{\frac{1}{n}} \tag{1}$$

fitting the velocity profile, for two values of the power exponent, $1/n=1/7$ ($A(n)=0.717$), and $1/n=1/12$ ($A(n)=0.797$).

It is seen from the figure that the measured profiles of flow velocity in the boundary layer well agree with the power velocity profile (1): In the low-turbulent flow ($Tu_0=0.2\%$), the measured flow velocity profile is best fitted with the power exponent $1/n=1/7$, whereas in the high-turbulence flow the exponent n grows in value (in line with the data of [9]), so that at $Tu_0=15\%$ the best fit could be obtained with $1/n=1/12$.

Based on the data obtained and on the data previously reported by other authors, we adopted the following empirical linear dependence of the power exponent n in (1) on Tu_0:

$$n=n_0+bTu_0 \tag{2}$$

Here, $n_0=5.5$, $b=0.43$, and the dimensions of Tu_0 is in percent.

In Fig. 2(*b*), the measured flow velocity profiles are plotted in the universal coordinates; the line in this figure shows the dependence

$$\varphi=\frac{1}{k}\ln\eta+B+\frac{\Pi}{k}f\left(\frac{y}{\delta}\right) \tag{3}$$

where Π is the flow profile parameter and $f(y/\delta)$ is the Coles-Hinze wake function.

The measured profiles closely follow the linear dependence for viscous sublayer, with the "law of wall" in the turbulent core of the flow (with turbulence constants $k=0.41$ and $B=5.0$) and with the "law of wake" with the Coles-Hinze wake function (3) in the outer region of the boundary layer. The velocity profile parameter varies from $\Pi=0.55$ in the low-turbulent flow (displacement thickness $\delta^*=0.37$ mm) to a negative value of $\Pi=-0.25$ at $Tu_0=15\%$ ($\delta^*=2.46$ mm), in line with the experimental data of [9,10].

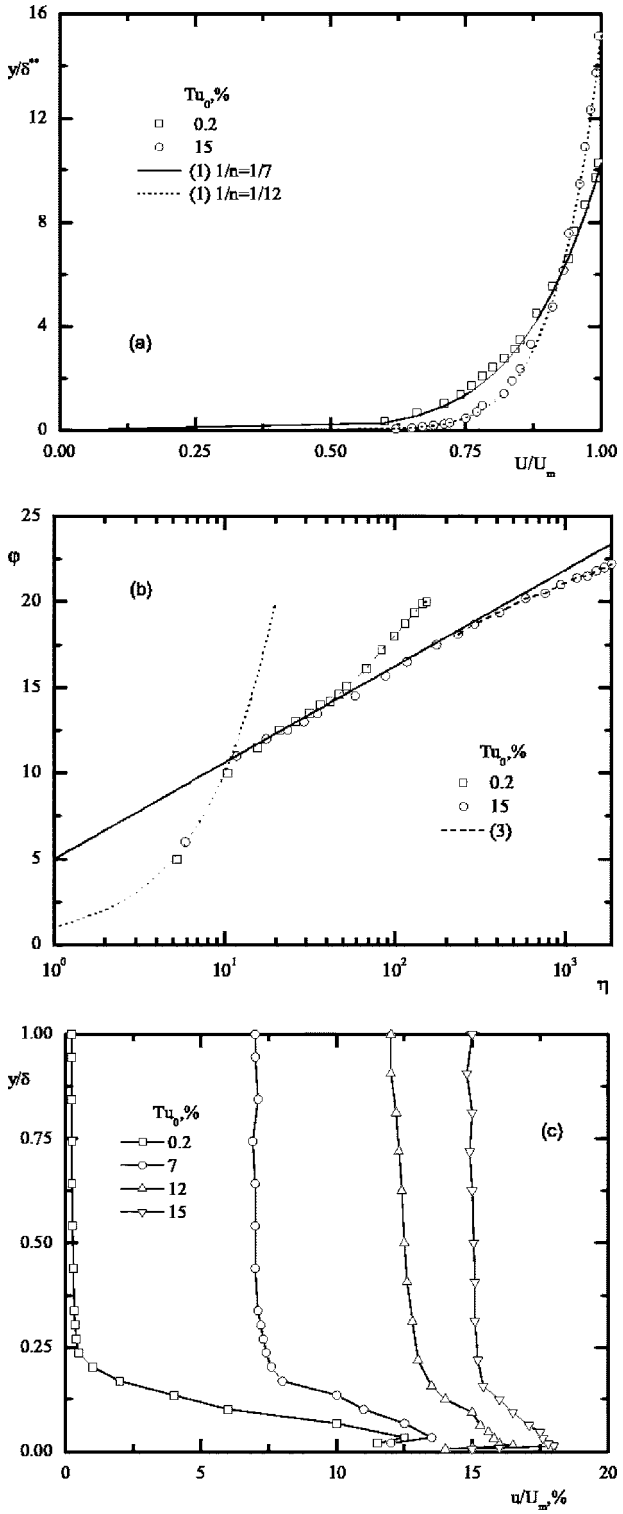

Fig. 2 (*a*) Profile of flow velocity in the main-flow boundary layer at the slot exit plane, (*b*) profile of flow velocity in the main-flow boundary layer in the universal coordinates, and (*c*) distribution of streamwise velocity fluctuations in the main-flow boundary layer

The distribution of streamwise velocity fluctuations in the boundary layer is shown in Fig. 2(*c*). The profiles show that, for all examined levels of freestream turbulence, we dealt with a developed turbulent near-wall flow displaying a characteristic maximum at the border between the viscous sublayer and the turbulent

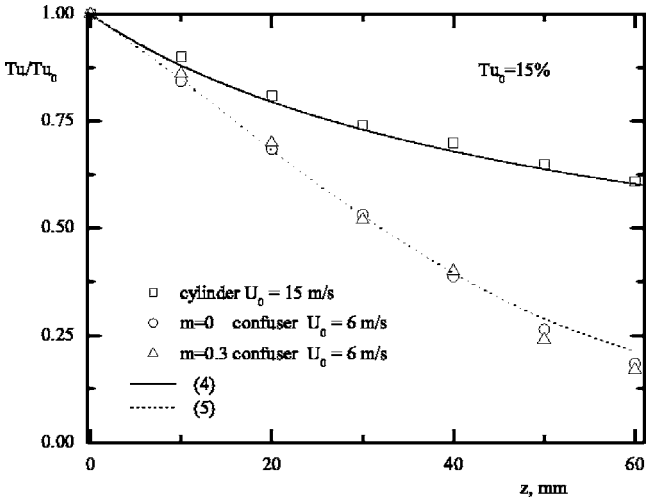

Fig. 3 Degeneration of turbulence in the convergent part of the nozzle and in the cylindrical pipe

core of the flow. With increase in the turbulence number, the fluctuations grow in intensity both in the outer and near-wall regions. For instance, in the low-turbulence flow ($Tu_0=0.2\%$) the intensity of the fluctuations at the maximum amounted to 12.5%; in the high-turbulence flow ($Tu_0=15\%$), the same value was 17.6%.

The profile of flow velocity in the annular slot was almost parabolic, with boundary-layer thickness equal to half the slot height. The turbulence number in the flow core was 4–6%.

4 Distribution of Flow Quantities Over the Length of the Nozzle

The turbulence decay pattern along the axis of the subsonic part of the nozzle (convergence semi-angle 30 deg) at the high freestream turbulence number is illustrated in Fig. 3. For comparison, the same figure presents data showing how the turbulence number Tu varies over the length of a cylindrical pipe at the inlet conditions identical to those for the converging flow. The coordinate z here is reckoned from the nozzle exit plane along the nozzle axis, and Tu_0 is the turbulence number at the inlet to the convergent part of the nozzle.

Variation of Tu in a gradientless flow is given by the law for uniform isotropic turbulence [17]

$$\frac{1}{\mathrm{Tu}^2} = c\left(\frac{x'}{M} + \frac{x'_e}{M}\right)^m \tag{4}$$

Here c and m are some constants, M is the cascade constant, and x'_e is the coordinate of the effective origin. The origin of x' coincides with the turbulizer position (indicated as T in Fig. 1(*a*)). Two characteristic sizes, the diameter of the holes and their spacing, govern the generated turbulence. For the perforated-disk-type turbulizers used in the present study, the choice of the dependence for turbulence-energy degeneration presents a problem because such turbulizers have several characteristic sizes, each influencing the generation and decay of velocity fluctuations. Yet, as it was shown in [9,19], relation (4) also applies to such turbulizers provided that, under the characteristic scale M, the hole diameter d is understood (see Fig. 1(*b*)). The least-squares method was applied to the experimental data to evaluate the coefficients in (4) for turbulizers with different numbers of holes. The power exponent was found to fall in the range $m=1.1$–1.6; these values refer to the early stage of turbulence decay [9,17].

However, as it follows from the figure, the turbulence decay pattern in accelerated flow is entirely different. The acceleration of the flow results in a rapider decay of turbulence intensity com-

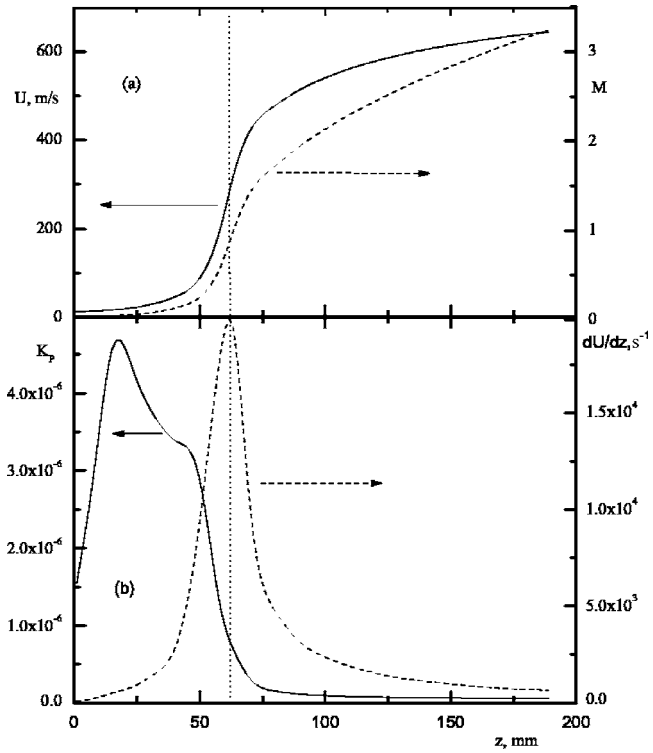

Fig. 4 Distribution of flow velocity, Mach number, acceleration factor, and velocity gradient over the length of the nozzle

pared to the case of cylindrical pipe. In a first approximation, variation of fluctuations can be predicted based on the theory of rapid deformation [17]

$$\frac{\mathrm{Tu}}{\mathrm{Tu}_0} = \frac{1}{c}\left[\frac{c}{2} + \frac{3}{4c^3\alpha}\ln\frac{1+\alpha}{1-\alpha}\right]^{1/2}, \quad \alpha^2 = 1 - 1/c^3 \tag{5}$$

Such a strong suppression of turbulence in the accelerated flow is expected to make the effect of flow turbulence on heat-transfer processes less pronounced compared to the case of cylindrical pipe.

The film-cooling efficiency in the Laval nozzle was examined for injection parameters $m \leqslant 0.3$. In this connection, data were obtained concerning the influence of the wall jet on the distribution of velocity fluctuations along the convergent part of the nozzle; these data are presented in Fig. 3. The experimental data show that the coolant flow injected at $m \leqslant 0.3$ had almost no effect on the measured distribution of turbulent fluctuations.

The gas-dynamic parameters of the flow along the nozzle were calculated assuming one-dimensional isentropic expansion of the flow. Figure 4(*a*) shows the predicted distributions of flow velocity and Mach number over the length of the nozzle. For the initial parameters $p_0 = 7.2 \times 10^5$ Pa, $T_0 = 292$ K, and $M_0 = 0.044$, the predicted flow velocity at the nozzle throat is $U_k = 330$ m/s, and the Mach number at the nozzle exit plane is $M = 3.4$.

In studies dealing with accelerated flows, it is common practice to use, as determining parameters, the streamwise velocity gradient dU/dz and the flow acceleration parameter K_p. For one-dimensional isentropic flow, the Kays acceleration parameter is given by the expression

$$K_p = \frac{\pi\mu D\dfrac{dD}{dz}\left(1 - \dfrac{k-1}{k+1}\lambda^2\right)}{2\rho_k U_k F_k(\lambda^2 - 1)} \tag{6}$$

Here μ and D are the viscosity and the nozzle diameter in the current cross section, and the subscript k refers to flow quantities

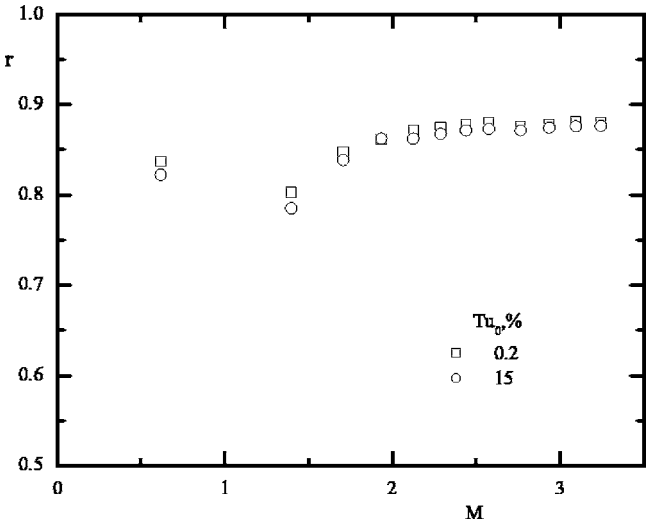

Fig. 5 Effect of Mach and turbulence numbers on the distribution of recovery factor in the nozzle

at the nozzle throat. The distribution of flow acceleration parameter for the inlet conditions of Fig. 4(*a*) is shown in Fig. 4(*b*). It is seen from the figure that the acceleration parameter varies nonmonotonically over the length of the nozzle, displaying a maximum in its subsonic part. The maximum value of K_p, $K_p = 4.75 \times 10^{-6}$, is observed in the inlet region, at the junction between two parts of the nozzle, the arc of the circle of radius $R = 28$ mm and the straight line making the angle $\varphi = 30$ deg with the nozzle axis, i.e., at the beginning of the conic part of the nozzle (see Fig. 1(*c*)).

For the longitudinal velocity gradient, the following dependence was obtained:

$$\frac{dU}{dz} = \frac{2U_k\dfrac{dD}{dz}\lambda\left(1 - \dfrac{k-1}{k+1}\lambda^2\right)}{D(\lambda^2 - 1)} \tag{7}$$

As it follows from Fig. 4(*b*), the velocity gradient dU/dz increases in the subsonic and decreases in the supersonic part of the nozzle. For the adopted inlet conditions, this gradient attains its highest value of $dU/dz = 2 \times 10^4$ s^{-1} near the nozzle throat, where the transonic transition occurs.

In the experiments, we also examined the effect of enhanced freestream turbulence on the distribution of wall static pressure and temperature over the length of the nozzle. The measurements performed at $p_0 = 7.2 \times 10^5$ Pa ($\mathrm{Tu}_0 = 0.2\%$) proved that no separation occurred in the flow. A good agreement between the experimental data and the values predicted for isentropic flow was observed. The wall stagnation temperature decreases with increasing Mach following the law:

$$\frac{T_w^*}{T_0} = \frac{1 + r\dfrac{k-1}{2}M^2}{1 + \dfrac{k-1}{2}M^2} \tag{8}$$

The turbulization of the flow has little effect on the distribution of static pressure and adiabatic-wall stagnation temperature.

The recovery factor r is known to depend on many parameters [2]. The experimental curves of r versus Mach number at various freestream turbulence numbers are shown in Fig. 5. The recovery factor displays a minimum at the nozzle throat. An increase in the turbulence number from 0.2% to 15% rather weakly affects the magnitude of the recovery factor. As the turbulence number increases, the recovery factor in the subsonic part of the nozzle slightly decreases. In the supersonic flow, turbulization exerts al-

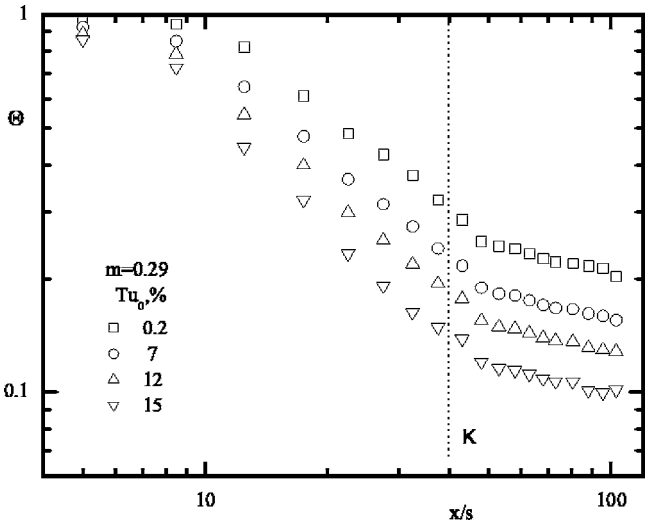

Fig. 6 Effect of initial turbulence on the film-cooling efficiency in the nozzle

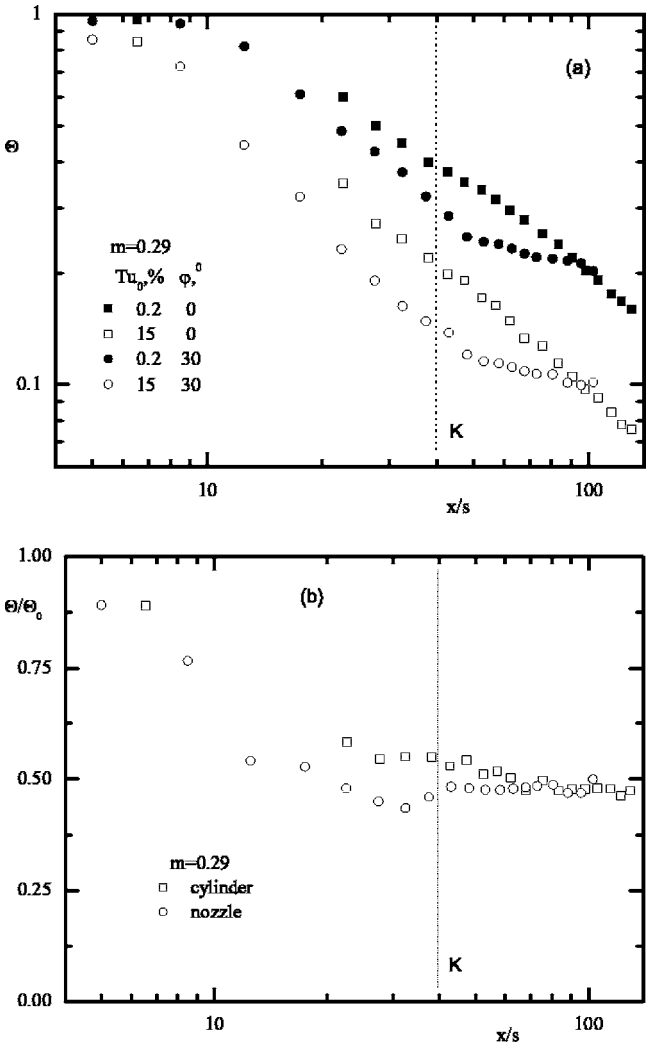

Fig. 7 Effect of freestream turbulence on the film-cooling efficiency in the cylindrical pipe and in the Laval nozzle

most no influence on the recovery factor, equal to $r=0.885$, in line with the well-known correlation $r=\sqrt[3]{\mathrm{Pr}}$ [2]. This relation can be used to determine the adiabatic-wall temperature, including the case of high-turbulence flows.

With injection of a protective gas flow, a question arises about the effect of the injected flow on the distribution of flow quantities over the length of the nozzle. For a protecting film organized by injecting a coolant through a tangential slot, it was found in [22] that the protective gas flow injected at the nozzle inlet has no influence on the distribution of static pressure and equilibrium wall temperature in supersonic nozzle nor does it affect the recovery factor. The present experiments performed in the high-turbulence flow ($\mathrm{Tu}_0=15\%$) showed that the wall jet ($m\leqslant 0.3$) had no effect on the distributions of adiabatic-wall pressure and temperature either. The recovery factor here was $r=0.885$.

5 Gas-Film-Cooling Efficiency in the Nozzle Under Design Conditions

The film-cooling efficiency in the cooled nozzle was calculated as

$$\Theta=\frac{T_w-T_w^*}{T_S-T_0} \tag{9}$$

Here, T_w and T_w^* are the adiabatic-wall temperatures in the current cross section of the nozzle in the presence and absence of the film. Typical results concerning the cooling efficiency in the Laval nozzle in the design flow regime are shown in Fig. 6. The coordinate x is reckoned from the slot exit plane along the generatrix of the nozzle (see Fig. 1(*c*)). The coordinate $x/s=40$ in Figs. 6, 7, and 9 refers to the nozzle throat K (see Fig. 1(*c*)). As it is seen from Fig. 6, the curves of film-cooling efficiency for different freestream turbulence numbers behave similarly; they descend rapidly in the subsonic region and more slowly in the supersonic region. This behavior can be attributed to the compensating effect due to flow compressibility, which becomes more pronounced as the Mach number increases along the length of the nozzle [2].

As it follows from Fig. 6, enhanced external turbulence has a profound effect on film-cooling efficiency. For instance, with increase in the freestream turbulence number from $\mathrm{Tu}_0=0.2\%$ to 15% the film-cooling efficiency decreases more than twofold. This decrease occurs not only in the initial cross sections, but also throughout the entire length of the subsonic part of the nozzle, where, according to the data of Fig. 3, strong turbulence degeneration occurs. At increased external turbulence, the large-scale main-flow pulsations in the subsonic part of the nozzle intensively smear the wall jet, and in the supersonic region the quantity Θ therefore remains low.

It was shown previously that the turbulence intensity in a converging flow decreases along the channel more rapidly than in a cylindrical pipe. It is of interest to compare the film-cooling efficiency in a flow through cylindrical pipe and in a film-cooled nozzle. This comparison is given in Fig. 7(*a*). The comparison was performed for identical injection parameters ($m=0.29$) and identical flow velocities ($U_0=15$ m/s) at the inlet to the channel for $\mathrm{Tu}_0=0.2\%$ and $\mathrm{Tu}_0=15\%$. With such values of initial parameters, the flow moves in the channel at almost constant velocity ($dU/dz\approx 0$). In the convergent part of the Laval nozzle, the maximum velocity gradient amounts to $dU/dz\approx 2\times 10^4\ \mathrm{s}^{-1}$ (see Fig. 4). As it follows from Fig. 7(*a*), the experimental points for the film-cooling efficiency in the low-turbulence nozzle flow lie 20–30% lower than the data for the flow through cylindrical pipe; this difference reflects the effect due to flow acceleration. These data comply with the data of [22] obtained for a nozzle with the convergence angle $\varphi=30$ deg. In the high-turbulence flow ($\mathrm{Tu}_0=15\%$), the effect of flow acceleration on the film-cooling efficiency is more pronounced; this circumstance results in that the film-cooling efficiency here is 30–40% decreased compared to the case of gradientless flow. By the exit from the nozzle, the values of Θ closely approach the data for the film-cooled pipe.

The data in Fig. 7(*b*) demonstrate the effect of freestream turbulence on the film-cooling efficiency in gradientless flow and in flow with acceleration. The initial data here are the data in Fig. 7(*a*). The dashed line shows the position of the nozzle throat ($x/s=40$). The parameters Θ_0 and Θ are the cooling efficiencies for $Tu_0=0.2\%$ and 15%. As it is seen from Fig. 7, at $x/s\approx 40$ the efficiency factor Θ in the high-turbulence flow (in the nozzle and in the cylindrical pipe) decreases approximately twofold compared to that (Θ_0) in the low-turbulence flow. Yet, in the cylindrical pipe the value of Θ/Θ_0 decreases in the region $x/s<40$ more smoothly, whereas in the nozzle the major change of Θ/Θ_0 is observed near the slot exit plane. For the nozzle flow, the ratio Θ/Θ_0 in its supersonic part is roughly uniform, amounting to $\Theta/\Theta_0=0.5$. The comparison shows that at $x/s>40$ the turbulization has roughly identical effects on the thermal mixing processes in the flow with pressure gradient and in gradientless flow. At $x/s<40$, i.e., at the beginning of the initial heated length, the effect of Tu_0 on the cooling efficiency is more pronounced in the accelerated flow compared to gradientless flow.

Over the initial heated length, the effect due to freestream turbulence is more pronounced in the accelerated flow compared to the flow without acceleration. Consider the mechanism of the "anomalous" behavior of the efficiency factor. Under the conditions of the present experiments, the level of fluctuations in the initial mixing region of the wall jet and the free flow is the same both for the film-cooled cylindrical pipe and for the film-cooled nozzle. Farther downstream, the mechanism governing the thermal mixing is controlled by two flow regions: the near-wall boundary layer and the jet boundary layer. For a wall jet in a cylindrical pipe, the processes are well understood; another matter is a wall jet in a converging nozzle flow. Here, relaminarization may occur in the near-wall zone, and the intensity of fluctuations in the jet boundary-layer flow may increase. In the latter case, the turbulence in the core of the flow considerably decreases over the length of the nozzle [19]. The relaminarization makes the film-cooling efficiency factor rise, whereas an increase in the turbulence-energy level interferes with this process. Thus, the main factors defining the behavior of film-cooling efficiency in high-turbulence accelerated flows are the level of turbulent fluctuations in the initial mixing region of the main and jet flows, and the behavior of turbulence energy in the jet boundary layer of the film flow. This result does not confirm the opinion expressed in [11,12] that, under the joint action of acceleration and turbulization, the main determining factor is the favorable pressure gradient.

6 Gas Screen Under Off-Design Conditions

It is well known that, in the supersonic part of a Laval nozzle in the regimes with flow overexpansion, the heat-transfer processes display specific features resulting from compression-shock interaction with the boundary layer [2,25]. As it was shown in [23], the film-cooling efficiency substantially decreases in the flow direction in the downstream region of the static-pressure rise.

Figure 8 shows the distributions of static pressure and adiabatic-wall stagnation temperature under off-design conditions. It is seen from the figure that the regime with $p_0=7.2\times10^5$ Pa is the design flow regime, whereas other regimes refer to off-design conditions. As the settling-chamber pressure decreases from 7.2×10^5 Pa to 2×10^5 Pa, the compression shock moves from the nozzle outlet toward the nozzle throat. At low settling-chamber pressure ($p_0=2\times10^5$ Pa), the pressure monotonically increases along the supersonic part of the Laval nozzle, starting from the region where the compression shock interacts with the boundary layer ($F/F_k\approx1.34$). The pressure rise in the compression-shock zone is insignificant, and in this case, the wall flow shows no separation. As the settling-chamber pressure increases, the compression-shock zone moves downstream and the pattern of shock interaction with the boundary layer changes [23,25]. Such a

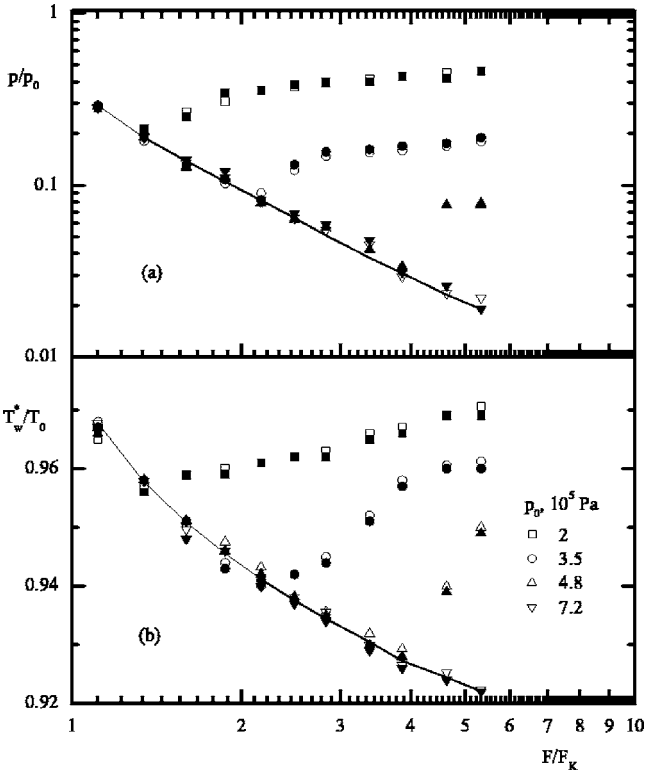

Fig. 8 Distribution of wall pressure (*a*) and temperature (*b*) along the nozzle in off-design regimes (symbols—experimental data, line—predicted data): open symbols—$Tu_0=0.2\%$, full symbols—$Tu_0=15\%$, line—data predicted by the model assuming one-dimensional isentropic expansion of the flow

flow was observed at a pressure close to its design value ($p_0=4.8\times10^5$ Pa). In this regime, the compression-shock zone is more localized, with a more pronounced rise of pressure and with flow separation from the wall. Farther downstream the pressure is practically uniform, roughly equal to the pressure at the nozzle exit plane. To obtain the position of the compression shock, it is common practice to use the generalizing relation [25]

$$\frac{p_1}{p_0}=\frac{2}{3}\left(\frac{p_2}{p_0}\right)^{1.2} \tag{10}$$

Here, p_1 is the pressure in the initial part of the compression region (which can be predicted by the one-dimensional isentropic approximation), and p_2 is the postshock pressure, in the first approximation close to the pressure p_A at the nozzle exit plane. Our experiments with separated flows ($p_0=4.8\times10^5$ Pa) proved the pressure in the compression-shock zone to follow the dependence (10).

The experiments showed that, under off-design conditions, the turbulization of the flow did not affect the distributions of static pressure and adiabatic-wall stagnation temperature over the length of the nozzle. Yet, it should be noted that in the high-turbulence stream with $Tu_0=15\%$ for the separation flow ($p_0=4.8\times10^5$ Pa) considerable fluctuations of wall temperature were observed at the position of the compression shock.

The data on the film-cooling efficiency at various turbulence intensities in an off-design regime are presented in Fig. 9. Like in the case of the design regime, the freestream turbulence results in substantial intensification of thermal mixing processes of the wall jet with the main flow. The turbulization of the main flow deteriorates the protective properties of the protecting film over the entire length of the nozzle, including the zone behind the compression shock. As a result, the value of Θ for $Tu_0=15\%$ decreases com-

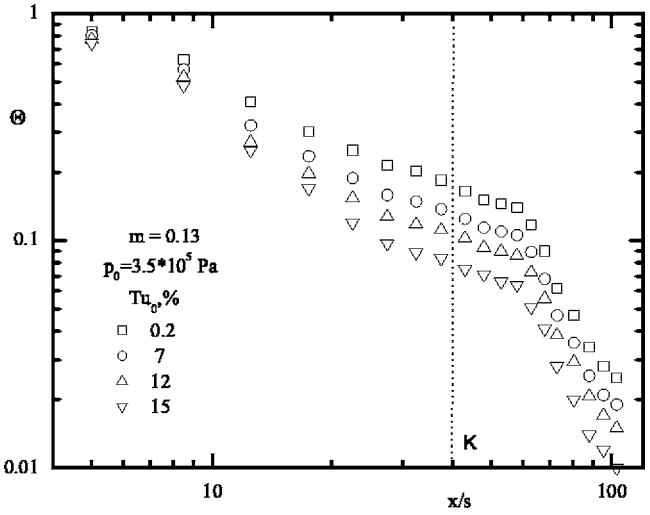

Fig. 9 Effect of freestream turbulence number on the film-cooling efficiency in the Laval nozzle under off-design conditions

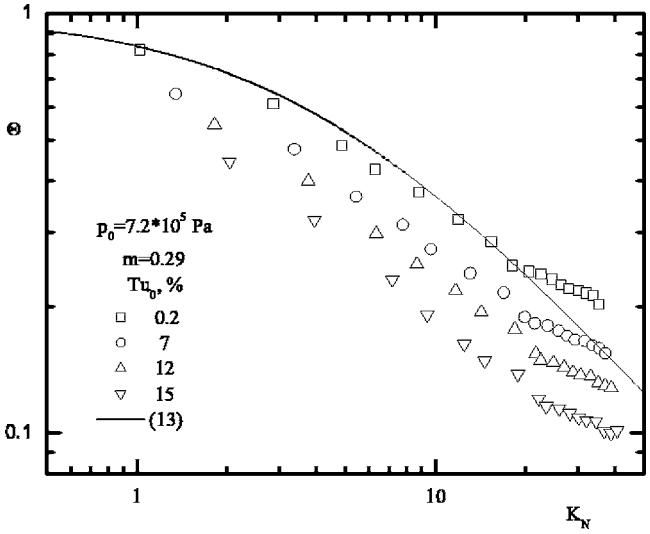

Fig. 10 Film cooling in the nozzle flow: Comparison between experimental and predicted data

pared to the case of low-turbulence flow ($Tu_0=0.2\%$) more than twofold in the nozzle throat zone. Thus, the major feature of the off-design regime is increase in the rate of fall of film-cooling efficiency in the downstream region of the point where the compression shock interacts with the boundary layer. This feature is indicative of considerable thermal mixing that occurs inside the boundary layer in this zone. The mechanism determining the sharp change in the behavior of adiabatic-wall temperature is related with the formation of compression shocks in off-design flow regimes; this matter calls for further investigation.

7 Generalization of Data on Film-Cooling Efficiency

To generalize the experimental data on the film-cooling efficiency in accelerated compressible flows with an arbitrary distribution of flow velocity at the outer edge of the boundary layer, we used the integral approach based on the Kuteteladze-Leont'ev asymptotic theory of boundary layer [2].

In low-turbulence flows without a streamwise velocity gradient, good results can be obtained using with the dependence [2]

$$\Theta = \left[1 + 0.016\beta_{\max}^{1.25}\Psi\frac{\mathrm{Re}_{\Delta x}}{\mathrm{Re}_s^{1.25}}\left(\frac{\mu_0}{\mu_s}\right)^{1.25}\right]^{-0.8} = [1 + CK_0]^{-0.8} \tag{11}$$

with $C=0.016\beta_{\max}^{1.25}\Psi$ and $K_0=\mathrm{Re}_{\Delta x}/\mathrm{Re}_S^{1.25}(\mu_0/\mu_S)^{1.25}$, $\Delta x=x-x_1$ Here, the form parameter

$$\beta = \frac{(\mathrm{Re}_T^{**})_{\mathrm{ad}}}{(\mathrm{Re}_T^{**})_q} \tag{12}$$

is used to allow for the deformation of the temperature field in the adiabatic-wall boundary layer compared to the flow with heat transfer. Expression (11) also contains the relative heat-transfer function

$$\Psi = \left(\frac{\mathrm{St}}{\mathrm{St}_0}\right) \quad \text{at} \quad \mathrm{Re}_T^{**} = \text{idem}$$

which allows for the variation of the Stanton criterion under the action of disturbing factors (nonisothermality, injection, compressibility, etc.) under the conditions of interest compared to the standard conditions with identical Re_T^{**} numbers based on the energy thickness δ_T^{**}. Previous generalization of experimental data on film-cooling efficiency in a high-turbulence flow through pipe was achieved with the complex $K=CK_0$, taking into account flow turbulization [14,15].

The authors of [22] proposed the following interpolation formula for the film-cooling efficiency in Laval nozzle:

$$\Theta = [1 + A\beta_{\max}^{1.25}K_N]^{-0.8} = [1 + CK_N]^{-0.8} \tag{13}$$

In (13), the generalizing complex is

$$K_N = \left(\frac{D_k}{D_1}\right)^{1.25}\frac{\mathrm{Re}_k}{\mathrm{Re}_s^{1.25}}\left(\frac{\mu_0}{\mu_s}\right)^{1.25}\int_{\bar{x}_1}^{\bar{x}}\Psi\left(\frac{\mu_w}{\mu_0}\right)^{0.25}\left(\frac{D_1}{D}\right)^{0.75}d\bar{x} \tag{14}$$

Preliminary generalization of the present experimental data was performed by the procedure of [22] using the complex

$$K_N = \left(\frac{D_k}{D_1}\right)^{1.25}\frac{\mathrm{Re}_k}{\mathrm{Re}_s^{1.25}}\left(\frac{\mu_0}{\mu_s}\right)^{1.25}\int_{\bar{x}_0}^{\bar{x}}\Psi_M\left(\frac{D_1}{D}\right)^{0.75}d\bar{x} \tag{15}$$

which allows for the effects due to velocity gradient and compressibility under quasi-thermal experimental conditions ($\Psi_T \approx 1$, $(\mu_0/\mu_S)^{1.25}\approx 1$). The generalized data are shown in Fig. 10. As it is seen from Fig. 10 for the freestream turbulence number $Tu_0=0.2\%$, a satisfactory agreement between the experimental data and the dependence (13) was achieved with $C=A\beta_{\max}^{1.25}=0.25$. For larger values of Tu_0, some deviation of experimental points from the values predicted by Eq. (13) is observed. Thus, the experimental data cannot be generalized versus turbulence intensity if treated using dependence (13) and generalizing complex (15), previously used for supersonic gas flows in [2,22]. The latter proves that the complex (15) and expression (13) can be applied only to low-turbulence flows, whereas in the case of high-turbulence flow modification of (15) is necessary.

In the Kutateladze-Leont'ev integral method, it is possible to take into account a high level of initial turbulence in compressed accelerated flow. In the present study, in estimating the film-cooling efficiency by Eq. (13), enhanced freestream turbulence can be taken into account through the following parameters:

(a) For an accelerated compressible flow the form parameter $\beta_{\max}$ can be calculated by formula (12). The Kutateladze-Leont'ev theory [2] predicts a weak dependence of $\beta_{\max}$ on the Mach number and streamwise pressure gradient. That is why for high-turbulence compressible accelerated flows the determining factor is the effect on $\beta_{\max}$ due to turbulence. Thus, to determine the parameter $\beta_{\max}$ in (13), for the form parameter one can use the analytical dependence $\beta_{\max}=n+2$ [2] with the power exponent $n=f(Tu_0)$ in the power profile of flow velocity given by Eq. (2).

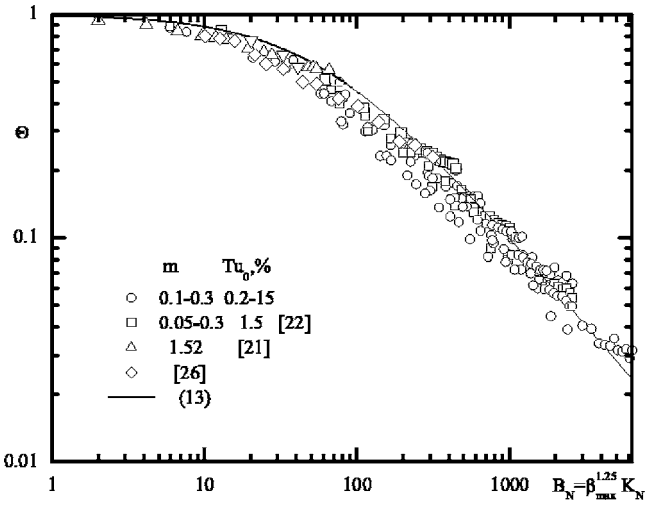

Fig. 11 Generalization of experimental data on the film-cooling efficiency in nozzle flows

(b) As it was shown in [2], under the joint action of several factors, the total effect on heat transfer can be taken into account assuming additive influence of these factors. Hence, the total effect due to nonisothermality, compressibility and enhanced turbulence on the relative heat-transfer function can be represented as

$$\Psi = \Psi_T \Psi_M \Psi_{\mathrm{Tu}} \tag{16}$$

$$\Psi_T = \left(\frac{2}{\sqrt{\Psi}+1}\right)^2, \quad \Psi_M = \left[\frac{\arctan M\sqrt{\dfrac{r(k-1)}{2}}}{M\sqrt{\dfrac{r(k-1)}{2}}}\right]^2,$$

$$\Psi_{Tu} = 1 + c\mathrm{Tu}_0 \tag{17}$$

(c) Flow turbulization makes the initial heated length x_1 substantially shorter [14,15]. Hence, the parameters $\overline{x_1}$ and D_1 in (15) must be determined with allowance for the effect due to freestream turbulence intensity; this yields the following modified formula for the initial heated length:

$$\frac{x_1}{s} = b_{\mathrm{Tu}}\frac{1+m_1}{|1-m_1|}\left(0.112+\frac{0.036}{m_1}\right), \quad b_{\mathrm{Tu}} = \frac{1}{1+a\mathrm{Tu}_0}, \quad a = 0.06$$

The experimental data on film-cooling efficiency shown in Fig. 11 were treated by the proposed procedure using the modified complex

$$B_n = \beta_{\max}^{1.25}K_n = \beta_{\max}^{1.25}\left(\frac{D_k}{D_1}\right)^{1.25}\frac{\mathrm{Re}_k}{\mathrm{Re}_s^{1.25}}\left(\frac{\mu_0}{\mu_s}\right)^{1.25} \times \int_{\overline{x_0}}^{\overline{x}} \Psi_T\Psi_M\Psi_{\mathrm{Tu}}\left(\frac{\mu_w}{\mu_0}\right)^{0.25}\left(\frac{D_1}{D}\right)^{0.75} d\overline{x}$$

$$\mathrm{Re}_k = \frac{\rho_0 u_0 D_0^2}{(\mu_0 D_k)}, \quad \mathrm{Re}_S = \frac{\rho_S u_S S}{\mu_S}, \quad \overline{x} = \frac{x}{D_k}, \quad \overline{x_1} = \frac{x_1}{D_1} \tag{18}$$

Here, x_1 is the initial length of the flow (where $\Theta \approx 1$), D and D_1 are the diameters of the channel in the cross sections x and x_1, $\mathrm{St}_0 = f(\mathrm{Re}, \mathrm{Pr})$ is the law of heat transfer for the standard conditions, n is the power exponent in the power profile of flow velocity, and Re_T^{**} is the Reynolds number based on the energy thickness δ_T^{**} in the thermal boundary layer.

The data on film-cooling efficiency for accelerated compressible turbulized flows are summarized in Fig. 11, which shows the experimental data of [21,22,26] and the data predicted, with the modified complex B_n, by the Kutateladze-Leont'ev procedure. The experimental data cover a wide range of injection parameters and Mach and turbulence numbers. As it is seen from Fig. 11, the experimental data reported by different authors can be generalized using the complex B_n (18). The experimental points closely coincide with the predicted curve (13). The good agreement between the experimental and predicted data is observed in a broad range of turbulence numbers, $\mathrm{Tu}_0 = 0.2-15\%$.

8 Conclusions

We experimentally examined the effect of enhanced freestream turbulence on the dynamic and thermal characteristics of flow in a supersonic axisymmetric Laval nozzle film cooled with a gas jet flow injected into the nozzle flow in the subsonic part of the nozzle.

The distribution of flow velocity and flow pulsations in the initial section of the flow complies well with the well-known regularities for high-turbulence flows. For the turbulence degeneration behind the turbulizers, one can use the formulas for the early stage of decay of uniform isotropic turbulence. The acceleration of the flow makes the turbulence more decreasing along the convergent part of nozzle compared to the case of a cylindrical pipe. In this case, the variation of velocity fluctuations obeys, in the first approximation, the theory of rapid deformation.

It is shown that initial freestream turbulence has almost no effect on the distributions of static pressure and adiabatic-wall temperature both in design and off-design regimes. In the design regime, these distributions well agree with those predicted by the one-dimensional approximation. The position and intensity of the compression shock does not depend on the turbulence level.

Enhanced flow turbulence results in a substantial decrease of film-cooling efficiency both in the subsonic and supersonic parts of the nozzle. In this case, the variation pattern of Θ along the nozzle closely resembles the pattern observed in the case of low-turbulence flow, exhibiting an abrupt decrease in the subsonic part of the nozzle and a slower one (due to the compensating influence of compressibility) in the subsonic part. The experimental data can be well generalized by dependence (13) using the complex B_n (18), which takes into account the velocity gradient, nonisothermality, compressibility, and freestream turbulence.

Turbulization of the flow in the off-design regime appreciably deteriorates the film-cooling efficiency both in the upstream and downstream region of the compression shock. The distribution of Θ over the length of the nozzle closely resembles the same distribution in the low-turbulence flow, displaying an abrupt decrease in the upstream region of the compression shock and an even more rapid decrease in the downstream region.

The performed study showed that the film cooling in the examined flow is primarily conditioned by the level of velocity fluctuations in the initial mixing zone of the wall jet and the main flow. For low slot height-to-channel radius ratios the level of these fluctuations is controlled by epy freestream turbulence intensity. The flow-core turbulence, which appreciably decreases over the convergent part of the nozzle and affects the downstream processes at the edge of the boundary layer, exerts a much weaker influence. This result disagrees with the opinion expressed in [11,12] that, under the conditions of joint action of flow acceleration and turbulization, the major determining factor is the favorable pressure gradient.

Acknowledgment

This work was supported, in part, by the Program of the President of the Russian Federation for supporting leading scientific schools (Grant No. 1308.2003.8).

Nomenclature

a = speed of sound
$c = U/U_1$ = flow acceleration factor
D, R = diameter, radius
F = area
$K_p = (\mu/\rho U^2)(dU/dx)$ = Kays acceleration parameter
k = adiabatic exponent, specific heat ratio
L, l = characteristic size, turbulence macroscale
$M = U/a$ = Mach number
$m = \rho_s U_s/\rho_0 U_0$ = injection parameter
$m_1 = U_s/U_0$ = jet-to-flow velocity ratio
p = pressure
$\mathrm{Pr} = \mu c_P/\lambda$ = Prandtl number
r = recovery factor of temperature
$\mathrm{Re} = \rho U L/\mu$ = Reynolds numbers
$\mathrm{Re}_0 = \rho_0 U_0 D_0/\mu_0$ = Reynolds numbers
$\mathrm{Re}_s = \rho_s U_s s/\mu_s$ = Reynolds numbers
$\mathrm{Re}_{\Delta x} = \rho_0 U_0 (x - x_1)/\mu_0$ = Reynolds numbers
$\mathrm{Re}^{**} = \rho U \delta^{**}/\mu$ = Reynolds numbers
s = slot height
$\mathrm{St}_0 = q_w/[\rho c_p U(T_w - T_w^*)]$ = Stanton number
$\mathrm{St}_0 = f(\mathrm{Re}, \mathrm{Pr})$ = power law of heat transfer under standard conditions (gradientless isothermal flow over a plate without blowing)
T = temperature
$\mathrm{Tu} = \sqrt{(\langle u^2\rangle + \langle v^2\rangle + \langle w^2\rangle)/3}/U$ = turbulence number
U = flow velocity
u, v, w = fluctuating velocity components
x, z = coordinates along the nozzle contour and along the nozzle axis
x_1 = initial length of jet

Greek Symbols

$\beta = (\delta_T^{**})_a/(\delta_T^{**})_T$ = Kutateladze-Leont'ev form parameter
δ, δ_T = thickness of dynamic and thermal boundary layers
$\delta^*, \delta^{**}, \delta_T^{**}$ = displacement thickness, momentum thickness, and energy thickness, respectively
$\eta = yU_\tau/v$ = dimensionless coordinate
Θ = film-cooling efficiency
$\lambda = U/a_k$ = normalized velocity
μ = dynamic viscosity
ρ = density
$\varphi = U/u_\tau$ = dimensionless velocity
$\Psi = (\mathrm{St}/\mathrm{St}_0)_{\mathrm{Re}_T^{**}}$ = relative heat-transfer function with allowance for nonisothermality Ψ_T, compressibility Ψ_M, and turbulence number Ψ_{Tu}
$\psi = T_W/T_W^*$ = nonisothermality factor

Subscripts

0 = in the main flow, "standard" conditions
1 = over the initial length of flow
s = in the slot
T = thermal
Tu = turbulized
w = at the wall
$*$ = adiabatic conditions
$**$ = integral parameters
k = in the nozzle throat

References

[1] Goldstein, R. J., 1971, "Film cooling," *Advances in Heat Transfer*, T. F. Irvine and J. P. Hartnett, eds., Academic Press, New York, Vol. 7, pp. 321–379.
[2] Kutateladze, S. S., and Leontiev, A. I., 1990, *Heat Transfer, Mass Transfer and Friction in Turbulent Boundary Layer*, Hemisphere, New York, p. 305.
[3] Volchkov, E. P., 1983, *Film Cooling*, Nauka, Novosibirsk, p. 259 (in Russian).
[4] Leontiev, A. I., 1999, "Heat and Mass Transfer Problems in Film Cooling," ASME J. Heat Transfer, **121**, pp. 509–527.
[5] Srinivasan, V., Simon, T. W., and Goldstein, R. J., 2001, "Technical Issues Covered in Turbine 2000," Ann. N.Y. Acad. Sci., **934**, pp. 1–10.
[6] Fukukawa, T., and Ligrani, P. M., 2002, "Transonic Film Cooling Effectiveness From Shaped Holes on a Simulated Turbine Airfoil," J. Thermophys. Heat Transfer, **16**, pp. 228–237.
[7] Ligrani, P. M., Saumweber, C., Schulz, A., and Wittig, S., 2001, "Shock Wave-Film Cooling Interactions in Transonic Flows," ASME J. Turbomach., **123**, pp. 785–797.
[8] Kovalev, V. I., Lushik, V. G., Sizov, V. I., and Yakubenko, A. E., 1992, "3rd Parametric Turbulence Model: Numerical Investigation of Boundary Layer With Film Cooling," Fluid Dyn., **27**, pp. 35–42.
[9] Duyban, E. P., and Epik, E. Ya., 1985, *Heat and Mass Transfer and Hydrodynamics of High Turbulence Flows*, Naukova Dumka, Kiev, p. 296.
[10] Kondjoyan, A., Peneau, F., and Boisson, H. C., 2002, "Effect of High Free Stream Turbulence on Heat Transfer Between Plates and Air Flows: A Review of Existing Experimental Results," Int. J. Therm. Sci., **41**, pp. 1–16.
[11] Carlson, L. W., and Talmor, E., 1968, "Gaseous Film Cooling at Various Degrees of Hot-Gas Acceleration and Turbulence Levels," Int. J. Heat Mass Transfer, **11**, pp. 1695–1713.
[12] Launder, B. E., and York, J., 1974, "Discrete-Hole Cooling in the Presence of Free Stream Turbulence and Strong Favorable Pressure Gradient," Int. J. Heat Mass Transfer, **17**, pp. 1403–1409.
[13] Lebedev, V. P., Lemanov, V. V., Misyura, S. Ya., and Terekhov, V. I., 1991, "Effects of Turbulence Intensity on Slot Protection Performance," J. Appl. Mech. Tech. Phys., **32**, pp. 360–364.
[14] Lebedev, V. P., Lemanov, V. V., Misyura, S. Ya., and Terekhov, V. I., 1994, "Efficiency of a Protective Gas Film With High Injection Ratios in a Highly Turbulent Main Flow," J. Appl. Mech. Tech. Phys., **35**, pp. 49–52.
[15] Lebedev, V. P., Lemanov, V. V., Misyura, S. Ya., and Terekhov, V. I., 1995, "Effect of Flow Turbulence on Film Cooling Efficiency," Int. J. Heat Mass Transfer, **38**, pp. 2117–2125.
[16] Lebedev, V. P., Lemanov, V. V., and Terekhov, V. I., 1999, "Heat Transfer in a Wall Jet at High Turbulence of Cocurrent Stream," Int. J. Heat Mass Transfer, **42**, pp. 599–612.
[17] Batchelor, G. K., 1953, *The Theory of Gomogeneous Turbulence*, Cambridge University Press, Cambridge, England.
[18] Lebedev, V. P., Lemanov, V. V., Misyura, S. Ya., and Terekhov, V. I., 1995, "Effect of Turbulence Intensity on Film Cooling Efficiency in Laval Nozzle" High Temp., **16**(4), pp. 832–836.
[19] Lebedev, V. P., Lemanov, V. V., Misyura, S. Ya., and Terekhov, V. I., 1993, "Effect of Flow Acceleration and Initial Turbulence Level on Velocity Fluctuations," Fluid Dyn., **28**(5), pp. 624–629.
[20] Librizzi, J., and Gresci, R. J., 1964, "Transpiration Cooling of a Turbulent Boundary Layer in an Axisimmetric Nozzle," AIAA J., **2**(4), pp. 617–624.
[21] Nicolas, I. I., and Izard, M., 1971, "Protection Thermique de Tuyeres Supersoniques par Film Gazeux," Rech. Aerosp., **4**, pp. 197–208.
[22] Volchkov, E. P., Koz'menko, V. K., and Lebedev, V. P., 1977, "Experimental Investigation of a Gas Screen Effectiveness in a Supersonic Axisymmetric Nozzle, Izv. SSSR, Ser. Tekh. Nauk, **2**(8), pp. 40–46 (in Russian).
[23] Volchkov, E. P., Koz'menko, V. K., and Lebedev, V. P., 1980, "Film Cooling Efficiency in Laval Nozzle at Off-Design Flow Conditions," J. Appl. Mech. Tech. Phys., **21**(4), pp. 511–516.
[24] Lemanov, V. V., and Misyura, S. Ya., 1991, "Measurements in a Two-dimensional Turbulent Flow by Means of an Automated Hot-wire Anemometer," Izv. SSSR, Sib. Phys Tech. J., **3**, pp. 112–115, (in Russian).
[25] Kalt, S., and Badal, D. L., 1965, "Characteristics of a Conical Nozzle with Separated Flow on a Wall," J. Spacecr. Rockets, **2**, pp. 447–449.
[26] Rozhdestvensky, V. I., Baruyshev, Y. V., and Peiker, N. K., 1974, "Investigation of Film Cooling Efficiency With Pressure Gradient," Institute of Mechanics MSU, Moscow, Report No. 1526, p. 22.

Natural Convection Measurements for a Concentric Spherical Enclosure

Peter M. Teertstra
e-mail: pmt@mhtlab.uwaterloo.ca

M. Michael Yovanovich

J. Richard Culham

Microelectronics Heat Transfer Laboratory,
Department of Mechanical Engineering,
University of Waterloo ,
Waterloo, Ontario, Canada N2L 3G1

An experimental test program is described for the measurement of natural convection for an isothermal, heated sphere centrally located in an isothermal, cooled spherical enclosure. A transient test method is used in a reduced pressure environment to provide data for a wide range of Rayleigh number, from the limiting case of laminar boundary layer convection to the diffusive limit. Tests are performed using a fixed outer diameter for four different inner sphere diameters, resulting in diameter ratios in the range $1.5 \leqslant d_o/d_i \leqslant 4.8$. *The data are in excellent agreement with the exact solution for the conductive limit and are shown to be bounded by a model for the isolated, isothermal sphere.*
[DOI: 10.1115/1.2188476]

Introduction

The problem of natural convection in the enclosed region formed between an isothermal heated body and its surrounding, isothermal cooled enclosure is currently of some interest to designers of microelectronics equipment. In an effort to protect electronics from environmental contaminants such as dust or moisture, circuits are often housed in sealed enclosures, especially in outside plant applications. The ability to model natural convection heat transfer within these sealed enclosures would be of great benefit, providing quick and easy-to-use design tools for preliminary design tasks such as parametric studies and trade-off analysis.

Research is currently underway to develop analytically based models to predict convective heat transfer in these systems. Of particular importance to the model development process is the enclosure formed between isothermal concentric spheres, the most fundamental type of doubly connected enclosure. It is anticipated that the lessons learned during the development of a natural convection model for the concentric spheres will be directly applicable to more complex enclosure geometries.

One of the most important elements in the development of analytical models is the availability of experimental data over the full range of the independent parameters. Accurate data are vital in order to reveal trends, such as limiting cases or transition behavior, and for the validation of the completed models. The current literature contains only a limited set of experimental data for the isothermal concentric sphere problem from Bishop et al. [1], Scanlan et al. [2], Weber et al. [3] and Powe et al. [4]. Bishop et al. [1] performed air measurements at atmospheric pressure for a single outer sphere diameter and four inner sphere diameters, leading to diameter ratios of $d_o/d_i = 1.25, 1.67, 2.0$, and 2.5. Scanlan et al. [2] performed measurements for water and silicon oil-filled spherical enclosures, with $4.7 \leqslant \mathrm{Pr} \leqslant 4148$ for five diameters ratios ranging from $d_o/d_i = 1.09$ to 2.81. The data are limited to a narrow range of high Rayleigh numbers indicative of the boundary layer flow limit. Weber et al. [3] repeated the measurements of Scanlan et al. [2] for vertically eccentric enclosures and Powe et al. [4] present a photographic study of flow patterns between an arbitrarily shaped body and its spherical enclosure, of which the concentric spheres is a special case. The remaining data available in the literature are derived from numerical simulations of the spherical enclosure, including those presented by Mack and Hardee [5], Astill et al. [6], Caltagirone et al. [7], Singh and Chen [8], Ingham [9], Wright and Douglass [10], Fujii et al. [11], Garg [12], Chu and Lee [13] and Chiu and Chen [14]. There are no experimental data in the current literature for the isothermal concentric spherical enclosure valid for the full range of Rayleigh number that includes the transition from convection to conduction-dominated heat transfer.

The objective of the current study is to perform measurements of natural convection heat transfer for isothermal concentric spheres for the full range of Rayleigh number, from the laminar boundary layer flow limit to the conductive limit. The procedure for performing the measurements will be developed, the test apparatus will be described, and data for four different diameter ratios will be presented.

Problem Definition

The problem of interest involves convective heat transfer from a sphere, diameter d_i, to a concentric spherical shell with inner diameter d_o, as shown in Fig. 1. Isothermal boundary conditions exist at both the inner and outer boundaries, as follows:

$$\begin{aligned} &\text{Inner boundary} \quad T = T_i \\ &\text{Outer boundary} \quad T = T_o \end{aligned}$$

where $T_i > T_o$. The total heat transfer rate through the enclosed region is determined at the inner boundary by

$$Q = \int\int_{A_i} -k\frac{\partial\theta}{\partial n}dA, \quad \theta = T(\vec{r}) - T_b \tag{1}$$

where $T(\vec{r})$ is the temperature distribution adjacent to the inner boundary along an outward-facing normal, and T_b is the bulk fluid temperature in the enclosure. Assuming constant fluid properties and nondimensionalizing yields the dimensionless total heat transfer rate

$$Q^*_{\mathcal{L}} = \frac{Q\mathcal{L}}{kA_i(T_i - T_o)} = \frac{\mathcal{L}}{A_i}\int\int_{A_i} -\frac{\partial\phi}{\partial n}dA \tag{2}$$

where $\mathcal{L}$ is a general scale length and the dimensionless temperature excess ϕ is defined as

Contributed by the Heat Transfer Division of ASME for publication in the JOURNAL OF HEAT TRANSFER. Manuscript received March 9, 2005; final manuscript received December 15, 2005. Review conducted by Jay M. Khodadadi. Paper presented at the 2002 ASME International Mechanical Engineering Congress & Exposition (IMECE2002), November 17–22, 2002, New Orleans, LA.

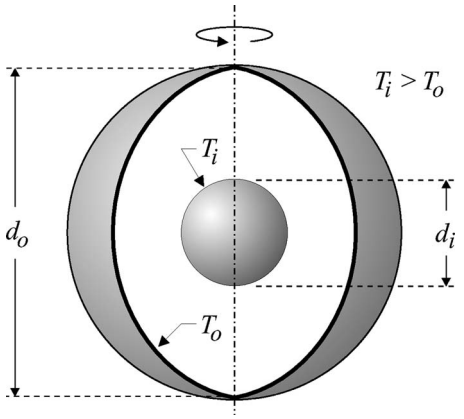

Fig. 1 Schematic of concentric spherical enclosure

$$\phi = \frac{T(\vec{r}) - T_b}{T_i - T_o} \tag{3}$$

The average heat transfer coefficient for the enclosure h is defined based on the average heat flux at the inner boundary and the overall temperature difference

$$h = \frac{(Q/A_i)}{\Delta T} \tag{4}$$

where $\Delta T = T_i - T_o$. Nondimensionalizing h using the general scale length $\mathcal{L}$ gives the area-mean Nusselt number, which can be shown to be equivalent to the dimensionless heat transfer rate

$$\mathrm{Nu}_{\mathcal{L}} = \frac{h\mathcal{L}}{k} = \frac{Q\mathcal{L}}{kA_i\Delta T} = Q^{\star}_{\mathcal{L}} \tag{5}$$

The Rayleigh number is defined using the same parameters

$$\mathrm{Ra}_{\mathcal{L}} = \frac{g\beta\Delta T\mathcal{L}^3}{\nu\alpha} \tag{6}$$

There exists several methods whereby the Rayleigh number can be varied during experimental testing. Changes to the temperature difference ΔT result in only small variations in $Ra_{\mathcal{L}}$, typically less than one decade. Varying the dimensions of the body requires fabrication and testing of a number of specimens of different sizes. The best method for providing a large variation in the Rayleigh number for natural convection is through variation of the fluid properties by a change of the gas pressure, as described by Saunders [15] and Hollands [16]. Varying $\mathrm{Ra}_{\mathcal{L}}$ by applying a partial vacuum to the test environment allows the use of a single test specimen operating over a small temperature difference to easily span four or more decades of Rayleigh number.

Modeling the air in the enclosure as an ideal gas at bulk temperature T_b gives the following expression for the density:

$$\rho = \frac{p}{\mathcal{R}T_bZ} \tag{7}$$

where $\mathcal{R}$ is the gas constant for air and Z is the compressibility factor for air. Substituting into Eq. (6) gives a new definition for the Rayleigh number as a function of p

$$\mathrm{Ra}_{\mathcal{L}} = \frac{g\beta\Delta T\mathcal{L}^3p^2c_p}{\mathcal{R}^2T_b^2k\mu Z^2} \tag{8}$$

where the fluid properties, β, c_p, k, and μ, are constant with respect to pressure and are evaluated at the bulk temperature T_b. The compressibility Z is a function of both the bulk fluid temperature and pressure.

For values of $\mathrm{Ra}_{\mathcal{L}}$ less than some critical value, the heat transfer in the enclosure is conduction dominated and independent of the Rayleigh number. In these cases, the dimensionless heat transfer rate is equivalent to the dimensionless conduction shape factor $Q^{\star}_{\mathcal{L}} = S^{\star}_{\mathcal{L}}$, which is defined by Yovanovich as [17]

Fig. 2 Spherical enclosure with 25 mm diameter sphere

$$S^{\star}_{\mathcal{L}} = \frac{\mathcal{L}}{A_i}\int\int_{A_i} -\frac{\partial\phi}{\partial n}dA \tag{9}$$

The conduction shape factor is related to the thermal resistance by

$$S^{\star}_{\mathcal{L}} = \frac{1}{k\mathcal{L}R} \tag{10}$$

Using the exact solution for the thermal resistance of a concentric spherical shell [19], the conduction shape factor is

$$S^{\star}_{\mathcal{L}} = \frac{2\mathcal{L}}{d_i\left(1 - \frac{d_i}{d_o}\right)} \tag{11}$$

Since the problem of interest involves only spherical body shapes and the size of the inner sphere is the only variable geometric parameter, the diameter of the inner sphere is selected as the scale length for all dimensionless parameters, such that $\mathcal{L} = d_i$.

Experimental Apparatus

In order to perform the required measurements, an experimental apparatus was created consisting of a single, spherical enclosure, and a series of inner spheres of various diameters. The outer spherical enclosure was constructed of two aluminum blocks with hemispherical cavities machined into one side, as shown in Fig. 2, so as to form a spherical shell when joined together. Aluminum 6061 was used due to its high value of thermal conductivity to provide a near-isothermal boundary condition, and the hemispherical surfaces were polished to minimize radiation heat transfer.

The size of the enclosure was selected based on two main criteria. First, because many of the tests were to be performed at reduced pressures, it was necessary that the maximum dimensions of the apparatus not exceed the space available within the available vacuum chamber. Second, in order to avoid rarefaction effects the gap spacing between the inner and outer boundaries δ had to be much larger than the mean free path of gas λ as defined by the Knudson number

$$\mathrm{Kn} = \frac{\lambda}{\delta} \tag{12}$$

The mean free path of air as a function of pressure and temperature can be determined by [18]

$$\lambda = 6.4 \times 10^{-8}\left(\frac{1}{p(\mathrm{atm})}\right)\left(\frac{T(\mathrm{K})}{288}\right)(\mathrm{m}) \tag{13}$$

Ensuring that $\mathrm{Kn} < 0.01$ for the full range of pressures and temperatures anticipated in the experimental program provides a lower limit for the outer sphere dimensions. Based on these two

Table 1 Enclosure dimensions

d_o (mm)	d_i (mm)	d_o/d_i
120.0	80.0	1.5
120.0	60.0	2.0
120.0	40.0	3.0
120.0	25.0	4.8

criteria, the dimensions of the outer enclosure were chosen such that its diameter was $d_o = 120$ mm.

In order to provide data for a wide range of diameter ratios, four different spherical inner bodies were machined from 6061 aluminum. The diameters of the spheres and the resulting diameter ratios are given in Table 1. Each sphere was suspended at the center of the enclosure using a 4–6 mm diameter threaded phenolic rod turned into tapped holes on both the inner and outer enclosure walls, as shown in Fig. 3. All wiring to the inner sphere was connected through a single, 6 mm diameter hole at the top of the enclosure.

All temperature measurements were performed using T-type copper-constantan thermocouples affixed at the surfaces of the inner and outer spheres in shallow, small diameter holes using aluminum-filled epoxy. The temperature at the outer surface of the enclosure was measured using six 30 AWG (0.254 mm) thermocouple wires distributed at the top, bottom, and midplane, while the two thermocouples at the top and bottom of the inner body used smaller diameter, 36 AWG (0.127 mm) wires to reduce conduction losses. All thermocouples measurements were based on an external reference junction that was maintained at $0 \pm 0.1\,^{\circ}\mathrm{C}$ by an ice point cell.

Each of the inner spheres were heated using an embedded dc-powered cartridge heater. Constantan wires were used for all connections rather than copper to reduce heat losses through the wires; 24 AWG (0.508 mm) to provide power to the heaters and 36 AWG to measure voltage. The current to the heater was measured using a calibrated shunt resistor.

The outer enclosure walls were cooled by six cold plates attached on the exterior surface of the blocks using thermally conductive grease at the joints. Heat was removed from the system using a glycol-water mixture circulated through the cold plates by a constant temperature bath.

Once assembled, the enclosure test apparatus was placed in vacuum chamber, as shown in Fig. 4, with feedthroughs available for the coolant, electrical, and instrumentation connections. The vacuum chamber used in this work uses a dual-pump system: a mechanical roughing pump capable of providing reduced pressure test conditions suitable for the convection tests and a diffusion pump for producing a totally evacuated environment for radiation heat transfer testing. The vacuum system also contains a high accuracy vacuum gauge suitable for absolute readings in the range 0.001–1 atm.

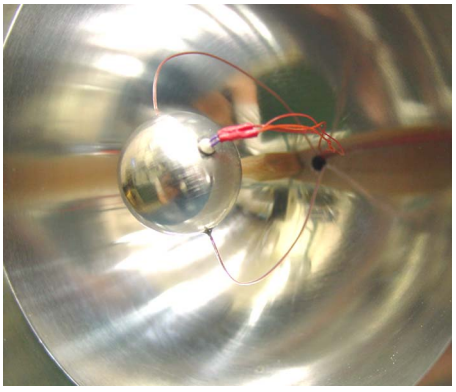

Fig. 3 Detail of 25 mm sphere mounted in enclosure

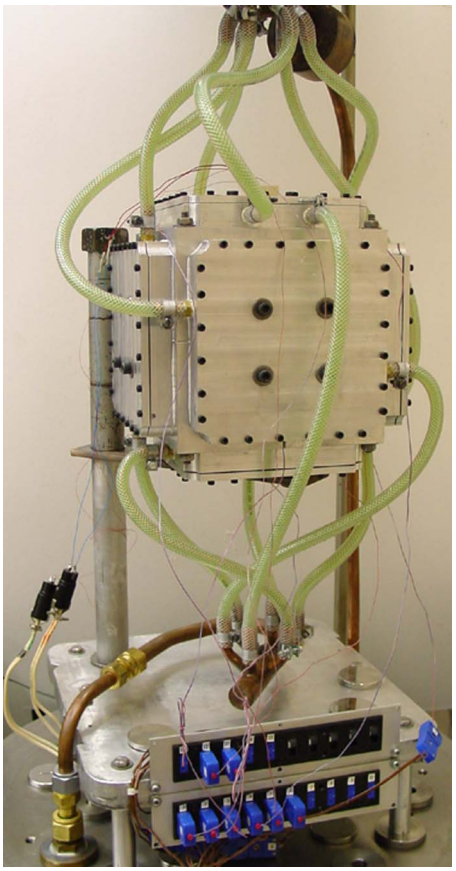

Fig. 4 Enclosure test apparatus in vacuum chamber

Data acquisition and control of the experiment was performed using a Keithley 2700 data acquisition system and a Windows-based PC computer running LABVIEW v5.1 software.

Measurement Procedure

The heat transfer rate due to convection through the enclosure Q can be determined based on an energy balance on the inner boundary

$$Q = Q_{\mathrm{tot}} - Q_{\mathrm{rad}} - Q_{\ell} \tag{14}$$

where Q_{tot} is the total heat transfer due to all modes, Q_{rad} is the net radiative heat transfer between the inner and outer surfaces, and Q_{ℓ} are the accumulated conduction losses through the wires. In order to predict Q, a means is required whereby the total heat transfer rate can be measured, along with a method to quantify the losses due to radiation and conduction.

Total Heat Transfer Rate. The simplest method to determine the total heat transfer rate Q_{tot} is through a direct measurement of electrical energy dissipated by the heater during a steady-state test. A fixed voltage would be applied to the heater and body temperatures would be monitored until sufficient time had elapsed such that the temperature change is less than some specified criteria. Then, the total heat transfer rate would be determined by

$$Q_{\mathrm{tot}} = VI$$

where V and I are the heater voltage and current, respectively.

Hollands [16] reports that, in the case of natural convection in

gases, approximately five times the time constant 5τ is required to achieve steady-state conditions, where the time constant is defined as

$$\tau = mc_p R \tag{15}$$

Due to the relatively large values of the heat capacity mc_p and the average thermal resistance R for the proposed tests, especially those to be performed in a reduced pressure environment, steady-state testing becomes a prohibitively time-consuming option. Instead, the current study will implement the transient test method of Hollands [16] that allows convective heat transfer measurements to be performed in a fraction of the time required for steady-state tests. This method is based on the assumption that, due to the slow rate of change of body temperature, a "quasi-steady" condition exists where the convective heat transfer is virtually identical to the steady-state results at the same temperature.

The use of a transient test to measure steady-state convection in the enclosure can be validated by a comparison of the time constants for the inner body and the enclosed air layer for the worst case condition, the smallest sphere, $d_i = 25$ mm, at atmospheric pressure. Using Eq. (15) and textbook values [19] for the thermophysical properties ρ and c_p, the time constant for the sphere is determined as a function of the film resistance at the inner boundary

$$\tau_i = \left(2770 \ \frac{\text{kg}}{\text{m}^3}\right)(8.18 \times 10^{-6} \ \text{m}^3)\left(875 \ \frac{\text{J}}{\text{kg K}}\right)R_i = 19.8 \cdot R_i \tag{16}$$

The time constant for the enclosed air layer τ_b is determined using the same method

$$\tau_b = \left(1.1614 \ \frac{\text{kg}}{\text{m}^3}\right)(8.97 \times 10^{-4} \ \text{m}^3)\left(1007 \ \frac{\text{J}}{\text{kg K}}\right)R_o = 1.05 \cdot R_o \tag{17}$$

where R_o is the film resistance at the outer boundary. Assuming that the film resistances at the inner and outer surfaces are similar $R_i \approx R_o$, the ratio of the time constants can be calculated

$$\frac{\tau_i}{\tau_b} \approx 19 \tag{18}$$

With a factor of 20 difference between the time constants for the worst case conditions, it is therefore reasonable to assume that the cooling rate of the inner body will control the heat transfer and that a "quasi-steady" condition exists in the enclosed fluid region.

In the transient test method, the body is heated to some initial, specified temperature while the temperature of the enclosure remains constant throughout the test. When the prescribed temperature difference is reached, the power to the heater is turned off and the transient response of the inner body is monitored. Measurements continue until ΔT falls below some minimum prescribed value. The total heat transfer rate at any time t and corresponding temperature difference ΔT can be determined based on the transient data by

$$Q_{\text{tot}} = -mc_p \frac{dT_i(t)}{dt} \tag{19}$$

where the heat capacity of the inner body mc_p is determined empirically using a method described in the next section. The time derivative in Eq. (19) is approximated for distinct time intervals t_n using a least-squares method to predict the slope of sets of 101 average inner body temperature versus time data points.

$$\left.\frac{dT}{dt}\right|_{t_n} = \text{slope}(T_i \text{ vs. } t) \text{ for } 1 \leqslant j \leqslant 101 \tag{20}$$

Then, Q_{tot} can be calculated for time t_n, corresponding to the time value of the middle data point

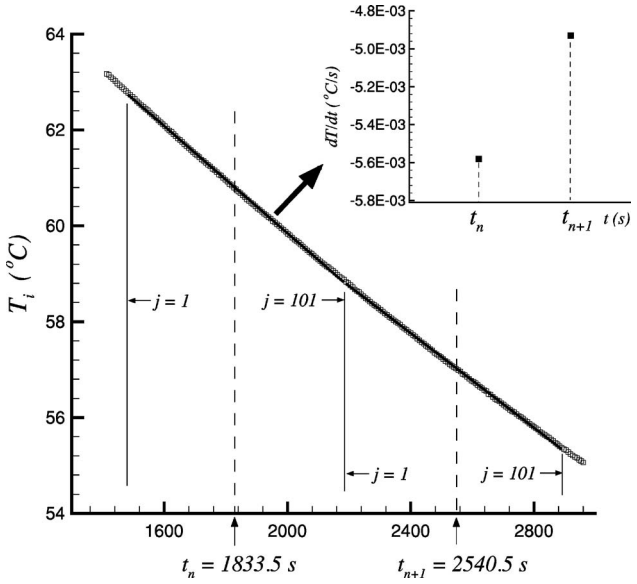

Fig. 5 Calculation of time derivative of temperature, $d_o/d_i = 1.5$

$$t_n = t_{j=51}$$

as shown in Fig. 5. Corresponding values at time t_n for the remaining parameters, T_i, T_o, p, and $V \cdot I$, are determined using an arithmetic average of nine values around the middle data point, as shown below and in Fig. 6 for the example of the inner body temperature.

$$T_{i,n} = \frac{1}{9}\sum_{j=47}^{9} T_{i,j} \tag{21}$$

Using this transient test method and data reduction procedure, Q_{tot} is determined for a number of ΔT values between the start and end conditions, where the number of points depends on the heat capacity of the body, the convective conditions and the time step selected for the measurement.

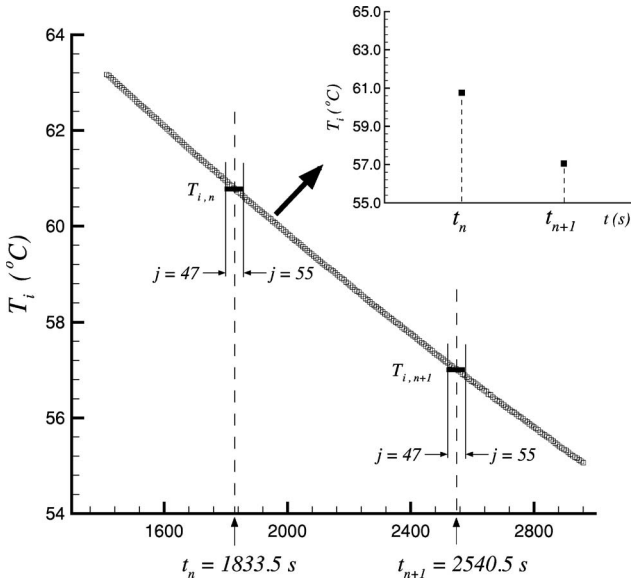

Fig. 6 Calculation of average inner body temperature $d_o/d_i = 1.5$

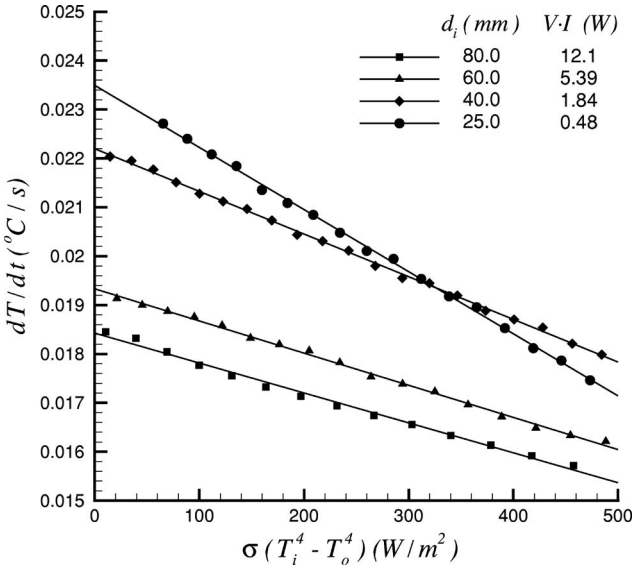

Fig. 7 Heating test data

Heat Capacity and Radiative Losses. The simplest method for determining the heat capacity of an isotropic body is to measure its mass and multiply by a tabulated value for specific heat capacity value from a handbook. However, in the case of the current study the inner spheres are not homogeneous but instead contain an embedded cartridge heater, a section of the phenolic mounting rod, and thermocouples. The radiation heat transfer through the enclosure could also be modeled using available analytical techniques, but without precise values for the emissivity of the inner and outer boundaries, it is difficult to produce accurate results. Therefore, both the heat capacity and the radiative heat transfer for each test case will be determined based on empirical data.

In order to provide an effective measure of both quantities, a two-stage test procedure is used. Starting at an initial condition $\Delta T \approx 0$, a heating test to a maximum value of ΔT is performed to determine the heat capacity, followed immediately by a cooling test back to a final ΔT value to measure radiative losses. For high vacuum conditions, such that $\mathrm{Kn} > 100$, it can be assumed that gaseous convection and conduction are eliminated and heat transfer occurs by radiation alone. The energy balance for the inner body for any time t is

$$mc_p \frac{dT_i}{dt} = V \cdot I - Q_{\mathrm{rad}} - Q_{\mathcal{L}} \tag{22}$$

In the heating test the constant value of electrical power $V \cdot I$ provided to the heater can be assumed to be large enough such that the conduction losses are minimal, $Q_{\mathcal{L}} \approx 0$, and Q_{rad} is assumed to be a linear function of the factor $\sigma(T_i^4 - T_o^4)$. Then Eq. (22) becomes

$$\frac{dT_i}{dt} = \frac{V \cdot I}{mc_p} - \frac{C_{\mathrm{rad}}}{mc_p}\sigma(T_i^4 - T_o^4) \tag{23}$$

where C_{rad} is assumed to be constant for each test body. Using a least-squares method to determine the time gradient of the inner body temperature, as described in the previous section, values of dT/dt can be plotted versus the radiation parameter $\sigma(T_i^4 - T_o^4)$, as shown in Fig. 7. Based on Eq. (23) it can be seen that the y intercept predicted by the linear fit of the data in Fig. 7 can be used to calculate the heat capacity of the body. The empirical predictions for the heat capacity of each of the inner spheres tested are presented in Table 2.

Table 2 Heat capacity and radiation coefficient values for inner spherical bodies

d_i (mm)	mc_p (J/K)	$C_{\mathrm{rad}} \times 10^4$ (m^2)
80.0	653	5.59
60.0	279	4.79
40.0	82.9	3.17
25.0	20.3	1.93

Once the maximum ΔT value had been achieved, the heater was shut down, $V \cdot I = 0$, reducing Eq. (22) to

$$Q_{\mathrm{rad}} = -mc_p \frac{dT_i}{dt} - Q_{\mathcal{L}} \tag{24}$$

where $Q_{\mathcal{L}}$ is assumed to be zero for all but the heat conduction through the mounting rod, modeled using a simple one-dimensional relationship

$$Q_{\mathrm{rod}} = \frac{\delta}{k_{\mathrm{rod}} \pi (d_{\mathrm{rod}}/2)^2} \tag{25}$$

The thermal conductivity of the phenolic rod material is $k_{\mathrm{rod}} = 0.4$ W/mK, δ is the enclosure gap spacing, and d_{rod} is the rod diameter. The time gradient of the average inner body temperature dT_i/dt is determined using the least-squares approximation and the corresponding heat capacity value from the heating test. Figure 8 presents the measured values of Q_{rad} versus the radiation parameter $\sigma(T_i^4 - T_o^4)$ and least-square fits of these data according to the relationship

$$Q_{\mathrm{rad}} = C_{\mathrm{rad}} \sigma (T_i^4 - T_o^4) \tag{26}$$

Values for the radiation correlation coefficient for each body are presented in Table 2.

Conduction Losses. There are four potential sources of conductive heat loss from the inner body: the power wires, the voltage measurement leads, the thermocouples, and the connecting rod. This analysis will consider losses by convection from the wires only; it is assumed that losses due to radiation from the wires have been accounted for by the correlation of the radiation test data and conduction losses through the connecting rod will be

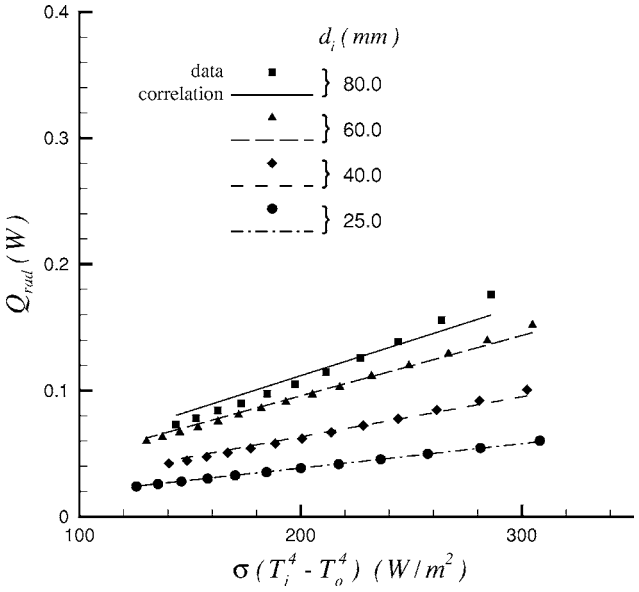

Fig. 8 Cooling test data

determined using Eq. (25).

The heat loss from each individual wire connected to the inner body can be modeled as an infinitely long fin [19]

$$Q_\ell = \sqrt{h_{\text{eff}} P_w k_w A_w}(T_i - T_b) \tag{27}$$

where P_w and A_w are the perimeter and cross sectional area of the conductor, k_w is the thermal conductivity of the conductor material, and T_b is the bulk fluid temperature. The effective heat transfer coefficient value h_{eff} has been modified to include the conductive resistance of the insulation on the wire, as described by Sparrow [21]. By assuming a series combination of a conduction resistance through a circular annulus and the convective film resistance at the insulation surface, the effective heat transfer coefficient can be determined by

$$h_{\text{eff}} = \frac{1}{\pi d_w L_e (R_{\text{cond}} + R_{\text{conv}})} = \frac{1}{d_w \left[\dfrac{ln(d_{\text{ins}}/d_w)}{2k_{\text{ins}}} + \dfrac{1}{h d_{\text{ins}}} \right]} \tag{28}$$

where d_{ins} and k_{ins} are the diameter and thermal conductivity of the insulation and L_e is an effective fin length. Convective heat transfer from the insulation is modeled as an infinitely long, horizontal circular cylinder [20]

$$h = \frac{k}{d_{\text{ins}}} \frac{2}{\ln\left[1 + \dfrac{2}{0.403 \text{Ra}_{d_{\text{ins}}}^{1/4}}\right]} \tag{29}$$

where the Rayleigh number is modified to include the gas pressure as described previously

$$\text{Ra}_{d_{\text{ins}}} = \frac{g\beta(\overline{T_w} - T_b) d_{\text{ins}}^3 p^2 c_p}{\mathcal{R}^2 T_b^2 k \mu Z^2} \tag{30}$$

The bulk fluid temperature T_b is assumed to be the arithmetic mean of the inner and outer boundary temperatures $(T_i + T_o)/2$ while the average wire temperature is determined from an integral of the temperature profile of the infinitely long fin

$$\overline{T_w} = \frac{1}{L_e} \int_0^{L_e} T(x) dx, \quad \frac{T(x) - T_b}{T_i - T_b} = e^{-\xi x} \tag{31}$$

where L_e is the effective fin length, determined by solving the temperature distribution equation for the x location where 95% of the temperature drop has occurred

$$\frac{T(x = L_e) - T_b}{T_i - T_b} = e^{-\xi L_e} = 0.05 \tag{32}$$

Solving for the effective fin length gives

$$L_e = -\frac{1}{\xi} \ln(0.05), \quad \xi = \sqrt{\frac{h_{\text{eff}} P_w}{k_w A_w}} \tag{33}$$

Substituting and solving for the average wire temperature yields

$$\overline{T_w} = 0.317 T_i + 0.683 T_b \tag{34}$$

In the case of the thermocouple wires, where two insulated wires are wrapped together with an additional insulation layer, effective wire and insulation diameters and thermal conductivity are used in the preceding calculations, as described by Sparrow [21]

$$d_{w,\text{eff}} = \sqrt{2} d_w, \quad d_{\text{ins,eff}} = (\Lambda_1 + \Lambda_2)/2, \quad k_{\text{eff}} = k_{w,1} + k_{w,2}$$

where Λ_1 and Λ_2 are the cross-sectional dimensions of the insulation.

Calculation of the conduction losses through each of the wires and reduction of Q_ℓ from the results leads to values of Q that are less than those of the pure conduction model, Eq. (11), when the pressure has been sufficiently reduced that the data has reached the diffusive limit and become independent of Ra. It is assumed that this overprediction of the wire loss is due to the approximations used in the model formulation, including the assumptions of a horizontal circular cylinder geometry and infinite fin length. Due to the complexity of the problem, it may be impossible to formulate a model to accurately predict all conduction losses from the heated body. Therefore, an empirically derived coefficient C_ℓ is introduced to correct the model predictions.

Assuming that the wire loss model correctly accounts for the variations in temperature and gas pressure and provides a maximum value for the total heat loss by conduction, a coefficient having a range of values $0 < C_\ell < 1$ is used to adjust the model as follows:

$$Q_\ell = C_\ell \sum_{i=1}^{N} Q_{\ell,i} \tag{35}$$

where $Q_{\ell,i}$ are the model predictions for heat loss from each of the N wires. The value of C_ℓ for a particular test setting is determined so as to minimize the % difference between the data and the conduction model, Eq. (11), when the pressure has been sufficiently reduced that the data has reached the diffusive limit. Values of C_ℓ and the relative portion of the overall heat transfer attributed to conduction losses through the wires are given in Table 3 for each test case. The differences in C_ℓ values in Table 3 are due to variations in wire length, material and orientation as well as body and heater size.

Table 3 Conduction losses model coefficients

d_i (mm)	C_ℓ	Q_ℓ/Q
80.0	0.45	1–3%
60.0	0.37	2–4%
40.0	0.15	1–3%
25.0	0.32	3–8%

Test Method. With the measurement procedure and data reduction techniques defined, the test method is established as follows:

1. Assemble test body in enclosure, fit cold plates, and install completed assembly in chamber.
2. Seal vacuum chamber and start mechanical and diffusion pumps to establish high vacuum conditions (Kn > 100).
3. Perform heat capacity and radiation heat transfer tests.
4. Analyze data to obtain mc_p and Q_{rad} correlation.
5. Perform convective heat transfer measurements, starting at atmospheric conditions.
6. Reduce air pressure in chamber and repeat convection measurements, such that at least two tests are performed per decade of Ra_{d_i} and the data overlaps.
7. Continue reducing pressure and repeating convection tests until diffusive limit is achieved for at least two decades of Rayleigh number.
8. Analyze data to correct for conductive losses.

Results

Measurements were performed for each of the four inner sphere diameters given in Table 1 according to the test method described in the previous section. The enclosure was maintained at a constant temperature of 22 °C, and the starting and ending values for the temperature difference for the transient convection tests were 50, and 10 °C, respectively. Figure 9 presents all data collected for the $d_o/d_i = 2$ tests, and demonstrates the overlap between data for subsequent tests performed at different pressure levels. Data are selected from each pressure range to provide a smooth transition and a continuous set of data over the full range of Rayleigh number. The resulting final data sets for each of the four enclosure geometries are plotted in terms of the dimensionless parameters Nu_{d_i} and Ra_{d_i} in Fig. 10.

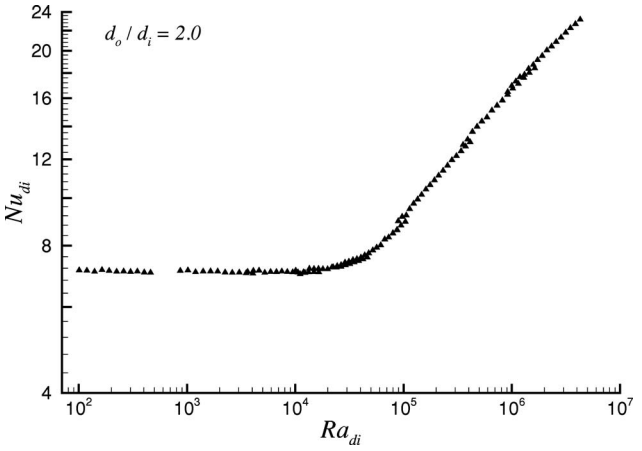

Fig. 9 Raw convection test data

A full uncertainty analysis was performed to evaluate the impact of the accuracy of each of the instruments and sensors used in the experiments, along with the experimental method and data reduction techniques, on the reported values of Nusselt and Rayleigh numbers. The procedure used for the uncertainty analysis was based on the method described by Moffat [22]. Accuracy of the thermocouple readings (±0.2°C), heater voltage and current measurements, vacuum transducer measurements, dimensions, thermophysical properties, and time readings were combined to form an overall uncertainty on the Nusselt number of 2.1–2.3%, while the uncertainty in the Rayleigh number varied from 1.4% to 3.4%. Error bars are included in Fig. 10 that represent the uncertainty in the data associated with both the Rayleigh and Nusselt numbers.

A number of observations can be made concerning the data and its trends, as seen in Fig. 10. First, the goal of this work, to conduct measurements over a wide range of Rayleigh number, has been achieved with data being generated over at least four decades of Rayleigh numbers in all cases. Second, the data are in excellent agreement with the conductive limit and show independence of Ra_{d_i} for at least two decades of Rayleigh numbers. Finally, the data indicate a smooth transition from convection to conduction-dominated heat transfer that occurs within a single decade of the Rayleigh number.

In Fig. 10 a model for the isolated, isothermal sphere [23] is included, which is equivalent to the limit of an infinitely large enclosure, $d_o/d_i \to \infty$

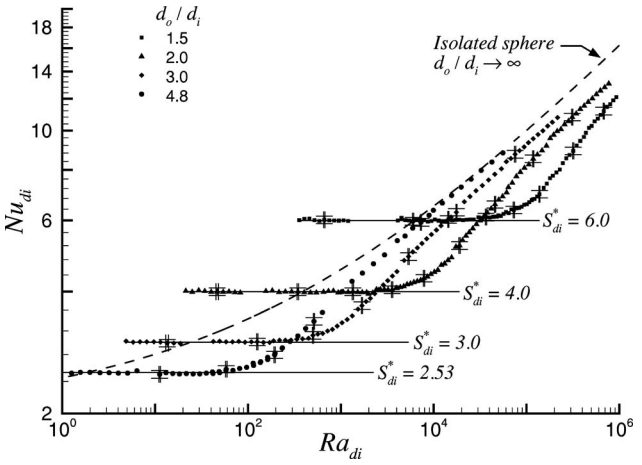

Fig. 10 Convection test results

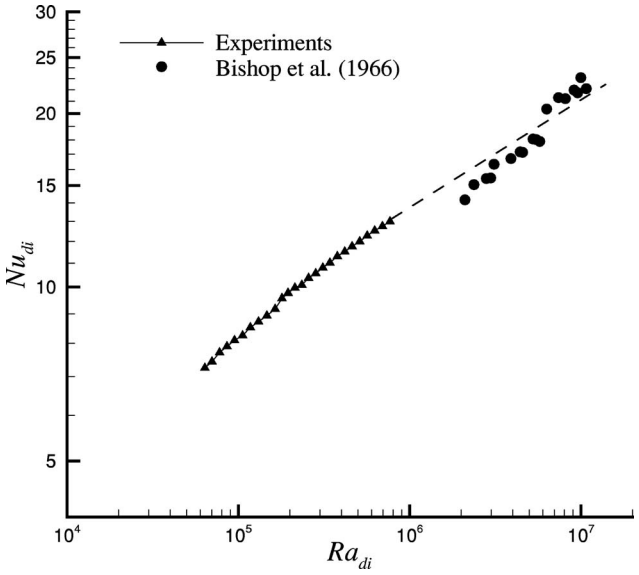

Fig. 11 Comparison with previous data d_o/d_i=2.0

$$\mathrm{Nu}_{d_i} = S^{\star}_{d_i} + F(\mathrm{Pr}) G_{d_i} \mathrm{Ra}^{1/4}_{d_i} \tag{36}$$

where the diffusive limit $S^{\star}_{d_i}=2$ and the body gravity function $G_{d_i}=0.879$ for the sphere. The value for the Prandtl number function for air at STP is $F(\mathrm{Pr})=0.513$. As expected, the isolated sphere model provides an upper bound to the data at the laminar boundary layer flow, high Rayleigh number limit. From Fig. 10 it can be seen that for $d_o/d_i=4.8$, the dimensions of the enclosure in relation to that of the inner body are large enough such that the system behaves similar to the isolated sphere. As d_o/d_i decreases, the enclosure walls start to have a larger effect, leading to a reduction in the heat transferred for a given value of ΔT.

Figure 11 compares the experimental data of the present study with the air data of Bishop et al. [1] for $d_o/d_i=2$. The Bishop data were measured for larger values of Rayleigh number than were possible in the current test apparatus, so a direct comparison of the data cannot be performed. However, by extrapolating a best fit line from the present data as shown by the dashed line in Fig. 11, the good agreement between the measurements, and the data of Bishop et al. [1] can be demonstrated.

Summary

An experimental procedure and apparatus for performing measurements of natural convection between an isothermal sphere and its surrounding enclosure have been described. The goal of the research project, to provide data over a wide range of Rayleigh numbers including the transition and diffusive limit, was achieved through the use of a transient test procedure performed in a reduced pressure environment. The proposed transient test method was shown to produce highly accurate data in a much shorter time than the more traditional, steady-state methods. Four different inner spherical bodies were tested and the data were shown to be in excellent agreement with the exact solution for conduction between spherical shells. The data were also compared to existing data from the literature, and were shown to be bounded by the limiting case of natural convection from an isolated, isothermal sphere.

Acknowledgment

The authors gratefully acknowledge the Natural Sciences and Engineering Research Council of Canada and Materials and Manufacturing Ontario for their continued financial support of this research.

Nomenclature

A = surface area, m^2
a,b,c = radiation correlation coefficients
C = coefficient
c_p = specific heat capacity, J/kgK
d = diameter, m
$F(\mathrm{Pr})$ = Prandtl number function
$G_{\mathcal{L}}$ = body gravity function
g = gravitation acceleration, m/s^2
h = convective heat transfer coefficient, W/m^2K
k = thermal conductivity, W/mK
Kn = Knudsen number, $\equiv\lambda/L$
I = heater current, A
L_e = effective fin length, m
$\mathcal{L}$ = general characteristic length, m
m = mass, kg
$\mathrm{Nu}_{\mathcal{L}}$ = Nusselt number, $\equiv Q\mathcal{L}/(kA_i\Delta T)$
P = perimeter, m
p = pressure, Pa
Pr = Prandtl number
Q = heat flow rate, W
R = thermal resistance, K/W
$\mathcal{R}$ = gas constant for air at STP; 287 J/kgK
$\mathrm{Ra}_{\mathcal{L}}$ = Rayleigh number, $\equiv g\beta\Delta T\mathcal{L}^3/(\nu\alpha)$
$S^{\star}_{\mathcal{L}}$ = conduction shape factor, $\equiv Q\mathcal{L}/(kA_i\Delta T)$
t = time, s
T = temperature, °C
$\overline{T}$ = average temperature, °C
ΔT = temperature difference, $\equiv T_i - T_o$, °C
V = heater voltage V
Z = compressibility factor

Greek

α = thermal diffusivity, m^2/s
β = thermal expansion coefficient, 1/K
δ = gap thickness, $\equiv(d_o-d_i)/2$, m
ϕ = dimensionless temperature excess
λ = mean free path, m
Λ = thermocouple wire dimensions, m
μ = dynamic viscosity, $N\,s/m^2$
ν = kinematic viscosity, m^2/s
ρ = mass density, kg/m^3
σ = Stefan-Boltzmann constant, $W/m^2\,K^4$
τ = time constant, $\equiv mc_pR$, s
θ = temperature excess
ξ = fin parameter, 1/m
ζ = radiation parameter, $\equiv\sigma(T_i^4-T_o^4)$, W/m^2

Subscripts

b = bulk fluid
i = inner body
o = outer body
cond = conduction
conv = convection
rad = radiation losses
eff = effective
tot = total
ℓ = conduction losses
w = wire conductor
ins = wire insulation

Superscript

$\star$ = dimensionless quantity

References

[1] Bishop, E. H., Mack, L. R., and Scanlan, J. A., 1966, "Heat Transfer by Natural Convection Between Concentric Spheres," Int. J. Heat Mass Transfer, **9**(7), pp. 649–662.
[2] Scanlan, J. A., Bishop, E. H., and Powe, R. E., 1970, "Natural Convection Heat Transfer Between Concentric Spheres," Int. J. Heat Mass Transfer, **13**(12), pp. 1857–1872.
[3] Weber, N., Powe, R. E., Bishop, E. H., and Scanlan, J. A., 1973, "Heat Transfer by Natural Convection Between Vertically Eccentric Spheres," ASME Trans. J. Heat Transfer, **95**(1), pp. 47–52.
[4] Powe, R. E., Warrington, R. O., and Scanlan, J. A., 1980, "Natural Convective Flow Between a Body and its Spherical Enclosure," Int. J. Heat Mass Transfer, **23**(10), pp. 1337–1350.
[5] Mack, L. R., and Hardee, H. C., 1968, "Natural Convection between Concentric Spheres at Low Rayleigh Numbers," Int. J. Heat Mass Transfer, **11**(3), pp. 387–396.
[6] Astill, K. N., Leong, H., and Martorana, R., 1980, "A Numerical Solution for Natural Convection in Concentric Spherical Annuli," *Natural Convection in Enclosures*, ASME-HTD Vol. 8, K. E. Torrance and I. Catton, eds ASME, New York, pp. 105–113.
[7] Caltagirone, J.-P., Combarnous, M., and Mojtabi, A., 1980, "Natural Convection between Two Concentric Spheres: Transition toward a Multicellular Flow," Numer. Heat Transfer, **3**(1), pp. 107–114.
[8] Singh, S. H., and Chen, J., 1980, "Numerical Solution for Free Convection between Concentric Spheres at Moderate Grashof Numbers," Numer. Heat Transfer, **3**(4), pp. 441–459.
[9] Ingham, D. B., 1981, "Heat Transfer by Natural Convection between Spheres and Cylinders," Numer. Heat Transfer, **4**(1), pp. 53–67.
[10] Wright, J. L., and Douglass, R. W., 1986, "Natural Convection in Narrow-gap, Spherical Annuli," Int. J. Heat Mass Transfer, **29**(5), pp. 725–739.
[11] Fujii, M., Takamatsu, H., and Fujii, T., 1987, "A Numerical Analysis of Free Convection around an Isothermal Sphere (Effects of Space and Prandtl Number)," *Proceedings of the 1987 ASME/JSME Thermal Engineering Joint Conference*, P. J. Marto and I. Tanasawa, eds., JSME, Tokyo, Vol. 4, pp. 55–60.
[12] Garg, V. K., 1992, "Natural Convection between Concentric Spheres," Int. J. Heat Mass Transfer, **35**(8), pp. 1935–1945.
[13] Chu, H-S., and Lee, T-S., 1993, "Transient Natural Convection Heat Transfer between Concentric Spheres," Int. J. Heat Mass Transfer, **36**(13), pp. 3159–3170.
[14] Chiu, C. P., and Chen, W. R., 1996, "Transient Natural Convection Heat Transfer between Concentric and Vertically Eccentric Spheres," Int. J. Heat Mass Transfer, **39**(7), pp. 1439–1452.
[15] Saunders, O. A., 1936, "The Effect of Pressure on Natural Convection in Air," Proc. R. Soc. London, Ser. A, **157**, pp. 278–291.
[16] Hollands, K. G. T., 1988, "Direct Measurement of Gaseous Natural Convection Heat Fluxes," *Proc. First World Conf. Experimental Heat Transfer, Fluid Mechanics and Thermodynamics*, R. K. Shah, E. N. Ganic, and K. T. Yang, eds., Sept. 4–9, Dubrovnik, Yugoslavia, Elsevier, New York, pp. 160–168.
[17] Yovanovich, M. M., 1998, "Conduction and Thermal Contact Resistances (Conductances)," *Handbook of Heat Transfer*, 3rd. ed., W. M. Rohsenow, J. P. Harnett, and Y. Cho, eds., McGraw Hill, New York, Chap. 3, pp. 3.1–3.73.
[18] Kennard, E. H., 1938, *Kinetic Theory of Gases*, McGraw Hill, New York.
[19] Incropera, F. P., and DeWitt, D. P., 1996, *Fundamentals of Heat and Mass Transfer*, 4th ed., Wiley, New York, pp. 96–99, 114–118.
[20] Raithby, G. D., and Hollands, K. G. T., 1998, "Natural Convection," *Handbook of Heat Transfer*, 4th ed., W. M. Rohsenow, J. P. Hartnett, and Y. Cho, eds., McGraw Hill, NY, Chap. 4.
[21] Sparrow, E. M., 1976, "Error Estimates in Temperature Measurement," *Measurements in Heat Transfer*, 2nd ed. E. R. G. Eckert and R. J. Goldstein, eds., Hemisphere, Washington, pp. 3–6.
[22] Moffat, R. J., 1988, "Describing the Uncertainties in Experimental Results," Exp. Therm. Fluid Sci., **1**, pp. 3–17.
[23] Lee, S., Yovanovich, M. M., and Jafarpur, K., 1991, "Effects of Geometry and Orientation on Laminar Natural Convection Heat Transfer from Isothermal Bodies," J. Thermophys. Heat Transfer, **5**, pp. 208–216.

Brownian-Motion-Based Convective-Conductive Model for the Effective Thermal Conductivity of Nanofluids

Ravi Prasher[1]
Intel Corporation,
CH5-157,
5000 W. Chandler Blvd.,
Chandler, AZ 85226-3699
e-mail: ravi.s.prasher@intel.com

Prajesh Bhattacharya

Patrick E. Phelan

Arizona State University,
Department of Mechanical & Aerospace Engineering,
Tempe, AZ 85287-6106

Here we show through an order-of-magnitude analysis that the enhancement in the effective thermal conductivity of nanofluids is due mainly to the localized convection caused by the Brownian movement of the nanoparticles. We also introduce a convective-conductive model which accurately captures the effects of particle size, choice of base liquid, thermal interfacial resistance between the particles and liquid, temperature, etc. This model is a combination of the Maxwell-Garnett (MG) conduction model and the convection caused by the Brownian movement of the nanoparticles, and reduces to the MG model for large particle sizes. The model is in good agreement with data on water, ethylene glycol, and oil-based nanofluids, and shows that the lighter the nanoparticles, the greater the convection effect in the liquid, regardless of the thermal conductivity of the nanoparticles. [DOI: 10.1115/1.2188509]

Keywords: nanofluid, nanoscale heat transfer, colloid, thermal conductivity, brownian motion

1 Introduction

The unusually high observed effective thermal conductivity k of nanofluids at small volume fractions ϕ of nanoparticles ($\phi < 0.05$) has intrigued the research community for the past several years [1–8]. Traditional thermal conductivity models for composites, such as the Maxwell-Garnett (MG) [9] model, fail to explain the enhancement in k in nanofluids [10,11], even though the MG model has been successfully applied for explaining k of solid-solid composites at small volume fractions [9]. What is even more confusing is that for nanosized particles, the impact of any interfacial resistance should be pronounced, and would tend to decrease the enhancement in k of the composite system as compared to micron-sized particles [9]. Recently Wilson et al. [12] and Huxtable et al. [13] experimentally measured the interfacial thermal resistance (R_b) between nanoparticles and different fluids. The magnitude of R_b in their study ranged from low ($\approx 0.77 \times 10^{-8}$ K m^2 W^{-1}) to high values ($\approx 20 \times 10^{-8}$ K m^2 W^{-1}). The thermal conductivity k of a composite for the MG model is given by [9]

$$\frac{k}{k_m} = \frac{[k_p(1+2\alpha)+2k_m]+2\phi[k_p(1-\alpha)-k_m]}{[k_p(1+2\alpha)+2k_m]-\phi[k_p(1-\alpha)-k_m]} \tag{1}$$

where k_m is the matrix conductivity and k_p is the nanoparticle conductivity. For highly conducting particles as compared to the matrix ($k_m \ll k_p$) Eq. (1) gives

$$\frac{k}{k_m} = \frac{(1+2\alpha)+2\phi(1-\alpha)}{(1+2\alpha)-\phi(1-\alpha)} \tag{2}$$

where $\alpha = 2R_b k_m/d$ is the nanoparticle Biot number, ϕ the volume fraction of the particles, and d the particle diameter. Equation (2) shows that for $\alpha > 1$, k is lower than k_m and will continue to decrease with increasing ϕ. Figure 1 presents a plot of Eq. (2) for different values of R_b, and shows that depending on the value of R_b, k can be smaller than k_m even for the case where $k_p \gg k_m$. A critical diameter of the particle can be defined, below which $k < k_m$ [9]. The critical diameter d_c is given by $\alpha = 1$, i.e., $d_c = 2R_b k_m$ such that $k = k_m$. Figure 1 shows that even for R_b as low as $\approx 0.77 \times 10^{-8}$ K m^2 W^{-1}, d_c is approximately 10 nm for water-based nanofluids. Nan et al. [9] have experimentally shown that $k < k_m$ in composites made from zinc sulphide filled with diamond particles, and silicon carbide filled with aluminum due to the presence of R_b. Below d_c these nanoparticles, in spite of having high thermal conductivity, reduce k because of the resistance at the interface [9].

Several mechanisms and models have been proposed in the literature for explaining the measured k of nanofluids using various assumptions [14–18]. Some mechanisms that could cause an increase in k of the nanofluid are (1) simple conduction through the liquid/solid composite, (2) ordered layering of liquid near the solid particle, (3) thermal energy transfer due to translational Brownian motion, (4) thermal energy transfer due to the existence of an interparticle potential, (5) thermophoresis, and (6) localized convection in the liquid due to the Brownian movement of the particles. Recently in a short paper we performed an order-of-magnitude analysis [19] for some of these possible mechanisms to show that local convection caused by the Brownian movement of the nanoparticles is the only mechanism which comes close to explaining the observed k enhancement. We showed in our earlier paper [19] that ordered layering of liquid, thermal energy transfer due to translational Brownian motion, and thermal energy transport due to interparticle potential is negligible. These mechanisms will not be discussed in this paper. Recently Kumar et al. [20] presented another model based on the energy carried due to the Brownian motion of the particles. They applied kinetic theory, however, they assumed that the mean free path is of the order of 10^7 nm (1 cm) to match their data, which is not at all realistic. They did not provide any justification for assuming such a large value of mean free path.

In a recent review article Eastman et al. [21] mentioned that thermophoresis can potentially affect the effective k of nanofluids.

[1]Corresponding author. Adjunct Professor, Dept. of Mechanical & Aerospace Engineering, Arizona State University.

Contributed by the Heat Transfer Division of ASME for publication in the JOURNAL OF HEAT TRANSFER. Manuscript received August 10, 2005; final manuscript received November 7, 2005. Review conducted by Yogesh Jaluria.

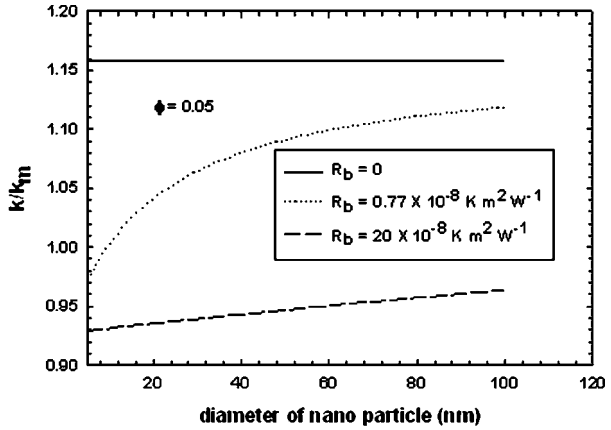

Fig. 1 Effect of particle diameter and interfacial thermal resistance (R_b) on the effective thermal conductivity predicted by the Maxwell-Garnett model, for water as the fluid

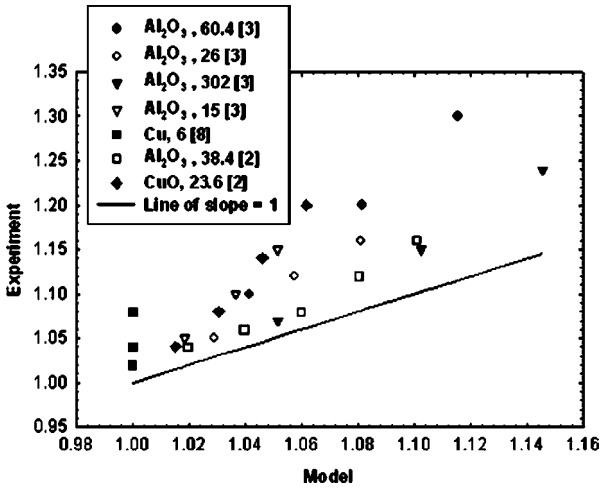

Fig. 3 Comparison of the Maxwell-Garnett predicted *k* and experimental data for EG-based nanofluids. The number in the legend indicates the diameter of the particles, in nanometers ($R_b = 1.2 \times 10^{-8}$ K m^2 W^{-1}).

Thermophoresis refers to the motion of colloidal particles in response to a temperature gradient [22]. The thermophoretic effect can be explained by applying the kinetic theory. The high energy molecules in the hot region of the liquid impinge on the particles with greater momentum than do molecules coming from the cold region, thus leading to the migration of the particles in the direction opposite to the temperature gradient. Eastman et al. [21] correctly pointed out that thermal gradients in the fluid and the presence of the heaters in the experiments could lead to thermophoresis of nanoparticles. Koo and Kleinstreuer [17] and Koo [23] considered the effect of thermophoresis on the *k* of nanofluids by applying kinetic theory, and found it to be negligible primarily because of the very small particle migration velocity.

One aspect that is important to realize is that if the observed exceptional enhancements in *k* are due to the small size of the particles, then at large particle sizes *k* should be well described by the traditional conduction-based theory (e.g., MG) of composites, because Brownian motion of the particles becomes increasingly negligible with increasing particle size. Therefore any model that describes the *k* of nanofluids should be able to make a transition such that at small particle sizes some other mechanism dominates, and at larger particle sizes a simple conduction-based mechanism dominates. Other requirements for any model for *k* is that it should include the effect of R_b, as it is very important for small particles as already shown by Wilson et al. [12].

Here we expand on the analysis presented in our previous short paper [19] by presenting additional comparisons with experimental data, and discussion of some of the key physics involved. Additional results for ethylene glycol- and oil-based nanofluids are included, as well as a comparison of the time scale for convection relative to that of the Brownian particles. We also perform some parametric studies to provide further insights into the design of high-thermal-conductivity nanofluids.

2 Pure Conduction With Thermal Boundary Resistance

Figures 2–4 show a comparison between the classical MG model (Eq. (1)) and experimental data for water, ethylene glycol (EG), and oil-based nanofluids [2–8] at room temperature. For water R_b is assumed to be $R_b \approx 0.77 \times 10^{-8}$ K m^2 W^{-1} [12]. For EG and oil there are no reported R_b measurements. The mechanisms for R_b between a liquid and a solid are not clear [12,24]. Molecular dynamics simulations by Xue et al. [24] showed that R_b can vary greatly depending on the type of bonding between the liquid and the solid. Predictions using the phonon-based diffuse mismatch model (DMM) by Wilson et al. [12] were within a factor of 2 for different types of liquids. Since experimental results on EG- and oil-based nanofluids are not available, an esti-

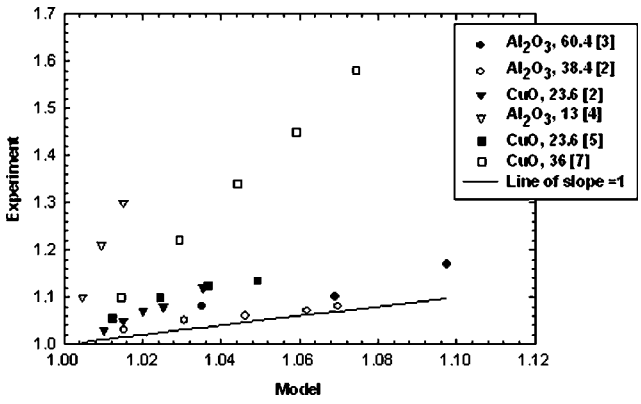

Fig. 2 Comparison of the Maxwell-Garnett predicted *k* and experimental data for water-based nanofluids. The number in the legend indicates the diameter of the particles, in nanometers ($R_b = 0.77 \times 10^{-8}$ K m^2 W^{-1}).

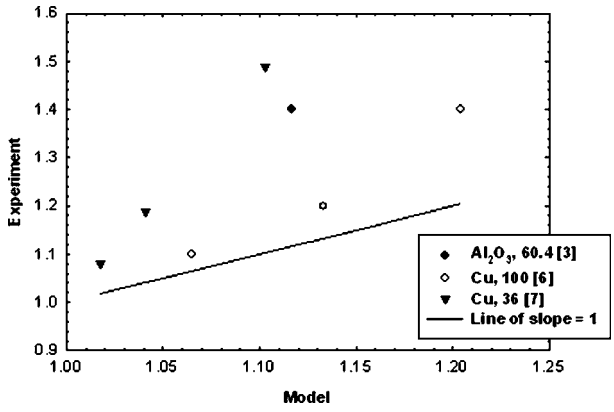

Fig. 4 Comparison of the Maxwell-Garnett predicted *k* and experimental data for oil-based nanofluids. The number in the legend indicates the diameter of the particles, in nanometers ($R_b = 1.925 \times 10^{-8}$ K m^2 W^{-1}).

mate for R_b for EG and oil will be made based on DMM. According to DMM [25] $R_b = g(\nu_1, \nu_2)C^{-1}$ where g is a function of the sound velocity in the two media (ν_1 and ν_2), and C is the heat capacity per unit volume. The velocity of sound in EG and water is approximately the same [26]. The velocity of sound in oil is not known, however, it is approximately the same for various organic liquids and water [26]. Therefore we assume that the velocity of sound in oil is approximately equal to the velocity of sound in water. For oil we assume the properties of engine oil apply, as exact details for the oils used in various experiments are not available [3,6,7]. Therefore, for a first approximation, we assume that $R_b(EG) = (C_{\text{water}}/C_{\text{EG}})R_b(\text{water})$ and $R_b(\text{oil}) = (C_{\text{water}}/C_{\text{oil}})R_b(\text{water})$. This gives $R_b(\text{EG}) \approx 1.2 \times 10^{-8}$ K m^2 W^{-1} and $R_b(\text{oil}) \approx 1.9 \times 10^{-8}$ K m^2 W^{-1}. Wilson et al. [12] also found experimentally that R_b for organic liquids was higher than the R_b for water. Figures 2–4 show that the MG model underpredicts the data for all three fluids by a considerable amount. This proves the point that conduction as a mechanism is not solely responsible for the observed enhancement in k of the nanofluid, as pointed out by other authors [10,11]. The difference between the work by other authors [10,11] and the work presented here is that we have also included the effects of R_b. Equation (1) includes conduction through both particles and the liquid. Keblinski et al. [11] showed by comparing the time scale of conduction with other mechanisms that conduction is present. Similarly, the positive correlation between the MG predictions and experimental data in Figs. 2–4 suggests that the conduction mechanism is present in these nanofluids, which is in line with the findings of Keblinski et al. [11]. Therefore conduction should be considered in any comprehensive model, even if it is not the dominant mechanism.

Recently Kumar et al. [20] proposed a conduction-based model for explaining the k of nanofluids. For their first conduction model they made unrealistic assumptions such as parallel paths for heat transfer between the fluid and particles and an arbitrarily defined fluid radius. Equation (8) in their model shows that if the particle radius is very large then the k of the nanofluid will be the same as the k of the base fluid, i.e., large particles will not enhance the conductivity of the particle-fluid composite, which is unrealistic.

3 Effect of Convection Due to the Brownian Motion of Nanoparticles

Keblinski et al. [11] calculated the time required by Brownian diffusion versus the time required for conduction in the liquid. Through an order-of-magnitude analysis based on the characteristic time of the two different mechanisms, they showed that energy transport due to Brownian diffusion is two orders of magnitude smaller than energy transport due to conduction in the liquid. Keblinski et al. [11], however, did not consider the energy transport due to *convection* caused by the Brownian movement of the particle. We perform a similar analysis regarding the time scale of Brownian movement of the particle (τ_b) and the time scale of the convection due to the movement of the particle (τ_c). The characteristic time scale to cover a distance equal to the diameter of the particle due to Brownian motion is given by [11] $\tau_b = d^2/(6D_b)$, where D_b is the Stokes-Einstein Brownian diffusivity

$$\tau_b = \frac{3\pi\eta d^3}{6k_bT} \tag{3}$$

where η is the viscosity of the liquid. For a 10-nm particle, τ_b is approximately 3×10^{-7} s at 300 K for water and 6×10^{-6} s for EG. The convection diffusivity is the kinematic diffusivity (ν) of the liquid, i.e., the momentum diffusivity [27,28], which is related to η as $\nu = \eta/\rho_f$ where ρ_f is the liquid density. Therefore the time required for the effect of convection to be felt at a distance equal to the nanoparticle diameter d, τ_c, is given as

$$\tau_c = \frac{d^2}{\nu} \tag{4}$$

At 300 K τ_c is approximately 1.2×10^{-10} s for water and 7.2×10^{-11} s for EG for $d = 10$ nm. This simple analysis shows that $\tau_c \ll \tau_b$, or that the effects of convection are propagated almost instantaneously relative to the Brownian diffusion of the particle.

Jang and Choi [16] were the first to suggest a model based on the convection caused by the Brownian movement of the nanoparticles. In our previous article [19] we showed that the model by Jang and Choi is not correct because of certain assumptions made by them. In spite of all the shortcomings, we recognize that Jang and Choi were the first group to take into account convection induced by Brownian motion [16].

Since the particles suspended in the liquid for nanofluids are very small, Brownian movement of the particles is probable due to the small mass of these particles. The root-mean-square velocity (ν_N) of a Brownian particle can be calculated as [17,29]

$$\nu_N = \sqrt{\frac{3k_bT}{m}} = \frac{1}{d}\sqrt{\frac{18k_bT}{\pi\rho d}} \tag{5}$$

In [19] we defined a Brownian-Reynolds number (Re) based on the Brownian velocity $\text{Re} = \nu_N d/\nu$ which leads to

$$\text{Re} = \frac{1}{\nu}\sqrt{\frac{18k_bT}{\pi\rho d}} \tag{6}$$

where ν is the kinematic viscosity of the liquid. Note that Re for Brownian motion is inversely proportional to $d^{0.5}$. The value of Re for 10-nm Al_2O_3 nanoparticles in water, $\text{Re} = 0.029$, is much less than one, and therefore for convection the flow falls in the Stokes regime. For a sphere imbedded in a stationary semi-infinite medium of thermal conductivity k_m, Nu based on the particle radius ($a = d/2$) can be shown to be 1, i.e., $h = k_m/a$ [28], where h is the heat transfer coefficient from the sphere to the surrounding medium. For convection in the Stokes regime, however, the average h from an isothermal moving particle is given as [30]

$$h = \frac{k_f}{a}[1 + (1/4)\text{Re} \cdot \text{Pr}] \tag{7}$$

Note that these relations are derived analytically from first principles. Equation (7) can be interpreted as meaning that the effective thermal conductivity of the fluid k_m due to the convection caused by the movement of a *single* sphere is

$$k_m = k_f[1 + (1/4)\text{Re} \cdot \text{Pr}] \tag{8}$$

For a 10-nm Al_2O_3 nanoparticle, the effective enhancement at room temperature is approximately 4.2% for water and 6.6% for EG. Therefore the enhancement due to convection is one order of magnitude higher than any of the other mechanisms (conduction, thermophoresis, etc.). Note that this is based on a single isolated sphere, whereas there will be interactions among the convection currents from different spheres (to be discussed later).

Equation (7), from which Eq. (8) is derived, needs some discussion as it is strictly valid for convection from an isothermal particle. In the nanofluid there will be a temperature gradient in the particle. The question now is to what extent will the nonuniform temperature distribution in the particle affect h? Referring to the convection literature it can be seen that the isothermal case [28] provides a conservative estimate of the average heat transfer coefficient, however the difference between the nonisothermal and isothermal cases is not large [28]. For example the average heat transfer coefficient for convection from an isothermal flat plate is only 2% less than that from a non-isothermal flat plate under constant heat flux conditions [28]. Therefore we feel that the use of Eq. (8) in the case of nanofluids, where the particles may not be at a constant temperature, is justified, and any deviation will be a second-order effect. However we emphasize that capturing the effect of the temperature gradient in the particle

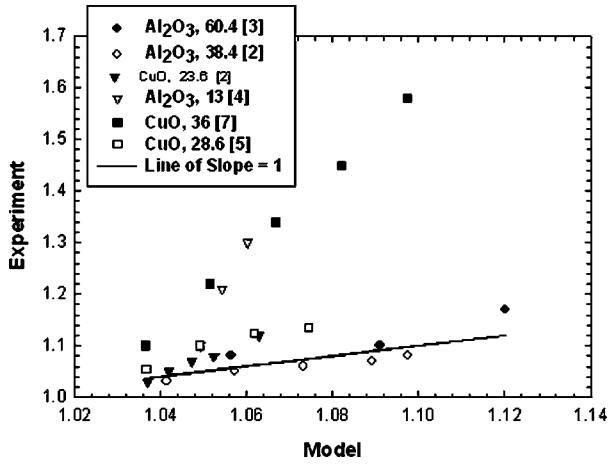

Fig. 5 Comparison of single sphere Brownian model (SGBM) with data on various water-based nanofluid

on the average heat transfer coefficient, although tedious, is achievable. We leave that derivation for a future report.

Substituting Eq. (8) for k_m in Eq. (1), the effective conductivity of the nanofluid can be written as

$$\frac{k}{k_f}\left(1+\frac{\mathrm{Re}\cdot\mathrm{Pr}}{4}\right)\left(\frac{[k_p(1+2\alpha)+2k_m]+2\phi[k_p(1-\alpha)-k_m]}{[k_p(1+2\alpha)+2k_m]-\phi[k_p(1-\alpha)-k_m]}\right) \tag{9}$$

Equation (9), together with the definition of Re given in Eq. (6), has all the necessary ingredients for predicting the thermal conductivity enhancement of nanofluids, in that it: (1) includes the conduction contribution of the particles; (2) includes the thermal boundary resistance between the particles and the fluid; (3) includes the convection contribution; and (4) reduces to the traditional MG model for larger particles, as Re goes to zero (see Eq. (6)) for larger particles. We call this model the single-sphere Brownian Model (SGBM). Although we have used a convective correction due to the movement of a single particle in Eq. (9), we have implicitly assumed that the entire fluid is agitated by the movements of the nanoparticles. The agitation of the entire fluid will depend on the nanoparticle volume fraction ϕ. A critical volume fraction of the nanoparticles can be defined below which the entire fluid will not be agitated (to be discussed later). So far we have not included any empiricism in the model. In our earlier paper [19] we compared SGBM with experimental data for water- and EG-based Al_2O_3 nanofluids [2] at room temperature. Although improved agreement was obtained between the SGBM predictions and data, compared with the MG model, this simple one-sphere Brownian model, however, is not expected to match the experimental data for all scenarios, as it completely ignores the interaction of the convection currents due to multiple spheres. Figure 5 presents a comparison between SGBM and various other data from the literature for water-based nanofluids. Figure 5 shows that the SGBM model predicts higher k than does the MG theory as seen from Fig. 2, however it still gives smaller values of k (compared to the data) for most of the data points.

Koo and Kleinstreuer [17] showed that the volume of the fluid affected due to the Brownian motion of the fluid is very large compared to the volume of the nanoparticle. Equation (5) was derived based on the convection due to a single isolated sphere in the Stokes regime. The axial velocity of the fluid due to the motion of the particles for Stokes flow can be written as [17,31]

$$\frac{u_x}{u_s}=1-[1-1.5(a/r)+0.5(a/r)^3]\cos^2(\theta) - [1-0.75(a/r)+0.25(a/r)^3]\sin^2(\theta) \tag{10}$$

where u_s is the fluid velocity at the surface of the sphere, a the particle radius, r the radial distance from the surface of the sphere, and θ the polar angle. Equation (10) shows that at $r=a$, the velocity of the fluid is the same as the velocity of sphere, i.e., there is no slip between the sphere and the fluid. This no-slip condition leads to the formation of a boundary layer and subsequent movement of the fluid with the nanoparticles. Assuming the 99% criterion for the velocity to define the hydrodynamic boundary layer ($u_r=0.01u_s$), Koo and Kleinstreuer [17] showed that the hydrodynamic boundary layer extends to $\psi=r/d\approx 37.5$ in the direction of the short axes and $\xi=r/d\approx 75$ in the direction of the long axes of a spheroidal body of fluid. That is, the boundary layer is spheroidal in shape for a single isolated sphere in Stokes flow. The thermal boundary layer (δ_T) is related to the hydrodynamic boundary layer (δ_H) by $\delta_T\approx\delta_H/\mathrm{Pr}^{0.333}$ [28] for $\mathrm{Pr}>1$. This means that the single-sphere model given by Eqs. (7) and (8) will be valid only if the interparticle distance is larger than the thermalboundary layer thickness. The smallest volume fraction where SGBM can be applied can thus be calculated from the volume of the thermal boundary layer. The volume of the hydrodynamic boundary layer (V_H) is $V_H=\pi/6(\psi^2\xi)$ and using $\delta_T=\delta_H/\mathrm{Pr}^{0.333}$ the volume of the thermal boundary layer (V_T) is $V_T=V_H/\mathrm{Pr}$. Therefore the critical volume fraction (ϕ_c) above which the boundary layers from different nanoparticles will interact, i.e., where convective currents from different particles interact, is given by $\phi_c=V_p/V_H=\mathrm{Pr}\,d^3/\psi^2\xi=\mathrm{Pr}/(37.5^2\times 75)$. At room temperature, for water ϕ_c is 0.000055 and for EG, ϕ_c is 0.00143. ϕ_c defines the smallest volume fraction above which the whole fluid is agitated. This shows that even at very small volume fractions, convection currents due to various particles will interact and Eq. (7) thus needs to be modified because Eq. (7) assumes that the heat transfer coefficient of each sphere is independent of each other.

Convection heat transfer in complex situations, such as convection from multiple spheres or cylinders where the convection currents from various particles are interacting, are mostly empirical in nature [28]. Since the convection currents in the nanofluids from various particles interact as shown above even for very small volume fractions, the simple SGBM cannot be used to estimate h. Mixing of the convection currents will lead to vigorous micromixing in the liquid at $\phi>\phi_c$. Therefore the expression for h needs to be modified.

Heat transport in nanofluid systems is in some ways similar to particle-to-fluid heat transfer in fluidized beds, as convective currents from various spheres interact in fluidized beds [32,33]. Similar to the argument above for nanofluids, vigorous micro-mixing takes place in fluidized beds. Brodkey et al. [32] showed that for fluidized beds made of micron-sized particles, Nu for particle-to-fluid heat transfer was 20–100 times greater than that of the single-particle Nu. It is also to be noted that except for very simple conditions and geometries, such as Stokes flow past a single sphere, the heat transfer correlations for convection in complicated situations, such as those due to the presence of multiple spheres, are always empirical in nature [28,32]. Taking the cue from the Nu correlations for particle-to-fluid heat transfer in fluidized beds [32], we proposed [19] a general correlation for the heat transfer coefficient for the Brownian motion-induced Stokes flow of multiple nanoparticles of the form

$$h=\frac{k_f}{a}(1+A\,\mathrm{Re}^m\mathrm{Pr}^{0.333}\phi) \tag{11}$$

where A and m are constants. The appearance of ϕ in Eq. (11) signifies stronger interaction between the convection currents from various spheres. Convective heat transfer relations are regime dependent [28], and so depending on Re these relations can

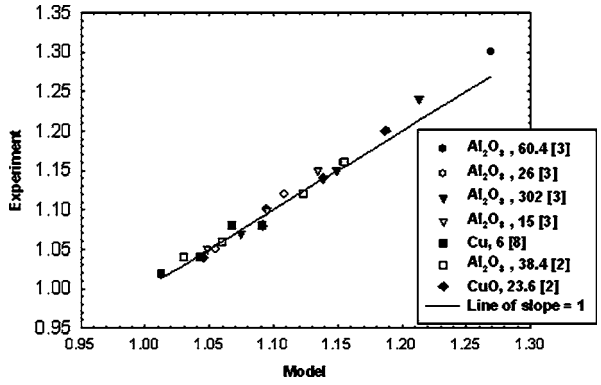

Fig. 6 Comparison of the multisphere Brownian model with experimental data on EG-based nanofluids for $R_b = 1.2 \times 10^{-8}$ K m^2 W^{-1}, $A = 4 \times 10^4$, and the corresponding values of m are given in Table 1. The number in the legend indicates the mean diameter of the particles, in nanometers.

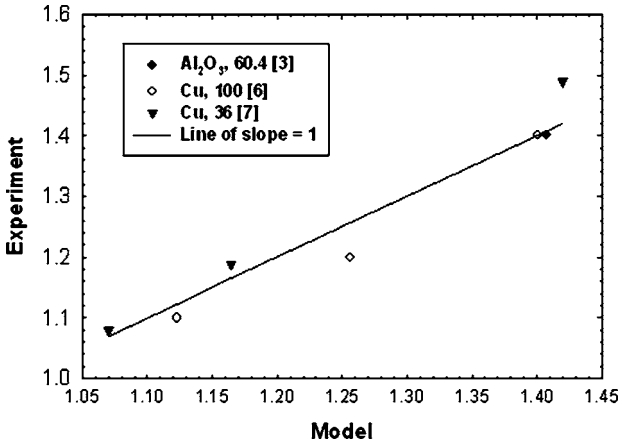

Fig. 7 Comparison of the multisphere Brownian model with experimental data on oil-based nanofluids for $R_b = 1.925 \times 10^{-8}$ K m^2 W^{-1}, $A = 4 \times 10^4$, and the corresponding values of m are given in Table 2. The number in the legend indicates the mean diameter of the particles, in nanometers.

change. Therefore most likely A should be independent of the fluid type, whereas m will depend on the fluid type, as the properties of different fluids can vary dramatically (e.g., water and EG) which affects Re. This modification leads to

$$\frac{k}{k_f} = (1 + A\,\mathrm{Re}^m\,\mathrm{Pr}^{0.333}\phi) \times \left(\frac{[k_p(1+2\alpha) + 2k_m] + 2\phi[k_p(1-\alpha) - k_m]}{[k_p(1+2\alpha) + 2k_m] - \phi[k_p(1-\alpha) - k_m]} \right) \quad (12)$$

If Eq. (12) is valid, then A and m should be the same for different experimental data for a particular fluid. We call this model the multisphere Brownian model (MSBM). This model matched well with all the data [19] for water-based nanofluids assuming a constant R_b of 0.77×10^{-8} K m^2 W^{-1}. The coefficient A was found to be 4×10^4 and m was found to be $2.5\% \pm 15\%$. For comparison, Holman et al. [34] obtained $m = 2.0$ for water-based fluidized beds made of large particles, which is relatively close to the value of m obtained here for the water-based nanofluids.

In this paper comparison between the MSBM and data for EG-based nanofluids is shown in Fig. 6 where R_b is assumed to be 1.2×10^{-8} K m^2 W^{-1} as calculated earlier. Table 1, in turn, gives the best-fit values of m. Table 1 shows that the variation in m between different data sets is not very large, and is centered around $m \cong 1.6$. If R_b is treated as a variable then the difference in m for different data sets will become even smaller. A was assumed to be 4×10^4 (the same as for water-based nanofluids).

The third type of liquid on which several nanofluids have been based is oil. Fig. 7 and Table 2 show the comparison of the semi-empirical Brownian model for such oil-based nanofluids. The physical properties of oil were assumed to be that of engine oil [28], as mentioned earlier, and R_b is assumed to be 1.925 $\times 10^{-8}$ K m^2 W^{-1}. Table 2 demonstrates, once again, that variation of m between different data sets is not very large for oil-based nanofluids. Assuming a variable value of R_b, the difference in m between different data sets will become even smaller. A was assumed to be 4×10^4 (the same as for water and EG) showing that to first order, A is independent of the fluid type.

In the earlier paper [19] MSBM was compared with the experimental data obtained on k for different fluid temperatures for water-based nanofluids with Al_2O_3 nanoparticles [5], and very good agreement was found between MSBM and the data. In this paper MSBM is instead compared with temperature-dependent data on k of water-based nanofluids with CuO nanoparticles [5], as shown in Fig. 8. $R_b = 0.77 \times 10^{-8}$ K m^2 W^{-1} was assumed. The model matches well with data by assuming $m = 2.35$ for $\phi = 4\%$ and $m = 2.05$ for $\phi = 1\%$. It is interesting to note that $m = 2.05$ was obtained as the best fit for CuO-water-based nanofluids from Ref. [7]. The multiplier A was again assumed to be the same ($A = 40{,}000$).

We also compare the proposed model with data for different particle sizes but of the same particle type, liquid, and volume fraction. Data for this condition are not available in abundance, but we have found two data sets on Al_2O_3 nanoparticles in water, at $\phi = 0.03$ for $d = 12$ nm and $d = 38.4$ nm [20]. Masuda et al. [4] reported measurements on Al_2O_3/water nanofluid for $d = 13$ nm at $\phi = 0.028$, which is very close to 0.03. Therefore we also use this data set in our comparison. Figure 9 shows the comparison between the MSBM, assuming $A = 4 \times 10^4$ and $m = 2.5$, and the data. Figure 9 shows that the model matches very well with the data for $R_b = 2.5 \times 10^{-8}$ K m^2 W^{-1}, but if $R_b = 0$ is assumed then the model prediction is much higher than the data, indicating the importance of R_b in determining k.

Based on the data for three different nanofluids (water, EG, and oil) we propose that $m = 2.5\% \pm 15\%$ is the best value for m where

Table 1 Best-fit values of m for different data sets for EG-based nanofluids, shown in Fig. 6, assuming constant $R_b = 1.2 \times 10^{-8}$ K m^2 W^{-1}

Reference	Nanoparticle material	Diameter (mm)	m
[3]	Al_2O_3	60.4	1.55
[3]	Al_2O_3	26	1.75
[3]	Al_2O_3	302	1.5
[3]	Al_2O_3	15	1.8
[8]	Cu	6	1.5
[3]	Al_2O_3	38.4	1.75
[3]	CuO	23.6	1.6

Table 2 Best-fit values of m for different data sets for oil-based nanofluids, shown in Fig. 7, assuming constant $R_b = 1.9 \times 10^{-8}$ K m^2 W^{-1}

Reference	Nanoparticle material	Diameter (mm)	m
[3]	Al_2O_3	60.4	1.08
[6]	Cu	100	1.1
[7]	Cu	36	1.05

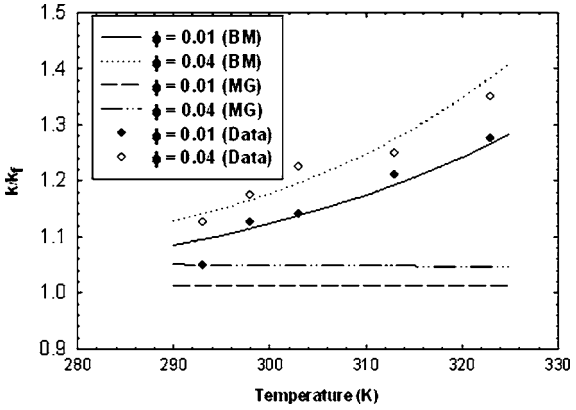

Fig. 8 Comparison of the semiempirical Brownian model with experimental data for 28.6-nm CuO nanoparticles in water [5], for varying temperatures assuming constant $R_b = 0.77 \times 10^{-8}$ K m^2 W^{-1}

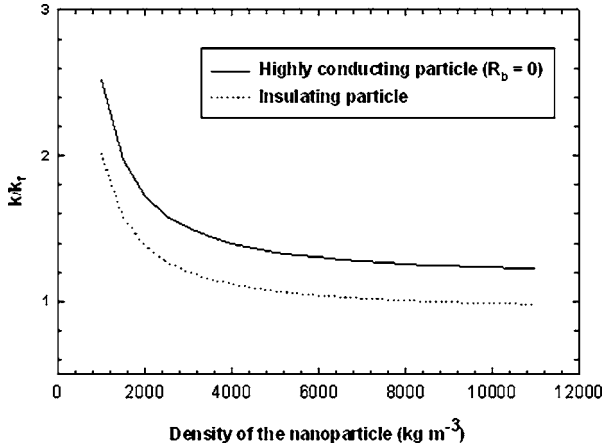

Fig. 10 Effect of nanoparticle density on the thermal conductivity of nanofluids

water is the base fluid, $m = 1.6\% \pm 15\%$ is the best value of m for EG-based nanofluids, and $m = 1.05\% \pm 15\%$ is the best value of m for oil-based nanofluids. The value of the exponent m has been found to depend on the type of fluid in a fluidized beds [32,33], which is consistent with our findings for nanofluids. It is also worthwhile to note that the variation in m for a particular base liquid could also be due solely to the experimental error in the measurement of k, or uncertainty in the mean diameter of the nanoparticles [2]. We have evaluated m based only on the reported values of k, and the reported mean nanoparticle diameter based on volume averaging. The variation in R_b due to other parameters, such as temperature, particle size, volume fraction, nanoparticle material, and bonding, can also lead to uncertainty in the value of m.

4 Discussion

The Brownian Reynolds number defined in this paper (Eq. (6)) increases with decreasing density of the nanoparticles. This shows that lighter nanoparticles will lead to larger Reynolds number, and hence greater k. The model developed here includes various material parameters that can change the effective k of nanofluids. The material parameters that involve the nanoparticles are the density of the nanoparticle, thermal conductivity of the nanoparticle, and R_b. The material parameters that involve the liquid are kinematic viscosity, Prandtl number, liquid thermal conductivity, and R_b. One study that is of interest is the impact of the density of the particles. Two extreme cases have been considered: (i) Thermal conductivity of the nanoparticle is much larger than the thermal conductivity of the liquid and $R_b = 0$ and (ii) the particles are insulating, which can be simulated by either taking the thermal conductivity of the particle to be much smaller than the liquid thermal conductivity, or taking R_b to be very large. For the first case Eq. (12) reduces to

$$\frac{k}{k_f} = (1 + A\,\mathrm{Re}^m\,\mathrm{Pr}^{0.333}\phi)\left[\frac{1 + 2\phi}{1 - \phi}\right] \tag{13}$$

whereas for the second case Eq. (12) reduces to

$$\frac{k}{k_f} = (1 + A\,\mathrm{Re}^m\,\mathrm{Pr}^{0.333}\phi)\left[\frac{2(1 - \phi)}{2 + \phi}\right] \tag{14}$$

Figure 10 shows the variation of k/k_f for $\phi = 0.05$, $d = 20$ nm for water-based nanofluid at room temperature. Figure 10 shows that the resulting k of the nanofluid, even with an insulating particle, can be much higher than that of a nanofluid containing highly conducting particles with $R_b = 0$, if the density of the insulating particle is much less than that of the conducting particle. One such example is nanoparticles made of polymers versus nanoparticles made of silver. Typical polymer density is around 1000 kg m^{-3} as compared to silver which is 10,490 kg m^{-3}. Lighter particles will also lead to smaller sedimentation rates.

Sedimentation of the nanoparticles is one of the biggest technical challenges for nanofluids. Lighter particles have a substantial advantage over heavier particles with regard to sedimentation. The Stokes velocity for sedimentation is proportional to the density difference between the particles and the liquid [35]. Therefore lighter nanoparticles, such as polymer nanoparticles, will take longer to sediment as compared to heavier metallic nanoparticles. Since lighter nanoparticles are also better in enhancing the thermal conductivity of nanofluids as shown in the previous paragraph, lighter nanoparticles may be a better choice for nanofluids.

One of the biggest challenges for enabling next-generation semiconductor microprocessors is the problem of efficient heat transfer. It is because of this reason both industry and academia are actively pursuing microchannel-based liquid cooling [36–38]. One of the typical requirements for electronics cooling is that the cooling solution should be able to withstand temperatures as low as −40°C. Most likely water cannot be used as a coolant in such a scenario because water freezes at 0°C and it expands below the freezing point. Expansion of water below its freezing point can lead to severe structural damage to the various components of a microchannel-based liquid cooling system. These components could include the microchannel itself, the pump, or the tubing. To solve this problem antifreeze liquid, such as ethylene glycol (EG),

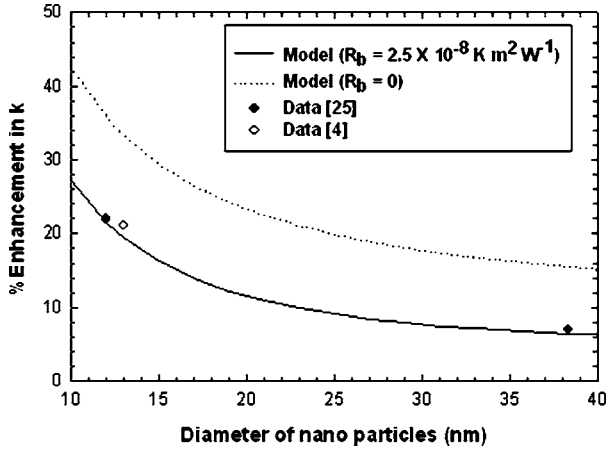

Fig. 9 Comparison of the multisphere Brownian model with data for different nanoparticle diameters

can be added to significantly reduce the freezing point. The problem with antifreeze such as EG or propylene glycol (PG) is that their thermal conductivity is very small compared to that of pure water, which leads to a smaller heat transfer coefficient. For example the thermal conductivity of water at room temperature is 0.6 $W\,m^{-1}\,K^{-1}$ and that of ethylene glycol is 0.25 $W\,m^{-1}\,K^{-1}$. If EG-based nanofluid with polymeric nanoparticles ($d=20$ nm) of density 1000 $kg\,m^{-3}$ are used, then applying Eq. (13) the thermal conductivity of the EG-based nanofluid can be as high as 0.5 $W\,m^{-1}\,K^{-1}$ for $\phi=0.05$, which is very close to pure water. This analysis shows that by using EG- or PG-based nanofluids it is possible to achieve the sameperformance as water. Another advantage of using nanofluids is that the relative enhancement in thermal conductivity increases with increasing temperature, as shown in Fig. 8. In liquid cooling of microprocessors the average temperature of the liquid will be around 50°C or higher. At 50°C the thermal conductivity of pure EG is 0.26 $W\,m^{-1}\,K^{-1}$ whereas for EG-based nanofluid with polymeric nanoparticles ($d=20$ nm) for $\phi=0.05$ it can be as high as 0.91 $W\,m^{-1}\,K^{-1}$ based on Eq. (13). These discussions suggest that nanofluids hold great promise, particularly for the electronics cooling industry.

Through an order-of-magnitude analysis we have shown that convection due to the Brownian movement of the nanoparticles is the most important mechanism for the observed enhancement in k of nanofluids, at least at the small volume fractions considered here.

To understand the exact origin of the empirical constants that we introduced in our MSBM, it seems that a numerical simulation is needed. Such a numerical simulation will include the solution of the Langevin equation for the particle motions [1,18], and the coupled Navier-Stokes and energy equations for the fluid. Origin, measurement, and modeling of R_b at a liquid/solid interface, for varying conditions such as particle size, volume fraction, temperature, nanoparticle material, etc., is also another area of important research.

5 Conclusions

We have shown through an order-of-magnitude analysis that convection caused by the Brownian movement of the nanoparticles is primarily responsible for the observed enhancement in the effective thermal conductivity of nanofluids. We introduced a Brownian-motion-based convective-conductive model which gives the correct physics for the behavior of nanofluids in various regimes. The model predicts the right trend with respect to different parameters such as nanoparticle volume fraction, nanoparticle diameter, and temperature. We have also provided general research directions for the future to remove the empiricism from the convective-conductive model.

Acknowledgment

The authors gratefully acknowledge the support of the National Science Foundation, through a GOALI award (Award No. CTS-0353543), and the direct support provided by the Intel Corporation. P.B. also acknowledges the additional support provided by Intel in the form of a graduate fellowship.

Nomenclature

A = empirical constant in Eq. (11)
a = radius of nanoparticles (nm)
BM = Brownian model
C = heat capacity per unit volume ($J\,m^{-3}\,K^{-1}$)
d = diameter of nanoparticles (nm)
DMM = diffuse mismatch model
EG = ethylene glycol
h = heat transfer coefficient ($W\,m^{-2}\,K^{-1}$)
k = thermal conductivity ($W\,m^{-1}\,K^{-1}$)
k_b = Boltzmann constant
l = mean free path [nm]
m = empirical constant in Eq. (11)
m = mass of the nanoparticle (kg)
MG = Maxwell-Garnett
Nu = Nusselt number
Pr = Prandtl number
R_b = thermal boundary resistance ($m^2\,K\,W^{-1}$)
Re = Reynolds number
T = temperature (K)
u_r = radial velocity in Stokes flow ($m\,s^{-1}$)
u_s = fluid velocity at the surface of the sphere ($m\,s^{-1}$)
v = velocity ($m\,s^{-1}$)

Greek

α = Biot number
ϕ = particle volume fraction
ϕ_c = critical volume fraction for the entire fluid to be agitated
η = viscosity ($kg\,m^{-1}\,s^{-1}$)
ν = kinematic viscosity ($m^2\,s^{-1}$)
ρ = density ($kg\,m^{-3}$)

Subscript

f = fluid
m = matrix
p = particle

References

[1] Phelan, P. E., Bhattacharya, P., and Prasher, R. S., 2005, "Nanofluids for Heat Transfer Applications," V. Prasad, Y. Jaluria, and G. Chen, eds., Annu. Rev. Heat Transfer, **14**, pp. 255–275.

[2] Lee, S., Choi, S. U. S., Li, S., and Eastman, J. A., 1999, "Measuring Thermal Conductivity of Fluids Containing Oxide Nanoparticles," J. Heat Transfer, **121**, pp. 280–289.

[3] Xie, H., Wang, J., Xi, T., Liu, Y., Ai, F., and Wu, Q., 2002, "Thermal Conductivity Enhancement of Suspensions Containing Nanosized Alumina Particles," J. Appl. Phys., **91**(7), pp. 4568–4572.

[4] Masuda, H., Ebata, A., Teramae, K., and Hishinuma, N., 1993, "Alternation of Thermal Conductivity and Viscosity of Liquid by Dispersing Ultra-fine Particles (Dispersion of γ-Al_2O_3, SiO_2, and TiO_2 Ultra-fine Particles," Netsu Bussei, **4**, pp. 227–233.

[5] Das, S. K., Putra, N., Thiesen, P., and Roetzel, W., 2003, "Temperature Dependence of Thermal Conductivity Enhancement for Nanofluids," J. Heat Transfer, **125**, pp. 567–574.

[6] Xuan, Y., and Le, Q., 2000, "Heat Transfer Enhancement of Nanofluids," Int. J. Heat Fluid Flow, **21**, pp. 58–64.

[7] Eastman, J. A., Choi, S. U. S., Li, S., Yu, W., Thompson, L. J., and Lee, S., 1997, "Enhanced Thermal Conductivity Through the Development of Nanofluids," S. Komarneni, J. C. Parker, and H. J. Wollenberger, eds., *Nanophase and Nanocomposite Materials II MRS*, MRS Symp. Proc., Pittsburgh, PA, pp. 3–11.

[8] Eastman, J. A., Choi, S. U. S., Li, S., Yu, W., and Thompson, L. J., 2001, "Anomalously Increased Effective Thermal Conductivities of Ethylene Glycol-Based Nanofluids Containing Copper Nanoparticles," Appl. Phys. Lett., **78**(6), pp. 718–720.

[9] Nan, C-W., Birringer, R., Clarke, D. R., and Gleiter, H., 1997, "Effective Thermal Conductivity of Particulate Composites With Interfacial Thermal Resistance," J. Appl. Phys., **81**, pp. 6692–6699.

[10] Yu, W., and Choi, S. U. S., 2003, "The Role of Interfacial Layers in the Enhanced Thermal Conductivity of Nanofluids: A Renovated Maxwell Model," J. Nanopart. Res., **5**, pp. 167–171.

[11] Keblinski, P., Phillpot, S. R., Choi, S. U. S., and Eastman, J. A., 2002, "Mechanisms of Heat Flow in Suspensions of Nano-sized Particles (Nanofluids)," Int. J. Heat Mass Transfer, **45**, pp. 855–863.

[12] Wilson, O. M., Hu, X., Cahill, D. G., and Braun, P. V., 2002, "Colloidal Metal Particles as Probes of Nanoscale Thermal Transport In Fluids," Phys. Rev. B, **66**, pp. 224301-1–224301-5.

[13] Huxtable, S., Cahill, D. G., Shenogin, S., Xue, L., Ozisik, R., Barone, P., Usrey, M., Strano, M. S., Siddons, G., Shim, M., and Keblinski, P., 2003, "Interfacial Heat Flow in Carbon Nanotube Suspensions," Nat. Mater., **2**, pp. 731–734.

[14] Xue, Q-Z, 2003, "Model for Effective Thermal Conductivity of Nanofluids," Phys. Lett. A, **307**, pp. 313–317.

[15] Wang, B-X., Zhou, L-P., and Peng, X-F., 2003, "A Fractal Model for Predicting the Effective Thermal Conductivity of Liquid With Suspension of Nanoparticles," Int. J. Heat Mass Transfer, **46**, pp. 2665–2672.

[16] Jang, S. P., and Choi, S. U. S., 2004, "Role of Brownian Motion in the En-

hanced Thermal Conductivity of Nanofluids," Appl. Phys. Lett., **84**(21), pp. 4316–4318.
[17] Koo, J., and Kleinstreuer, C., 2004, "A New Thermal Conductivity Model for Nanofluids," J. Nanopart. Res., to appear.
[18] Bhattacharya, P., Saha, S. K., Yadav, A., Phelan, P. E., and Prasher, R. S., 2004, "Brownian Dynamics Simulation to Determine the Effective Thermal Conductivity of Nanofluids," J. Appl. Phys., **95**(11), pp. 6492–6494.
[19] Prasher, R. S., Bhattacharya, P., and Phelan, P. E., 2005, "Thermal Conductivity of Nanoscale Colloidal Solutions (Nanofluids)," Phys. Rev. Lett., **94**(2), p. 025901.
[20] Kumar, D. H., Patel, H. E., Kumar, V. R. R., Sundarajan, T., Pradeep, T., and Das, S. K., 2004, "Model for Heat Conduction in Nanofluids," Phys. Rev. Lett., **93**(14), p. 144301.
[21] Eastman, J. A., Phillpot, S. R., Choi, S. U. S., and Keblinski, P., 2004, "Thermal Transport in Nanofluids," Annu. Rev. Mater. Res., **34**, pp. 219–246.
[22] Chen, S. H., 2000, "Thermophoretic Motion of a Spher Parallel to an Insulated Plane," J. Colloid Interface Sci., **224**, pp. 63–75.
[23] Koo, J., 2004, "Computational Nanofluid Flow and Heat Transfer Analysis as Applied to Micro-Systems," Ph.D. thesis, North Carolina State University, Raleigh, NC.
[24] Xue, L., Keblinski, P., Phillpot, S. R., Choi, S. U. S., and Eastman, J. A., 2003, "Two Regimes of Thermal Resistance at Liquid-Sold Interface," J. Chem. Phys., **118**, pp. 337–339.
[25] Swartz, E. T., and Pohl, R. O., 1989, "Thermal Boundary Resistance," Rev. Mod. Phys., **61**, pp. 605–668.
[26] *CRC Handbook of Chemistry and Physics*, 2003–2004, 84th ed., CRC Press, Boca Raton, FL.
[27] Kays, W. M., and Crawford, M. E., 1993, *Convective Heat and Mass Transfer*, McGraw-Hill International Editions, New Delhi.
[28] Incropera, F. P., and Dewitt, D. P., 1996, *Fundamentals of Heat and Mass Transfer*, 4th ed., John Wiley and Sons, New York.
[29] Mcquarrie, D. A., *Statistical Mechanics*, 2003, 1st Indian ed., Viva Books Pvt. Ltd., New Delhi.
[30] Acrivos, A., and Taylor, T. D., 1962, "Heat and Mass Transfer from Single Spheres in Stokes Flow," Phys. Fluids, **5**, pp. 387–394.
[31] Lamb, H., *Hydrodynamics*, 1945, Dover Publication, New York.
[32] Brodkey, R. S., Kim, D. S., and Sidner, W., 1991, "Fluid to Particle Heat Transfer in a Fluidized Bed and to Single Particles," Int. J. Heat Mass Transfer, **34**, pp. 2327–2337.
[33] Kunii, D., and Levenspiel, O., 1991, *Fluidization Engineering*, Butterworths, Boston.
[34] Holman, J. P., Moore, T. W., and Wong, V. M., 1965, "Particle-to-Fluid Heat Transfer in Water-Fluidized Systems," Ind. Eng. Chem. Fundam., **4**, pp. 21–31.
[35] Russel, W. B., Saville, D. A., and Schowalter, W. R., 1989, *Colloidal Dispersions*, Cambridge University Press, New York.
[36] Sobhan, C. B., and Garimella, S. V., 2001, "A Comparative Analysis of Studies on Heat Transfer and Fluid Flow in Microchannels," Microscale Thermophys. Eng., **5**, pp. 293–311.
[37] Colgan, E. G., Furman, B., Gaynes, M., Graham, W., LaBianca, N., Polastre, R. J., Rothwell, M. B., Bezama, R. J., Choudhary, R., Marston, K., Toy, H., Wakil, J., Zitz, J., and Schimdt, R., 2005, "A Practical Implementation of Silicon Microchannel Coolers For High Power Chips," *21st IEEE SEMI-THERM Symposium*, March 15–17, San Jose, CA.
[38] Chang, J-Y., Prasher, R., Chau, D., Myers, A., Dirner, J., Prstic, S., and He, D., 2005, "Convective Performance of Package Based Single Phase Microchannel Heat Exchanger," *Proc. of InterPack 2005, San Francisco, CA*, ASME, July 17–22.

Journal of Heat Transfer

Technical Briefs

Analytical Solution of Forced Convection in a Duct of Rectangular Cross Section Saturated by a Porous Medium

Kamel Hooman
School of Engineering,
The University of Queensland,
Brisbane, Australia

Ali A. Merrikh
Applied Thermal Technologies LLC,
2700 Via Fortuna,
Suite 301, Austin, TX 78746

A theoretical analysis is presented to investigate thermally and hydrodynamically fully developed forced convection in a duct of rectangular cross section filled with a hyper-porous medium. The Darcy-Brinkman model was adopted in the present analysis. A Fourier series type solution is applied to obtain the exact velocity and temperature distribution within the duct. The case of uniform heat flux on the walls, i.e., the H boundary condition in the terminology of Kays and Crawford (1993, Convective Heat and Mass Transfer, 3rd ed., McGraw-Hill, NY), is treated. Values of the Nusselt number and the friction factor as a function of the aspect ratio, the Darcy number, and the viscosity ratio are reported. [DOI: 10.1115/1.2188510]

1 Introduction

Flow through porous media is important in numerous engineering applications as reviewed by Cheng [2]. Application of flow through rectangular porous ducts was investigated for cooling of electronics in radar equipment with close attention to unraveling the behavior of temperature-dependent viscosity of (PAO) in [3]. Narasimhan et al. [4] developed two new theories for hydraulics in porous ducts of parallel plate cross section for temperature-dependent viscosity fluids by modifying the Forchheimer-Darcy flow model. The focus was on extremely low permeability, for Al foam as the porous substrate and Poly-Alpha-Olefin (PAO) as the fluid. Furthermore, a perturbation method was employed that captured predictive theoretical global pressure-drop equations using the Forchheimer-Darcy model.

Contributed by the Heat Transfer Division of ASME for publication in the JOURNAL OF HEAT TRANSFER. Manuscript received August 24, 2005; final manuscript received December 16, 2005. Review conducted by Jose L. Lage.

Further investigation is necessary for understanding the flow and thermal behavior of non-circular porous ducts of high porosity, i.e., the Brinkman porous media [5] (cited in [6]). Recently, Lage [7] presented a general review of the historical background of the developed models in porous media. In cases of high permeability porous media (porosity higher than 0.6 according to [6]), it is known that the Darcy-Brinkman model can predict hydraulics through porous media as closely as the general model of Vafai and Tien [8] for incompressible flow, as presented for natural convection in Merrikh and Mohamad [9], for example. As stated by Nield and Bejan [6], it is suitable to use the Darcy-Brinkman flow model to cope with hyperporous materials. The term "hyperporous" has been proposed for materials with high porosity such as the example in [6] for which the Darcy number is higher than unity. This large Darcy number was observed in a sample of compressed aluminum foam with 1 mm thickness. A substantial amount of literature on the accuracy and the limitation of the Darcy-Brinkman model can be found in [6–8].

Analytical solutions are very useful in benchmarking numerical computations. They are also useful for parametric studies when a large number of parameters are involved wherever numerical results cannot be experimentally verified, or no experiments are possible due to time, cost, and other limiting factors. Thus, the question naturally arises as to whether analytical solutions for ducts of cross section other than circular tube or parallel plates are possible.

Haji-Sheikh and Vafai [10] studied thermally developing forced convection (the Graetz problem) in ducts of various shapes, including elliptical ones, by the method of weighted residuals. This method is especially convenient when the boundary conditions are homogeneous, with a uniform temperature imposed on the walls. Adopting the Graetz problem is advantageous because in conjunction with standard computing packages, it allows one-time computation of all the required eigen values all at once, rather than having to get them one at a time.

Hooman [11] has reported closed form analytical solution for the fully developed flow and temperature distribution, as well as the local entropy generation rate by applying the Darcy model for flow in a duct of elliptical cross section. By observing the fully developed temperature profile, he found that heat transfer is conduction dominated as a result of very slow (creeping) velocities in such low-porosity media. However, when non-Darcy effects are to be considered, the problem becomes more complicated and one can no longer obtain such simple expressions for the temperature profile and the Nusselt number.

Using Fourier series expansion, we present an analytical solution for the velocity profile in a rectangular duct by solving the Darcy-Brinkman momentum equation. We then make use of this Fourier solution to solve the energy equation and thereby investigate flow and heat transfer characteristics of rectangular ducts. Up until now, to the authors' knowledge, no analytical solution is available for the studied problem.

Table 1 Comparison between present results with those reported for clear flow case

Parameter	Reference	$a=1$	$a=4$	$a=8$	$a\to\infty$
Nusselt number	Present	3.60	5.33	6.48	8.23
	[1]	3.61	5.33	6.49	8.23
Fiction factor	Present	14.25	18.26	20.51	24
	[13]	14.25	18.25	20.50	24

2 Analysis

The Darcy-Brinkman momentum equation for the case of unidirectional (fully developed) flow in the x^*-direction in a rectangular duct occupied by a porous medium with velocity $u^*(y^*,z^*)$ is [6]

$$\tilde{\mu}\left(\frac{\partial^2 u^*}{\partial y^{*2}}+\frac{\partial^2 u^*}{\partial z^{*2}}\right)-\frac{\mu}{K}u^*+G=0 \tag{1}$$

In the above equation, μ is the fluid viscosity and $\tilde{\mu}$ is the effective viscosity of the porous medium, K is the permeability, and G is the negative of the applied pressure gradient, i.e., the body force term. The following nondimensional variables are defined by:

$$y=\frac{y^*}{H},\quad z=\frac{z^*}{H},\quad u=\frac{\mu u^*}{GH^2} \tag{2}$$

Using the nondimensional parameters and the viscosity ratio $M=\tilde{\mu}/\mu$ and defining the Darcy number as $\mathrm{Da}=K/H^2$, the momentum equation takes the following form:

$$\frac{\partial^2 u}{\partial y^2}+\frac{\partial^2 u}{\partial z^2}-s^2u+\frac{1}{M}=0 \tag{3}$$

In the above equation, the porous medium shape factor s is defined as $s=(M\mathrm{Da})^{-1/2}$. Brinkman [5] assumed $\tilde{\mu}=\mu$ leading to $M=1$ for this case. However, it is known that $\tilde{\mu}$ is related to the geometry of the porous media [6]. We assume $M=1$ leading to Darcy number K/H^2 which yields $s=H/K^{1/2}$. When one is to cope with an engineering problem it can be observed that changes in permeability will alter the value of s for a fixed H. Equation (3) has to be solved subject to the boundary conditions $u=0$ when $y=\pm 1$ and $z=\pm a$, i.e., impermeable walls assumption. Hence, the well-known eigen-function expansion approach leads to the solution for the velocity

$$u=\frac{4}{\pi M}\sum_{n=1}^{\infty}\frac{(-1)^{n-1}}{(2n-1)m^2}\left(1-\frac{\cosh mz}{\cosh ma}\right)\cos\lambda_n y \tag{4}$$

With $\lambda_n=(2n-1)\pi/2$, the value of m is found to be

$$m=(s^2+\lambda_n^2)^{1/2} \tag{5}$$

The mean velocity is thus

$$\overline{u}=\frac{2}{M}\sum_{n=1}^{\infty}\frac{1}{\lambda_n^2 m^2}\left(1-\frac{\tanh ma}{ma}\right) \tag{6}$$

and the normalized velocity is

$$\hat{u}=\frac{u}{\overline{u}}=\frac{1}{A}\sum_{n=1}^{\infty}B_n(z)\cos\lambda_n y \tag{7}$$

where

$$A=\frac{2}{\pi}\sum_{n=1}^{\infty}\frac{1}{(2n-1)^2m^2}\left(1-\frac{\tanh ma}{ma}\right) \tag{8a}$$

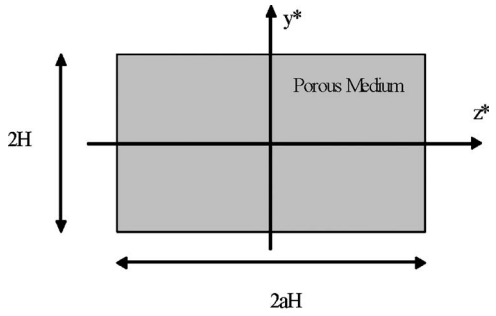

Fig. 1 Schematic of the studied problem

$$B_n(z)=\frac{(-1)^{n-1}}{(2n-1)m^2}\left(1-\frac{\cosh mz}{\cosh ma}\right)=D_n\left(1-\frac{\cosh mz}{\cosh ma}\right) \tag{8b}$$

The Fanning friction factor is defined as

$$C_f=\frac{2\mu\left(\int_0^{aH}\left.\frac{\partial u^*}{\partial y^*}\right|_{y^*=H}dz^*+\int_0^{H}\left.\frac{\partial u^*}{\partial z^*}\right|_{z=aH}dy^*\right)}{\rho U_m^2(1+a)H} \tag{9}$$

The multiplication of the Fanning fiction factor and the Reynolds number yields

$$C_f\mathrm{Re}=\frac{16}{\pi A}\left(\frac{a}{a+1}\right)^2\sum_{n=1}^{\infty}\frac{\lambda_n^2+s^2\frac{\tanh ma}{ma}}{m^2(2n-1)^2} \tag{10}$$

The characteristic length in the Reynolds number definition is the hydraulic diameter D_H defined by $D_H=4Ha/(a+1)$. From here on, we call the term $C_f\,\mathrm{Re}$ the friction factor for short. With thermal conduction in the x^*-direction neglected, the energy equation becomes

$$u^*\frac{\partial T^*}{\partial x^*}=\frac{k}{\rho c_P}\left(\frac{\partial^2 T^*}{\partial y^{*2}}+\frac{\partial^2 T^*}{\partial z^{*2}}\right) \tag{11}$$

Here T^* is the temperature, ρ is the density of the fluid, c_P is the specific heat at constant pressure, and k is the effective thermal conductivity of the medium ($k=(1-\varphi)k_s+\varphi k_f$ with k_s and k_f being the solid and fluid thermal conductivity and φ denoting porosity [6]). For the case of boundaries at uniform heat flux q'' the first law of thermodynamics implies

$$\frac{\partial T^*}{\partial x^*}=\frac{q''}{\rho c_P H\overline{u}}\left(\frac{a+1}{a}\right) \tag{12}$$

leading to the dimensionless form of the energy equation as

$$\frac{\partial^2\theta}{\partial y^2}+\frac{\partial^2\theta}{\partial z^2}=-\mathrm{Nu}\,\hat{u}\left(\frac{a+1}{2a}\right)^2 \tag{13}$$

where the dimensionless temperature profile is $\theta=(T^*-T_w)/(T_m-T_w)$. One can easily verify the that the thermal boundary conditions are $\theta=0$ at $y=\pm 1$ and at $z=\pm a$. The Nusselt number is defined as

$$\mathrm{Nu}=\frac{q''D_H}{k(T_w^*-T_m^*)} \tag{14}$$

The bulk temperature is defined as $T_m=\langle\hat{u}T^*\rangle$. The angle brackets denote an average taken over the duct cross section. The solution satisfying the differential Eq. (13) and the boundary conditions may be written as

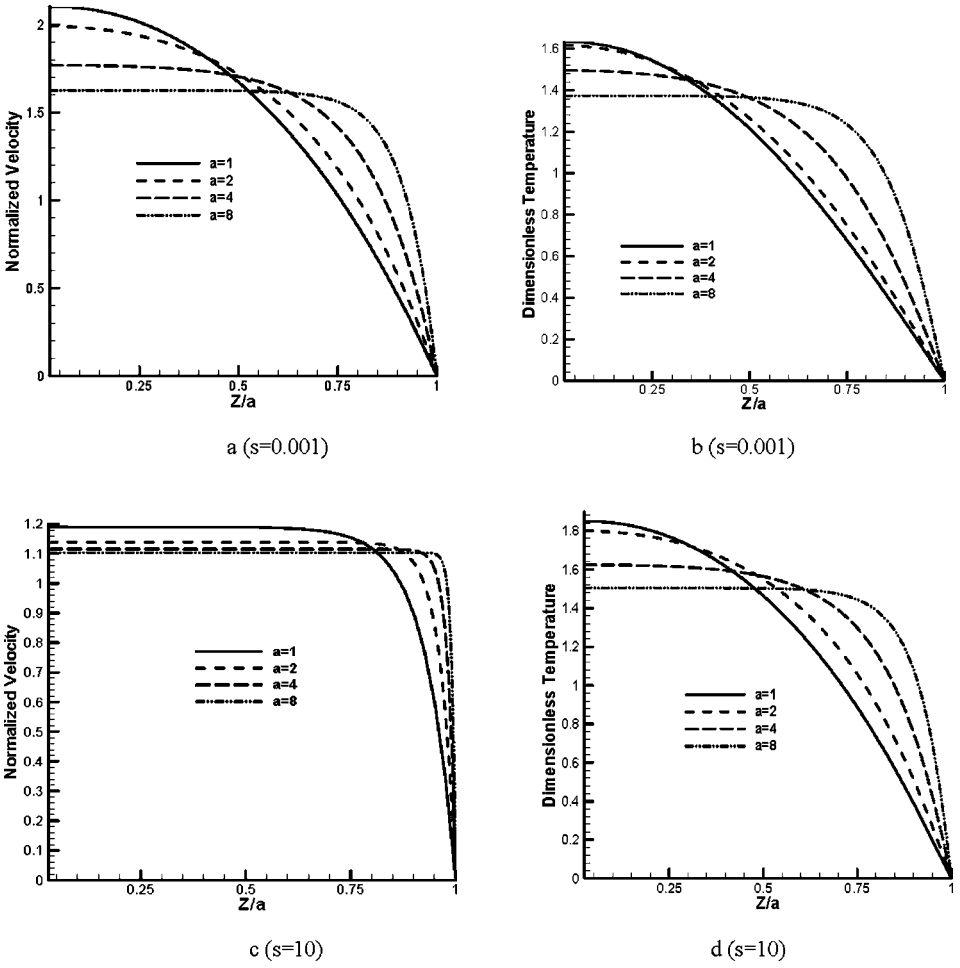

Fig. 2 Midplane normalized velocity predicted by Eq. (7) and midplane dimensionless temperature profile predicted by Eq. (16), versus *z*/*a* for some values of *s* and *a*

$$\theta = \sum_{n=0}^{\infty} f_n(z)\cos \lambda_n y \tag{15}$$

After some algebraic manipulation one finds the dimensionless temperature profile as

$$\theta = \left(\frac{a+1}{2as}\right)^2 \frac{\mathrm{Nu}}{A} \sum_{n=1}^{\infty} \frac{D_n}{\lambda_n^2} \cos \lambda_n y \left(s^2 - m^2 \frac{\cos h\lambda_n z}{\cos h\lambda_n a} + \lambda_n^2 \frac{\cosh mz}{\cosh ma}\right) \tag{16}$$

The compatibility condition (an identity resulting from the definitions)

$$\langle \hat{u}\theta \rangle = 1 \tag{17}$$

yields an expression for the Nusselt number, namely,

$$\mathrm{Nu} = 2\left(\pi A s^2 \frac{a}{a+1}\right)^2 \Bigg/ \sum_{n=1}^{\infty} \frac{K_n}{(2n-1)^4} \tag{18}$$

where

$$K_n = \frac{\tanh ma}{ma} - \frac{\tanh \lambda_n a}{\lambda_n a} - s^2\left(\frac{\lambda_n^2 - 2s^2}{2m^4}\right)\left(1 - \frac{\tanh ma}{ma}\right) + \frac{\lambda_n^2 s^2}{2m^4}\tanh^2 ma \tag{19}$$

Hence the final expression for Nusselt number becomes

$$\mathrm{Nu} = 8s^4\left(\frac{a}{a+1}\right)^2 \frac{S_1^2}{S_2} \tag{20}$$

where

$$S_1 = \sum_{n=1}^{\infty} \frac{1}{(2n-1)^2 m^2}\left(1 - \frac{\tanh ma}{ma}\right) \tag{21a}$$

$$S_2 = \sum_{n=1}^{\infty} \frac{K_n}{(2n-1)^4} \tag{21b}$$

Within the limit, as $a \to \infty$ (parallel plates case) and $s \to 0$ (clear fluid case) we obtain

$$S_1 = \frac{4}{\pi^2} \sum_{n=1}^{\infty} \frac{1}{(2n-1)^4} = \frac{\pi^2}{24} \tag{22a}$$

$$S_2 = \frac{16s^4}{\pi^4} \sum_{n=1}^{\infty} \frac{1}{(2n-1)^8} = \frac{17s^4\pi^4}{10{,}080} \tag{22b}$$

which is the Nusselt number that represents laminar flow through parallel plates [12], i.e., Nu=8.236. On the other hand, in the limit as $a \to \infty$ and $s \to \infty$ one obtains

$$S_1 = \frac{1}{s^2}\sum_{n=1}^{\infty}\frac{1}{(2n-1)^2} = \frac{\pi^2}{8s^2} \tag{23a}$$

$$S_2 = \sum_{n=1}^{\infty}\frac{1}{(2n-1)^4} = \frac{\pi^4}{96} \tag{23b}$$

The above yield a Nusselt number value that represents Darcy flow through parallel plates [6], i.e., Nu=12.

In addition to the two limiting cases (very large aspect ratio, i.e., parallel plate channel), one can easily compare the results of friction factor (Eq. (10)) and Nusselt number (Eq. (20)) for various aspect ratios with those previously reported. The comparisons of the benchmarking are shown in Table 1. As seen, the present results are in good agreement with those of clear flow case.

3 Results and Discussion

Figure 2 shows the effects of aspect ratio and shape factor on the velocity and temperature distribution. Figures 2(*a*) and 2(*b*) show the midplane velocity and temperature for a small shape factor, $s=10^{-3}$, and Figs. 2(*c*) and 2(*d*) illustrate the midplane velocity and temperature for a relatively large shape factor, i.e., for $s=10$. It is evident that increasing *s* leads to strong velocity variations in a thin near-wall region, i.e., a thinner hydrodynamic boundary layer near the walls. This phenomenon is more pronounced for large aspect ratios. Compared to the small aspect ratios, for large aspect ratios, the midplane velocity variation is steeper in the region adjacent to the sidewalls and one expects the flow direction to be unidirectional for large values of *a*, i.e., the parallel plates case. It can also be concluded that the value of the midplane normalized velocity at the duct center, which is the maximum fluid velocity decreases as *a* increases. This is verified for both small and large shape factors. However, this maximum value decreases as *s* increases since the boundary effects become less significant with the no-slip condition becoming less important in this case. Hence, the velocity profile bears a "flat" shape near the wall. Based on the figures, it may also be concluded that the dimensionless midplane temperature at the duct center, which is also the maximum dimensionless temperature, would decrease as a result of an increase in *a*. Decreasing *s* reduces the maximum temperature as a result of increase of the friction drag within the porous medium which lower the steepness of the profile [13].

For $s=0.001$, the midplane temperature profile is similar to the midplane velocity distribution. For large values of *s*, however, one no more observes similar profiles since the velocity distribution is highly dependent on *s* while the temperature is affected by *s* indirectly through velocity distribution. It can also be deduced that for small aspect ratios, the temperature distribution is more or less similar to the velocity distribution especially for large values of *s* where the temperature distribution is a conductionlike. This fact is not surprising when one observes that the Darcy-Brinkman momentum equation is similar to the energy equation when $s\to\infty$.

Figure 3(*a*) represents the values of $C_f\,\mathrm{Re}$ varying as a function of *s*. To benchmark the analytical predictions, we compare our results with those of Kaviany [14] for the largest aspect ratio, $a=16$ to represent the parallel plates case. It is evident that our results demonstrate a similar trend to those reported by [14]. It is also evident that the results of [14] overpredict our results, however; the difference decays when *s* becomes very large.

Figure 3(*b*) shows plots of the fully developed Nusselt number versus *s* for different values of *a*. For small values of *s*, the results are in good agreement with those previously reported for the clear flow case [1]. For the case of large aspect ratios, it is evident that the values of Nu fall within the range between those of clear flow and slug flow, as expected. Increasing *s* from 10 to beyond $s=10^3$, Nu climbs from a low to a high value irrespective of *a* value. This is justified by observing that for such high values of *s* the velocity distribution is close to slug flow regime and since the temperature distribution is not changed that much, the net effect would increase Nu. The trend shown in this figure is similar to that previously reported for forced convection in a fluid-saturated porous medium for flow between isothermal parallel plates (e.g., Fig. 6 of [14]) or in a circular tube with an isoflux wall (Figs. 3 of [15]). Observe that an increase in *s* increases both Nu and $C_f\,\mathrm{Re}$. This important result requires optimization in design of engineering systems, which is left for a later report.

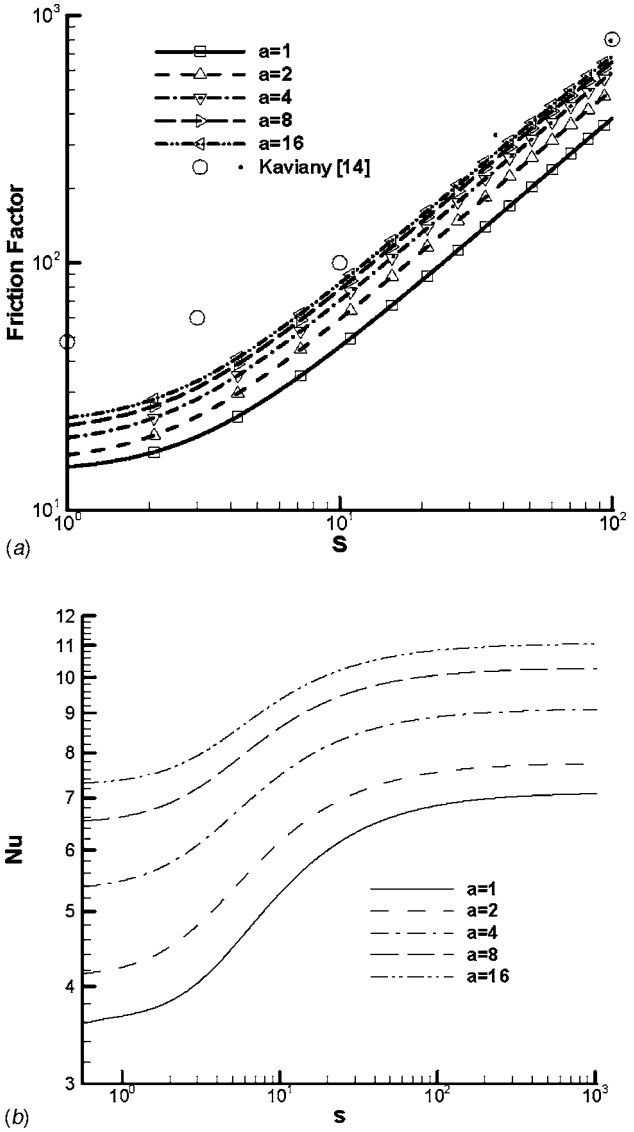

Fig. 3 (*a*) Plots of the friction factor by Eq. (10) versus *s* for various aspect ratios and (*b*) plots of the Nusselt number predicted by Eq. (20) versus *s* for various aspect ratios

Acknowledgment

The authors are indebted to Professor D. A. Nield of the University of Auckland and Professor A. Haji-Sheikh of the University of Texas at Arlington for their guidelines and improving comments. Ali A. Merrikh would like to thank the Thermal Center of Excellence of Applied Thermal Technologies for the support.

References

[1] Kays, W. M., and Crawford, M. E., 1993, *Convective Heat and Mass Transfer*, 3rd ed., McGraw-Hill, New York.
[2] Cheng, P., 1978, "Heat Transfer in Geothermal Systems," Adv. Heat Transfer, **14**, pp. 1–105.

[3] Narasimhan, A., and Lage, J. L., 2001, "Modified Hazen-Dupuit-Darcy Model for Forced Convection of a Fluid With Temperature-Dependent Viscosity," J. Heat Transfer, **123**, pp. 31–38.
[4] Narasimhan, A., Lage, J. L., and Nield, D. A., 2001, "New Theories for Forced Convection Through Porous Media by Fluids With Temperature-Dependent Viscosity," J. Heat Transfer, **123**, pp. 1045–1051.
[5] Brinkman, H. C., 1947, "A Calculation of the Viscous Force Exerted by a Flowing Fluid on a Dense Swarm of Particles," Appl. Sci. Res., **1**, pp. 27–34.
[6] Nield, D. A., and Bejan, A., 1999, *Convection in Porous Media*, 2nd ed., Springer-Verlag, New York.
[7] Lage, J. L., 1998, "The Fundamental Theory of Flow Through Permeable Media From Darcy to Turbulence," in *Transport Phenomena in Porous Media*, D. B. Ingham and I. Pop, eds., Pergamon, Oxford, pp. 1–30.
[8] Vafai, K., and Tien, C. L., 1981, "Boundary and Inertia Effects on Flow and Heat Transfer in Porous Media," Int. J. Heat Mass Transfer, **24**, pp. 195–203.
[9] Merrikh, A. A., and Mohamad, A. A., 2000, "Transient Natural Convection in a Porous Enclosure," J. Porous Media, **3**(2), pp. 165–178.
[10] Haji-Sheikh, A., and Vafai, K., 2004, "Analysis of Flow and Heat Transfer in Porous Media Imbedded Inside Various-Shaped Ducts," Int. J. Heat Mass Transfer, **47**, pp. 1889–1905.
[11] Hooman, K., 2005, "Fully Developed Temperature Distribution in a Porous Saturated Duct of Elliptical Cross-Section, With Viscous Dissipation Effects and Entropy Generation Analysis," Heat Transfer-Jpn. Res., **36**, pp. 237–245.
[12] Holman, J. P., 2002, *Heat Transfer*, 9th ed., McGraw-Hill, New York.
[13] White, F. M., 1991, *Viscous Fluid Flow*, McGraw-Hill, New York.
[14] Kaviany, M., 1985, "Laminar Flow Through a Porous Channel Bounded by Isothermal Parallel Plates," Int. J. Heat Mass Transfer, **28**, pp. 851–858.
[15] Hooman, K., and Ranjbar-Kani, A. A., 2004, "A Perturbation Based Analysis to Investigate Forced Convection in a Porous Saturated Tube," J. Comput. Appl. Math., **162**, pp. 411–419.

Thermal Ignition in a Reactive Viscous Flow Through a Channel Filled With a Porous Medium

O. D. Makinde
Applied Mathematics Department,
University of Limpopo,
Private Bag X1106,
Sovenga 0727, South Africa
e-mail: makindeo@ul.ac.za

This paper examines the steady-state solutions of a strongly exothermic reaction of a viscous combustible material in a channel filled with a saturated porous medium under Arrhenius kinetics, neglecting reactant consumption. The Brinkman model is employed and analytical solutions are constructed for the governing nonlinear boundary-value problem using a perturbation technique together with a special type of Hermite-Padé approximants and important properties of the temperature field including bifurcations and thermal criticality are discussed.
[DOI: 10.1115/1.2188511]

Keywords: porous medium flows, arrhenius kinetics, hermite-Padé approximants, thermal criticality

1 Introduction

Studies related to thermal ignitions and heat transfers in inert porous media are extremely useful in improving the design and operation of many engineering devises ([1–3]). For instance, the catalytic converter in an automobile's exhaust system is made up of a finely divided platinum-iridium catalyst (i.e., forming a porous matrix) and provides a platform for exothermic chemical reaction where unburned hydrocarbons completely combust. This helps to reduce the emissions of toxic car pollutant such as carbon monoxide (CO) into the environment. However, in order to ignite, stabilize, and operate under steady-state conditions, the thermal criticality of a burner based on combustion in inert porous media like catalytic converter must be determined [3]. Mathematically speaking, thermal ignition and heat transfer in inert porous media constitutes a nonlinear reaction diffusion problem and the long-time behavior of the solutions in space will provide an insight into the inherently complex physical process of thermal runaway in the system [4,5].

The theory of nonlinear reaction diffusion equations is quite elaborate and their solution in rectangular, cylindrical, and spherical coordinate remains an extremely important problem of practical relevance in the engineering sciences [6,7]. Several numerical approaches have developed in the last few decades, e.g., finite differences, spectral method, shooting method, etc., to tackle this problem. More recently, the ideas on classical analytical methods have experienced a revival, in connection with the proposition of novel hybrid numerical-analytical schemes for nonlinear differential equations. One such trend is related to Hermite-Padé approximation approach [8–10]. This approach, over the last few years, proved itself as a powerful benchmarking tool and a potential alternative to traditional numerical techniques in various applications in sciences and engineering. This semi-numerical approach is also extremely useful in the validation of purely numerical scheme.

Contributed by the Heat Transfer Division of ASME for publication in the JOURNAL OF HEAT TRANSFER. Manuscript received May 17, 2005; final manuscript received January 28, 2006. Review conducted by Sumanta Acharya.

In this paper, we intend to construct approximate solution for a steady-state reaction diffusion equation that models thermal runaway problem in a porous medium using perturbation technique together with a special type of Hermite-Padé approximants. The mathematical formulation of the problem is established and solved in Secs. 2 and 3. In Sec. 4 we introduce and apply some rudiments of Hermite-Padé approximation technique. Both numerical and graphical results are presented and discussed quantitatively with respect to various parameters embedded in the system in section five.

2 Mathematical Model

We consider a steady-state hydrodynamically and thermally developed unidirectional flow of a viscous combustible reacting fluid in the x direction between impermeable isothermal boundaries at $y=0$ and $y=a$, filled with a homogeneous and isotropic porous medium as illustrated in Fig. 1 below.

Neglecting reactant consumption, the governing momentum and energy balance equations are

$$\frac{d^2u}{dy^2} - \frac{u}{K} - \frac{1}{\mu}\frac{dP}{dx} = 0 \tag{1}$$

$$\frac{d^2T}{dy^2} + \frac{QC_0A}{k}e^{-E/RT} + \frac{\mu}{k}\left(\frac{du}{dy}\right)^2 + \frac{\mu u^2}{Kk} = 0 \tag{2}$$

Equation (1) is a well-known Brinkman momentum equation [1] while the additional viscous dissipation term in Eq. (2) is due to Al-Hadhrami et al. [6] and is valid in the limit of very small and very large porous medium permeability.

The appropriate boundary conditions are

$$u = 0 \quad T = T_0 \quad \text{on} \quad y = a \tag{3}$$

$$u = 0 \quad T = T_0 \quad \text{on} \quad y = 0 \tag{4}$$

where T is the absolute temperature, P the fluid pressure, T_0 the geometry wall temperature, k the thermal conductivity of the material, K the porous medium permeability parameter, Q the heat of reaction, A the rate constant, E the activation energy, R the universal gas constant, C_0 the initial concentration of the reactant species, a the channel width, (x,y) the distance measured in the axial and normal directions, respectively, and μ is the combustible material dynamic viscosity coefficient. Let $M=(a^2/U\mu)(dP/dx)$ be a constant axial pressure gradient parameter and U the fluid characteristic velocity. We introduce the following dimensionless variables into Eqs. (1)–(4):

$$\theta = \frac{E(T-T_0)}{RT_0^2} \quad \varepsilon = \frac{RT_0}{E} \quad \bar{y} = \frac{y}{a} \quad \lambda = \frac{QEAa^2C_0e^{-E/RT_0}}{T_0^2Rk} \tag{5}$$

$$W = \frac{u}{UM} \quad \delta = \frac{\mu M^2U^2e^{E/RT_0}}{QAa^2C_0} \quad \beta = \sqrt{\frac{1}{\mathrm{Da}}} \quad \mathrm{Da} = \frac{K}{a^2}$$

and obtain the dimensionless governing equation together with the corresponding boundary conditions as (neglecting the bar symbol for clarity)

$$\frac{d^2W}{dy^2} - \beta^2W - 1 = 0 \tag{6}$$

$$\frac{d^2\theta}{dy^2} + \lambda\left(e^{(\theta/(1+\varepsilon\theta))} + \delta\left(\frac{dW}{dy}\right)^2 + \delta\beta^2W^2\right) = 0 \tag{7}$$

$$W(0) = W(1) = 0 \quad \theta(0) = \theta(1) = 0 \tag{8}$$

where λ, ε, δ, β, Da represent the Frank-Kamenetskii parameter, activation energy parameter, the viscous heating parameter, the porous medium permeability parameter, and the Darcy number, respectively. In the following sections, Eqs. (6)–(8) are solved

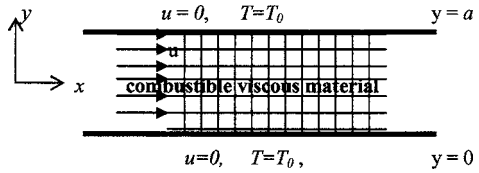

Fig. 1 Geometry of the problem

using both perturbation and multivariate series summation techniques.

3 Perturbation Method

It is very easy to obtain the solution for the fluid velocity profile exactly, however, due to the nonlinear nature of the temperature field, Eq. (7), it is convenient to form a power series expansion in the Frank-Kamenetskii parameter λ, i.e.,

$$\theta = \sum_{i=0}^{\infty} \theta_i \lambda^i \tag{9}$$

Substituting the solution series (9) into Eq. (7) and collecting the coefficients of like powers of λ, we obtained and solved the equations of the coefficients of solution series iteratively. The solution for the velocity and temperature fields are given as

$$W(y;\beta > 0) = -\frac{(\cosh(y\beta) - 1)}{\beta^2} - \frac{(1 - \cosh(\beta))\sinh(y\beta)}{\beta^2 \sinh(\beta)} \tag{10a}$$

$$W(y;\beta \to 0) = -\frac{1}{2}(y^2 - y) - \frac{\beta^2}{24}(y^4 - 2y^3 + y) - \frac{\beta^4}{720}(y^6 - 3y^5 + 5y^3 - 3y) + O(\beta^6) \tag{10b}$$

$$\begin{aligned}\theta(y) = -\frac{\lambda}{2\beta^4(\cosh(\beta)+1)}[&\cosh(\beta)y^2\beta^4 - \cosh(\beta)y\beta^4 \\ &- y\delta\beta^2\cosh(\beta) - 4\delta\cosh(\beta)\cosh(y\beta) \\ &+ 4\delta\sinh(\beta)\sinh(y\beta) - 4\delta\cosh(y\beta) + \delta y^2\beta^2\cosh(\beta) \\ &+ 2\delta\cosh(\beta)\cosh^2(y\beta) - 2\delta\sinh(\beta)\sinh(y\beta)\cosh(y\beta) \\ &+ \delta y^2\beta^4 + 2\delta\cosh(\beta) - y\delta\beta^2 - y\beta^4 + y^2\beta^4 + 4\delta] + O(\lambda^2).\end{aligned} \tag{11}$$

Using a computer symbolic algebra package (MAPLE), we obtained the first 30 terms of the above solution series (11) as well as the series for the wall heat transfer rate, $\mathrm{Nu} = -d\theta/dy$ at $y = 1$.

4 Thermal Criticality and Bifurcation Study

The concept of thermal criticality or non-existence of steady-state solution to nonlinear reaction diffusion problems for certain parameter values is extremely important from application point of view. This characterizes the thermal stability properties of the materials under consideration and the onset of thermal runaway phenomenon. In order to determine the appearance of thermal runaway in the system together with the evolution of temperature field as the exothermic reaction rate increases (i.e., $\lambda > 0$), we employ a special type of Hermite-Padé approximation technique. Suppose that the partial sum

$$U_{N-1}(\lambda) = \sum_{i=0}^{N-1} a_i \lambda^i = U(\lambda) + O(\lambda^N) \quad \text{as } \lambda \to 0, \tag{12}$$

is given. We are concerned with the bifurcation study by analytic continuation as well as the dominant behavior of the solution by using partial sum (12). We expect that the accuracy of the critical parameters will ensure the accuracy of the solution. It is well known that the dominant behavior of a solution of a differential equation can often be written as Guttamann [11],

$$U(\lambda) \approx \begin{cases} H(\lambda_c - \lambda)^{\alpha} & \text{for } \alpha \neq 0,1,2,\ldots \\ H(\lambda_c - \lambda)^{\alpha}\ln|\lambda_c - \lambda| & \text{for } \alpha = 0,1,2,\ldots \end{cases} \quad \text{as } \lambda \to \lambda_c \tag{13}$$

where H is some constant and λ_c is the critical point with the exponent α. However, we shall make the simplest hypothesis in the contest of nonlinear problems by assuming the $U(\lambda)$ is the local representation of an algebraic function of λ. Therefore, we seek an expression of the form

$$F_d(\lambda, U_{N-1}) = A_{0N}(\lambda) + A_{1N}^d(\lambda)U^{(1)} + A_{2N}^d(\lambda)U^{(2)} + A_{3N}^d(\lambda)U^{(3)} \tag{14}$$

such that

$$A_{0N}(\lambda) = 1, \quad A_{iN}(\lambda) = \sum_{j=1}^{d+i} b_{ij}\lambda^{j-1} \tag{15}$$

and

$$F_d(\lambda, U) = O(\lambda^{N+1}) \quad \text{as } \lambda \to 0 \tag{16}$$

where $d \geqslant 1$, $i = 1, 2, 3$. The condition (15) normalizes the F_d and ensures that the order of series A_{iN} increases as i and d increase in value. There are thus $3(2+d)$ undetermined coefficients b_{ij} in expression (15). The requirement (16) reduces the problem to a system of N linear equations for the unknown coefficients of F_d. The entries of the underlying matrix depend only on the N given coefficients a_i. Henceforth, we shall take

$$N = 3(2 + d) \tag{17}$$

so that the number of equations equals the number of unknowns. Equation (16) is a new special type of Hermite-Padé approximants. Both the algebraic and differential approximants forms of Eq. (16) are considered. For instance, we let

$$U^{(1)} = U \quad U^{(2)} = U^2 \quad U^{(3)} = U^3 \tag{18}$$

and obtain a cubic Padé approximant. This enables us to obtain solution branches of the underlying problem in addition to the one represented by the original series. In the same manner, we let

$$U^{(1)} = U \quad U^{(2)} = DU \quad U^{(3)} = D^2U \tag{19}$$

in Eq. (15), where D is the differential operator given by $D = d/d\lambda$. This leads to a second order differential approximants. It is an extension of the integral approximants idea by Hunter and Baker [8] and enables us to obtain the dominant singularity in the flow field, i.e., by equating the coefficient $A_{3N}(\lambda)$ in Eq. (16) to zero. Meanwhile, it is very important to know that the rationale for chosen the degrees of A_{iN} in Eq. (15) in this particular application is based on the simple technique of singularity determination in second order linear ordinary differential equation with polynomial coefficients as well as the possibility of multiple solution branches for the nonlinear problem [12]. In practice, one usually finds that the dominant singularities are located at zeroes of the leading polynomial $A_{3N}^{(d)}$ coefficients of the second order linear ordinary differential equation. Hence, some of the zeroes of $A_{3N}^{(d)}$ may provide approximations of the singularities of the series U and we expect that the accuracy of the singularities will ensure the accuracy of the approximants.

The critical exponent α_N can easily be found by using Newton's polygon algorithm. However, it is well known that, in the case of algebraic equations, the only singularities that are structurally stable are simple turning points. Hence, in practice, one almost

Table 1 Computations showing the procedure rapid convergence for $\varepsilon=0.0$, $\delta=0.0$

d	N	Nu	λ_c	α_{cN}
4	18	3.999999	3.513830	0.499999
6	24	4.000000	3.513830	0.500000
8	30	4.000000	3.513830	0.500000

invariably obtains $\alpha_N=1/2$. If we assume a singularity of algebraic type as in Eq. (13), then the exponent may be approximated by

$$\alpha_N = 1 - \frac{A_{2N}(\lambda_{CN})}{DA_{3N}(\lambda_{CN})} \tag{20}$$

5 Results and Discussion

The bifurcation procedure above is applied on the first 30 terms of the solution series and we obtained the results shown in Tables 1 and 2 below.

The result in Table 1 shows the rapid convergence of our procedure for the dominant singularity (i.e., λ_c) together with its corresponding critical exponent α_c with gradual increase in the number of series coefficients utilized in the approximants. In Table 2, we noticed that the magnitude of thermal criticality at very large activation energy ($\varepsilon=0$) decreases with a decrease in the porous medium permeability ($\beta>0$). This shows clearly that reducing the permeability of a porous medium will enhance the early appearance of ignition in a reactive viscous flow of a combustible fluid. It is noteworthy that a decrease in the combustible fluid activation energy (i.e., $\varepsilon>0$) will lead to an increase in the magnitude of thermal ignition criticality, hence, delaying the appearance of thermal runaway in the system. A slice of the bifurcation diagram for $0\leqslant\varepsilon\ll 1$ is shown in Fig. 2. In particular, for every $\beta\geqslant 0$, there is a critical value λ_c (a turning point) such that, for $0\leqslant\lambda<\lambda_c$ there are two solutions (labeled I and II) and solution II diverges to infinity as $\lambda\to 0$. The fully developed dimensionless velocity distribution is shown in Fig. 3. We observed that the magnitude of the fluid velocity increases and tend to that of plane Poiseuille flow with a gradual increase in the porous medium permeability (i.e., $\beta\to 0$). Similarly, an increase in the fluid temperature is observed with increasing values of λ due to a combined effects of viscous dissipation and exothermic reaction as shown in Fig. 4.

Table 2 Computations showing thermal ignition criticality for different parameter values (δ, β, ε)

δ	β	ε	Nu	λ_c	α_{cN}
0.0	0.0	0.0	4.000000	3.513830	0.500000
1.0	0.0	0.0	4.136946	3.454198	0.500000
1.0	0.1	0.0	4.136787	3.454184	0.500000
1.0	0.2	0.0	4.136314	3.454144	0.500000
1.0	0.5	0.0	4.133093	3.453000	0.500000
1.0	0.5	0.1	5.256251	3.893308	0.500000

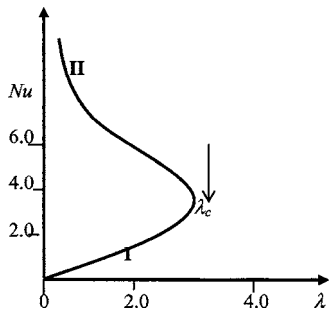

Fig. 2 A slice of approximate bifurcation diagram in the (λ, $Nu(\beta,\varepsilon)$) plane

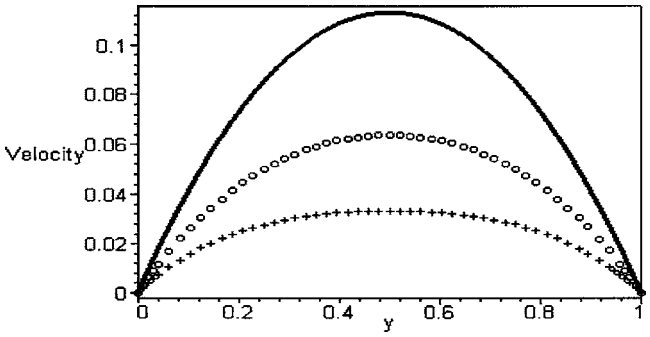

Fig. 3 Fluid velocity profile:——$\beta=1$; oooooo$\beta=3.0$; ++++++ $\beta=5.0$

6 Conclusion

The development of thermal runaway in a reactive viscous fluid flowing through a channel filled with a saturated porous medium is investigated using perturbation technique together with a special type of Hermite-Padé approximants. We obtained accurately the steady-state thermal ignition criticality conditions as well as the solution branches. It is observed that a reduction in porous medium permeability will facilitate the early appearance of thermal ignition. Finally, the above analytical and computational procedures are advocated as an effective tool for investigating several other parameter dependent nonlinear boundary-value problems.

Acknowledgment

The valuable comments and suggestions of the anonymous referees are highly appreciated. Financial support from the African Mathematics Millennium Science Initiative (AMMSI) is acknowledged.

Nomenclature

a = channel width
A = rate constant
C_0 = concentration of the reactant
Da = Darcy number
E = activation energy
k = thermal conductivity
K = permeability
P = fluid pressure
Q = heat of reaction
R = universal gas constant
T_0 = wall temperature

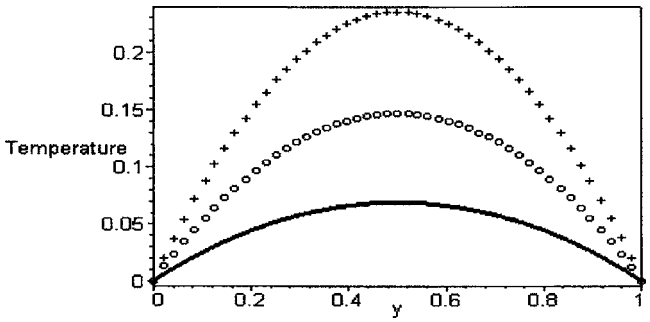

Fig. 4 Fluid temperature profile:——$\lambda=0.5$; oooooo $\lambda=1.0$; +++++++ $\lambda=1.5$

T = absolute temperature
W = fluid velocity
x = axial distance
y = normal distance

Greek symbols

μ = fluid dynamics viscosity
λ = Frank-Kamenetskii
ε = activation energy parameter
δ = viscous heating parameter
β = porous medium permeability parameter
θ = dimensionless temperature

References

[1] Brinkman, H. C., 1947, "On the Permeability of Media Consisting of Closely Packed Porous Particles," Appl. Sci. Res., Sect. A, **1**, 81–86.

[2] Makinde, O. D., and Sibanda, P., 1998, "On Suction Driven Flow and Heat Transfer in a Pipe Filled with Porous Media," Comp. Assist. Mech. Eng. Sc., **5**, pp. 389–398.

[3] Som, S. K., Mondal, S. S., and Dash, S. K., 2005, "Energy and Exergy Balance in the Process of Pulverized Coal Combustion in a Tubular Combustor," ASME J. Heat Transfer, **127**, pp. 1322–1333.

[4] Frank Kamenetskii, D. A., 1969, *Diffusion and Heat Transfer in Chemical Kinetics*, Plenum, New York.

[5] Makinde, O. D., 2004, "Exothermic Explosions in a Slab: A Case Study of Series Summation Technique," Int. Commun. Heat Mass Transfer, **31**, pp. 1227–1231.

[6] Al-Hadhrami, A. K., Elliott, L., and Ingham, D. B., 2003, "A New Model for Viscous Dissipation in Porous Media Across a Range of Permeability Values," Transp. Porous Media, **53**, pp. 117–122.

[7] Makinde, O. D., 2005, "Strong Exothermic Explosions in a Cylindrical Pipe: A Case Study of Series Summation Technique," Mech. Res. Commun., **32**, pp. 191–195.

[8] Hunter, D. L., and Baker, G. A., 1979, "Methods of Series Analysis III: Integral Approximant Methods," Phys. Rev. B, **19**, 3808–3821.

[9] Makinde, O. D., 1999, "Extending the Utility of Perturbation Series in Problems of Laminar Flow in a Porous Pipe and a Diverging Channel," J. Aust. Math. Soc. Ser. B, Appl. Math., **41**, pp. 118–128.

[10] Tourigny, Y., and Drazin, P. G., 2000, "The Asymptotic Behaviour of Algebraic Approximants," Proc. R. Soc. London, Ser. A, **456**, pp. 1117–1137.

[11] Guttamann, A. J., 1989, "Asymptotic Analysis of Power-Series Expansions," *Phase Transitions and Critical Phenomena*, C. Domb and J. K. Lebowitz, eds., Academic, New York, pp. 1–234.

[12] Vainberg, M. M., and Trenogin, V. A., 1974, *Theory of Branching of Solutions of Nonlinear Equations*, Noordoff, Leyden.

Soret and Dufour Effects in a Non-Darcy Porous Medium

M. K. Partha

P. V. S. N. Murthy[1]
e-mail: pvsnm@maths.iitkgp.ernet.in

G. P. Raja Sekhar

Department of Mathematics,
Indian Institute of Technology,
Kharagpur, 721 302,
West Bengal, India

The effect of double dispersion on free convection heat and mass transfer from a vertical surface embedded in a non-Darcy electrically conducting fluid saturated porous medium with Soret and Dufour effects is studied using similarity solution technique. The heat and mass transfer coefficients are effected greatly due to these secondary effects and also due to the complex interaction among the dispersion parameters $\mathrm{Ra}_\gamma, \mathrm{Ra}_\xi$*, and Lewis number Le and buoyancy ratio N. In both aiding and opposing buoyancies,* D_f *and* S_r *have significant influence on the Nusselt and Sherwood numbers in the presence and absence of thermal and solutal dispersion in the medium. It is also observed that the magnetic field parameter lowered heat and mass transfer coefficients. The results are presented through comparison tables and plots.*
[DOI: 10.1115/1.2188512]

Keywords: porous media, convection, heat and mass transfer, Soret and Dufour effects

Introduction

Transport phenomena in porous media have received considerable attention due to the increasing interest in geothermal processes, petroleum reservoirs, chemical catalytic reactors, etc. Diffusion of matter caused by temperature gradients (Soret effect) and diffusion of heat caused by concentration gradients (Dufour effect) become very significant when the temperature and concentration gradients are very large. Generally these effects are considered as second order phenomenon. The importance of these effects in convective transport in clear fluids has been studied in Eckert and Drake [1], Zimmerman and Muller [2], Hurle and Jakerman [3], Bergman and Srinivasan [4]. Weaver and Viskanta [5] studied free convection in an enclosure subjected to horizontal thermal and concentration gradients considering both Dufour and Soret effects. The influence of these effects on free convection flow on a vertical surface embedded in an electrically conducting Darcian fluid saturated porous medium has been studied by Anghel et al. [6] and Postelnicu [7].

Using integral method Cheng [8] has shown that the application of a transverse magnetic field normal to the flow of an electrically conducting fluid in a saturated Darcy porous medium along a vertical surface decreased the Nusselt number and Sherwood number. A similar problem for mixed convection case in non-Darcy porous medium has been discussed by Chandrasekhara and Namboodiri [9] and the effect of porosity and permeability on the flow field in the case of Newtonian fluids under the influence of magnetic field has been discussed.

For moderate and fast flows inertia effects are prevalent and thermal and solutal dispersion effects due to hydrodynamic mixing also will become significant. This has been studied by Bear [10], Kvernvold and Tyvand [11] and Murthy [12]. Considering the Soret and Dufour effect, Postelnicu [7] has investigated influence of a magnetic field on free convection heat and mass transfer from vertical surfaces in a Darcy porous medium. In this paper we attempt to analyze Soret and Dufour effects on free convection from a vertical plate embedded in an electrically conducting fluid saturated non-Darcy porous medium taking into consideration both thermal and solutal dispersion in the medium. The results are analyzed thoroughly for different cases of Le via $\mathrm{Le}<1$, $=1$, >1.

Governing Equations

Free convection heat and mass transfer from a vertical plate embedded in an electrically conducting fluid saturated non-Darcy porous medium has been considered. The wall is maintained at constant temperature and concentration T_w and C_w, respectively. The ambient medium temperature and concentration are T_∞ and C_∞, respectively. The x axis is taken along the plate and the y axis is normal to it. A uniform magnetic field H_0 is imposed along the normal direction of the plate. We assume that the electrically conducting fluid and the porous medium have constant physical properties. The fluid flow is moderate and the permeability of the medium is low so that the Forchhiemer flow model is applicable and the boundary effect is neglected. Also, the fluid and the porous medium are in local thermodynamical equilibrium, the flow is steady, laminar, and two-dimensional. With the usual boundary layer and Boussinesq approximations, the governing equations in the isotropic and homogeneous porous medium may be written as

$$\frac{\partial u}{\partial x}+\frac{\partial v}{\partial y}=0 \tag{1}$$

$$\frac{\partial u}{\partial y}\left(1+\frac{K\sigma\mu_e^2H_0^2}{\mu}\right)+\frac{c\sqrt{K}}{\nu}\frac{\partial u^2}{\partial y}=\frac{Kg\beta_T}{\nu}\frac{\partial T}{\partial y}+\frac{Kg\beta_C}{\nu}\frac{\partial C}{\partial y} \tag{2}$$

$$u\frac{\partial T}{\partial x}+v\frac{\partial T}{\partial y}=\frac{\partial}{\partial y}\left(\alpha_e\frac{\partial T}{\partial y}\right)+\frac{D}{C_s}\frac{k_T}{C_p}\frac{\partial^2 C}{\partial y^2} \tag{3}$$

$$u\frac{\partial C}{\partial x}+v\frac{\partial C}{\partial y}=\frac{\partial}{\partial y}\left(D_e\frac{\partial C}{\partial y}\right)+\frac{Dk_T}{C_sC_p}\frac{\partial^2 T}{\partial y^2} \tag{4}$$

along with the boundary conditions

$$y=0,\quad v=0,\quad T=T_w,\quad C=C_w \tag{5}$$

$$y\to\infty,\quad u\to 0,\quad T\to T_\infty,\quad C\to C_\infty \tag{6}$$

Here u and v are the velocity components along x and y directions, T is the temperature, C is concentration and c is the inertia coefficient, K is the permeability constant, β_T, β_C are the coefficients of thermal and solutal expansions, ν is the kinematic viscosity, ρ is the density, g is the acceleration due to gravity, α_e, D_e are the effective thermal and solutal diffusivities, respectively, C_p, C_s are the specific heat at constant pressure and concentration susceptibility, k_T is the thermal diffusion ratio, and σ, μ_e, H_0 are electrical conductivity, magnetic permeability, and magnetic field intensity, respectively. The thermal and solutal dispersion diffusivities can be written as $\alpha_e=\alpha+\gamma\, du$, $D_e=D+\xi\, du$ (see Murthy [12]) where γ and ξ are coefficients of thermal and solutal dispersions respectively, α and D are constant thermal and molecular diffusivities, respectively.

Making use of the following similarity transformation:

[1]Corresponding author.

Contributed by the Heat Transfer Division of ASME for publication in the JOURNAL OF HEAT TRANSFER. Manuscript received December 31, 2004; final manuscript received December 11, 2005. Review conducted by N. K. Anand.

$$\eta = \frac{y}{x}\mathrm{Ra}_x^{1/2}, \quad f(\eta) = \frac{\psi}{\alpha\,\mathrm{Ra}_x^{1/2}}, \quad \theta(\eta) = \frac{T - T_\infty}{T_w - T_\infty}, \quad \phi(\eta) = \frac{C - C_\infty}{C_w - C_\infty} \tag{7}$$

the above partial differential equations are transformed into ordinary differential equations

$$(1 + M)(f'') + 2Ff'f'' = (\theta' + N\phi') \tag{8}$$

$$\theta'' + \frac{1}{2}f\theta' + \mathrm{Ra}_\gamma(f'\theta'' + f''\theta') + D_f\phi'' = 0 \tag{9}$$

$$\phi'' + \frac{\mathrm{Le}}{2}f\phi' + \mathrm{Le}\,\mathrm{Ra}_\xi(f'\phi'' + f''\phi') + S_r\mathrm{Le}\theta'' = 0 \tag{10}$$

along with the boundary conditions

$$\eta = 0: \quad f = 0, \quad \theta = 1, \quad \phi = 1 \tag{11}$$

$$\eta \to \infty: \quad \theta \to 0, \quad \phi \to 0, \quad f' \to 0 \tag{12}$$

Here, $F = (c\sqrt{K}Kg\beta\theta_w/\nu^2)$ represents the inertia effects, $\mathrm{Ra}_d = Kg\beta_T\theta_w d/\alpha\nu$ is the Rayleigh number, $M = K\sigma\mu_e^2H_0^2/\mu$ is the magnetic parameter, $\mathrm{Ra}_\gamma = \gamma\,\mathrm{Ra}_d$ and $\mathrm{Ra}_\xi = \xi\,\mathrm{Ra}_d$ represent the thermal and solutal dispersion effects respectively, $\mathrm{Le} = \alpha/D$ is the diffusivity ratio (Lewis number), and $N = \beta_c\phi_w/\beta_T\theta_w$ is the buoyancy ratio. $D_f = Dk_T\phi_w/C_sC_p\alpha\theta_w$ is the Dufour number and $S_r = Dk_T\theta_w/C_sC_p\alpha\phi_w$ is the Soret number. The parameter $N > 0$ represents the aiding buoyancy and $N < 0$ represents the opposing buoyancy. The heat transfer and mass transfer coefficient in their nondimensional form are written as

$$\mathrm{Nu}_x/\mathrm{Ra}_x^{1/2} = -[1 + \mathrm{Ra}_\gamma f'(0)]\theta'(0) \tag{13}$$

$$\mathrm{Sh}_x/\mathrm{Ra}_x^{1/2} = -[1 + \mathrm{Ra}_\xi f'(0)]\phi'(0) \tag{14}$$

Results and Discussion

The resulting ordinary differential Eqs. (8)–(10) along with the boundary conditions (11), (12) are solved using NAG (D02HAFE) routine which uses fourth order Runge Kutta method coupled with Newton-Raphson method for solving the initial boundary value problem. The results observed here are accurate up to the fourth decimal place. Extensive calculations have been performed with different values of the parameters to obtain the flow, temperature, and concentration fields inside the boundary layer.

When $F = 0$, $\mathrm{Ra}_\gamma = 0$, $\mathrm{Ra}_\xi = 0$ the present problem reduces to the one analyzed by Postelnicu [7]. Here, the nondimensional heat and mass transfer coefficients are calculated for parameters in the ranges $0 < \mathrm{Ra}_\gamma < 10$, $0 < \mathrm{Ra}_\xi < 10$, $0 < F < 7$, $0 < \mathrm{Le} < 50$, $-1 < N < 10$, $0 < D_f < 1.4$, and $0 < S_r < 2.0$. In the absence of double dispersion effects, it is observed that the heat and mass transfer coefficients are decreased as the value of the magnetic parameter M is increased in both aiding and opposing buoyancies. This character is further supplemented by increasing the value of non-Darcy parameter F.

Interestingly if $D_f \ll S_r$, change in sign of the mass transfer coefficient is observed. Similarly, if $D_f \gg S_r$, change in the sign of the heat transfer coefficient is observed. These results are in conformity with the results reported in Postelnicu [7]. It is interesting to explore the effect of thermal and solutal dispersion on this phenomenon for aiding and opposing buoyancies separately.

Aiding Buoyancy. The effect of the diffusivity ratio Le has been analyzed for the three categories (i) $\mathrm{Le} < 1$, (ii) $\mathrm{Le} = 1$ and (iii) $\mathrm{Le} > 1$ as Le has been observed to be a crucial parameter in changing the heat and mass transfer characteristics. For $\mathrm{Le} < 1$, we find that with the increase of D_f, nondimensional heat transfer coefficient is decreasing and mass transfer coefficient is increasing in the absence of dispersion effects. This is because, either increase in concentration difference or decrease in temperature difference leads to an increase in the value of D_f, hence follows the above observation. Similarly either a decrease in concentration difference or an increase in temperature difference leads to an increase in the value of the parameter S_r. Hence increasing the parameter S_r increases the non dimensional heat transfer coefficient and decreases the mass transfer coefficient. The similar results are observed in the presence of dispersion effects in the medium. In accordance with the results presented in Postelnicu [7], in the present study also, the mass transfer coefficient becomes negative for large value of S_r when D_f is fixed. This is evident from Table 1(*a*) where the results are presented for $\mathrm{Le} = 0.1$, $N = \mathbf{1}$, $M = \mathbf{2}$. But when dispersion effects are considered, for the same value of parameters the mass transfer coefficient will remain positive. Similarly for fixed S_r, increasing the value of D_f beyond a certain value makes the heat transfer coefficient negative. By considering the thermal dispersion effects in the medium, this phenomenon is delayed. It is natural to expect both the heat and mass transfer coefficients to be higher when dispersion effects are considered than when they are neglected. Hence heat and mass transfer coefficients becomes positive even when D_f, S_r assume very high values in the presence of dispersion effects. Also, with the increase of D_f or S_r, it is observed that the magnitude of local Nusselt number and Sherwood number are lesser when the dispersion effects are zero than when these effects are not zero.

When Le is increased from 0.1 to 1 and 3 and further, the heat transfer coefficient is decreased whereas the mass transfer coefficient is increased for fixed values of other parameters. For $\mathrm{Le} = 1$, $N = \mathbf{1}$, $M = \mathbf{2}$ the heat and mass transfer coefficients are presented in Table 1(*b*). The behavior of heat and mass transfer coefficients with the increase of both D_f and S_r in the absence and presence of dispersion remain the same as indicated for $\mathrm{Le} = 0.1$ with the following exception. That is when $S_r = 1.4$, $D_f = 0.6$ the value of the heat transfer coefficient without dispersion is becoming more than that with dispersion. A similar result with the mass transfer coefficient is observed when $S_r = 0.6$, $D_f = 1.4$. This indicates that the Soret/Dufour effects becomes more influential than the double dispersion effects. Also it is worth mentioning that the heat and mass transfer coefficients are becoming negative for relatively small values of D_f and S_r, respectively, as the value of Le increases. Also it is noted that the difference in the heat transfer coefficients (when S_r is varying) and mass transfer coefficients (when D_f is varying) with and without dispersion is decreasing.

From the results presented in the Table 1(*c*) for $\mathrm{Le} > 1$, $N = \mathbf{1}$, $M = \mathbf{2}$ it is seen that the heat transfer coefficient is becoming negative for increasing values of S_r (smaller than those when $\mathrm{Le} = 0.1$ and 1.0) and fixed D_f as well as for fixed S_r and increasing values of D_f. But the mass transfer coefficient is never negative as Le becomes larger (>1). In this case, the heat transfer coefficient in the presence of dispersion is more than that in the absence of dispersion, but the mass transfer coefficient without solutal dispersion is observed to be more than that with solutal dispersion effects in the medium.

The Nusselt and Sherwood numbers are presented in Table 2 indicate the effect of the individual parameters such as the non-Darcy parameter F (for fixed Ra_γ, Ra_ξ), the thermal dispersion parameter Ra_γ (for fixed F, Ra_ξ), the solutal dispersion parameter Ra_ξ (for fixed F, Ra_γ) for $(D_f, S_r) = (0,0)$ and (0.6, 0.1) in case of the heat transfer coefficient and $(D_f, S_r) = (0,0)$ and (0.05, 1.2) in case of the mass transfer coefficient. As the inertial coefficient is increased, both heat and mass transfer decreases. An increase in Ra_γ increases both heat and mass transfer coefficients when $(D_f, S_r) = (0,0)$ and (0.6, 0.1), while an increase in Ra_ξ also favored the heat and mass transfer in the presence and absence of D_f, S_r.

The effect of double dispersion and Le on heat and mass transfer are represented in Figs. 1 and 2. Increasing Le decreases the

Table 1 Nondimensional heat and mass transfer coefficients with D_f and S_r for Le=0.1 (Table 1(*a*)), Le=1.0 (Table 1(*b*)), Le=3 (Table 1(*c*)) in the aiding buoyancy case $F=0$, $Ra_\gamma=0$, $Ra_\xi=0$; $F=5$, $Ra_\gamma=5$, $Ra_\xi=5$

		$M=2$, Le=0.1, $N=1$	$Nu_x/Ra_x^{1/2}$	$Sh_x/Ra_x^{1/2}$	$Nu_x/Ra_x^{1/2}$	$Sh_x/Ra_x^{1/2}$
			(a)			
$S_r=0.6$		$D_f=0.1$	0.4025	0.0765	0.5129	0.2069
		0.9	0.3870	0.0791	0.4932	0.2104
	$D_f\downarrow$	6	0.2589	0.0963	0.3557	0.2308
		13	−0.1565	0.1331	0.1254	0.2574
		14	−0.3051	0.1437	0.0873	0.2612
		16	−1.1881	0.2005	0.0063	0.2690
$D_f=0.6$		$S_r=0.1$	0.3853	0.0937	0.4968	0.2230
		0.4	0.3898	0.0844	0.4992	0.2147
		0.9	0.3976	0.0685	0.5028	0.2006
	$S_r\downarrow$	2.9	0.3438	0.0856	0.5181	0.1421
		6.0	0.5029	−0.1477	0.5434	0.0435
		$M=2$, Le=1, $N=1$	$Nu_x/Ra_x^{1/2}$	$Sh_x/Ra_x^{1/2}$	$Nu_x/Ra_x^{1/2}$	$Sh_x/Ra_x^{1/2}$
			(b)			
$S_r=0.6$		$D_f=0.1$	0.3655	0.2425	0.4684	0.4233
		0.3	0.3379	0.2579	0.4564	0.4278
		0.6	0.2864	0.2864	0.4346	0.4346
	$D_f\downarrow$	0.9	0.2135	0.3266	0.4122	0.4414
		1.4	−0.0716	0.4868	0.3734	0.4528
		1.6	−0.6704	0.8364	0.3573	0.4574
$D_f=0.6$		$S_r=0.1$	0.2426	0.3655	0.4233	0.4564
		0.3	0.2579	0.3389	0.4278	0.4334
		0.6	0.2865	0.2653	0.4346	0.4122
	$S_r\downarrow$	0.9	0.3266	0.2135	0.4414	0.3891
		1.4	0.4868	−0.0716	0.4528	0.3734
		1.6	0.5822	−0.237	0.4552	0.3656
		$M=2$, Le=3, $N=1$	$Nu_x/Ra_x^{1/2}$	$Sh_x/Ra_x^{1/2}$	$Nu_x/Ra_x^{1/2}$	$Sh_x/Ra_x^{1/2}$
			(c)			
$S_r=0.6$		$D_f=0.1$	0.3316	0.4284	0.4592	0.4779
		0.3	0.2455	0.5441	0.4424	0.4838
	$D_f\downarrow$	0.4	0.1616	0.6676	0.4349	0.4808
		0.5	−0.0632	1.0304	0.4253	0.4898
$D_f=0.6$		$S_r=0.1$	0.4140	0.7185	0.4031	0.5339
		0.3	0.0011	0.7885	0.4086	0.5177
	$S_r\downarrow$	0.4	−0.0553	0.8845	0.4113	0.5095
		0.5	−0.2562	1.2234	0.4139	0.5012

heat transfer. But when dispersion effects are considered to be high, the magnitude of heat transfer coefficient attained is more than when they are not considered. It is shown in Fig. 1. The parameter Le favors the mass transfer rate. At high values of dispersion the magnitude of mass transfer coefficient is lesser than when it is not considered and is seen in Fig. 2.

Increasing the value of the parameter Ra_γ increases the heat transfer rate and the magnetic field, inertia effect decreases the heat transfer rate. But, though the effect of magnetic field is to decrease the heat transfer in both Darcy and non-Darcy porous medium, its effect on Darcy porous medium is larger than in non-Darcy and can be seen in Fig. 3. The similar effect on mass transfer by the magnetic field is exhibited in Fig. 4 with the increase of Ra_ξ. That is, the effect of magnetic field in decreasing mass transfer in Darcy porous medium is more pronounced than in non-Darcy porous medium.

Opposing Buoyancy. The effect of Le is observed to be more significant in the opposing buoyancy and hence its effect on heat and mass transfer coefficients is studied in three categories Le <1, Le$=1$, and Le>1. Even though the effect of increasing D_f on heat and mass transfer coefficients remains the same as in the case of aiding buoyancy, the effect of increasing S_r on heat and mass transfer coefficients in the opposing buoyancy differs from that in the aiding buoyancy only when Le$\leqslant 1$. When Le<1, increase in

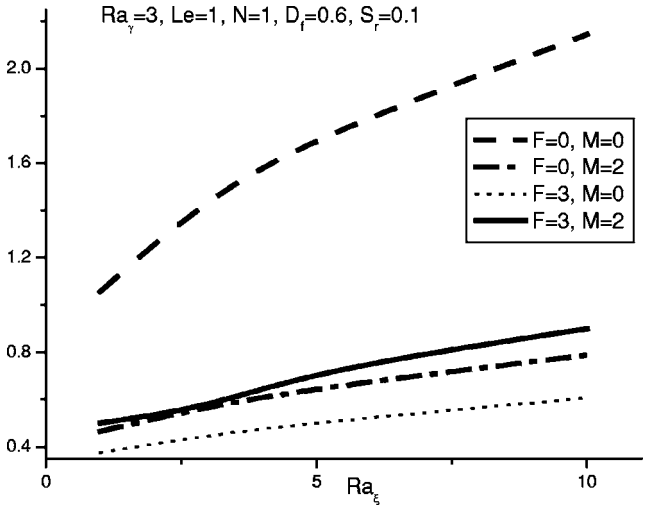

Fig. 4 Variation of nondimensional mass transfer coefficient to Darcy and non-Darcy porous medium with the increase of Ra_ξ in the presence of magnetic field

Table 2 Nondimensional heat and mass transfer coefficients with the inertia parameter F, and dispersion parameters Ra_γ and Ra_ξ when $M=2$, Le=1, $N=1$; $Ra_\gamma=1$, $Ra_\xi=1$; $F=1$, $Ra_\xi=1$; $F=1$, $Ra_\gamma=1$

		$Ra_\gamma=1$, $Ra_\xi=1$			$F=1$, $Ra_\xi=1$			$F=1$, $Ra_\gamma=1$	
	F	$D_f=0$ $S_r=0$	$D_f=0.6$, $S_r=0.1$	Ra_γ	$D_f=0$ $S_r=0$	$D_f=0.6$, $S_r=0.1$	Ra_ξ	$D_f=0$ $S_r=0$	$D_f=0.6$, $S_r=0.1$
$Nu_x/Ra_x^{1/2}$	0.0	0.4413	0.3598	0	0.3477	0.2784	0	0.3918	0.2676
	1	0.4041	0.3241	1	0.4041	0.3241	1	0.4041	0.3241
	2	0.3811	0.3015	3	0.4858	0.3922	3	0.4189	0.3745
	5	0.3371	0.2623	5	0.5468	0.4457	5	0.4241	0.3971
	7	0.3191	0.2461	10	0.6588	0.5456	10	0.4394	0.4246
	F	$D_f=0$ $S_r=0$	$D_f=0.05$, $S_r=1.2$	Ra_γ	$D_f=0$ $S_r=0$	$D_f=0.05$, $S_r=1.2$	Ra_ξ	$D_f=0$ $S_r=0$	$D_f=0.05$, $S_r=1.2$
$Sh_x/Ra_x^{1/2}$	0.0	0.4413	0.2689	0	0.3918	0.1314	0	0.3477	0.1983
	1	0.4041	0.2349	1	0.4041	0.2351	1	0.4041	0.2349
	2	0.3812	0.2142	3	0.4189	0.3244	3	0.4858	0.2919
	5	0.3372	0.1792	5	0.4277	0.3626	5	0.5345	0.3371
	7	0.3191	0.1651	10	0.4397	0.4074	10	0.6588	0.4254

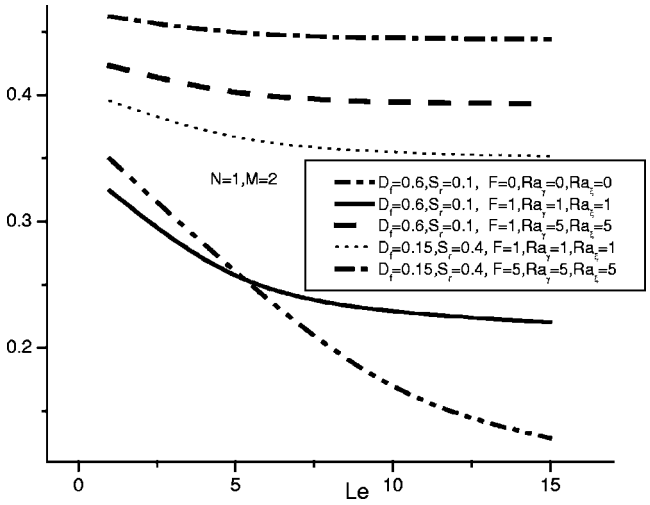

Fig. 1 Dispersion effects on nondimensional heat transfer coefficient with the increase of Le for fixed values of D_f, S_r in Darcy and non-Darcy porous medium

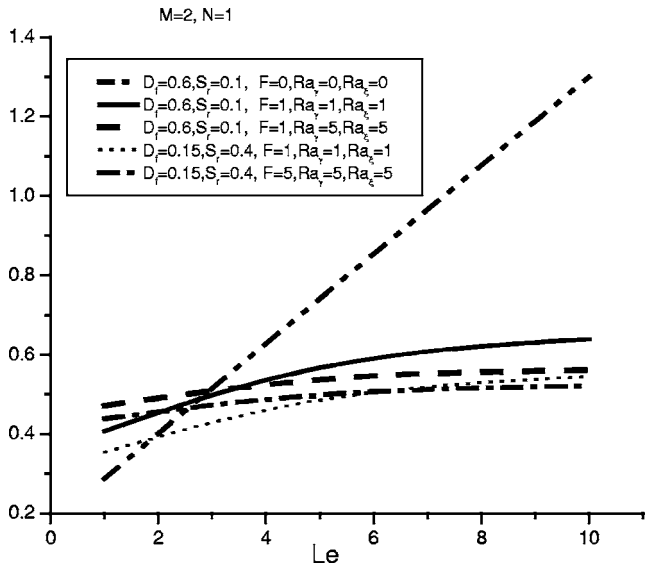

Fig. 2 Dispersion effects on nondimensional mass transfer coefficient with the increase of Le for fixed values of D_f, S_r in Darcy and non-Darcy porous medium

S_r in the absence of dispersion effects increases the heat transfer coefficient and decreases the mass transfer coefficient. Whereas in the presence of dispersion effects, both non dimensional heat transfer coefficient and mass transfer coefficient decreases. When Le=1, the effect of increasing D_f (for fixed value of S_r and other parameters) and S_r (for fixed value of D_f and other parameters) on heat and mass transfer coefficient remains the same as in the case of Le<1. Similarly the effect of increasing S_r and D_f for fixed values of Le (>1) on heat and mass transfer coefficients remains the same as in the case of aiding buoyancy. These results are tabulated in the Tables 3(*a*)–3(*c*) for Le<1, Le=1 and Le>1, respectively.

Like in the aiding buoyancy when Le≤1, the heat transfer coefficient becomes negative with the increase of D_f (for fixed values of S_r and other parameters) and the mass transfer coefficient becomes negative with the increase of S_r (for fixed values of D_f and other parameters). But heat transfer coefficient becomes

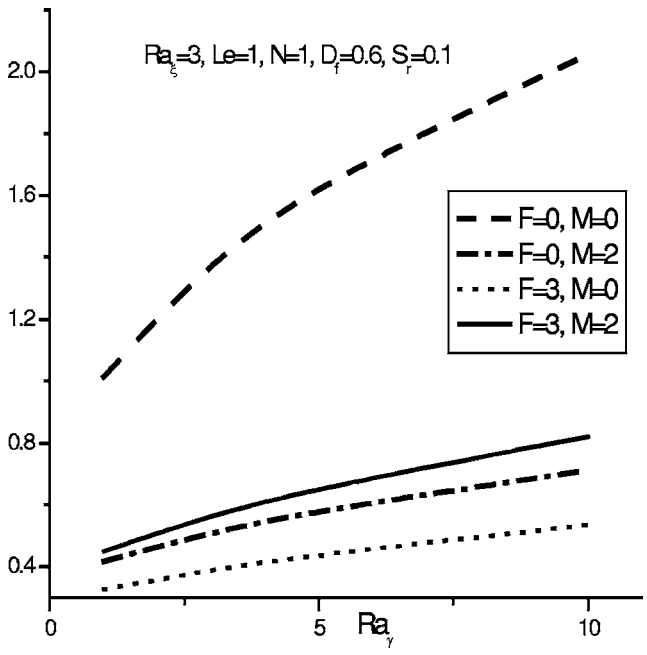

Fig. 3 Variation of nondimensional heat transfer coefficient to Darcy and non-Darcy porous medium with the increase of Ra_γ in the presence of magnetic field

Table 3 Nondimensional heat and mass transfer coefficients with D_f and S_r for Le=0.7 (Table 3(*a*)), Le=1.0 (Table 3(*b*)), Le=3 (Table 3(*c*)) in the opposing buoyancy case $F=0$, $Ra_\gamma=0$, $Ra_\xi=0$; $F=5$, $Ra_\gamma=5$, $Ra_\xi=5$

		$M=2$, Le=0.7, $N=-0.5$	$F=0$, $Ra_\gamma=0$, $Ra_\xi=0$		$F=5$, $Ra_\gamma=5$, $Ra_\xi=5$	
			$Nu_x/Ra_x^{1/2}$	$Sh_x/Ra_x^{1/2}$	$Nu_x/Ra_x^{1/2}$	$Sh_x/Ra_x^{1/2}$
			(a)			
$S_r=0.6$		$D_f=0.4$	0.1504	0.0877	0.1787	0.1361
		0.9	0.1345	0.1192	0.1691	0.1602
	$D_f\downarrow$	1.9	−0.0040	0.2114	0.1249	0.2007
		2.0	−0.0451	0.2319	0.1198	0.2054
$D_f=0.6$		$S_r=0.4$	0.1448	0.1219	0.1776	0.1623
		0.9	0.1495	0.0643	0.1728	0.1216
	$S_r\downarrow$	1.0	0.1507	0.0502	0.1715	0.1126
		1.3	0.1555	−0.0755	0.1663	0.0831
		1.4	0.1574	−0.0219	0.1613	0.0719
		$M=2$, Le=1, $N=-0.5$	$Nu_x/Ra_x^{1/2}$	$Sh_x/Ra_x^{1/2}$	$Nu_x/Ra_x^{1/2}$	$Sh_x/Ra_x^{1/2}$
			(b)			
$S_r=0.6$		$D_f=0.1$	0.1607	0.0911	0.1891	0.1498
		0.3	0.1572	0.1175	0.1865	0.1628
	$D_f\downarrow$	0.6	0.1432	0.1432	0.1793	0.1793
		0.9	0.1161	0.1737	0.1681	0.1946
		1.4	−0.0211	0.2120	0.1401	0.2205
		1.6	−0.3477	0.4829	0.1248	0.2318
$D_f=0.6$		$S_r=0.1$	0.1365	0.1992	0.1811	0.2207
		0.3	0.1385	0.1791	0.1804	0.2046
		0.6	0.1432	0.1432	0.1797	0.1797
	$S_r\downarrow$	0.9	0.1515	0.0960	0.1773	0.1519
		1.28	0.177863	−0.0033	0.1735	0.1138
		1.4	0.1985	−0.0606	0.1719	0.1001
		$M=2$, Le=3, $N=-0.5$	$Nu_x/Ra_x^{1/2}$	$Sh_x/Ra_x^{1/2}$	$Nu_x/Ra_x^{1/2}$	$Sh_x/Ra_x^{1/2}$
			(c)			
$S_r=0.6$		$D_f=0.1$	0.1762	0.2252	0.2043	0.2228
		0.3	0.1438	0.2998	0.1958	0.2391
	$D_f\downarrow$	0.4	0.1056	0.3736	0.1904	0.2475
		0.5	−0.0095	0.5839	0.1842	0.2562
$D_f=0.6$		$S_r=0.1$	0.0635	0.4374	0.1753	0.3181
		0.3	0.0363	0.4716	0.1760	0.2980
	$S_r\downarrow$	0.4	0.0028	0.5232	0.1763	0.2875
		0.5	−0.1107	0.7139	0.1766	0.2766

negative with the increase of S_r when Le>1 which is similar to the case of Le>1 in aiding buoyancy. Even though the effect of D_f in decreasing the heat transfer coefficient in the opposing buoyancy is almost the same as in the case of aiding buoyancy, it appears that the Soret effect is more influential in decreasing the mass transfer in the opposing buoyancy in comparison with aiding buoyancy. In other words, for Le=0.7, $N=1$, when $S_r=1.6$, the mass transfer coefficient is becoming negative whereas for the same Le=0.7, $N=-0.5$, when $S_r=1.3$ (lesser than the aiding buoyancy) the mass transfer coefficient is becoming negative. The same is observed for Le=1 and Le=3. These results are shown in Table 4. It is worth noting that both heat and mass transfer coefficients are becoming negative for relatively small values of D_f and S_r as the value of Le increases.

Table 4 Particular values of D_f, S_r for which the nondimensional heat and mass transfer coefficients are becoming negative for the same value of Le in aiding and opposing buoyancy

	D_f	$Nu_x/Ra_x^{1/2}$	S_r	$Sh_x/Ra_x^{1/2}$
$N=1$, Le=0.7	1.85	−0.0029	1.6	−0.0038
$N=-0.5$, Le=0.7	1.9	−0.0040	1.3	−0.0075
$N=1$, Le=1	1.34	−0.0088	1.35	−0.0181
$N=-0.5$, Le=1	1.37	−0.0037	1.28	−0.0033
$N=1$, Le=3	0.49	−0.0209	0.4	−0.0553
$N=-0.5$, Le=3	0.5	−0.0095	0.5	−0.1107

Even though the effect of increasing F, Ra_γ on heat and mass transfer coefficients remains the same as in the case of aiding buoyancy, this becomes different with increasing Ra_ξ. An increase in Ra_ξ increases the heat transfer coefficient when $(D_f, S_r) = (0.6, 0.1)$ and decreases the heat transfer coefficient when $(D_f, S_r) = (0.0, 0.0)$. But the mass transfer coefficient is decreased both in the presence and absence of D_f, S_r with the increase of Ra_ξ, refer to Table 5.

To conclude, very significant changes in heat and mass transfer coefficients are observed with Soret and Dufour effects in the presence of thermal and solutal dispersions and these depend on the complex interaction between all the parameters.

Conclusions

Free convection heat and mass transfer from a vertical plate embedded in an electrically conducting fluid saturated non-Darcy porous medium has been considered. The wall is maintained at constant temperature and concentration T_w and C_w, respectively. The ambient medium temperature and concentration are T_∞ and C_∞, respectively. The x axis is taken along the plate and the y axis is normal to it. We assume that the electrically conducting fluid

Table 5 Nondimensional heat and mass transfer coefficients with the inertial parameter F, and dispersion parameters Ra_γ and Ra_ξ when $M=2$, Le=1, $N=-0.9$; $Ra_\gamma=1$, $Ra_\xi=1$; F=1, $Ra_\xi=1$; F=1, $Ra_\gamma=1$

		$Ra_\gamma=1$, $Ra_\xi=1$			$F=1$, $Ra_\xi=1$			$F=1$, $Ra_\gamma=1$	
	F	$D_f=0$ $S_r=0$	$D_f=0.6$, $S_r=0.1$	Ra_γ	$D_f=0$ $S_r=0$	$D_f=0.6$ $S_r=0.1$	Ra_ξ	$D_f=0$ $S_r=0$	$D_f=0.6$, $S_r=0.1$
$Nu_x/Ra_x^{1/2}$	0.0	0.0820	0.0868	0	0.0781	0.0825	0	0.0818	0.0854
	1	0.0817	0.0861	1	0.0817	0.0861	1	0.0817	0.0861
	2	0.0813	0.0855	3	0.0893	0.0935	3	0.0766	0.0881
	5	0.0804	0.0837	5	0.0974	0.1013	5	0.0721	0.0903
	7	0.0798	0.0827	10	0.1187	0.1214	10	0.0634	0.0974
	F	$D_f=0$ $S_r=0$	$D_f=0.06$, $S_r=0.1$	Ra_γ	$D_f=0$ $S_r=0$	$D_f=0.06$ $S_r=0.1$	Ra_ξ	$D_f=0$ $S_r=0$	$D_f=0.06$, $S_r=0.1$
$Sh_x/Ra_x^{1/2}$	0.0	0.0820	0.1184	0	0.0762	0.1199	0	0.0837	0.1175
	1	0.0817	0.1174	1	0.0817	0.1174	1	0.0791	0.1174
	2	0.0813	0.1166	3	0.0933	0.1283	3	0.0776	0.1162
	5	0.0804	0.1136	5	0.1053	0.1390	5	0.0737	0.1142
	7	0.0798	0.1128	10	0.1358	0.1651	10	0.0656	0.1079

and the porous medium have constant physical properties. The fluid flow is moderate and the permeability of the medium is low so that the Forchhiemer flow model is applicable. In this paper we attempt to analyze Soret and Dufour effects on free convection in non-Darcy porous medium taking into consideration both thermal and solutal dispersion in the medium. The results are analyzed thoroughly for different cases of Le via Le<1, $=1$, >1.

Nomenclature

c = Forchheimer coefficient
C = concentration
C_p = specific heat at constant pressure
C_s = concentration susceptibility
d = pore diameter
D_e = effective solutal diffusivity
D_f = parameter representing Dufour effect
F = parameter representing inertia effects
g = acceleration due to gravity
H_0 = magnetic field intensity
K = permeability
k = thermal conductivity the fluid
k_T = thermal diffusion ratio
Le = Lewis number
M = parameter representing magnetic effects
N = buoyancy ratio
Ra_γ, Ra_ξ = represent thermal and solutal dispersion effects
Ra_d = pore diameter dependent Rayleigh number
S_r = parameter representing Soret effect
T = temperature
u, v, = velocity in x, y directions

Greek Symbols

α = thermal diffusivity
α_e = effective thermal diffusivity
β_T = coefficient of thermal expansion
β_C = coefficient of solutal expansion
σ = electrical conductivity
μ_e = magnetic permeability
θ = nondimensional temperature
θ_w = T_w-T_∞
ϕ_w = C_w-C_∞
μ = viscosity
ν = kinematic viscosity
ρ = density of the fluid
ψ = nondimensional stream function
η = similarity variable

Subscripts

w, ∞ = conditions on the wall and in the ambient medium

References

[1] Eckeret, E. R. G., and Drake, R. M., 1972, *Analysis of Heat and Mass Transfer*, McGraw Hill, New York.
[2] Zimmerman, G., and Muller, U., 1992, "Benard Convection in a Two Component System with Soret Effect," Int. J. Heat Mass Transfer, **35**, pp. 2245–2256.
[3] Hurle, D. T., and Jakerman, E., 1989, "Soret Driven Thermo Solutal Convection," J. Fluid Mech., **447**, pp. 667–687.
[4] Bergman, T. L., and Srinivasan, R., 1989, "Numerical Solution of Soret Induced Double Diffusion in an Initially Uniform Concentration Binary Liquid," Int. J. Heat Mass Transfer, **32**, pp. 679–687.
[5] Weaver, J. A., and Viskanta, R., 1991, "Natural Convection due to Horizontal Temperature and Concentration Gradients-2, Species Inter-diffusion, Soret and Dufour Effects," Int. J. Heat Mass Transfer, **34**, pp. 3121–3133.
[6] Anghel, M., Takhar, H. S., and Pop, I., 2000, "Dufour and Sorret Effects on Free Convection Boundary-Layer Flow over a Vertical Surface Embedded in a Porous Medium," *Studia Universitatics Babes-Bolyai, Mathematica*, XLV, pp. 11–23.
[7] Postelnicu, A., 2004, "Influence of Magnetic Field on Heat and Mass Transfer from Vertical Surfaces in Porous Media Considering Soret and Dufour Effects," Int. J. Heat Mass Transfer, **47**, pp. 1467–1472.
[8] Cheng, C. Y., 1993, "Effect of a Magnetic Field on Heat and Mass Transfer by Natural Convection from Vertical Surfaces in Porous Media An Integral Approach," Int. Commun. Heat Mass Transfer, **26**, pp. 935–943.
[9] Chandrasekhara, B. C., and Namboodiri, P. M. S., 1985, "Influence of Variable Permeability on Combined Free and Forced Convection about Inclined Surfaces in Porous Media," Int. J. Heat Mass Transfer, **28**, pp. 199–206.
[10] Bear, J., 1972, *Dynamics of Fluids in Porous Media*, Elsevier, New York.
[11] Kvernvold, O., and Tyvand, P., 1980, "Dispersion Effect on Thermal Convection in Porous Media," J. Fluid Mech., **99**, pp. 673–686.
[12] Murthy, P. V. S. N., 2000, "Effect of Double Dispersion on Mixed Convection Heat and Mass Transfer in non-Darcy Porous Media," J. Heat Transfer, **122**, pp. 476–484.

Thermodynamics of Void Fraction in Saturated Flow Boiling

Francisco J. Collado
e-mail: fjk@unizar.es

Carlos Monné

Departamento Ingeniería Mecánica,
CPS-B Universidad Zaragoza,
Zaragoza, 50018, Spain

Antonio Pascau

Daniel Fuster

Departamento Ciencia Material and Fluidos,
CPS-B Universidad Zaragoza,
Zaragoza, 50018, Spain

Andrés Medrano
Departamento Ingeniería Mecánica,
CPS-B Universidad Zaragoza,
Zaragoza, 50018, Spain

Recently, Collado (Proc, IMECE 2001, Symposium on Fluid Physics and Heat Transfer for Macro- and Micro-Scale Gas-Liquid and Phase Change Flows) suggested calculating void fraction, an essential element in thermal-hydraulics, working with the "thermodynamic" quality instead of the usual "flow" quality. The "thermodynamic" quality is a state variable, which has a direct relation with the actual vapor volumetric fraction, or void fraction, through phase densities. This approach provides a procedure for predicting void fraction, if values of "thermodynamic" quality are available. However, the standard heat balance is usually stated as a function of the "flow" quality. Therefore, we should search for a new heat balance between the mixture enthalpy, based on "thermodynamic" quality, and the absorbed heat. This paper presents the results of such analysis based on the accurate measurements of the outlet void fraction measured during the Cambridge project by Knights (1960, "A Study of Two-Phase Pressure Drop and Density Determination in a High-Pressure Steam-Water Circuit," Ph.D. thesis, Cambridge University Engineering Lab, Cambridge, UK) in the 1960s for saturated flow boiling. In the 286 tests analyzed, the pressure and mass fluxes range from 1.72 MPa to 14.48 MPa and from 561.4 to 1833.33 $\mathrm{kg\,m^{-2}\,s^{-1}}$*, respectively. As the main result, we find that the slip ratio would close this new thermodynamic heat balance. This has allowed the accurate calculation of void fraction from this balance, provided we can predict the slip ratio. Finally, the strong connection of this new thermodynamic heat balance with the standard one through the slip ratio is highlighted.*
[DOI: 10.1115/1.2190696]

Keywords: saturated flow boiling, void fraction, thermodynamic quality, slip ratio

1 Introduction

A large number of correlations [1,2] have been proposed for the evaluation of the cross-sectional average volumetric fraction or void fraction of vapor bubbles, α, which is of considerable interest to nuclear and fossil power industries because void fraction significantly affects neutron absorption, heat transfer, and pressure drop [1–6]. Many of them are expressed in terms of the phase velocity ratio or slip ratio, S, which is defined as the cross-sectional area mean vapor velocity, u_G (m/s), divided by the cross-sectional area mean liquid velocity, u_L (m/s). Collier [1], reviewed the better-known correlations for α, and concluded that for the most accurate ones the standard deviation of error on the mean density is about 30%. However, depending on the data bank used for the comparison, these best void fraction correlations, which also include the calculation of the slip ratio, may show a standard deviation for S ranging from 30 to 80%.

In this work, which is focused on saturated flow boiling, we suggest using the "thermodynamic" quality to calculate the void fraction, instead of the "flow" quality used in classic treatments.

The standard energy balance [1–6] for saturated flow boiling is, assuming negligible kinetic and gravity terms,

$$q = \underbrace{x_o h_G + (1 - x_o) h_L}_{\text{'flow' mixture enthalpy}} - h_L \Rightarrow x_o = q / (h_G - h_L) = q / \Delta h_{LG} \tag{1}$$

where q denotes the total absorbed heat along the duct per unit mass inlet liquid (in short, heat per unit mass) in (kJ/kg), subscript G and L denotes saturated vapor and saturated liquid, respectively, h is enthalpy (kJ/kg), and x_o is the outlet standard flow quality. The further assumptions that only liquid enters into the duct exactly at saturation conditions [4–6], and that the pressure drop along the duct is negligible so that h_L and h_G are constant saturation values, are included in Eq. (1).

The classic definition of x as a mass flow rate ratio clearly shows that it includes the slip ratio, S,

$$\begin{aligned} x &= W_G/(W_G + W_L) \\ &= u_G \rho_G A_c \alpha / [u_G \rho_G A_c \alpha + u_L \rho_L A_c (1 - \alpha)] = \rho_G \alpha S / [\rho_G \alpha S + \rho_L (1 - \alpha)] \end{aligned} \tag{2}$$

where W denotes mass flow rate (kg/s), ρ is mass density ($\mathrm{kg/m^3}$), A_c is the cross-sectional area of the duct ($\mathrm{m^2}$), and the standard definitions of mass flow rate and the slip ratio, $S = u_G/u_L$, are used. For the sake of convenience, void fraction can be derived from Eq. (2),

$$\alpha = 1/\{1 + S[(1 - x)/x](\rho_G/\rho_L)\} = x\beta/[x\beta + S(1 - x)] \tag{3}$$

where we have followed Ref. [5] to denote the liquid-vapor mass density ratio as β. Furthermore, the slip ratio can be expressed as a function of the void fraction and the flow quality using the standard mass flow rates (see p. 7 in [2]),

$$\begin{aligned} S = u_G/u_L &= [W_G \rho_L (1 - \alpha) A_c]/(W_L \rho_G \alpha A_c) \\ &= [x\rho_L (1 - \alpha)]/[(1 - x)\rho_G \alpha] \\ &= \beta [x(1 - \alpha)]/[(1 - x)\alpha] \end{aligned} \tag{4}$$

The key point of this work is to use the well-known thermodynamic quality, x_{th}, classically defined as [3],

$$x_{\mathrm{th}} = \rho_G \alpha / \rho_m \tag{5}$$

where ρ_m denotes the standard mixture density of the vapor-liquid mixture ($\mathrm{kg/m^3}$).

There is a direct connection between void fraction and thermodynamic quality, x_{th}, through phase densities, which is derived from the strict definitions of α and the mixture density. So following Refs. [2–4], the void fraction is strictly defined as, α = Area occupied by steam/Total cross-sectional area of flow $= dA_G/dA$, which is directly measured by gamma or x-ray attenuation.

Contributed by the Heat Transfer Division of ASME for publication in the JOURNAL OF HEAT TRANSFER. Manuscript received July 22, 2005; final manuscript received October 18, 2005. Review conducted by: Satish G. Kandlikar. Paper presented at the NURETH11, 2005.

Furthermore, for an element of area dA, the mixture density is given by [2–4]

$$\rho_m = (\rho_L dA_L + \rho_G dA_G)/dA = (1-\alpha)\rho_L + \alpha\rho_G \quad (6)$$

Now the inverse of the mixture density is the mixture specific volume, v_m. Then, if we write v_m as a combination of the saturated liquid and vapor specific volumes weighted by the actual vapor mass fraction, x',

$$v_m = x' v_G + (1-x')v_L = x'/\rho_G + (1-x')/\rho_L$$
$$= 1/\rho_m \Rightarrow x' = x_{\text{th}} = \alpha\rho_G/\rho_m \quad (7)$$

Therefore, it is evident that the actual vapor mass fraction, which corresponds to the actual (directly measured) vapor void fraction, is the thermodynamic quality, x_{th}, and not the flow quality.

Finally, the derivation of α from Eq. (5), also including Eq. (6), is immediate,

$$\alpha = x_{\text{th}}\beta/[x_{\text{th}}\beta + (1-x_{\text{th}})] \quad (8)$$

The obvious advantage of Eq. (8) on Eq. (3) is that S does not appear. However, as we will show later, really this is not true because we need to predict S for the closure of the new thermodynamic relation found.

Now the question is how heat transfer can be related to the mixture enthalpy increment, Δh_m, which here will be based on thermodynamic quality, x_{th},

$$h_m = x_{\text{th}} h_G + (1-x_{\text{th}})h_L \Rightarrow \Delta h_m = h_{m,o} - h_L = x_{\text{th},o}\Delta h_{LG} \quad (9)$$

Notice the difference of this thermodynamic mixture enthalpy from the flow mixture enthalpy in Eq. (1).

In this work, we will compare this thermodynamic mixture enthalpy increment of the fluid passing through the heated duct versus the heat input per unit mass using the careful void fraction data of Knights [4] taken during the Cambridge Project for vertical and horizontal saturated flow boiling. For the data set analyzed, the main result is that the slip ratio should be explicitly used for the closure of this new energy balance. Furthermore, based on the same data set, a new and improved slip ratio correlation is presented. The void fraction values calculated through the new heat relation and the new slip ratio correlation compare quite well with the measured ones. Finally, the equivalence of the standard heat balance with the new thermal relation through the slip ratio is highlighted.

2 Flow Boiling Measurements in the Cambridge Project

In his dissertation [4], Knights presented experimental measurements of the void fraction made at the outlet of a water boiling flow in 1.5 in. (0.0381 m) bore 24 ft (7.32 m) long pipe in vertical (upwards flow) and horizontal position at several inlet pressures of industrial interest. The operating pressures for the main test series were 1.72 MPa (250 psia), 4.14 MPa (600 psia), 8.62 MPa (1250 psia), and 14.48 MPa (2100 psia). The closed loop rig was operated at pressures up to 22.1 MPa (3206 psia), and electrical heating was employed to ensure ease of control and uniformity of heating of the test section. The outlet flow quality, Eq. (1), was less than 0.2 in the 286 tests analyzed here. Circulation was assisted by a centrifugal pump, and the mass flux range from 561.4 to 1833.3 kg m^{-2} s^{-1}. The inlet pressure was accurate to better than ±1% at all operating pressures. The overall accuracy of the flow rate measurements, through a sharp edged orifice plate, could be expected to lie within ±4%. The electrical power supplied to the pipe was measured with a Wattmeter, and the heat losses were normally less than 10% of the total power input, and these were measured to ±5%. The outlet void fraction data were taken through chordal scanning by a collimated gamma-ray beam, with a scintillation counter as the detector. Thus, the dispersion pattern was investigated. For horizontal flow boiling, the factor 1.014 converted the center line scanning void fraction to the mean void fraction on the section within 1.5% of the difference. For vertical (upwards) flow boiling, it was also found that the factor 0.8 could convert quite well with the center line chordal scanning of the void fraction to the mean void fraction. The maximum deviation from the factor of 0.8 was 11.5% and the mean deviation was 4.3%.

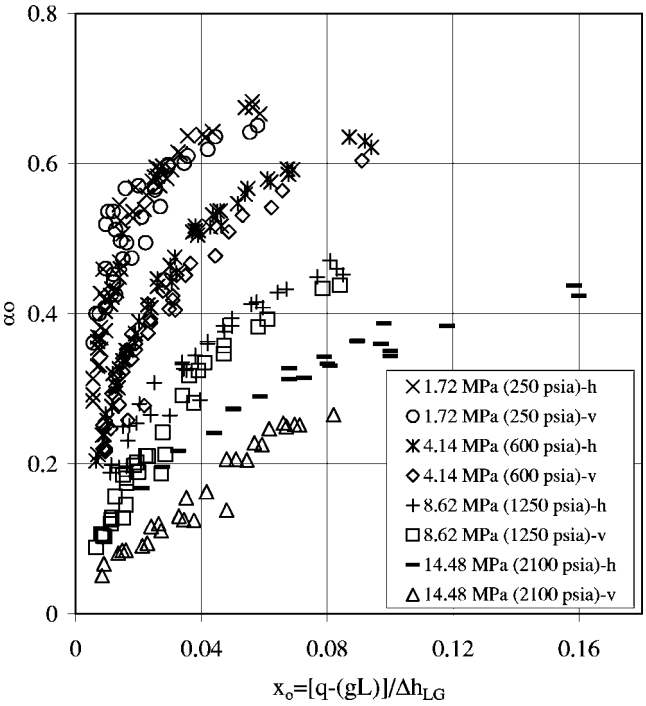

Fig. 1 Outlet void fraction versus outlet "flow" quality

Figure 1 shows the measured outlet mean void fraction versus the outlet flow quality, the last one calculated from Eq. (1), using the measured effective power input, the inlet mass flow rate, and the inlet pressure.

3 New Thermodynamic Heat Balance

Figure 2 compares the thermodynamic mixture enthalpy increment in (kJ/kg), Eq. (9), versus the measured absorbed heat per unit mass inlet water, also in (kJ/kg). The outlet thermodynamic quality, included in Eq. (9), has been calculated using the measured outlet void fraction and inlet pressure, see Eqs. (5) and (6). The disagreement between enthalpy increment and heat is rather strong and cannot be justified by measurement uncertainties. In vertical tests, the specific potential energy, gL, has also been included, L being the height of the pipe, 24 ft, i.e., $gL = 0.071$ kJ/kg. Now the question is which parameter could balance this thermodynamic relation.

We have found (see Fig. 3) that the slip ratio, S, from Eq. (4), which includes x_o and α_o data, would balance quite well with this thermodynamic comparison, suggesting a new heat balance for saturated flow boiling.

From the basic equations stated before, it is easy to expand the $q/\Delta h_m$ ratio to check whether the relation suggested by Fig. 3 is a trivial one or not,

$$q/[\Delta h_m + (gL)] = x/x_{\text{th}} = x[\rho_m/(\rho_G\alpha)] = x + \beta x(1-\alpha)/\alpha \quad (10)$$

Equation (10) should be compared to the classic expression of S, Eq. (4). Only at very low values of flow quality, x, Eq. (10) could reduce to Eq. (4). Furthermore, Fig. 3 has been also verified in [6] using Thom data [5] for 1 in. (0.0254 m) bore horizontal

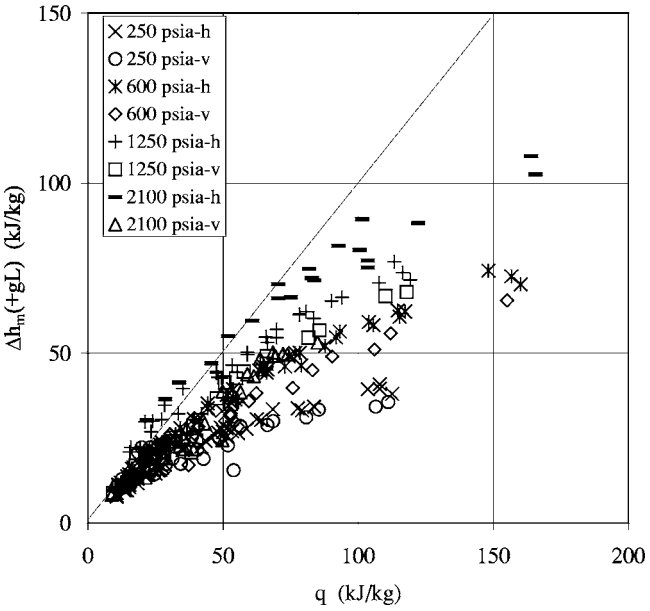

Fig. 2 Thermodynamic heat balance discrepancy

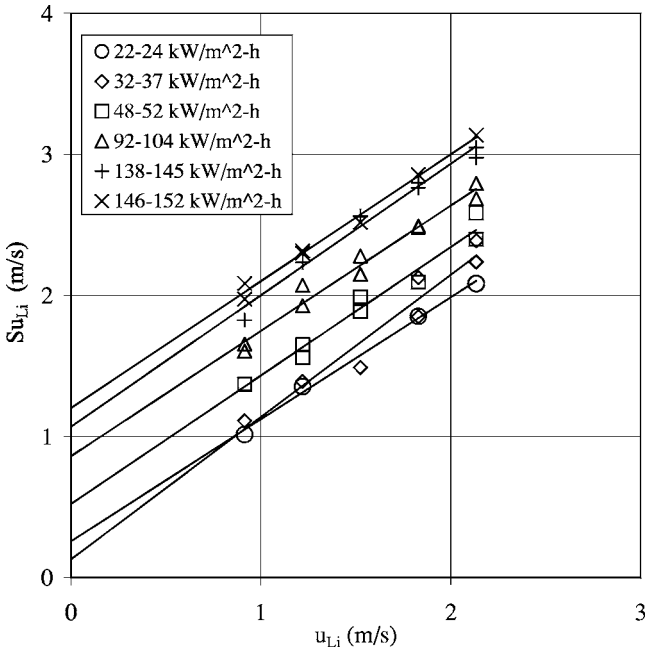

Fig. 4 *S* correlation for horizontal flow at 600 psia (4.14 MPa)

pipe, in which more than half of the flow qualities were higher than 0.1 and the higher one was near 0.8. Therefore, Fig. 3 would suggest that,

$$q/[\Delta h_m + (gL)] \approx S \tag{11}$$

A possible justification of Eq. (11), already suggested elsewhere [6], could be that the time scales of the phases are different because we are treating two different velocities (that of the liquid and the vapor) in the same length (the same control volume), and this physical fact should be included in the heat balance in some manner. So taking into account that the heat input per unit mass inlet water is $q[\mathrm{kJ/kg}]=Q[\mathrm{kW}]/W_{L,i}[\mathrm{kg/s}]$, and assuming that heat enters into the control volume exclusively through vapor bubbles (vapor time scale) that condense in the saturated liquid, Eq. (11) would mean that the slip ratio S could act as a time scale factor conversion between the liquid ($W_{L,i}$) and vapor (Q, i.e., bubbles) phases.

Finally, in comparing Eqs. (1), (10), and (11), we could say that, for saturated flow, the standard heat balance based on flow quality and the one proposed here and based on thermodynamic quality, are indeed equivalent, the difference between them merely being a time scale factor conversion i.e., the slip ratio S.

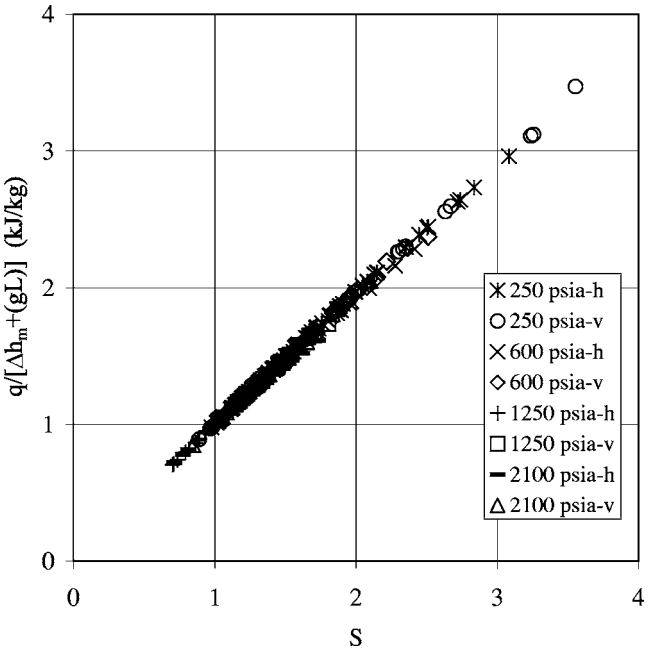

Fig. 3 New thermodynamic heat balance, which explicitly includes *S*, for saturated flow boiling

4 New Slip Ratio Correlation and Void Fraction Prediction

For horizontal flow boiling and based on previous work [6], Fig. 4 shows the new fitting equations proposed for the slip ratio, S. The water inlet velocity, $u_{L,i}$ (m/s) multiplied by S is clearly a linear function of $u_{L,i}$, which varies with the inlet pressure and the heat flux. It has also been checked at the other pressures that the straight lines, function of heat flux, are practically parallel. Therefore, it has been suggested that a parametric fitting such as

$$Su_{L,i} = u_0 + S_1 u_{L,i} \Rightarrow S = u_0/u_{L,i} + S_1 \tag{12}$$

where u_0 is the point of crossing with the ordinate axis and S_1 is the slope of the straight lines, see Fig. 4. Logically, S_1 would be the same for all the parallel lines at the same pressure and u_0 will change with heat flux.

As best fitting, we have found a potential curve to represent S_1 as a function of pressure (in MPa), see Fig. 5. Furthermore, a linear relation fits well u_0 (in m/s) as a function of heat flux ($\mathrm{kW/m^2}$) for the different pressures, see Fig. 6.

As an approximation to vertical flow, see Fig. 7, we could say that the straight lines converge at some point below $Su_{L,i}=1.0$. After checking the lines at different pressures and for the sake of generality, we have chosen a fitting such as Eq. (12), but now u_0 is fixed at 0.77 m/s for all the fluxes (straight lines) and pressures. With this restriction, we have fitted the lines to find the corresponding S_1. Figure 8 shows its behavior; at low heat fluxes, it seems that S_1 varies more or less linearly with heat flux, but after some value which depends on pressure, S_1 remains constant.

Using the fittings for S in horizontal and vertical flow (Figs. 5, 6, and 8, respectively), we can calculate the thermodynamic mix-

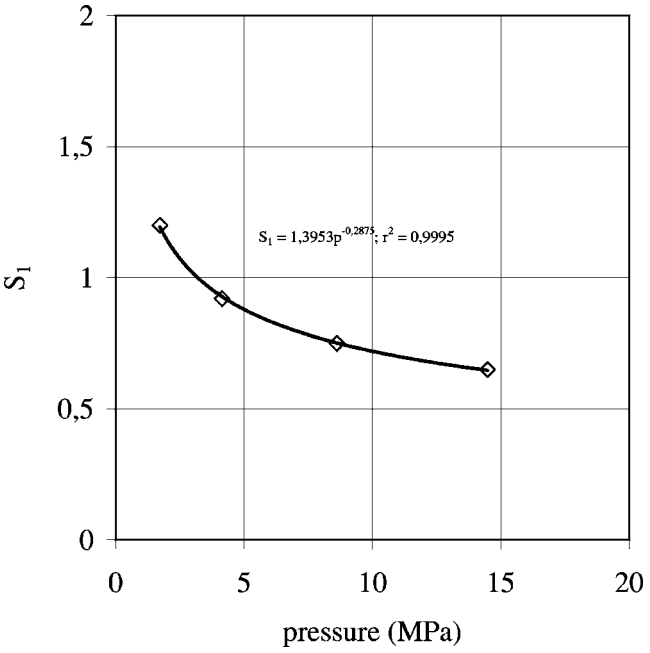

Fig. 5 Slope of the *S* correlation versus pressure for horizontal flow

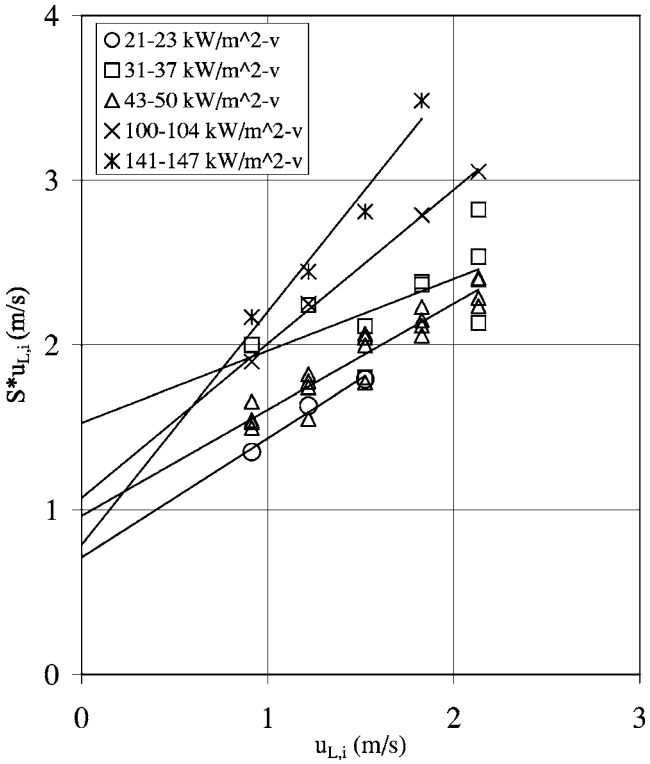

Fig. 7 *S* correlation for vertical flow at 600 psia (4.14 MPa)

ture enthalpy increment from the new heat balance, Eq. (11). So from a known inlet pressure, we can derive the outlet thermodynamic quality using Eq. (9). Finally, from Eq. (8), we obtain the predicted void fraction for horizontal flow (see Fig. 9) with a mean absolute error of 0.0019, and the predicted void fraction for vertical flow (see Fig. 10) with a mean absolute error of −0.0054.

Alternatively, following the classical procedure, we could directly insert the calculated slip ratio into Eq. (3) for obtaining the void fraction. In this case, the mean absolute error in the prediction of the void fraction for horizontal flow is −0.0014, and that of the vertical one is −0.0085.

5 Conclusions

The main result of this paper is reflected in Fig. 3, which clearly shows that, for vertical and horizontal saturated flow boiling, the slip ratio closes the heat balance between the thermodynamic mixture enthalpy increment (calculated with the measured void fraction and the densities and enthalpies of the two phases) and the heat input per unit mass inlet water.

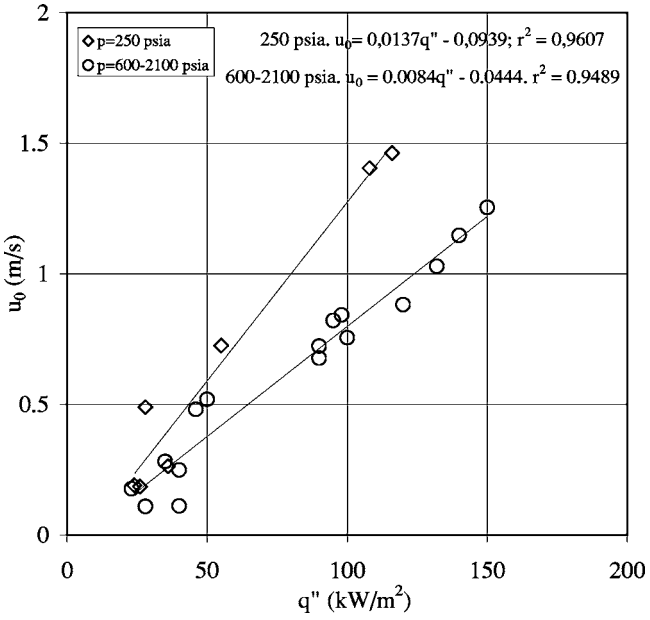

Fig. 6 Point of crossing with the ordenate axis of the *S* correlation versus heat flux for horizontal flow

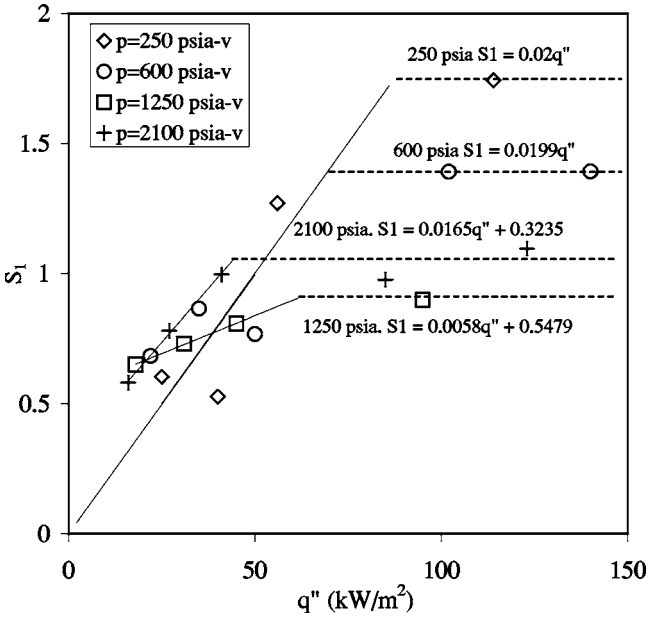

Fig. 8 Slope of the *S* correlation versus heat flux at different pressures for vertical flow

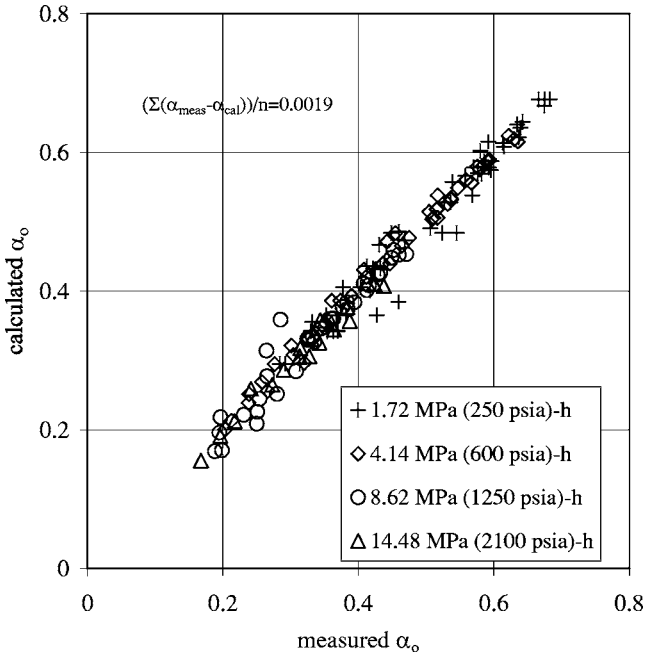

Fig. 9 Void fraction prediction in horizontal flow with Eq. (8)

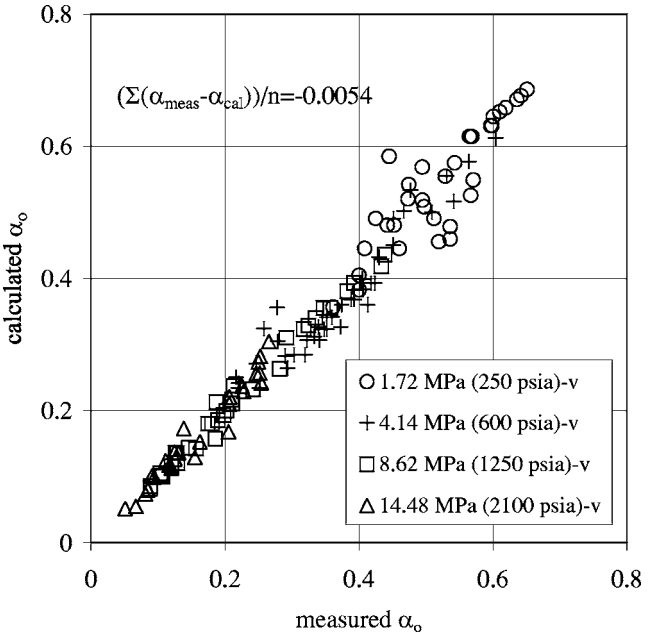

Fig. 10 Void fraction prediction in vertical flow with Eq. (8)

The validity of the suggested new heat balance for horizontal and vertical saturated flow boiling, Eq. (11), is limited to the range of the flow quality measured in [4], i.e., $x \leqslant 0.2$. However, other verifications of this new heat balance, using Thom data [5] for horizontal saturated flow boiling, was presented elsewhere [6], in which the flow quality was higher, $x \leqslant 0.8$.

The introduction of the slip ratio in the new heat balance could be justified because we consider two different velocities (two phases) in the same length (the same control volume), which would imply different time scales for the phases. This should be included in the heat balance in some manner. Thus, the slip ratio would act as a time scale factor between the phases.

New slip ratio fittings, function of the inlet pressure, and the absorbed heat flux, have also been proposed. However, more data are needed to obtain full correlations. Also the behavior of the straight line fittings for vertical flow (convergent) is rather different from horizontal flow (parallel). With the new fittings of S, the prediction of the mean outlet void fraction through the new suggested procedure is quite acceptable for saturated flow. On the other hand, the void fraction prediction through the standard equations, with the new S fittings, is of the same order of accuracy.

Finally we could say that, for saturated flow, the standard heat balance based on the flow quality and the new one proposed here using the thermodynamic quality are indeed equivalent, the difference between them merely being a time scale factor, i.e., the slip ratio S.

Acknowledgment

The authors are indebted to Dr. Geoffrey A. Knights AM. FTS., Retired Deputy Chancellor of Monash University, for his kind permission to photocopy his dissertation. The authors also want to thank to the Spanish Minister of Education and Science (MEC) the funding of this research through the special action ENE2004-0279-E and the research project DPI2005-08654-C04-04.

References

[1] Collier, J. G., 1991, "Nuclear Steam Generators and Waste Heat Boilers," in *Boilers, Evaporators and Condensers*, S. Kakaç, ed., Wiley, New York, Chap. 9.
[2] Collier, J. G., and Thome, J. R., 1994, *Convective Boiling and Condensation*, 3rd ed., Oxford University Press, Oxford, UK.
[3] Lahey, Jr., R. T., and Moody, F. J., 1979, *The Thermal Hydraulics of a Boiling Water Nuclear Reactor*, American Nuclear Society, La Grange Park, IL.
[4] Knights, G. A., 1960, "A Study of Two-Phase Pressure Drop and Density Determination in a High-Pressure Steam-water Circuit," Ph.D. thesis, Cambridge University Engineering Laboratory, Cambridge, UK.
[5] Thom, J. R. S., 1959, "A Study of Pressure Drop and Allied Phenomena During the Flow of a Fluid in the Presence and Absence of Vaporization," Ph.D. thesis, Cambridge University Engineering Laboratory, Cambridge, UK.
[6] Collado, F. J., 2001, "Mass Quality, Void Fraction and Slip Ratio in Bulk Flow Boiling," Proceedings of the IMECE 2001, Symposium on Fluid Physics and Heat Transfer for Macro- and Micro-Scale Gas-Liquid and Phase-Change Flows, HTD, New York.